

INFORMATION TO USERS

This manuscript has been reproduced from the microfilm master. UMI films the text directly from the original or copy submitted. Thus, some thesis and dissertation copies are in typewriter face, while others may be from any type of computer printer.

The quality of this reproduction is dependent upon the quality of the copy submitted. Broken or indistinct print, colored or poor quality illustrations and photographs, print bleedthrough, substandard margins, and improper alignment can adversely affect reproduction.

In the unlikely event that the author did not send UMI a complete manuscript and there are missing pages, these will be noted. Also, if unauthorized copyright material had to be removed, a note will indicate the deletion.

Oversize materials (e.g., maps, drawings, charts) are reproduced by sectioning the original, beginning at the upper left-hand corner and continuing from left to right in equal sections with small overlaps. Each original is also photographed in one exposure and is included in reduced form at the back of the book.

Photographs included in the original manuscript have been reproduced xerographically in this copy. Higher quality 6" x 9" black and white photographic prints are available for any photographs or illustrations appearing in this copy for an additional charge. Contact UMI directly to order.

U·M·I

University Microfilms International
A Bell & Howell Information Company
300 North Zeeb Road, Ann Arbor, MI 48106-1346 USA
313/761-4700 800/521-0600

Order Number 9403892

**I. Vibration isolation for gravitational radiation detectors.
II. QSO heavy-element absorption systems**

Aldcroft, Thomas Lytell, Ph.D.

Stanford University, 1993

U·M·I
300 N. Zeeb Rd.
Ann Arbor, MI 48106

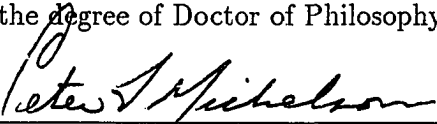
I. VIBRATION ISOLATION FOR GRAVITATIONAL
RADIATION DETECTORS
II. QSO HEAVY-ELEMENT ABSORPTION SYSTEMS

A DISSERTATION
SUBMITTED TO THE DEPARTMENT OF PHYSICS
AND THE COMMITTEE ON GRADUATE STUDIES
OF STANFORD UNIVERSITY
IN PARTIAL FULFILLMENT OF THE REQUIREMENTS
FOR THE DEGREE OF
DOCTOR OF PHILOSOPHY

By
Thomas L. Aldcroft
August 1993

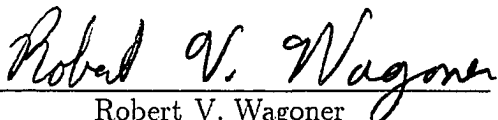
© Copyright 1993 by Thomas L. Aldcroft
All Rights Reserved

I certify that I have read this dissertation and that in my opinion it is fully adequate, in scope and in quality, as a dissertation for the degree of Doctor of Philosophy.



Peter F. Michelson
(Principal Adviser)

I certify that I have read this dissertation and that in my opinion it is fully adequate, in scope and in quality, as a dissertation for the degree of Doctor of Philosophy.



Robert V. Wagoner

I certify that I have read this dissertation and that in my opinion it is fully adequate, in scope and in quality, as a dissertation for the degree of Doctor of Philosophy.



Blas Cabrera

Approved for the University Committee on Graduate Studies:



Abstract

In Part I of the thesis we discuss passive vibration isolation systems for ultralow temperature gravitational radiation detectors, using the detector at Stanford University as the primary example. The basic theory of such isolation systems is reviewed and we describe methods of analysis for one-degree-of-freedom isolators. With these methods it is possible to derive fundamental constraints on the performance of gravitationally loaded isolators. Next we discuss general design considerations, optimization and detailed analysis of six-degree-of-freedom isolators. We conclude with experimental data from isolators designed for the Stanford gravitational radiation detector.

Part II of the thesis is concerned with the study of quasi-stellar object (QSO) absorption lines. There are two distinct classes of these lines. The first class contains the “Lyman- α forest” systems, whose physical origin is not understood. The second class is due to intervening gas-rich galaxies along the line of sight to the QSO, and is the focus of work in this thesis.

In Chapter 2 we give a comprehensive review of the empirical properties of QSO absorption line systems, including the evidence that the absorption arises because of intervening galaxies. We also give the basic foundations in cosmology, radiative transfer, and properties of the Milky Way interstellar medium which are necessary for understanding the absorption line results.

In Chapter 3 we present a sample of quasars which are lobe-dominated in their radio emission and contain Mg II absorption line systems. This sample will be useful in a search for redshifted HI 21 cm absorbers which are along lines of sight different from the optical. These systems will allow the measurement of the linear size and related physical parameters of the absorption line clouds. Since quasars appropriate

for this study are rare, building this sample requires a substantial database of radio and optical observations. We have defined a set of criteria for selecting these objects and obtained the necessary data, from the literature and from new optical and VLA observations, to assemble a sample based on these criteria. In this chapter we give an analysis of our criteria, discuss the sample, and present new VLA observations of 16 quasars. We also give a detailed overview of practical issues associated with observing HI 21 cm at high-redshift and describe our forthcoming observations at the NRAO 140 foot telescope in November, 1993.

In Chapter 4 we carry out an analysis of the statistical properties of Mg II absorbers found in a sample of 56 quasars. The details of the observations are given and we present all of the spectra which were obtained. We then describe the procedure for finding and identifying the absorption lines in a statistically complete manner. Next we give details of the statistical analysis in which the number density distribution as a function of redshift and equivalent width is calculated. We determine values of a number of model parameters for our sample alone and our sample combined with other surveys, and find they are consistent with previously published results.

Preface

In this thesis I cover a wide spectrum of subjects, ranging from the very down-to-earth vibration isolators to galaxies at the far reaches of the universe. However, underneath these apparently disconnected topics there is unity. The goal of the gravitational radiation detector is more than simply detection, but rather to provide a new probe with which to study astrophysical phenomenon such as supernovae or coalescing compact objects. In this sense it is proper to call this work *astronomical instrumentation*, albeit in the early stages, which is then complemented by the QSO absorption line study, which is *astronomical observation*. In a deeper way more related to my personal preferences, the topics covered here are similar in the way they rest on fairly straightforward theoretical foundations and require primarily hard work and diligence mixed in with a bit of innovation and creativity. This reflects my bias toward science which is not mired in volumes of equations and can be comprehensibly explained in a one hour colloquium.

There are many people deserving of great thanks for their help and support during my graduate career at Stanford. First I want to thank my parents Gary and Sue Aldcroft for their unfaltering support, which was especially important during the first year of classes. I am deeply indebted to my advisor Peter Michelson, who gave me great freedom to pursue my interests and always inspired me with his enthusiasm. Next I want to thank Jane Luu, without whose help and encouragement I never would have been able to make the leap into observational astronomy. She not only suggested applying for the NASA fellowship which gave me support in my final year, but she also introduced me to my collaborator and soon-to-be-employer Martin Elvis.

For the gravity wave work, I want to acknowledge the amazing technical skills of

Wolfgang Jung, Karl Heinz, Don Bravo, and Mike Hennessey. Without these people, fabrication and testing of the isolator would not have been possible. Bob Taber deserves credit for laying the foundation for my work and for his great insight into the issues which arose. Frank McLoughlin taught me how engineers view the isolation problem. I also want to acknowledge useful discussions with Thomas Stevenson, Rob Penny, Laurie Mann, Guy Moore and Dan DeBra. This work was supported by the National Science Foundation under grants PHY89-14914 and PHY90-20744.

For the QSO absorption line work I want to thank my collaborators, Jill Bechtold at the University of Arizona and Martin Elvis at the Harvard Center for Astrophysics. They initiated the projects on which I worked and provided invaluable comments and discussion. I want to thank Pat Nolan for his help with the Sun computer I was graciously allowed to use. Finally, I thank the NASA Graduate Student Researchers Program, who provided my support for the last year and allowed me to seriously engage in observational astronomy.

Lastly, I want to thank all the friends I have made at Stanford, and the friends I kept from Caltech, who have been responsible for making my graduate years at Stanford enjoyable.

Contents

Abstract	iv
Preface	vi
I Vibration Isolation for Gravitational Radiation Detectors	1
1 Multi-stage vibration isolation	2
1.1 Introduction	2
1.2 Stanford 4 K detector	3
1.3 Multipole isolation	8
1.3.1 Basic concepts	8
1.3.2 Internal spring resonances	12
1.3.3 Loaded isolators	14
1.4 Design considerations	17
1.4.1 General	17
1.4.2 Nonlinear processes	18
1.4.3 Material choice	20
1.5 Optimization of six-DOF isolators	21
1.5.1 Baseline design	22
1.5.2 Finite element analysis	26
1.5.3 Numerical search	26
1.6 Isolation system analysis	27

1.6.1	Finite element models	28
1.6.2	Steady state frequency response function	29
1.6.3	Impulsive excitation response	33
1.7	Matrix representation of six-DOF springs	34
1.8	Determination of six-DOF spring constants	37
1.9	Experimental results	38
1.10	Integrated suspension system	44
1.11	Discussion	46
Bibliography		47
 II QSO Heavy-element Absorption Systems		 50
2	Introduction to QSO absorption lines	51
2.1	Overview of observed properties	52
2.2	Basic picture	55
2.3	Cosmology and all that	56
2.4	Line strengths	60
2.4.1	HI 21 cm line	61
2.4.2	Optical lines	62
2.5	Milky Way disk and halo interstellar medium	63
2.6	Metal-line absorber – galaxy connection	66
2.7	Detailed empirical properties	68
2.7.1	Lyman- α forest	68
2.7.2	C IV	69
2.7.3	Mg II	70
2.7.4	Damped Ly- α	71
2.7.5	HI 21 cm	72
2.7.6	Absorber kinematics	73
2.7.7	Emission from absorption line systems	75
2.8	Discussion	76

3	Lobe-dominated quasars with MgII absorption	78
3.1	Introduction	78
3.2	Radio Sample Selection	81
3.2.1	Finding Lobe-dominated Quasars	81
3.2.2	VLA Observations	87
3.3	Finding MgII Absorption Systems	91
3.3.1	Notes on Individual Objects	93
3.4	Conclusions	95
3.5	Planned HI 21 cm observations	97
3.5.1	Sensitivity and integration time calculations	97
3.5.2	Sources of Radio Frequency Interference	99
3.5.3	Green Bank 140' Program	101
3.5.4	Future possibilities	103
4	Absorption in a sample of 56 quasars	105
4.1	Observations and data reduction	106
4.2	QSO spectra	107
4.3	Line extraction	131
4.3.1	Results of line extraction in our sample	137
4.4	Notes on individual objects	149
4.5	Statistical analysis	162
4.5.1	Sample properties	162
4.5.2	Calculation of distribution functions	172
4.6	Discussion	181
5	Conclusion	183
A	QSO absorption line analysis program	185
A.1	Building and installing	186
A.2	General Usage	186
A.3	Command summary	188
A.4	Command descriptions	190

A.4.1	Miscellaneous commands – no prefix	190
A.4.2	Spectrum manipulation commands – Prefix “s”	192
A.4.3	Plot commands – prefix “p”	194
A.4.4	Continuum fitting commands – Prefix “f”	197
A.4.5	Finding and identifying significant lines – Prefix “l”	197
A.5	Spectrum file data format	201
A.6	Parameter file keywords	202
Bibliography		204

List of Tables

1.1	Natural frequencies of antenna suspension isolator	41
2.1	Lower limits on observed HI column densities	56
2.2	Local ISM properties	64
2.3	Extragalactic HI 21 cm absorbers	73
3.1	Lobe-dominated quasars	86
3.2	VLA observations	92
3.3	Properties of MgII absorbers in lobe-dominated quasars	94
3.4	Potential sources of RFI between 500 - 1400 MHz	100
3.5	Source list for Green Bank HI 21 cm absorption observations	102
4.1	Journal of observations	108
4.2	Absorption lines in sample	138
4.3	MgII λ 2796, λ 2803 absorption lines	171
4.4	Results of statistical analysis	179
A.1	Parameter file keywords	203

List of Figures

1.1	Schematic diagram of Stanford 4 K gravitational radiation detector.	4
1.2	Wire isolator used in Stanford 4 K detector.	7
1.3	Major components of the Stanford ultralow temperature detector.	9
1.4	Frequency response function $x_N(\omega)/x_0(\omega)$	10
1.5	Schematic diagram of suspension and antenna vibration isolation system	11
1.6	Contour plot of the total isolator attenuation	16
1.7	Exploded view showing actual isolator geometry	23
1.8	One of the four antenna suspension isolators	24
1.9	Contour plot of the stress in the antenna suspension isolator	25
1.10	Predicted frequency response functions for antenna suspension isolator	32
1.11	Schematic diagram of six stage isolator	39
1.12	Experimental frequency response functions for antenna suspension iso- lator	43
1.13	Detail of antenna suspension system.	45
2.1	Typical QSO spectra	53
2.2	Schematic plot of histogram of known absorption redshifts	54
2.3	Schematic diagram of and extended halo	57
3.1	Spectral index α_{PGK} vs. spectral index α_{VCV}	83
3.2	Spectral index vs. lobe dominance in sample quasars	84
3.3	f_{LD} and f_{inc} vs. α_{cut}	85
3.4	VLA maps at 1.5 GHz and 5 GHz	88
3.5	VLA maps at 1.5 GHz and 5 GHz	89

3.6	VLA maps at 1.5 GHz and 5 GHz	90
4.1	Quasar spectra	110
4.2	Local χ^2_ν deviation and gaussian deviation for QSO spectrum	134
4.3	Rest equivalent width limits	164
4.4	Redshift path length vs. rest equivalent width limit and sightlines vs. redshift	172
4.5	Equivalent width distribution and best fit power law forms	177
4.6	Power law distribution function parameters vs. upper cutoff W_{cut}	177
4.7	Number of absorbers per unit equivalent width	180

Part I

Vibration Isolation for Gravitational Radiation Detectors

Chapter 1

Multi-stage vibration isolation

This chapter is based on a paper entitled “Six-degree-of-freedom vibration isolation systems with application to resonant-mass gravitational radiation detectors,” which appeared in the Review of Scientific Instruments journal, volume 63, page 3815. The contributing authors were Thomas Aldcroft, Peter Michelson, Robert Taber, and Frank McLoughlin. T. A. was the primary author of the paper.

1.1 Introduction

Any experiment utilizing precise measurements of motion in mechanical systems must take into account the possibility of contamination of the data due to unwanted external sources of vibrational motion. These include man-made sources and natural seismic motion. The former are *cultural disturbances* and include human activity in the lab, cars or machinery operating nearby, etc. These can be eliminated to some degree by careful control of the environment near the laboratory, but for very sensitive experiments such as a gravity wave detector this alone is wholly inadequate. The latter noise source, *seismic motion*, is unavoidable even in principle. Thus it is clear that adequate vibration isolation is of great importance in designing any sensitive experiment measuring mechanical motions.

Resonant mass gravity wave detectors are among the most sensitive motion detectors in existence, currently measuring displacements of 3×10^{-18} m or smaller at

frequencies near 1 kHz (Amaldi et al. 1990, Boughn et al. 1982). With the current generation of ultralow temperature detectors under development at Stanford University and at the University of Rome, displacements that are two orders of magnitude smaller should be observable (Michelson et al. 1988, Bassan et al. 1989). In this regime the vibration isolation system becomes a central component of the overall design. To date a number of low temperature (4 K) and room temperature resonant mass gravity wave detectors have been constructed and operated successfully, each using a somewhat different vibration isolation scheme (Michelson, Price, and Taber 1987, Coccia 1982, Karim 1984, Veitch 1991, Hamilton et al. 1989, Davis et al. 1983). However, they all share the common theme of using a multistage arrangement of inertial (mass) elements and compliance (spring) elements to form a passive multipole mechanical low pass filter. In this paper we will describe the general design, analysis, optimization and experimental characterization of such systems for use in ultralow temperature detectors, placing emphasis on higher order systems which are not amenable to exact analytical treatments. Specific details from the Stanford gravity wave detector will be given throughout the paper as illustration of the concepts presented.

1.2 Stanford 4 K detector

In order to provide the context in which to discuss the vibration isolation systems for the ultralow temperature (50 mK) gravitational radiation detector (ULTD), it is useful to digress into a brief overview of the mechanical design of both the Stanford 4 K detector and the ULTD. The theory (generation and detection of gravitational radiation) and detailed operation of these detectors have been exhaustively described in the literature and will not be reviewed here. See for example Stevenson (1991), Paik (1974), Thorne (1987), Wald (1984), and references therein.

In Fig. 1.1 we show a schematic diagram of the Stanford 4 K detector. The major components in this system are the 4800 kg aluminum bar; the transducer and SQUID electronics; the cryostat consisting of the outer vacuum can, the 77 K, 30 K, and 4 K shells; the liquid nitrogen and liquid helium reservoirs; and the suspension and

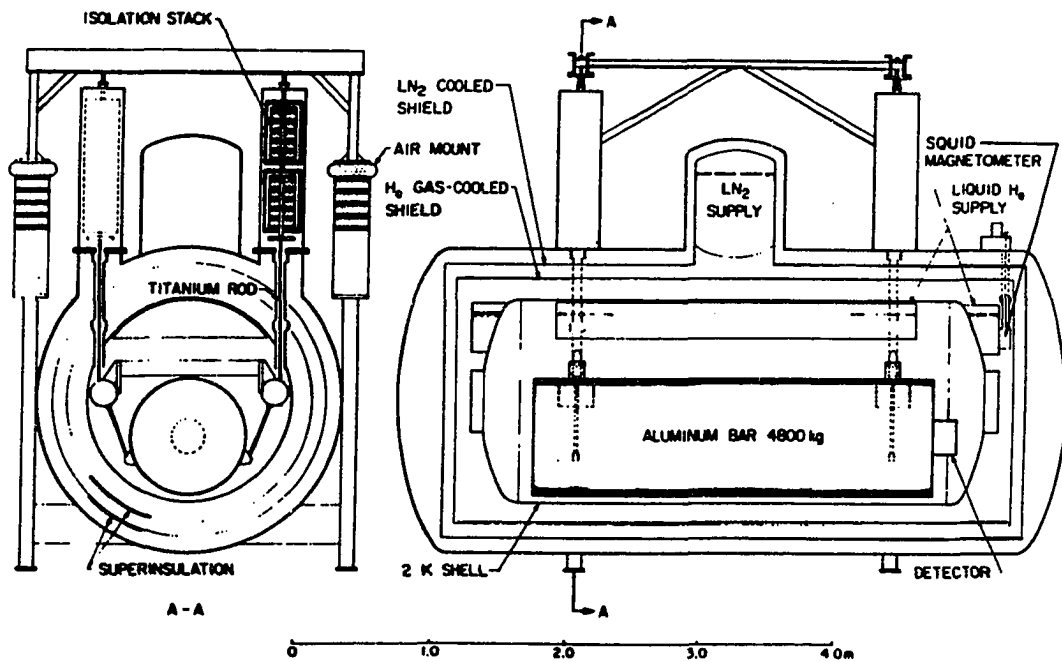


Figure 1.1: Schematic diagram of Stanford 4 K gravitational radiation detector.

vibration isolation system. One important component which is not shown is the wire isolator on which the wire leads connecting the transducer to the SQUID electronics are placed.

The antenna suspension system contains several stages of vibration isolation. It is integrated into the cryostat but is essentially an independent mechanical structure. Beginning at the ground there are four aluminum legs, each of which has at the top a five-stage rubber and steel plate mechanical filter followed by a pneumatic mount. The rubber and steel stacks provide isolation in all degrees of freedom at frequencies near the antenna frequency ~ 800 Hz. The pneumatic mounts provide low frequency isolation and in addition the pressure can be changed to make small adjustments in their vertical displacement. On top of the pneumatic mounts sits a table frame made of aluminum tubing and I-beams. From this frame hang the main isolation stacks, consisting of two sets of five-stage rubber and steel plate isolators. This structure is housed within the outer vacuum space. Note that these are necessarily in compression (the rubber has little tensile strength), and the arrangement can be seen by carefully examining Fig. 1.1. The stack is broken into two stages to avoid mechanical instabilities. Below the stack is a 1/4" titanium rod which attaches to a horizontal cross beam within the 4 K experimental space. At each end of this beam is a large aluminum mass which in conjunction with the titanium rod provides another stage of vibration isolation. Finally, there is another 1/4" titanium rod which attaches to the aluminum bar via a collet. This connection becomes quite tight under load and the modes of the final rod have a high observed quality factor, indicating low losses at the joint.

The main rubber and steel plate isolation stack has proved in operation to be quite effective, and the simple design and construction are very attractive. Straightforward analytical estimates indicate that this system gives about 200 dB of mechanical isolation from the top of the stack to the aluminum bar. Empirically it is observed during operation of the antenna that there is no significant non-thermal component to the bar excitations. Thus this level of mechanical isolation is sufficient at strain sensitivities $h \approx 3 \times 10^{-18}$. Of course this result is dependent on the input power spectrum of ground vibrations, but since the ULTD is housed in the same laboratory

in which the 4 K detector was operated for a lengthy period, we can extrapolate this result with some confidence. This bypasses difficulties associated with characterizing the ground vibrations, especially since the most important sources of noise are likely to be man-made disturbances such as pumps and heavy machinery in the laboratory.

The wire isolators which were mentioned near the beginning of this section consist of two stacks on each end. These elegant and simple isolators were designed and tested primarily by Bob Taber. Each stack has six stages of circular brass masses (approximately 4" in diameter and 1.5" thick) connected by thin steel wires. The detailed stack design is illustrated in Fig. 1.2. In the masses are machined grooves in which the lead encased wire leads are placed and packed with grease. At each end of the antenna two of these stacks were hung vertically, one from the cryostat and one from the antenna endface. The wires were run down the cryostat stack and up the antenna stack. These wire isolators are necessary because it was found during operation of the 4 K antenna that acoustic transmission down the wire leads to the transducer was sufficient to short out the vibration isolation. The wire isolators were successful in removing this problem, but in time two problems in this design became apparent.

The first problem was noticed as the result of a sporadic but very large noise component in the antenna output. Upon detailed investigation we found that when the antenna support structure was driven at a frequency near 20 Hz that the antenna had an enormous response at its resonant frequency. This frequency upconversion was traced to two steel wires in the wire isolator which were rubbing together when a particular resonant mode of the isolator was excited. This violin mode upconversion pointed out to us the importance of avoiding any sort of frictional contacts which might be subject to movement or slippage, even on a microscopic level. This led to a major constraint in the design of the isolation for the ULTD, namely that all stress bearing joints be brazed or welded. The second shortcoming of the wire isolator design became apparent in the magnitude 7.1 Loma Prieta earthquake in October 1989, when the isolators impacted against the cryostat endcaps and were destroyed. It would be quite difficult to design a system completely immune to vibrations of that magnitude, but with this experience we have designed the ULTD to be much

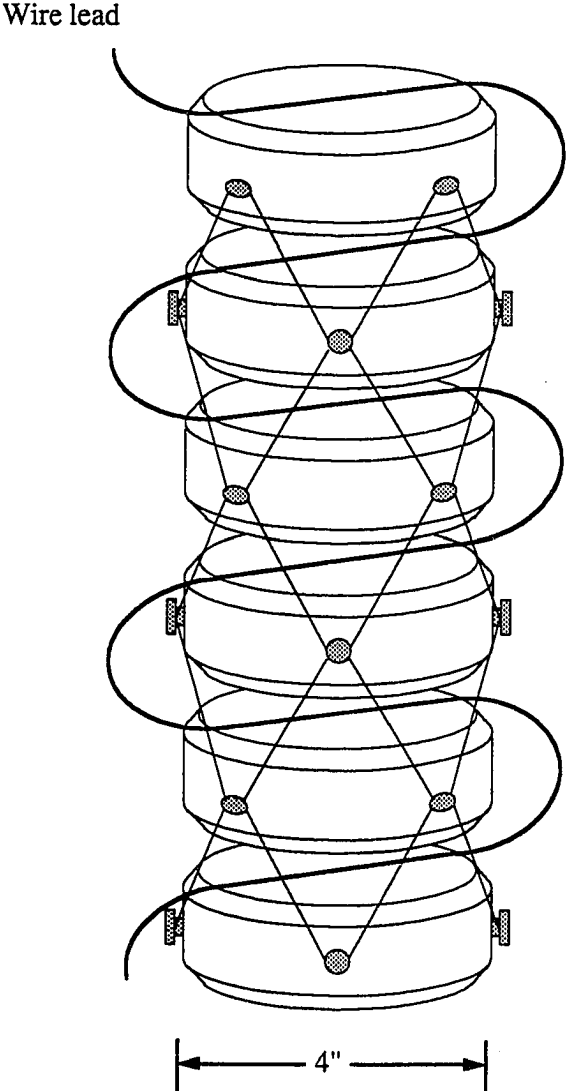


Figure 1.2: Wire isolator used in Stanford 4 K detector.

less prone to catastrophic failure of this nature. The wires are now carried down the sturdy suspension isolators.

A schematic diagram of the Stanford ultralow temperature gravitational radiation detector is shown in Fig. 1.3. The design is roughly similar to that of the 4 K system, but there are a number of major distinctions. The most obvious is of course the addition of the Oxford model 1000 dilution refrigeration unit, which will cool the antenna to a base temperature of 50 mK. At this low temperature the allowable heat leak is very much less than at 4 K, where simple liquid helium cooling is utilized. This constraint drives a number of major design changes from the 4 K system. First, the mass of the bar has been reduced to 1700 kg. Although this reduces the cross-section to gravitational radiation, the other system improvements more than compensate the reduction. Second, two more copper shields are added inside the 4 K experimental space. These must be thermally grounded to the dilution refrigerator. Third, the bulk of the vibration isolation is now also in the 4 K space. This is discussed more in Sec. 1.4. Finally, a thermal link isolator has been added to provide a direct thermal connection between the refrigerator and the bar, as shown in Fig. 1.3. Since the refrigerator is vibrationally noisy the link must also isolate mechanically. In this isolator the masses are made of low grade copper, the springs which support the static load are made of beryllium copper, and the thermal path is made of highly annealed OFHC copper.

1.3 Multipole isolation

1.3.1 Basic concepts

A single spring and mass system with one degree of freedom acts as a single stage mechanical low pass filter. The displacement frequency response function (FRF) $T_1(\omega)$ of the system is given by

$$T_1(\omega) \equiv \frac{x_1(\omega)}{x_0(\omega)} = \frac{\omega_0^2}{\omega_0^2 - \omega^2}, \quad (1.1)$$

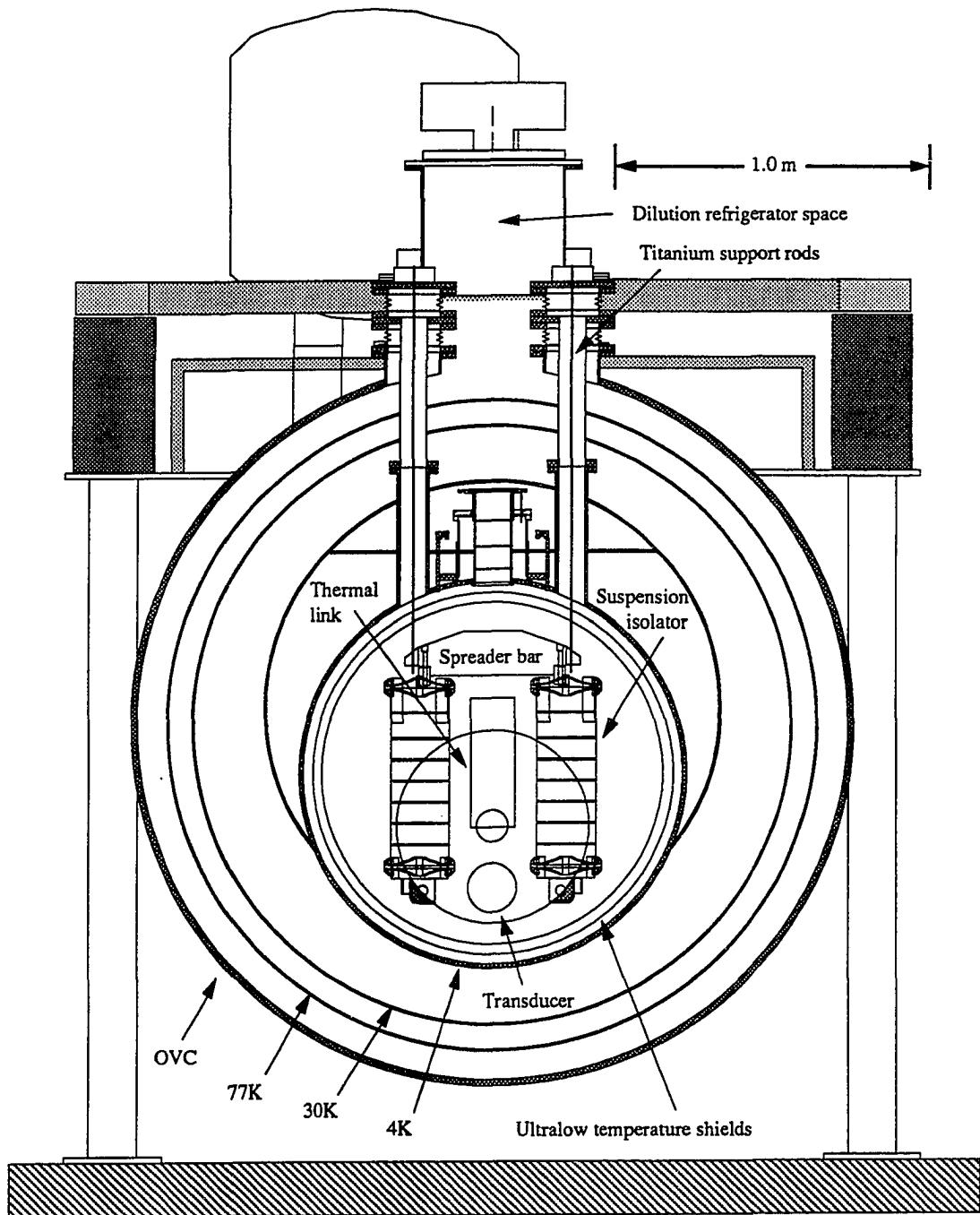


Figure 1.3: Major components of the Stanford ultralow temperature detector.

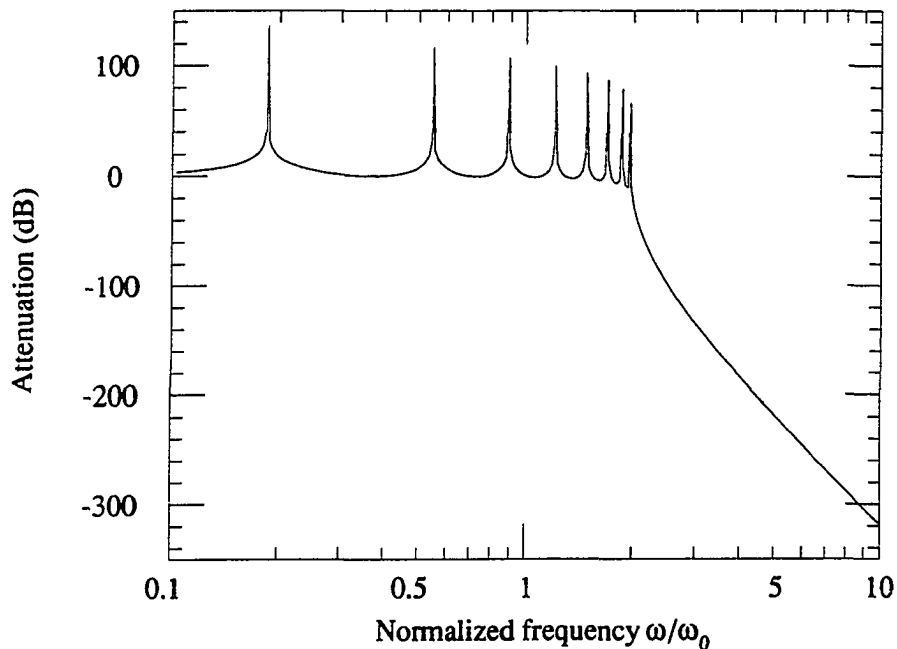


Figure 1.4: Frequency response function $x_N(\omega)/x_0(\omega)$ for an N -mass system ($N = 8$) driven harmonically with amplitude $x_0(\omega)$.

where $\omega_0 = \sqrt{k/m}$, $x_0(\omega)$ is the input displacement to the spring and $x_1(\omega)$ is the output displacement at the mass. At frequencies well above the resonant frequency ω_0 of the system there is an attenuation in amplitude equal to $(\omega_0/\omega)^2$. To achieve the required vibration isolation for a gravity wave experiment with a single such stage would require $f_0 = \omega_0/2\pi \simeq 1$ millihertz. We will show in part 1.3.3 of this section that such an isolator can not in general provide isolation at 1 kHz due to internal spring resonances. If instead one cascades N such filters the attenuation in displacement from the input to the N^{th} mass becomes $(\omega_0/\omega)^{2N}$ for $\omega \gg \omega_0$. Such a multipole low pass filter can provide the necessary isolation. Fig. 1.4 shows the frequency response function for an eight mass system. Clearly visible are the poles at each of the eight natural frequencies, with the highest mode (the cutoff frequency) near $2\omega_0$, as well as the ultimate $(\omega_0/\omega)^{2N}$ rolloff. This concept is the foundation of the design for vibration isolation systems for ultralow temperature gravitational radiation

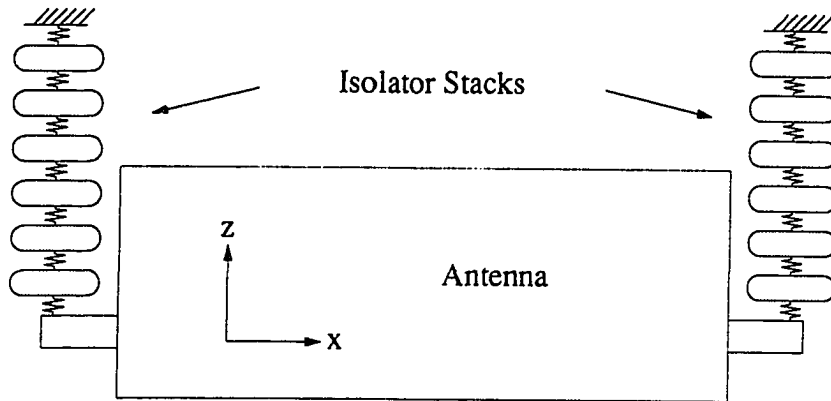


Figure 1.5: Schematic diagram showing the geometry and coordinate system of the antenna suspension and vibration isolation system which we are modeling.

detectors. Fig. 1.5 gives a schematic representation of such a system, showing the antenna being suspended at each endface by an isolation stack.

In reality vibrations in all six degrees of freedom¹ (DOF) can couple to the longitudinal modes of the antenna, so it is necessary that isolation be provided in all six DOF. Because the degrees of freedom are in general coupled an exact analysis becomes unwieldy and instead we use numerical methods, as described in Sec. 1.6.

Nevertheless, it is worthwhile to study further the case of one DOF per mass, as in Eqn. 1.1, since the equations can be solved analytically, thus affording an understanding of the structure of the solutions. For an undamped system with N spring-mass stages with spring constants k_i and masses m_i for $i = 1, N$, the displacement transfer

¹For the finite element description of the system (explained in Sec. 1.5) each point has six degrees of freedom, three translational and three rotational. This is a consequence of using rigid body dynamics to derive the equations of motion.

function from the input to the N^{th} mass is²

$$T_N(\omega) \equiv \frac{x_N(\omega)}{x_0(\omega)} = \prod_{j=1}^N \frac{(k_j/m_j)}{\Omega_j^2 - \omega^2}. \quad (1.2)$$

Here $\omega_j^2 = k_j/m_j$ and Ω_j is the j^{th} eigenfrequency of the system when it is grounded at the driving point. This response function displays the characteristic $(1/\omega)^{2N}$ rolloff as well as the poles at $\omega = \Omega_j$.

1.3.2 Internal spring resonances

Eqn. 1.2 is exact for massless springs and point masses, but in reality neither of these conditions holds perfectly. For typical gravity wave isolators (at frequencies $\leq f_A$, where f_A is the frequency of the first longitudinal mode of the antenna) the only significant deviation is due to the non-zero mass of the springs. This is manifested as an internal resonance in the spring and constitutes a short circuit in the vibration isolation. This can be intuitively seen by noting that when the isolator is driven at the spring resonant frequency, all the springs will have a substantial response, even for negligible motion of the masses. The final spring which attaches to the antenna will provide a large driving force. For one dimensional springs there are several ways of modeling the new dynamics introduced by such an internal resonance. One simple method is to model a spring with a frequency dependent stiffness $k_{\text{eff}}(\omega) = \eta(\omega)k$, where k is the static stiffness. The single stage frequency response function $T_1(\omega)$ then becomes

$$T_1(\omega) = \frac{\omega_0^2}{\omega_0^2 - \omega^2/\eta(\omega)}, \quad (1.3)$$

²This was suggested to us by G. Moore, at the time an undergraduate at Harvey Mudd College. T. R. Stevenson (Stanford University) gave us an elegant proof using the chain matrix two-port formalism of network theory.

where we still have $\omega_0 = \sqrt{k/m}$. Similarly, the frequency response function for a cascaded system of N identical springs and masses becomes

$$T_N(\omega) = \prod_{j=1}^N \frac{\omega_0^2}{\Omega_j^2 - \omega^2/\eta(\omega)}, \quad (1.4)$$

where Ω_j is the j^{th} natural frequency of the system using the *static* stiffnesses.

Now it remains to specify a form for the frequency dependence function $\eta(\omega)$. A simple approach is to demand that the FRF have another pole at a specified spring internal resonant frequency ω_i . This allows us to experimentally observe ω_i and thus determine the corrections to the calculated FRF. This gives us the single stage frequency response function

$$T_1(\omega) = \frac{1}{(1 - \omega^2/\omega_0^2)(1 - \omega^2/\omega_i^2)}.$$

Comparing with Eqn. 1.3 gives

$$\eta(\omega) = \frac{1}{1 - \omega^2/\omega_i^2 + \omega_0^2/\omega_i^2}.$$

In the following section and Sec. 1.6 we will give applications of these ideas.

The true utility of this formalism lies in the analysis of a complex six-DOF isolation system. With the techniques of modal analysis it is possible to exactly account for the internal spring resonances, using a finite element analysis package to calculate the mode shapes of the resonances. However, this procedure is difficult and computationally expensive, especially in light of the relatively small corrections it gives. A better alternative is to approximate the true frequency dependent stiffness by multiplying *all* the spring constants for the six-DOF spring by a factor $\eta(\omega)$ which reflects the known first internal resonance of the spring. This will give a conservative estimate of the actual transfer function at or below the antenna frequency.

1.3.3 Loaded isolators

To this point all the parameters in the isolation equations have been essentially arbitrary, so one might suppose that any degree of isolation could be obtained by choosing appropriate mass and spring values. However the fact that the antenna and isolator are suspended in the Earth's gravitational field imposes important fundamental constraints on both the bandwidth and the amount of vibration isolation that can be obtained. Note that we are ignoring such possibilities as active vibration isolation and using "special" features such as an exact zero in the transfer function. Both these are difficult in practice, especially for six-DOF isolators.

We start by comparing the total energy stored in a spring to the maximum permissible energy storage within the spring,

$$\frac{P^2}{2k} < \frac{V\sigma_{max}^2}{2E\zeta^2}.$$

In this expression, k is the spring constant, P is the force applied to the spring, E is the Young's modulus, σ_{max} is the maximum stress allowed, V is the spring volume and ζ is the ratio of peak stress to average stress in the spring when it is under load. For efficient springs typical values of ζ are between 1 and 2.5, depending on the detailed spring geometry. From this we can obtain a lower limit on the mass of the spring,

$$m_s = V\rho > \frac{E\rho P^2\zeta^2}{k\sigma_{max}^2}.$$

The self resonant frequency of the spring f_i can be written in the form

$$f_i = \frac{1}{S}\sqrt{\frac{k}{m_s}} < \frac{1}{S\zeta} \left(\frac{k}{P}\right) \frac{\sigma_{max}}{\sqrt{E\rho}}$$

where S is a geometric factor that results from the detailed distribution of stress, mass and compliance within the specific spring configuration chosen. Specific calculations for a variety of spring types, including simple cantilevers, helical springs and simple rods in tension, produce values of S that fall in the range between 2 and 3. The significance of S arises from the fact that it depends on the spring type, but not on

the size or material composition. We can rewrite this expression so that it specifies the minimum spring constant achievable given an intended self-resonant frequency, a specific load and particular values of the materials constants:

$$k > (S\zeta)(P f_i) \left(\frac{\sqrt{E\rho}}{\sigma_{max}} \right). \quad (1.5)$$

This result is analogous to an expression developed by Coccia (1982). Here, the materials coefficient is the reciprocal of the square root of twice the maximum energy storage per unit mass of spring material. The importance of this coefficient seems intuitively compelling. It allows us to easily rank materials for use in isolator designs as well as give definite limits on isolator performance using known materials. One can also note from this equation that since the springs are in series, the “best spring” for a given load is independent of the number of isolator masses.

As an application of these concepts we can calculate the cutoff frequency below which there is no vibration isolation for an N stage isolator which is at the limit of Eqn. 1.5. For a large N the cutoff frequency is $f_{cut} \approx 2f_0$ where f_0 is the resonant frequency of a single spring-mass pair. Using $P = (M_I + M_A)g$ where M_I is the total mass of the isolator, M_A is the mass of the antenna and g is the gravitational acceleration, we can rewrite Eqn. 1.5 as

$$k > (S\zeta\beta)M_I f_i \left(\frac{g\sqrt{E\rho}}{\sigma_{max}} \right).$$

Here $\beta = (M_I + M_A)/M_I$ and gives the ratio of mass which must be supported against gravity to inertial mass available for isolation. The last term in parentheses is a characteristic “frequency” of the material, f_m . Thus we have

$$f_{cut} \approx \frac{2}{2\pi} \sqrt{\frac{k}{m}} = \frac{1}{\pi} \sqrt{\frac{kN}{M_I}} > \frac{1}{\pi} [(S\zeta\beta)(f_i f_m)N]^{1/2}. \quad (1.6)$$

The significance of this expression is that, within the limiting assumptions outlined at the beginning of this section, no purely passive vibration isolation system which is suspended in a gravitational field can provide a substantial amount of isolation at

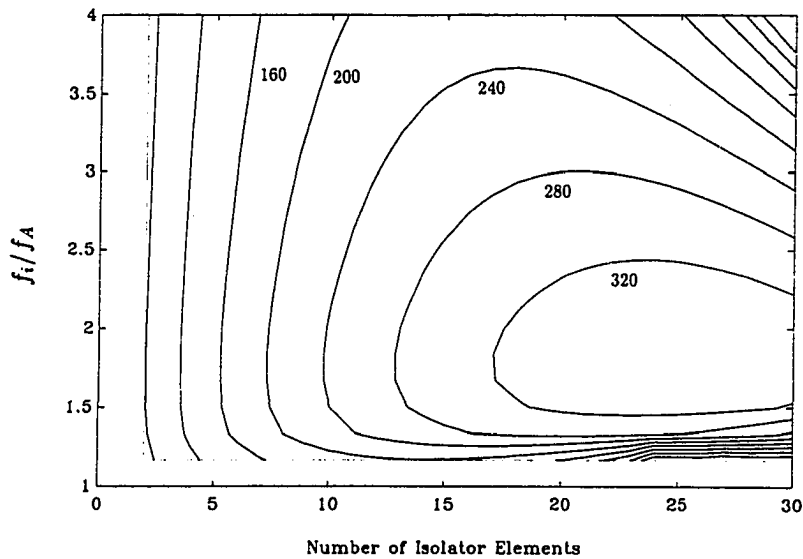


Figure 1.6: Contour plot of the total attenuation in decibels for a one dimensional multistage isolator as a function of f_i/f_A and the number of isolator masses. Here f_i is the spring internal resonance frequency and f_A is the antenna frequency.

frequencies near f_m or lower. For typical materials, f_m is on the order of a few hertz, and for aluminum $f_m = 4.5$ Hz. As an example, if the spring internal resonance is $f_i = 2.0$ kHz, $\zeta = S = \beta = N = 1$, then $f_{cut} > 30$ Hz. These numbers represent firm limits on the bandwidth over which isolation can be provided. For more realistic numbers ($\zeta = S = 2$, $\beta = N = 10$), then $f_{cut} = 600$ Hz.

We can also calculate the total attenuation as a function of the number of stages N and the spring internal resonance frequency f_i , given a specified volume for the isolator and values for the remaining system parameters. Using Eqns. 1.4 and 1.6 and parameters typical of the Stanford gravity wave detector yields the results shown in Fig. 1.6. This shows a contour plot of the total attenuation in decibels as a function of f_i/f_A and the number of isolator masses, where f_i is the spring internal resonance frequency and f_A is the antenna frequency. The plot indicates that the optimum is near $N = 20$ and $f_i = 1.7f_A$. However, other considerations preclude the use of such a high number of stages. At $N = 20$ the cutoff frequency of the filter f_{cut} is perilously close to the antenna frequency and so small changes in the system parameters could result in significant degradation of the isolation. Furthermore, N can be limited by the

physical dimensions of reasonable spring designs which meet the stress requirements discussed in Sec. 1.4, or because this simple optimization neglected the fact that the volume occupied by an individual spring is fixed, so for large N the volume of the springs becomes comparable to the volume of the masses. For the Stanford antenna suspension isolators the physical dimensions of the springs restricts N to be less than 10.

1.4 Design considerations

There are a number of factors which must be taken into account in the design of a vibration isolation system. These considerations encompass both the global features of the system as well as details of the mass and spring elements which comprise the isolator. Although the following discussion will generally be applicable to any vibration isolation system, many of the points only present a design challenge in the context of isolators which are subject to significant stresses, for example the antenna suspension isolators.

1.4.1 General

The first requirement of a vibration isolation system is that it provide the necessary isolation in all six DOF. Even though it may appear that certain couplings to the longitudinal modes of the antenna are geometrically or otherwise forbidden (for instance motion perpendicular to the axis of the antenna), detailed analysis will usually show them to be suppressed by no more than a factor of 60 dB. This is inadequate isolation for gravity wave detectors and thus the spring elements must have compliance in six DOF. There are also requirements specific to different kinds of isolators. For instance, an antenna suspension isolator must be able to support the weight of the antenna, and a thermal link between the dilution refrigerator (which cools to ultralow temperatures) and the antenna must have an adequate thermal cross section.

For ultralow temperature detectors, thermal considerations require that there be

several ultralow temperature shields surrounding the antenna and that the suspension rods supporting the antenna be thermally grounded to these shields (Chiang and Michelson 1989). This then allows two choices in the overall design of a vibration isolation system. The first possibility is to have most of the isolation outside the cryostat at room temperature. Previously, the Stanford group has built and successfully operated a 4 K detector using such a scheme. However, in an ultralow temperature detector there would be the added requirement that the entire dilution refrigeration system and low temperature shields be vibrationally isolated. We feel that this is too cumbersome and unreliable. Instead, the isolation is placed completely within the ultralow temperature environment and hence the isolation design is separated from the refrigerator and cryostat design. This imposes the very important constraint that the spring elements must retain their compliance at low temperature, thus precluding the use of rubber pads as spring elements as in existing detectors. In addition, the space available within the ultralow temperature environment for the isolators is limited, and thus the overall volume of the isolators becomes a major factor in the design.

A diagram showing the major components of the Stanford ultralow temperature gravity wave detector is given in Fig. 1.3. We see that the volume for each isolator of the antenna suspension isolators is limited and that space on the end faces of the antenna must be kept available for the transducer, the dilution refrigerator thermal link and other instrumentation and hardware.

1.4.2 Nonlinear processes

Reducing the possibility of nonlinear processes is a major driving factor in many facets of the design, especially for an antenna suspension isolator. The most important consequence of a nonlinearity is the upconversion of low frequency excitations in the passband of the filter to high frequencies near that of the antenna. There are several mechanisms by which this can occur.

Perhaps the most obvious source of nonlinearity is creaking. If there are cracks in the joints of the suspension they can creak as the result of a large low frequency excitation. Cracks can also serve as stress concentration points, resulting in localized

hysteretic deformation of the material, which in turn results in the emission of broadband acoustic energy. The process of acoustic emission in highly stressed materials has been widely studied by the mechanical engineering community (Larsen 1979). The significance of these studies to the isolator design problem is that all components should be kept as far from their elastic yield points as possible - an objective that is at odds with the desire to keep the elastic components of the isolators as compliant and as compact as possible. A reasonable design goal is to keep the maximum stress within any of the isolator components at a value below 10% of the 0.2% yield stress. This value is suggested by the absence of measurable creep at low temperature in materials such as copper stressed at this level or lower (Tien and Yen 1984).

Simple pressure joints between isolation elements can also be a cause of upconversion, as there can be slippage on a microscopic scale. Moreover, since the mating surfaces cannot be made perfectly flat there are bound to be localized regions of stress concentration, with the resulting possibility of acoustic emission. This leads to the requirement that all highly stressed mechanical joints either be welds, brazes or other bonds of similar quality. Note that we feel that pressure joints are allowable in non-stressed elements, such as the wire lead mounts on the Stanford antenna suspension isolators, which are screwed in place. This is a tremendous convenience in the assembly and debugging of the detector. However, should these joints prove to be a source of excess noise during operation they can be welded or brazed at that time without serious redesign.

For most of the highly stressed joints in the Stanford antenna suspension isolators we have used the process of aluminum dip brazing, whereby one can make high quality aluminum to aluminum brazes. Application of filler alloys to the joint interfaces allows capillary action to take place when the assembly is immersed in a special superheated salt solution. Since the part is slowly pre-heated to just below the salt bath temperature, there is uniform heating and cooling throughout the assembly so that stresses are minimized.

As a further precaution against upconversion, some sort of six-DOF dampers should be placed on the isolators, especially those made of materials with high intrinsic quality factors (McLoughlin 1990). If the Q is high then seismic and cultural

disturbances in the passband of the filter can produce very large RMS excitations in the isolators. This leads to high dynamic stresses and the associated risk of acoustic emission. A simple analysis shows that $\langle x(t)^2 \rangle \propto Q$ where $x(t)$ is a typical motion in the isolator and Q is the quality factor of the modes. A good goal is to design the dampers to reduce the Q of all isolator modes to a level such that the dynamic stress in the isolator is less than 10% of the static stress due to the antenna load. This must be done without significant degradation of the antenna Q or the overall vibration isolation. For the Stanford antenna suspension isolators, Frank McLoughlin has designed and tested a six-DOF eddy current damper as part of his PhD thesis on optimal damping design (McLoughlin 1990). An important observation discussed in this thesis is that almost any damping mechanism will be somewhat nonlinear, which implies that the dampers should be placed near the top of the isolator stack so that any signals upconverted by the damper can be effectively attenuated.

1.4.3 Material choice

There are a number of factors that enter into the choice of material for fabrication of the isolators. From a purely theoretical standpoint, the mass density and the energy storage capability per unit mass are the two key elements. These determine the amount of isolation that can be attained within the previously mentioned constraints. From the materials coefficient in Eqn. 1.5 we calculate that beryllium copper, titanium and cold worked stainless steel are among the materials with the highest energy storage capacity. Aluminum is also good in this respect.

There are also important practical considerations in the material choice, including cost, ease of machining, quality of joints within the isolator and quality of the final joint to the antenna. For an aluminum antenna, aluminum is excellent in all four of these factors, while each the other three materials mentioned is marginal in at least one of the factors. The quality of the final joint to the antenna is an issue in light of the fact that aluminum has a very high thermal contraction coefficient (0.4% from 300 K to 4 K) so care must be taken in making any transitions to different materials so as to avoid high stresses due to differential thermal contraction. Such a transition is, however, possible, as in the case of the Stanford thermal link which is made of

copper. For this interface we can arrange a press fit in which the differential thermal stresses are kept small.

1.5 Optimization of six-DOF isolators

In Secs. 1.3 and 1.4 we presented the general features and specific constraints of the design for a six-DOF vibration isolation system. We now address the problem of optimizing the design for maximum isolation. We showed previously for one dimensional systems that for a load bearing isolator there is a lower limit on the spring constant achievable. This implies that there is a “best spring” for a given isolator which is independent of position within the isolator and so we can narrow the problem to optimizing the design of a single spring element. The two major ingredients for this procedure are a baseline design for the spring and mass elements, and method for calculating the properties of a particular realization of the baseline design. With these tools we can search for an optimal spring design.

There is an obvious and substantial practical benefit obtained by adopting a single spring design for all of the sites with the isolator, but it is worthwhile to question whether a simple generalization of the one dimensional model overlooks optimization possibilities which might yield improved performance. There are two possibilities to consider. First, the load-bearing problem only arises in the vertical direction, so one could hope to adopt a strategy that would provide very much greater performance for the other degrees of freedom. The second possibility worth considering is that there might be some benefit obtained by varying the transverse stiffness of the isolator as a function of vertical position. Some of the modes of the isolator will have the approximate form of the bending modes of a beam. For such modes, the quantitative influence of springs near the middle of the isolator will be different than that of the springs at the ends.

It appears that neither one of these strategies actually offers more than a modest improvement. In the case of the first approach, the problem is that the total mass of each spring is dictated by the gravitational stress and so a large compliance in any direction will produce internal spring resonances that have harmfully low frequencies.

In the case of the second approach, the important consideration is that the modes with the highest frequencies are the ones that are most significant in determining the isolation above the cutoff frequency, and these modes are governed by the individual spring stiffnesses in a more uniform manner.

1.5.1 Baseline design

The baseline design gives the general geometry and topology of the isolator and its elements, and it is specified by a small number of dimensional and physical parameters. The principles which guide the spring design for one-DOF isolators were quantified in Sec. 1.3 and we can use those same ideas to generate the baseline spring and mass design for a six-DOF isolator which can be numerically optimized. The key factors to consider are the spring compliances in six DOF, the mass and rotational inertias of the mass, the internal spring resonances and the static stress distribution under load. The baseline design should allow adequate variation of each of these factors.

For the Stanford antenna suspension isolators we considered a number of spring geometries and settled on a configuration in which a central mass is surrounded by four semi-circular spring elements. This is illustrated in Fig. 1.7, which shows an exploded view of three masses and an example of how a single spring connects two masses. Also shown is the spring from several different angles and the isolator “ear” which is used to attach the spring to the mass. In Fig. 1.8 we see a complete isolator. Further details of the baseline spring design follow from trying to avoid stress concentration (especially near the joints) and keeping fabrication relatively simple. The final result for the baseline design is a circular arc spring which can subtend any angle between $\frac{1}{4}$ turn and $\frac{3}{4}$ turn. This acts partly as a cantilever and partly as a torsional spring. The taper in the height of the spring serves to move the stress away from the joints. This is illustrated in Fig. 1.9, which shows a typical contour plot of the stresses which develop in the spring when loaded with the antenna weight.

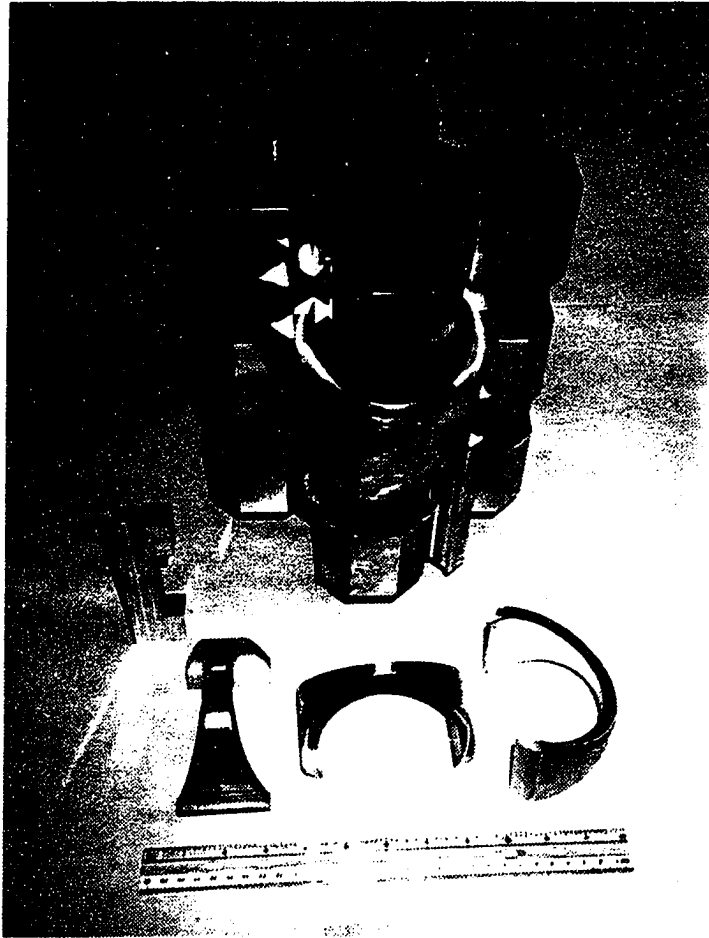


Figure 1.7: Exploded view showing how the isolator masses fit together, as well as the isolator spring from several angles and the isolator “ear” which connects the spring to the mass.

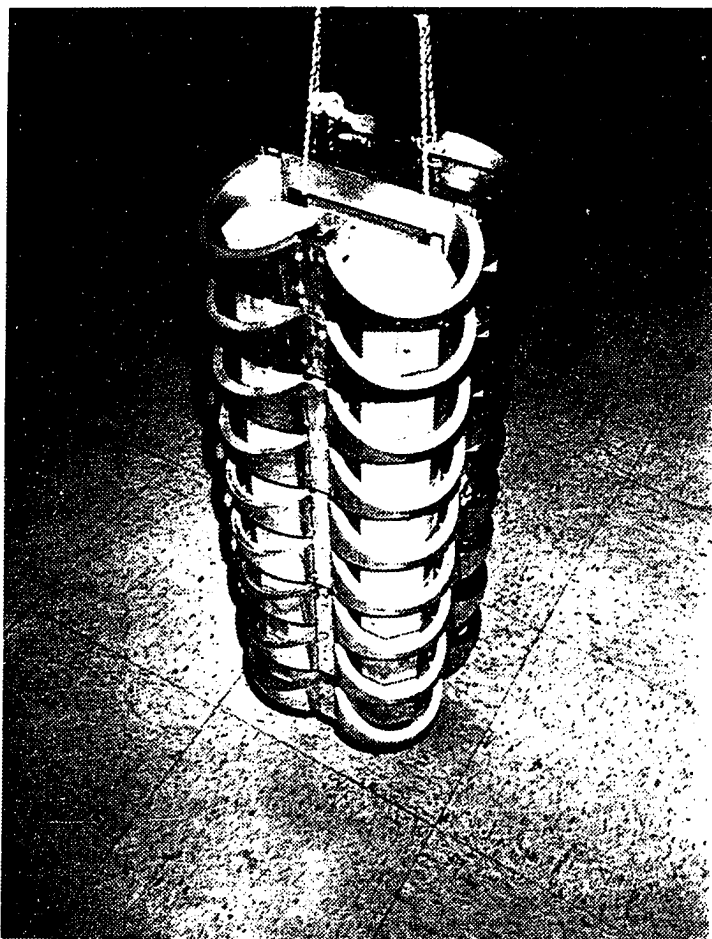


Figure 1.8: One of the four antenna suspension isolators which will be used in the Stanford ultralow temperature detector.

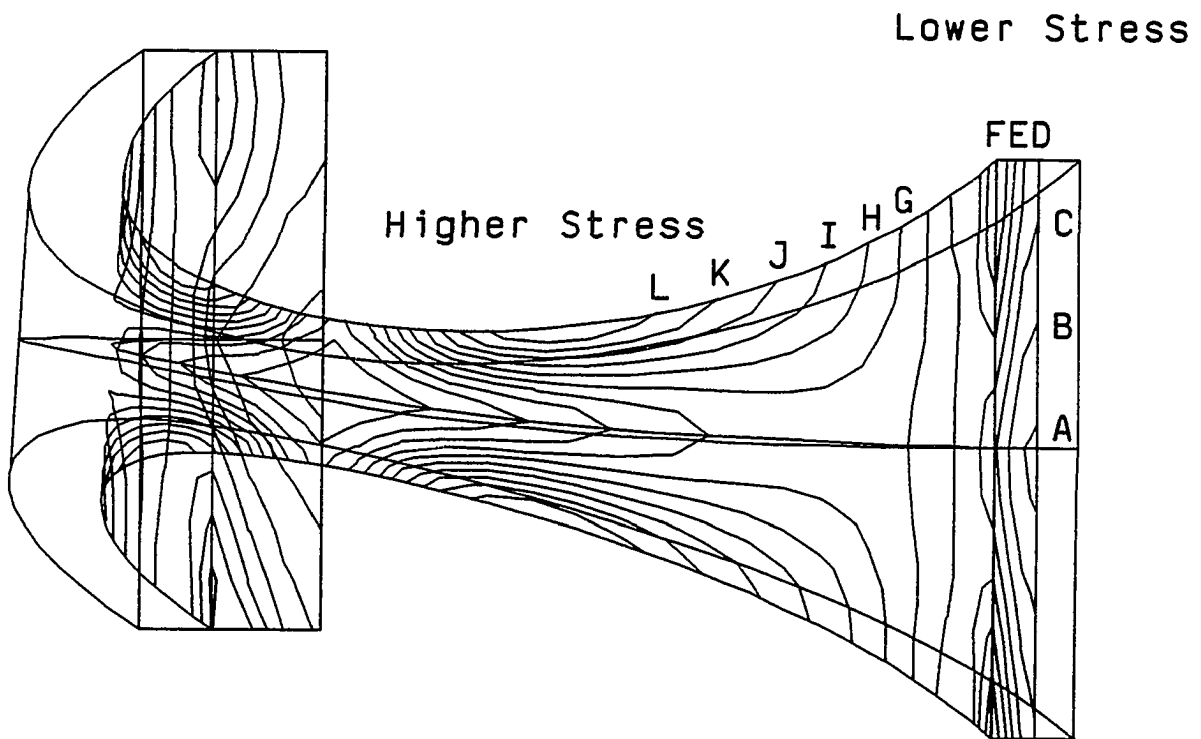


Figure 1.9: Contour plot of the stress in the antenna suspension isolator spring due to the gravitational load of the antenna. "A" corresponds to the lowest stress and "L" corresponds to the highest stress.

1.5.2 Finite element analysis

A vibration isolation system generally consists of a number of complicated three dimensional solid objects. An analytical characterization of the complete dynamics of such a system via the equations of elasticity of materials is essentially impossible. Far more preferable are numerical finite element models (FEM) which are generated and analyzed with the aid of computers. These afford a great deal of versatility in being able to solve for the dynamics of numerous different system configurations, such as different geometries or materials, within one calculational framework. In finite element analysis the values of normally continuous physical variables (such as displacement, stress or temperature) are calculated only at a finite number of locations, or nodes, which define the model. The equations governing the variables are reformulated for the discrete grid and then solved numerically.

For the optimization procedure we need a detailed characterization of a single spring element, which includes calculation of the stiffness properties, the stress distribution under load and the internal resonance structure. This can be done using a general purpose commercial finite element analysis (FEA) package such as GIFTS³ or ANSYS⁴. These programs allow for the input of a three dimensional solid model which is then broken down into numerous small cubic or tetrahedral elements for which the equations of elasticity can be solved approximately. We will refer to this detailed model of the spring element as the SPRING model.

1.5.3 Numerical search

The actual optimization procedure consists of a broad search through the phase space of possible baseline spring and mass parameters. In each case we use the SPRING model and the FEA program to calculate the compliance of the spring in the vertical direction as well as the maximum stress, using the Von Mises stress criterion (Stevenson and Callander 1974), which develops due to the load of the antenna. The

³CASA/GIFTS Inc., Country Club Office Plaza, 2761 N. Country Club, Tucson, AZ 86716.

⁴Swanson Analysis Systems Inc., PO Box 65, Houston PA, 15342.

compliance in one or more of the other degrees of freedom can also be calculated, depending on the available computing power. We then define a utility function with which to rank the springs. This function includes a cut on springs in which the static stress is too large and a factor utilizing the internal resonance frequencies of the spring, the compliances and the maximum mass that the spring shape allows. With this utility function we can then identify promising regions in phase space and perform further calculations with smaller variations in the parameters. With sufficient care in choosing the utility function and the parameter variations it is possible to optimize the spring design.

For the Stanford antenna suspension isolators there are four spring parameters (outer radius, wall thickness, height and bevel angle) which can be varied, so if we choose three values for each parameter we must run the program for a total of 81 models. We have followed this procedure and arrived at an optimal design for the springs and masses. Using this design we have fabricated the first of four antenna suspension isolators and we present an experimental characterization of the isolator in Sec. 1.9

1.6 Isolation system analysis

Calculating the theoretical performance of a six-DOF vibration isolation system is a non-trivial problem. The primary challenge lies in generating a numerical model which is accurate and computationally tenable. In Sec. 1.6.1 we describe a procedure for producing such a model. In Secs. 1.6.2 and 1.6.3 we discuss two methods by which we can use this model to characterize the performance of a vibration isolation system. In the first method we calculate a response function similar to a force-force transfer function but which is modified so as to be more appropriate to the gravity wave detector. In the second method we calculate the maximum impulsive force we can deliver to the top of an isolator stack which is not detectable for a given a detector noise temperature.

1.6.1 Finite element models

We wish to generate a numerical model of the isolation system together with the gravity wave antenna. Modeling this entire system at the same level of detail used in the SPRING model is beyond the capability of typical workstation computers. Fortunately this is not necessary because in the frequency range of interest (near or below the first longitudinal mode of the antenna) a well designed isolation system conveniently divides into two classes of elements, compliance and inertial. The compliance elements (springs) are much more compliant and much less massive than the inertial elements (masses). Thus it is a good approximation to model the system as a series of six DOF point masses connected by massless springs. As was mentioned in Sec. 1.3 this approximation can be improved by giving the springs a frequency dependent spring constant which accounts for their non-zero mass. Each point mass is characterized by a 6×6 symmetric mass matrix which is often diagonal, having the total mass and the three principal moments of inertia along the diagonal. Each spring is specified by a 12×12 symmetric stiffness matrix which has five independent parameters. These matrices form the basis for a lumped-element analysis of the system, the details of which are given in Sec. 1.7. The antenna is modeled as a series of beams of a circular cross section. We use several nodes in the antenna, instead of the usual single effective mass and spring constant formulation, to accurately represent the system dynamics far from the first longitudinal mode. This model of the isolation system and the gravity wave antenna, consisting of point masses, massless six DOF springs and a series of beams, is denoted by SYSTEM . We also have a model called ISOLATOR which uses the same stiffness and mass elements, but contains only a single isolator and no antenna.

Computing the mass matrix for each mass in the isolator reduces to computing its mass and moments of inertia. To calculate the 12×12 stiffness matrix which connects the masses we begin by making a detailed model (using a commercial FEA package) consisting of two isolator masses connected by one or several of the SPRING model(s) discussed in the optimization section. As an example the Stanford antenna suspension isolators have four semi-circular springs surrounding the masses in a cloverleaf pattern. We then compute the first six resonant frequencies of this structure, which along with

the known inertial properties of the masses allows us to derive the stiffness matrix parameters. The details of this analysis are given in Secs. 1.7 and 1.8. This analysis gives us a single equivalent six-DOF spring connecting the center of masses of the two masses.

If the SPRING model has a large number of nodes we can greatly facilitate the resonant frequency calculations for the two mass model by condensing the stiffness matrix of the spring to form a *constrained substructure* which has only a small number of nodes on each end of the spring. The condensed stiffness matrix gives an approximate representation of the stiffness elements connecting the two ends of the spring. For dynamic calculations such as determination of natural frequencies the condensed model is a good approximation provided the mass of the substructure (the spring) is much less than the mass of the rest of the model (the mass). This is typically the case.

1.6.2 Steady state frequency response function

In Sec. 1.3 we characterized a one-dimensional multi-mass vibration isolation system by defining the transfer function $T_n(\omega) = x_n(\omega)/x_0(\omega)$, where $x_n(\omega)$ is the motion of the n^{th} mass at frequency ω . In the case of an actual vibration isolation system this approach is inadequate for three reasons. First, there are six DOF per mass and several of the DOF are in general coupled so that the simple analytical methods of Sec. 1.3 no longer apply. Instead we write down and solve the coupled system of linear differential equations in matrix notation. Second, the output of interest is not the motion of the final mass of the isolator but rather the motion of the end face of the antenna. This is significant because the antenna is by definition resonant at the frequencies of interest and we wish to characterize the isolation in a way which is independent of that resonance. In particular, our results should not depend strongly on the antenna quality factor. Third, we must specify a total of six FRF, since there are six input DOF and one output DOF (the antenna). Note that since we prefer to present dimensionless FRF, we always assume a typical length scale over which the angular variables act. In this way they have the same dimensions as the antenna output (either force or displacement).

The two most obvious choices for the FRF are displacement-displacement or force-force. The first choice, the ratio of displacement of “ground” at the input of the isolator to the displacement of the end face of the antenna, is in some sense more intuitive, but is actually less relevant in calculating ultimate detector sensitivity. A more relevant quantity is the ratio of the force applied to the top of the isolator to “equivalent force” at the antenna (this has been called the force “referred to the antenna input” in previous papers). Equivalent force is the force applied to the end face of the antenna along its axis that reproduces the antenna displacement caused by the force at the top of the isolator. This is useful for two reasons. First, this function is well behaved and smooth near the antenna resonance and second, it allows for a more direct comparison to known quantities such as the Brownian motion noise force and the effective tidal force due to a gravitational wave. Note that this formulation is essentially one dimensional, where equivalent force and antenna displacement are taken to be scalars. In the following analysis we will generalize this to our six-DOF models.

The dynamics of the SYSTEM model for a harmonic motion $\vec{X}(t) = \vec{X}e^{i\omega t}$ are governed by the equation

$$-\omega^2\mathbf{M}\vec{X} + i\omega\mathbf{B}\vec{X} + \mathbf{K}\vec{X} = \vec{F}, \quad (1.7)$$

where \mathbf{M} is the symmetric positive definite mass matrix, \mathbf{K} is the symmetric positive semi-definite stiffness matrix and \mathbf{B} is the viscous damping matrix. We calculate \mathbf{B} by assuming a quality factor Q_A for the antenna and Q_I for each of the six modes of a single spring-mass pair in the isolator. The generalized displacement and force vectors \vec{X} and \vec{F} for this N DOF system are in the form

$$\vec{X} = \begin{Bmatrix} \vec{x}_1 \\ \vdots \\ \vec{x}_N \end{Bmatrix}, \vec{x}_m = \begin{Bmatrix} x_{m,x} \\ x_{m,y} \\ x_{m,z} \\ \theta_{m,x} \\ \theta_{m,y} \\ \theta_{m,z} \end{Bmatrix}, \vec{F} = \begin{Bmatrix} \vec{f}_1 \\ \vdots \\ \vec{f}_N \end{Bmatrix}, \vec{f}_m = \begin{Bmatrix} f_{m,x} \\ f_{m,y} \\ f_{m,z} \\ \tau_{m,x} \\ \tau_{m,y} \\ \tau_{m,z} \end{Bmatrix}.$$

Thus \vec{x}_m gives the translational and angular displacement for node m and \vec{f}_m gives the force and torque acting on node m .

Solving Eqn. 1.7 for \vec{X} gives $\vec{X} = \mathbf{G}(\omega)\vec{F}$ with $\mathbf{G}(\omega) = (-\omega^2\mathbf{M} + i\omega\mathbf{B} + \mathbf{K})^{-1}$. To calculate the force-force frequency response function defined previously we first consider a perfect transducer which is sensitive only to motion along the longitudinal axis of the antenna, which we take to be the \hat{x} direction. In this case the antenna displacement D^A due to a force at the antenna endface is $D^A = X_a^A = G_{aa}f^A$, where a is the DOF corresponding to the \hat{x} DOF of the endface of the antenna. Similarly, the antenna displacement D_i^I due to a force in the i^{th} DOF is $D_i^I = X_a^I = G_{ai}f^I$. In reality, however, the transducer can be mounted off the axis of the antenna (as is the case for the Stanford ultralow temperature detector) and can have non-zero coupling to motion in other DOF. We can lump both of these effects together in one sensitivity function S_j which gives the transducer response due to a motion in the j^{th} DOF of the antenna endface. As a worst case estimate we can write $D_i^I = \sum_{j=1}^6 |S_j G_{a-1+j,i} f^I|$. The expression for D^A is unchanged. From the definition of equivalent force and the expression for D^A , we see that the equivalent force is given by $f_i^{EQ} = D_i^I / G_{aa}$. The FRF as a function of ω is then

$$T_i(\omega) \equiv \frac{f_i^{EQ}}{f^I} = \sum_{j=1}^6 \frac{|S_j G_{a-1+j,i}(\omega)|}{G_{aa}}. \quad (1.8)$$

Note that for the angular input forces (torques about x, y, z) we implicitly divide f^I by the typical length scale of a single isolator stage so that it has the dimensions of force.

Using Eqn. 1.8 we have calculated the six FRF for the Stanford antenna suspension isolators corresponding to the six input DOF of the top mass of one of the isolator stacks. These are shown in Fig. 1.10. There are a number of details of this calculation which need to be mentioned: the \hat{x} DOF is along the antenna axis and the \hat{z} DOF is in the vertical direction; we have used an internal spring resonance of 2.5 kHz, which is the value calculated with the SPRING model; for the angular DOF we have used a length scale of 10 cm over which torques act; the sensitivity function was derived by assuming a 2% coupling to motion in the \hat{y} and \hat{z} directions and 10 cm

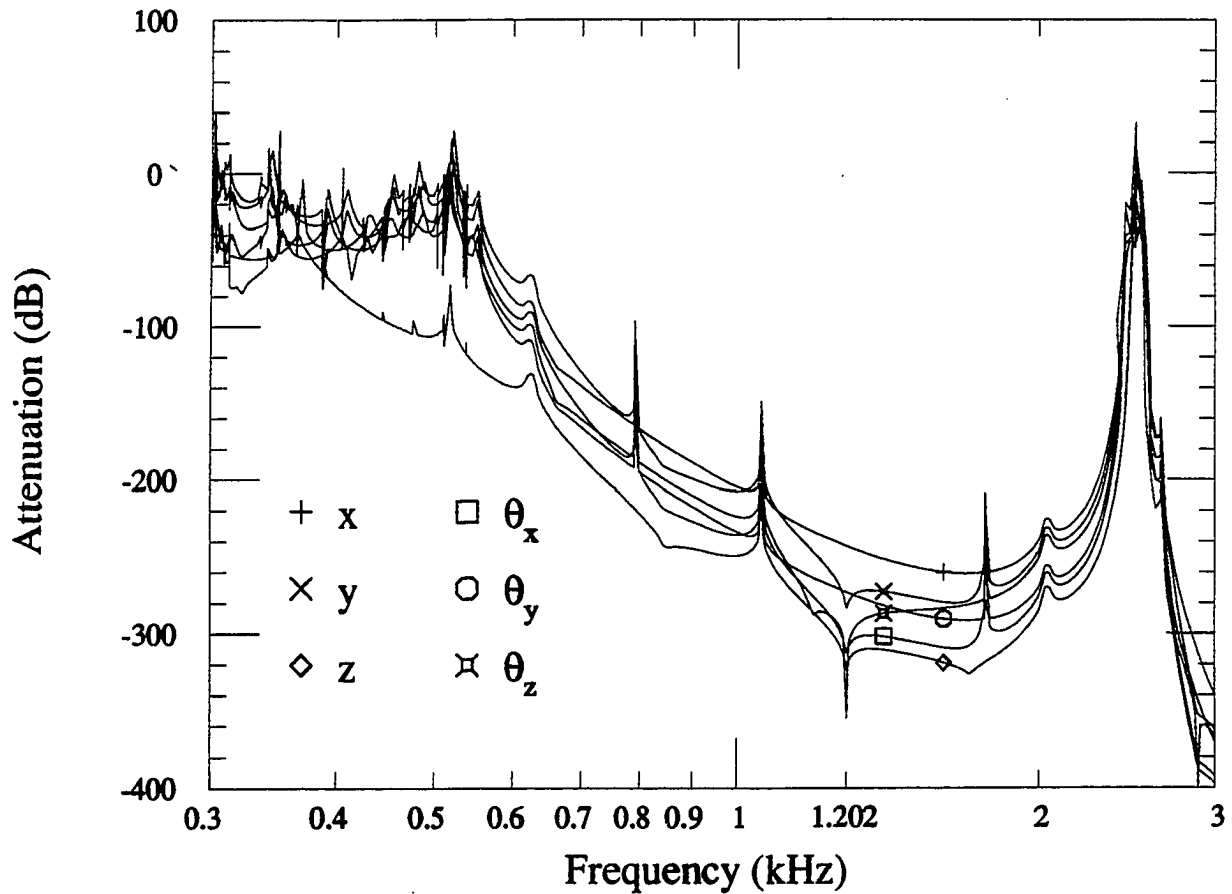


Figure 1.10: Predicted frequency response functions for each of the six input DOF at the top mass of one antenna suspension isolator. These FRF represent the expected performance of the isolation system for the Stanford ultralow temperature detector. The worst case isolation at the antenna frequency (1.202 kHz) is -235 dB. The peak at about 2.5 kHz is due to the internal resonance in the spring.

displacement of the transducer from the antenna axis; the antenna was skewed slightly in the \hat{y} and \hat{z} directions to prevent any couplings from being geometrically forbidden; finally, the stiffness parameters for the isolators were derived from an experimental characterization of an actual isolator. Looking at the graph we see that the worst case isolation at the first longitudinal mode of the antenna (1.202 kHz) is -235 dB in the \hat{x} direction. The dips in other DOF at that frequency occur because they are weakly coupled to the fundamental mode, so that most of the transducer “signal” is due to the cross-coupling terms introduced by the sensitivity function. Since this response is relatively flat across the antenna resonance, we get a dip when we divide by the antenna response due to a force at the endface. The poles visible near 0.8, 1.0 and 1.7 kHz are bending modes of the antenna.

1.6.3 Impulsive excitation response

The ultimate criterion for success of the vibration isolators is that typical external disturbances found in the lab not produce excitation of the antenna above its Gaussian noise level. It is not seismic motion that presents a concern (there is virtually no spectral content in the kilohertz range), but rather cultural disturbances such as lab machinery and human activity. These are, unfortunately, difficult to characterize. However, we can imagine an experiment in which we impulsively excite the top of the isolation system, for instance by hitting it with a hammer. If there is no excitation detected then the isolation is sufficient. The problem is now to calculate the maximum allowed impulse P which is undetectable given an expected detector noise temperature T_d .

Let U_{kr} be the k^{th} component of the r^{th} eigenvector of the undamped N DOF system described by $(-\omega^2\mathbf{M} + \mathbf{K} + i\omega\mathbf{B})\vec{x} = \vec{f}$. For this analysis we restrict \mathbf{B} to be a “proportional damping” matrix, which means that $\mathbf{B} = \alpha\mathbf{M} + \beta\mathbf{K}$. Since the FRF we calculate are independent of the damping (as long as it is small), this assumption has little physical consequence. Then the matrix \mathbf{U} diagonalizes \mathbf{M} , \mathbf{K} , and \mathbf{B} . Let $m_r = (\mathbf{U}^T\mathbf{M}\mathbf{U})_{rr}$ and similarly for k_r and b_r . Finally, we define a set of N matrices, $(\mathbf{A}_r)_{jk} = U_{jr}U_{kr}$. Then a fundamental result of modal analysis states that (see e.g.

Ewins 1984)

$$\vec{x} = \left[\sum_{r=1}^N \frac{\mathbf{A}_r}{k_r - \omega^2 m_r + i\omega b_r} \right] \vec{f}. \quad (1.9)$$

This formula represents a sum over N single DOF oscillators, each weighted by an influence coefficient matrix determined by the geometrical mode shapes.

Let \vec{f} be an impulsive excitation at time $t = 0$ with the form $\vec{f}(t) = \vec{p}\delta(t)$, or $\vec{f}(\omega) = \vec{p}$. We wish to find the time domain solution $x(t)$ for $t > 0$. To do this we take the inverse fourier transform of the solution $x(\omega)$ to Eqn. 1.9. We do the integral by contour integration around the poles (the natural frequencies of the system). Assuming the quality factor of each mode is large, we find

$$\vec{x}(t) = \sum_{r=1}^N \mathbf{A}_r \vec{p} \frac{\sin(\omega_r t)}{m_r \omega_r} \exp\left(\frac{-b_r t}{2m_r}\right).$$

With this equation it is a simple matter to determine the total energy imparted to the fundamental longitudinal mode of the antenna as a result of an impulse p to the top of one of the isolator stacks.

For the Stanford ultralow temperature gravity wave detector we expect a noise temperature of $T_d = 1\mu\text{K}$, corresponding to a strain sensitivity $h \sim 10^{-20}$). We thus calculate that an impulse of $p = 3$ N-sec to the top mass of the antenna suspension isolators in the \hat{x} direction would impart an energy $k_B T_d$ into the fundamental mode, where k_B is Boltzmann's constant. This impulse is roughly the impulse delivered by the impact of a 2 kg mass dropped from 0.2 m.

1.7 Matrix representation of six-DOF springs

In this section we describe in detail the mass and stiffness matrices used in the SYSTEM and ISOLATOR models.

Consider an undamped system which has a single six-DOF mass connected to ground by a six-DOF spring which only has coupling between the y and θ_x DOF and the x and θ_y DOF. The z and θ_z DOF are completely uncoupled. This is a reasonable model of certain class of physical six-DOF springs. The behavior of the system is

then given by $(\mathbf{K} - \omega^2 \mathbf{M})\vec{x} = \vec{f}$ with

$$\mathbf{K} = \begin{bmatrix} k_x & 0 & 0 & 0 & -k_{x\theta_y} & 0 \\ 0 & k_y & 0 & k_{y\theta_x} & 0 & 0 \\ 0 & 0 & k_z & 0 & 0 & 0 \\ 0 & k_{y\theta_x} & 0 & k_{\theta_x} & 0 & 0 \\ -k_{x\theta_y} & 0 & 0 & 0 & k_{\theta_y} & 0 \\ 0 & 0 & 0 & 0 & 0 & k_{\theta_z} \end{bmatrix},$$

$$\mathbf{M} = \text{diagonal} \left[m \quad m \quad m \quad I_{xx} \quad I_{yy} \quad I_{zz} \right].$$

We see that \mathbf{K} is specified by eight positive parameters. One might then naively expect the dynamics for two six-DOF masses connected by such a spring to be a simple generalization of the usual formula in one-DOF, giving

$$\left(\begin{bmatrix} \mathbf{K} & -\mathbf{K} \\ -\mathbf{K} & \mathbf{K} \end{bmatrix} - \omega^2 \begin{bmatrix} \mathbf{M}_1 & \mathbf{0} \\ \mathbf{0} & \mathbf{M}_2 \end{bmatrix} \right) \begin{Bmatrix} \vec{x}_1 \\ \vec{x}_2 \end{Bmatrix} = \begin{Bmatrix} \vec{f}_1 \\ \vec{f}_2 \end{Bmatrix}.$$

However, this expression is not rotationally invariant. If we plug in values for \vec{x}_1 and \vec{x}_2 corresponding to a rigid body rotation of the system we see a resultant force, which cannot be physically correct. Instead we can *derive* the correct stiffness matrix for the two mass system by starting from the one mass case and then imposing invariance under small rotations and translations, assuming a distance l between the two centers of mass. We also impose conservation of momentum. This yields the following for the mass and stiffness matrices:

$$\mathcal{M} = \begin{bmatrix} \mathbf{M}_1 & \mathbf{0} \\ \mathbf{0} & \mathbf{M}_2 \end{bmatrix}, \mathcal{K} = \begin{bmatrix} \mathbf{K} & -\mathbf{D}^T \\ -\mathbf{D} & \mathbf{E} \end{bmatrix}$$

with

$$\mathbf{D} = \begin{bmatrix} k_x & 0 & 0 & 0 & -k_{x\theta_y} & 0 \\ 0 & k_y & 0 & k_{y\theta_x} & 0 & 0 \\ 0 & 0 & k_z & 0 & 0 & 0 \\ 0 & k_{y\theta_x} - lk_y & 0 & k_{\theta_x} - lk_{y\theta_x} & 0 & 0 \\ -k_{x\theta_y} + lk_x & 0 & 0 & 0 & k_{\theta_y} - lk_{x\theta_y} & 0 \\ 0 & 0 & 0 & 0 & 0 & k_{\theta_z} \end{bmatrix} \quad (1.10)$$

$$\mathbf{E} = \begin{bmatrix} k_x & 0 & 0 & 0 & -k_{x\theta_y} + lk_x & 0 \\ 0 & k_y & 0 & k_{y\theta_x} - lk_y & 0 & 0 \\ 0 & 0 & k_z & 0 & 0 & 0 \\ 0 & k_{y\theta_x} - lk_y & 0 & k_{\theta_x} & 0 & 0 \\ -k_{x\theta_y} + lk_x & 0 & 0 & 0 & k_{\theta_y} & 0 \\ 0 & 0 & 0 & 0 & 0 & k_{\theta_z} \end{bmatrix} \quad (1.11)$$

We notice that the matrix \mathcal{K} has almost exactly the same form as the 12×12 matrix describing the stiffness properties of an elastic beam of length l . In fact it turns out to be isomorphic if we impose the restrictions that $lk_y = 2k_{y\theta_x}$ and $lk_x = 2k_{x\theta_y}$. It is apparent from Eqns. 1.10 and 1.11 that the above restrictions considerably simplify the form of \mathbf{D} and \mathbf{E} . At this point to keep the notation simple we consider only beams which have the symmetry properties typical of actual isolator springs, namely invariance under $x \leftrightarrow y$. We can thus make the identifications

$$\begin{aligned} k_x = k_y &= \frac{12EI}{l^3(1 + \Phi)}, & k_z &= \frac{EA}{l}, \\ k_{\theta_x} = k_{\theta_y} &= \frac{(4 + \Phi)EI}{l(1 + \Phi)}, & k_{\theta_z} &= \frac{GJ}{l}, \\ k_{y\theta_x} = k_{x\theta_y} &= \frac{6EI}{l^2(1 + \Phi)}. \end{aligned}$$

Here we used the standard parameters of beam properties as given in Przemieniecki (1985): E is the Youngs modulus, I is the area moment of inertia, A is the cross sectional area, G is the shear modulus, J is the polar area moment of inertia and Φ

is a unitless shear parameter.

1.8 Determination of six-DOF spring constants

We now show how the stiffness matrix is empirically derived from the eigenfrequencies of spring-mass systems which are calculated via FEA or which are experimentally observed.

Assume that the system is composed of identical springs which are characterized by a small number of parameters $\{a_i\}$ and arbitrary (but well known) masses. For instance, we see in Sec. 1.7 that the springs used in the Stanford antenna suspension isolators are characterized by the four free parameters EI, GJ, A and Φ . Note that l is fixed by the geometry. Using this characterization we construct a numerical model of the isolator, which for a given set of parameters can be used to calculate the natural frequencies f_j^{calc} as well as the mode shapes. Note that this model is at the level of detail of the SYSTEM model, which consists of lumped element springs and masses.

Next we are given a set of J observed natural frequencies f_j^{obs} and an identification of the corresponding mode shapes. These are either experimentally observed or calculated via FEA (for instance, by using a two-mass one-spring model as described in Sec. 1.6).

A Nelder-Mead polytope algorithm (Nelder and Mead 1965) is then used to minimize the following multi-variable cost function,

$$C(\{a_i\}) = \left[\sum_{j=1}^J \left| \frac{f_j^{calc}(\{a_i\}) - f_j^{obs}}{f_j^{obs}} \right|^2 \right]^{1/2}$$

If there are many more observed frequencies than parameters then we expect this method will give a robust determination of both the spring parameters as well as the validity of the model and parametrization itself. In our experience it is generally possible to fit all the frequencies to within 5% with this method.

1.9 Experimental results

We have built the first of four antenna suspension isolators using the spring and mass designs which resulted from the optimization procedure described earlier. A six stage version of this isolator is shown schematically in Fig. 1.11. This figure shows how the masses are interleaved and are connected together by the springs. In Fig. 1.8 we see photographs of the actual isolator, which consists of eight masses, nine sets of springs and a special interface mass at the top and bottom. It occupies a volume of $8.75'' \times 8.75'' \times 25''$. As was mentioned earlier, the joints in this piece were formed by aluminum dip brazing and we observe that they appear quite clean and satisfactory.

In the experiments described below, all acceleration sensing was done with PCB Piezoelectronics⁵ accelerometers, models 303A02, 303A03 (uni-axial accelerometers weighing less than three grams) and model 306A06 (a tri-axial accelerometer). These were attached to various points on the isolator either by a screw mount or with wax.

The experimental characterization of the isolator proceeded in two stages. The first stage consisted of measuring the normal mode frequencies of the isolator with free-free boundary conditions. With this set of numbers we can test the numerical ISOLATOR model (which was derived purely from the isolator geometry and material properties) and then refine the numerical model so that predictions of overall system performance will be more accurate. In the second stage we measured frequency response functions between masses and compared these to the predictions of the refined model.

We measured the values of the first 32 normal mode frequencies by impulsively exciting the structure with a mallet and monitoring several accelerometers with a spectrum analyzer. For each mode we placed the accelerometers in various positions on the isolator to verify that the observed mode shape was consistent with the expected mode shape. For higher frequency modes this modal identification proved difficult (which is to be expected) and so these modes were not included in any analyses. The agreement with the predicted frequencies was quite good, with one major

⁵PCB Piezoelectronics, Inc., 3425 Walden Avenue, Depew, NY 14043

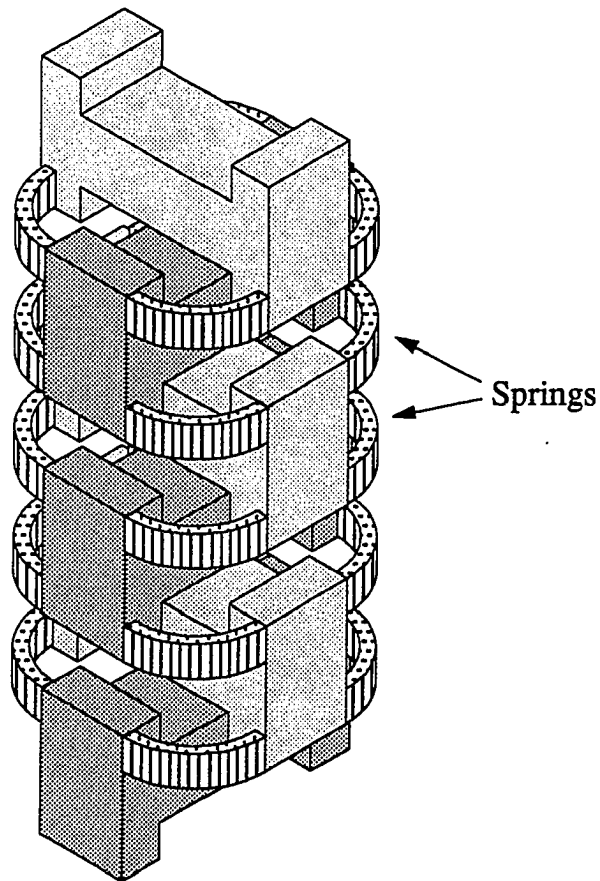


Figure 1.11: Schematic diagram of six stage isolator, showing how masses are inter-leaved and connected together by springs.

qualification, namely that all the predicted frequencies were uniformly about 12% too high, as if the wrong Young's modulus had been used in the calculations. The observed frequencies and the scaled theoretical frequencies are listed in Table 1.1. With the ISOLATOR stiffness matrix scaled by a constant factor all the predicted and observed frequencies matched to within 5% and most matched to within 2%. The overall discrepancy is still unresolved and warrants investigation, but for the present we are satisfied that the refined numerical model is an accurate representation of the actual isolator.

The second characterization was to measure frequency response functions between masses. This measurement is difficult because the masses can in general undergo complex six-DOF motion. This implies that sensing the motion of the mass with only one or two accelerometers is insufficient unless great care is taken to excite only one DOF. A better approach is to use six or more accelerometers on each mass to determine the six-DOF motion of the center of mass. With more than six sensors the problem is overdetermined and we calculate the best center of mass motion in a least squares sense.

To excite the structure we used a VTS300 shaker which was connected to the input mass via a short stinger rod and driven harmonically with an amplified frequency synthesizer signal. In typical experimental modal analysis, one places a force transducer inline with the stinger rod and then assumes that the total force is only along the one DOF measured by the transducer. In our case, however, this could be a poor approximation and instead we chose to measure the complete center of mass motion of the mass which was being driven. With this information all the complicated dynamics of the shaker and stinger rod drop out of the equations of motion and we can make accurate predictions about the motions of the other masses. It is important to note, however, that while the above assertion holds exactly in theory, the situation is not quite so simple in practice. There is a certain art to experimental modal analysis, primarily dealing with the design of the stinger rod. Our experience, which is also reflected in the literature (Ewins 1984), is that some stinger rod designs yield good results and some do not. An unfortunate result of this was that we were unable to get satisfactory results when doing vacuum tests because these required a long stinger

Table 1.1: Natural frequencies of antenna suspension isolator

Observed	FEM Prediction	Percent Error
50.2	50.2	0.0
50.8	50.5	0.6
63.0	62.7	0.5
96.2	96.2	0.0
104.1	101.7	2.4
104.5	102.7	1.8
126.0	122.9	2.5
156.4	154.8	1.0
158.6	156.6	1.3
183.7	179.1	2.6
184.8	186.6	-1.0
184.8	187.9	-1.6
191.8	188.8	1.6
220.1	220.4	-0.1
222.2	222.4	-0.1
227.5	227.7	-0.1
227.5	228.4	-0.4
233.7	229.3	1.9
261.1	263.0	-0.7
263.2	265.9	-1.0
271.1	271.4	-0.1
273.5	272.7	0.3
277.6	273.9	1.4
281.6	274.7	2.5
299.3	293.7	1.9
302.5	294.2	2.8
314.1	303.7	3.4
308.1	308.1	0.0
306.5	309.3	-0.9
338.5	323.9	4.5
343.1	351.9	-2.5
349.7	362.4	-3.5

rod. Thus, with one exception to be noted, all of the tests were performed in air at room temperature and pressure.

In Fig. 1.12 we see four graphs showing FRF for different DOF of the antenna suspension isolator. In each case we measured the six-DOF motion of the driven input mass (\vec{x}_0) and the motion of from one to four test masses ($\vec{x}_1, \vec{x}_2, \dots$) below the input mass. The FRF that we have plotted is $T_n(\omega) = x_{n,d}(\omega)/x_{0,d}(\omega)$ which is the displacement in the d^{th} DOF of mass n divided by the displacement in the d^{th} DOF of the input mass. Using the motion of the input mass and the ISOLATOR model we predicted the motion of the test masses. The experimentally measured points, taken every 50 Hz, are shown as symbols while the predicted values are drawn as solid curves.

It is apparent that the model generally fits the experimental data quite well in the frequency range 0.6 kHz to 1.0 kHz, but that there are systematic deviations both below and above this range. The deviations at low frequency are not surprising, since the model has little predictive power of the exact mode shapes of the highest isolator modes. The high frequency behavior is due to acoustic coupling between the shaker and the test mass. This is demonstrated in Fig. 1.12(a), where we performed two identical FRF measurements in the z DOF for mass 2, one in air and one with the entire apparatus enclosed in a helium filled bag. In the helium environment the speed of sound is much higher so we expect to change any acoustically based phenomenon, and indeed we see that the helium FRF is quite different. We thus understand the coupling as a broad acoustic resonance which will not affect the final isolator performance. Fig. 1.12(b) shows the FRF in the y and θ_x DOF. The apparent pole-zero pair in the top curve is an artifact resulting from structure in the shaker driving point impedance. Note that the model used to generate the predicted curve is essentially the same as the one used in Fig. 1.10, in which no such feature is visible. Figs. 1.12(c) and (d) show the FRF in the z and θ_z DOF respectively. Note that all of the data shown were taken in an air environment at room temperature and pressure, with the one exception that was described.

A similar experiment was performed in vacuum in order to conclusively determine the cause of the systematic deviations above 1 kHz. However, because of the long

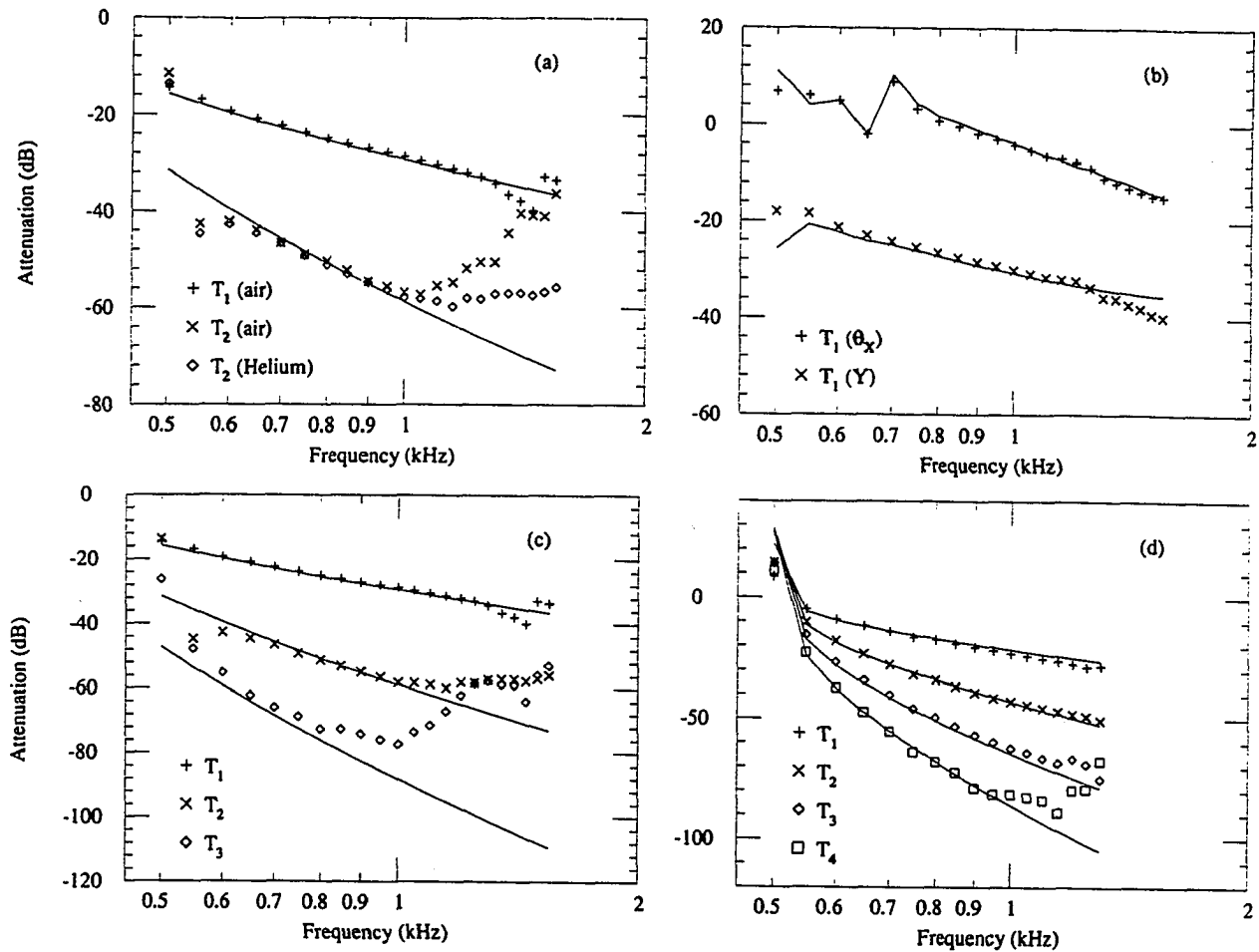


Figure 1.12: Experimental frequency response functions for one Stanford antenna suspension isolator. The FRF we have plotted is $T_n(\omega) = x_{n,d}(\omega)/x_{0,d}(\omega)$, which is displacement in d^{th} DOF of mass n divided by displacement in d^{th} DOF of input mass. The individual points are experimentally observed and the solid lines give the predicted values using the isolator model. (a) Z DOF in air and in Helium. (b) Y DOF and θ_x DOF. (c) Z DOF. (d) θ_z DOF.

stinger rod required to excite the isolator through the cryostat, the results were very poor and we were unable to reproduce the atmospheric results at low frequencies.

1.10 Integrated suspension system

Thus far we have presented a detailed analysis of the design and performance of the suspension isolators. The remaining task is to specify the rest of the suspension system and the manner in which we integrate the isolators. This is shown in Figs. 1.3 and 1.13. Starting from the ground outside the cryostat we have the same arrangement as in the 4 K detector, with four legs on top of which lies a table-frame platform. However, instead of rubber - steel plate stacks and inflated air mounts we use Newport pneumatic isolation legs. These are typically used for optical tables and give excellent low frequency vibration isolation as well as convenient leveling capability. From the table-frame there are titanium rods which hang down and attach to a heavy aluminum spreader bar on each end. The spreader bars provide additional vibration isolation. The titanium rods are attached at both ends with a collet arrangement in which the male and female parts are machined with the same lathe setup to give a perfect fit. On one end of the antenna there are two $5/8$ " rods as shown in the figure but on the other end there is just one $3/4$ " rod (which attaches to the center of the spreader bar). This three point suspension assures that the load will be equalized among the four isolators. The spreader bar is attached to each isolator with three $3/8$ " bolts which screw into heli-coil tapped holes in the top mass of the isolator. Assembly of the suspension system is greatly facilitated by using bolt fasteners at this point instead of welding. At each end of the spreader bars is an isolator. The bottom of each isolator is then welded to the antenna via a cantilever sticking out perpendicular to the endface of the bar. All of the suspension components in the ultralow temperature space (i.e. the spreader bar and below) were designed with the same constraints which apply to the isolator, namely low stress and no internal resonances below 2 kHz. Both the spreader bar and the cantilever were modeled with GIFTS in the design process.

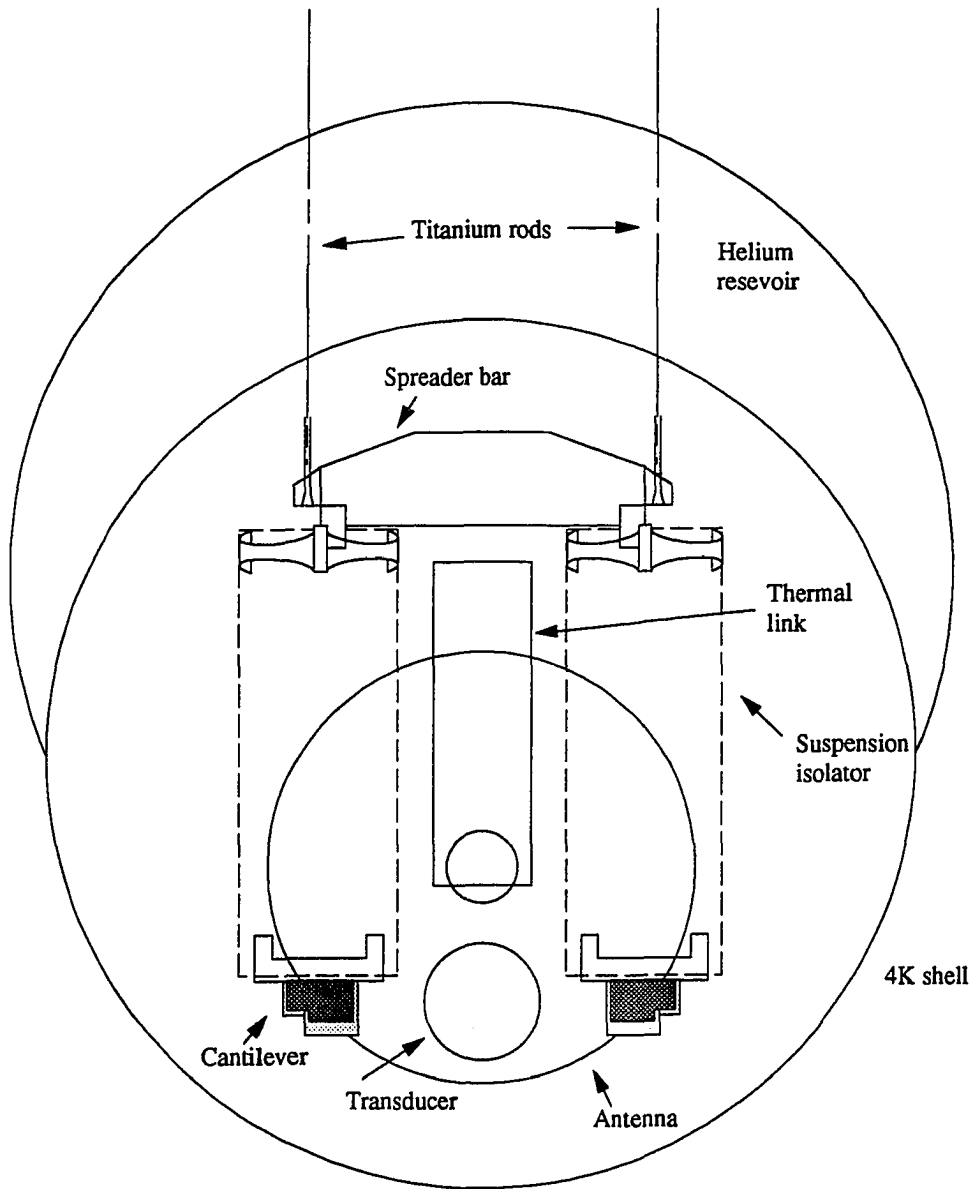


Figure 1.13: Detail of antenna suspension system.

1.11 Discussion

The goal of improving the strain sensitivity of current 4 K resonant-mass gravitational radiation detectors by two orders of magnitude is ambitious in the sense that hitherto unseen effects may rise out of the noise. It is this possibility that has prompted us to design the vibration isolation system for our ultralow temperature detector as conservatively as possible, demanding a thorough understanding of the system dynamics and applying rigorous design constraints to minimize the possibility that ill understood effects will compromise the isolation.

In this chapter we have described the general design, analysis, optimization and experimental characterization of six-DOF vibration isolation systems for ultralow temperature gravitational radiation detectors. Perhaps the most important result is that we have demonstrated the feasibility of an efficient single pass process of design, fabrication and detailed experimental verification of a complex six-DOF isolator. It is possible to build such systems without extensive prototyping and design iteration. An important ingredient in this procedure has been the use of the engineering techniques of finite element analysis and modal analysis. We have utilized a concise methodology with which to understand of the dynamics and modal structure of vibration isolation systems. This is in contrast to previous treatments which have not been systematic in analyzing all degrees of freedom. Finally, we have suggested a quantitative definition for the “system isolation”, or frequency response function, which is applicable to six-DOF vibration isolation systems attached to a gravity wave antenna.

Bibliography

- E. Amaldi, P. Astone, M. Bassan, P. Bonifazi, M. G. Castellano, G. cavallari, E. Coccia, C. Cosmelli, S. Frasca, E. Maiorana, I. Modena, and Pallottin, *Europhysics Letters* **12**, 5 (1990).
- M. Bassan, E. Coccia, I. Modena, G. Pizzella, P. Rapagnani and F. Ricci, in *Proceedings of the Fifth Marcel Grossmann Meeting on General Relativity*, edited by D. G. Blair and M. J. Buckingham (World Scientific, Singapore, 1989), pp. 1723-1732.
- S. P. Boughn, W. M. Fairbank, R. P. Giffard, J. N. Hollenhorst, E. R. Mapoles, M. S. McAshan, P. F. Michelson, H. J. Paik and R. C. Taber, *Astrophysical Journal Letters* **261**, L19 (1982).
- J. Chiang and P. F. Michelson, *Search for Gravitational Radiation Using Ultralow Temperature Techniques - Proposal to the National Science Foundation*, (Unpublished), Appendix D (1989).
- E. Coccia, *Rev. Sci. Instrum.* **53**, 148 (1982).
- W. S. Davis, F. Desrosier, W. Folkner, D. Gretz, K. Krack, M. V. Moody, H. J. Paik, J.-P. Richard, J. Weber and G. Wilmot, in *Proceedings of the Third Marcel Grossmann Meeting on General Relativity*, edited by H. Ning (North-Holland, Amsterdam, 1983), pp. 1433-1436.
- D. J. Ewins, *Modal Testing: Theory and Practice* (John Wiley & Sons, New York, 1984).

- W. O. Hamilton, Xu B.-X., W. W. Johnson, N. D. Solomonson, O. D. Aguiar, B. Price, J. Harper, G. Griffin and D. Duncan, in *Proceedings of the Fifth Marcel Grossmann Meeting on General Relativity*, edited by D. G. Blair and M. J. Buckingham (World Scientific, Singapore, 1989), pp. 1701-1708.
- M. Karim, *Rev. Sci. Instrum.* **55**, 103 (1984).
- F. Larsen, *Acoustic Emission* (IFI/Plenum, New York, 1979).
- F. A. McLoughlin, *Integrated Structural Damping and Control System Design for High-order Flexible Systems*, Stanford University Ph.D. thesis (1990).
- P. F. Michelson, W. M. Fairbank, J. M. Henderson, K. R. Lane, M. S. McAshan, J. C. Price, T. R. Stevenson, R. C. Taber and B. A. Vaughan, in *International Symposium on Experimental Gravitational Physics*, edited by P. F. Michelson, Hu E.-K. and G. Pizzella (World Scientific, Singapore, 1988), pp. 371-378.
- P. F. Michelson, J. C. Price and R. C. Taber, *Science* **237**, 150 (1987).
- J. A. Nelder and R. Mead, *Computer Journal* **7**, 308 (1965).
- H. J. Paik, *Analysis and development of a very sensitive low temperature gravitational radiation detector*, Stanford University Ph.D. thesis (1974).
- J. S. Przemieniecki, *Theory of Matrix Structural Analysis* (Dover, New York, 1985).
- T. R. Stevenson, *I. First coincidence experiments between cryogenic resonant-mass gravitational wave detectors. II. Development of a thin-film superconducting transducer for a gravitational wave antenna*, Stanford University Ph.D. thesis (1991).
- J. Stevenson and R. A. Callander, *Engineering Design* (John Wiley & Sons, Sydney, 1974).
- K. S. Thorne, in *300 Years of Gravitation*, ed. S. W. Hawking and W. Israel (Cambridge University Press, Cambridge, 1987).

J. Tien and Yen C.-T., *Adv. Cryog. Eng.* **30**, 319 (1984).

P. J. Veitch, *Rev. Sci. Instrum.* **62**, 140 (1991).

R. M. Wald, *General Relativity* (University of Chicago Press, Chicago, 1984).

Part II

**QSO Heavy-element Absorption
Systems**

Chapter 2

Introduction to QSO absorption lines

In the last 20 years there has been a revolution in the study of the very distant universe. From galaxies at $z = 0.1 - 4$ to quasi-stellar objects (QSO) at $z \approx 4.5$ to the cosmic microwave background at $z \approx 1000$, our observational knowledge of the deep universe has grown immensely. This is in large part due to advances in detector technology, especially the CCD detector for telescopes. With the advent of 8 - 10 m class telescopes and highly efficient multi-object spectrographs, this field is sure to continue producing exciting results.

At the very largest scale is the field of cosmology, which is no longer a sanctuary for theoreticians in which there was very little experimental data to disprove their theories. Instead, observational cosmology is now the focus of intense research on many fronts. The detection of structure in the microwave background radiation by the COBE satellite (if in fact this detection stands the test of time) is a triumph of precision measurements and gives us critical information about the state of the very early universe. In combination with numerous surveys of large-scale galaxy structure, the COBE measurement has placed severe constraints on theories of galaxy and structure formation in the early universe. Independent of formation questions, the galaxy redshift surveys have produced a rather remarkable view of the large-scale structure in our universe, consisting of sheets, filaments, and voids on scales of

100 Mpc or more.

In addition to studying the spatial distribution of galaxies, the new technology allows study of detailed galaxy properties out to redshifts as high as 2 - 2.5. Above this redshift normal galaxies reach the sky confusion limit. One expected result of deep imaging surveys has been an excess over no evolution of galaxies fainter than $B = 24$. These so-called “faint blue” galaxies may be dwarf galaxies undergoing starburst at redshifts near 0.3. On the other hand, spectroscopic galaxy surveys are essentially consistent with no-evolution models.

Another important probe of the deep universe are the QSOs which are now observed out to redshifts of 4.5. In addition to placing constraints on structure formation by their mere presence at such an early epoch, they provide valuable cosmological probes. The phenomenon of gravitational lensing in particular provides a means of studying dark matter along the line of sight. Another important probe is the presence of narrow absorption lines in the otherwise smooth QSO spectrum. It has been determined that these lines are due to cosmologically distributed material along the QSO line of sight. These lines allow determination of the statistical distribution and detailed kinematic and chemical properties of the gas out to $z \approx 4$. It will be shown that one class of absorption lines are in fact due to intervening spiral galaxies, and so these lines provide a valuable tool for studying the properties of galaxies out to very high redshifts. This is the focus of Part II of the thesis.

2.1 Overview of observed properties

In the optical spectrum of a typical QSO at redshift ~ 3.5 one observes on the order of 100 absorption lines. These lines generally fall into five distinct absorber populations: Ly- α , Lyman limit, damped Ly- α , metal line, and broad absorption line (BAL). In radio loud quasars, absorption can also be observed in the HI 21 cm line. The BAL systems have redshifts very near that of the quasar and are widely accepted to be intrinsic to the quasar. In contrast, the other types of absorption systems are now primarily attributed to intervening material which is cosmologically distributed.

Before going further, it may be instructive to give a picture of what the actual data

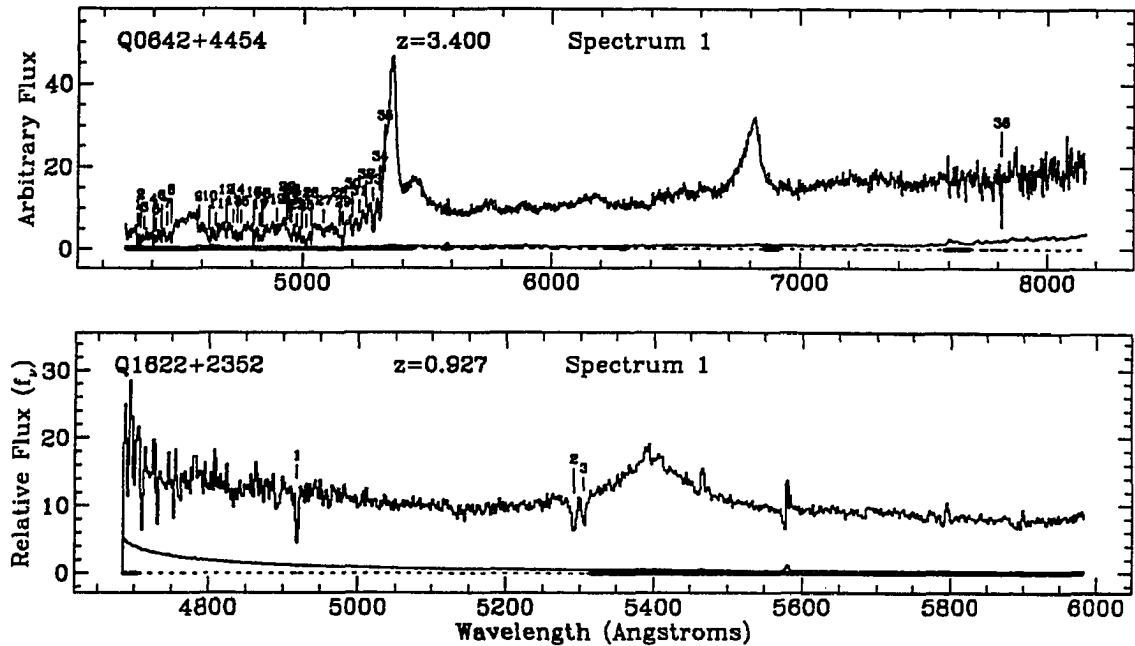


Figure 2.1: Typical QSO spectra

look like. We have plotted in Fig. 2.1 optical spectra from two QSOs, Q0624+4454 (OH 471) at a redshift of 3.400 and Q1629+2352 (3C 336) at a redshift of 0.927. At the bottom of each plot is a spectrum showing the $1\text{-}\sigma$ uncertainty as a function of wavelength. In the top spectrum the two broad emission lines are Ly- α (1215 Å) and CIV(1548,1550 Å). To the left of the Ly- α peak is the Ly- α forest, which at first sight may appear to be noise. However, the instrumental noise is very much smaller than the deviations (compare with the spectrum to the right of Ly- α) and so we are seeing the dense “forest” of Ly- α absorption. This spectrum does not show damped Ly- α or Lyman-limit absorption. Damped Ly- α would appear as a very broad line which is optically thick (black) at the center with characteristic radiation damping wings. A Lyman-limit system has the unmistakable signature of being optically thick below the redshifted 912 Å edge. In the lower spectrum we see a fairly strong Mg II absorber at $z_{abs} = 0.916$ (lines 2 and 3) as well as Fe II(2600) (line 1) at the same redshift.

The Ly- α absorbers are quite clearly distinct from the other distributed absorbers

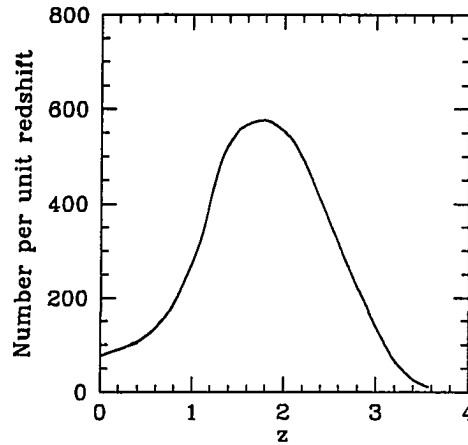


Figure 2.2: Schematic plot of the histogram of known metal-line absorption redshifts, adapted from Junkkarinen, Hewitt, and Burbidge (1991).

in terms of number density, chemical composition, equivalent width distribution, and clustering properties. The origin of this class of absorbers is still a very open question, and the theories include diverse ideas ranging from isolated clouds or sheets of primordial hydrogen to highly extended disks of normal spiral galaxies. On the other hand, the absorption systems associated with metal lines, Lyman limit, damped Ly- α and HI 21 cm have characteristics consistent with a galactic origin. In fact, although there is some controversy about the details, there is little doubt now that these absorption lines are due to intervening galaxies along the line of sight to the QSO. The detailed evidence for this conclusion is presented in Sec. 2.6.

The sketch in Fig. 2.2 demonstrates vividly why QSO metal-line absorption systems provide a powerful tool for looking at galaxy properties and evolution. We show a schematic diagram of the number density of all known metal-line absorbers (as of December 1990) per unit redshift as a function of redshift. This has been sketched from the histogram given in Junkkarinen, Hewitt, and Burbidge (1991). It is remarkable to note that the distribution peaks around $z = 2$ and that there are significant numbers above $z = 3$! There are seven absorbers above $z = 3.5$ and one at $z = 4.1$. This means we can study galaxies over nearly the entire lifetime of the universe. This

is in contrast to direct imaging and spectroscopic galaxy studies, which are mostly sampling $z \lesssim 0.5$. Furthermore, we will see in Sec. 2.7 that at $z \lesssim 1$, Mg II absorbers appear to be typical spiral field galaxies, as opposed to optically selected samples which at high redshifts are necessarily sampling the bright end of the luminosity function.

2.2 Basic picture

In order to provide the context with which to understand the discussion which follows, we present here the basic physical picture of QSO metal-line absorption systems. There are two main models which have been used to explain the observed data. The first is that the absorption occurs in relatively normal spiral galaxies with very extended gaseous halos with filling factor near unity. This means any QSO sightline within a certain radius of the galaxy will show absorption. The main difficulty with this model is that the radius required from statistical studies is uncomfortably large, at least three times the typical optical radius. The other model is that the absorption is due to a collection of star-forming dwarf galaxies which are in the process of merging to form present-day galaxies (see e.g. York et al. 1986; Yanny, York, and Williams 1990). In this scenario, the filling factor is low, but there are enough dwarf galaxies to give the proper cross section. It is assumed that the bright galaxies which are always found at the correct redshift near the QSO are not responsible for the absorption. Instead, the absorption is due to a dwarf galaxy which lies directly on top of the QSO image and is thus unseen. This model requires the formation of present-day spiral galaxies at a surprisingly recent epoch. More importantly, in its current incarnation the model is in severe contradiction with the results of Steidel (1992) and Lanzetta and Bowen (1992). These authors find correlations between the QSO line-of-sight impact parameter (with respect to the galaxy center) and both luminosity and equivalent width. These correlations should not be observed in the merging gas-dwarf scenario. The findings of Yanny, York, and collaborators must be understood, but it is the opinion of this author that they represent the minority of absorption line systems. For this reason we adopt the first model as the basis for understanding the observations.

Table 2.1: Lower limits on observed H I column densities

Absorber class	$\log N(\text{H I})/\text{cm}^{-2}$
C IV	15.5
Mg II, Lyman limit	17
H I 21 cm	19-20
damped Ly- α	20.5

The first point to emphasize is that all of the different kinds of absorption, with the exception of the Ly- α clouds, are consistent with origin in spiral galaxies with large extended gaseous halos. The primary difference between the absorber classes is simply the neutral hydrogen column density along the line of sight. This is strongly linked with position in the galaxy, ranging from very high column density H I clouds with $N(\text{H I}) > 10^{21} \text{ cm}^{-2}$ in the protected environment of the galactic disk to C IV clouds with $N(\text{H I}) \sim 10^{15} \text{ cm}^{-2}$ in the highly ionized outer galactic halo. The approximate minimum H I column density observed in the different absorber classes is given in Table 2.1.

In Fig. 2.3 we show a schematic edge-on view of an absorbing galaxy. Visible are spiral disk in which the high column density clouds reside, and the extended hot halo with both low- and high-ionization clouds. The actual size of the absorbing clouds is rather uncertain, but they have been drawn so that a line of sight will encounter from one to ten clouds depending on the impact parameter.

2.3 Cosmology and all that

In the following sections we will be discussing statistical quantities such as the number density per unit redshift and effective cross section of absorbers. Here we will present the foundation for these calculations, following the discussions of Weinberg (1972), Burbidge et al. (1977), Weedman (1986), and Bechtold and Ellingson (1993).

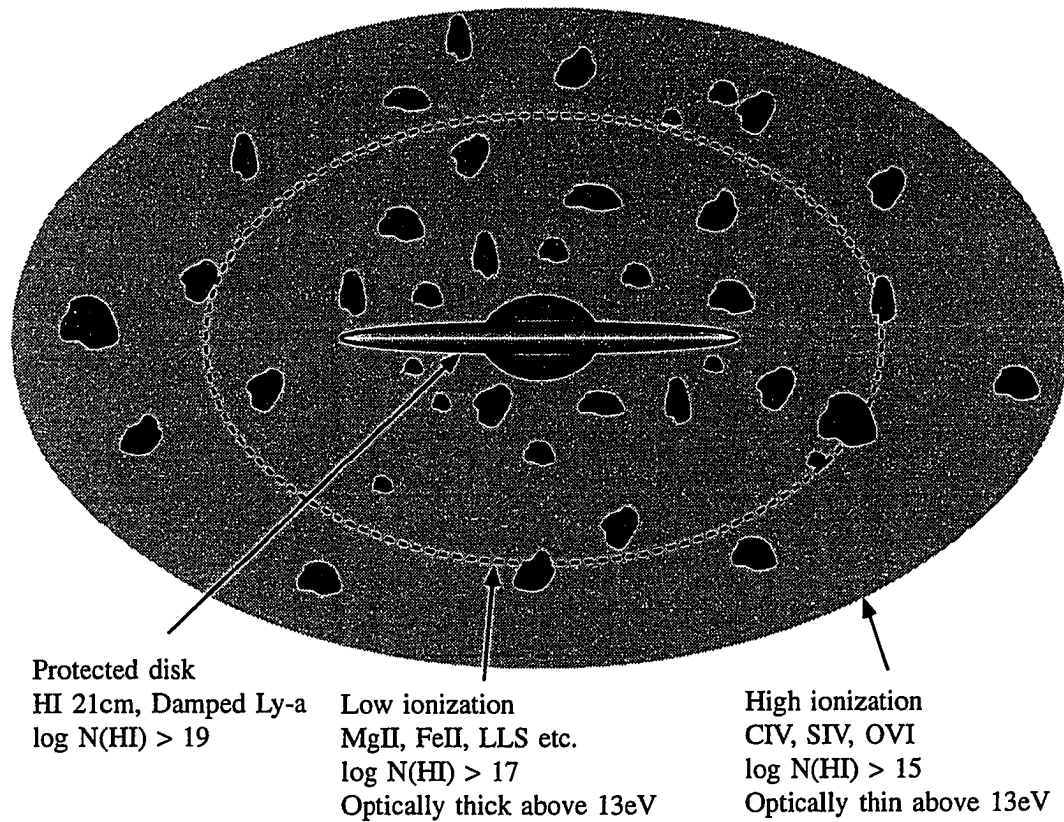


Figure 2.3: Highly schematic diagram of a galaxy with extended halo and absorption clouds. The central bulge and disk are visible, as well as MgII and CIV clouds in the extended hot halo.

For an isotropic, homogenous universe, spacetime is described by the Robertson-Walker metric

$$d\tau^2 = dt^2 - R^2(t) \left\{ \frac{dr^2}{1 - kr^2} + r^2 d\theta^2 + r^2 \sin^2 \theta d\phi^2 \right\}.$$

$R(t)$ is the cosmic scale factor and k is the curvature, either -1 , 0 , or $+1$. The dynamical equation describing $R(t)$ is

$$\dot{R}^2 + k = \frac{8\pi G}{3} \rho R^2, \quad (2.1)$$

where G is the gravitational constant and ρ is the matter density. Using $\rho/\rho_0 = (R/R_0)^{-3}$, which is appropriate for a matter dominated universe with zero cosmological constant, and defining the Hubble constant $H_0 \equiv \dot{R}/R$ and deceleration parameter $q_0 \equiv -R\ddot{R}/\dot{R}^2$ gives

$$\left(\frac{\dot{R}}{R} \right)^2 = H_0^2 \left[1 - 2q_0 + 2q_0 \left(\frac{R_0}{R} \right) \right].$$

We can now calculate the differential proper distance dl in terms of the redshift z by considering the propagation of a light ray during an interval of time dt . This gives

$$dl = c dt = \frac{c dR}{\dot{R}} = \frac{-c dz}{H_0(1+z)^2(1+2q_0z)^{1/2}}$$

If the total number of absorbers is constant, then the number per unit volume satisfies $n(z)/n_0 = (R/R_0)^{-3} = (1+z)^3$. Assuming also that the absorber cross section does not evolve, we arrive at the standard form for the number per unit redshift,

$$n(z) = n_0 (1+z)(1+2q_0z)^{-1/2}.$$

For the limiting cases $q_0 = 0$ ($\Omega = 0$) and $q_0 = 0.5$ ($\Omega = 1$) we have $n(z) = n_0 (1+z)$ and $N(z) = n_0 (1+z)^{1/2}$, respectively. These limits suggest the convenient power-law form,

$$n(z) = n_0 (1+z)^\gamma. \quad (2.2)$$

This functional form is the one most commonly used to describe the redshift distribution of absorbers. Despite the prejudice of theorists for $\Omega = 1$, values of γ between 0.5 and 1.0 are considered consistent with no evolution. With the largest statistical samples now available, it is not currently possible to set useful limits on cosmological parameters such as Ω and Λ (cosmological constant) (Sargent and Steidel 1992, hereafter SS). The main limitation is the knowledge of n_0 , the density at zero redshift. This should change with completion of the HST absorption line key project.

Calculation of the mean free path for absorption is based on the following two empirical relations concerning galaxies. First is the galaxy luminosity function as given by Schechter (1976),

$$dn = \phi^* \left(\frac{-L}{L^*}\right)^{-\alpha} \exp\left(\frac{L}{L^*}\right) d\left(\frac{L}{L^*}\right),$$

where dn is the number of galaxies per unit volume with luminosity between L and $L + dL$, ϕ^* is the density normalization, L^* is a characteristic luminosity, and α describes the low-luminosity behavior. Second, the galaxy luminosity is related to the absorbing radius with the Holmberg relation (Holmberg 1976), giving

$$\frac{R}{R^*} = \left(\frac{L}{L^*}\right)^{5/12}.$$

R^* is thus the absorbing radius of an L^* galaxy. R^* will depend on the particular absorption line being studied. The local ($z = 0$) mean free path between absorbers, l_0 is simply

$$\begin{aligned} l_0^{-1} &= \int_0^\infty f \pi R^2 dn \\ &= f \pi R^{*2} \Gamma(\alpha + 11/6), \end{aligned} \quad (2.3)$$

where $\Gamma(x)$ is the gamma function and f is the filling factor for an absorber within radius R^* . Combining Eqns. 4.9 and 2.3 and using $l_0^{-1} = n_0 H_0 / c$ gives

$$R^*(z) = \left(\frac{1}{\pi} \frac{H_0}{c} \frac{1}{\phi^* \Gamma(\alpha + 11/6)}\right)^{1/2} \left(\frac{1}{f}\right)^{1/2} \left(\frac{N(z)}{(1+z)^\gamma}\right)^{1/2} \quad (2.4)$$

Finally, for reference we write down the equations relating observed angular separation to the physical separation. For $q_0 = 0$,

$$R_{obs} = \Delta\Theta \left(\frac{1453}{H_0} \right) \frac{z(1+z/2)}{(1+z)^2},$$

and for $q_0 = 0.5$

$$R_{obs} = \Delta\Theta \left(\frac{2907}{H_0} \right) \frac{(1+z)^2}{(1+z) - \sqrt{1+z}}.$$

In these formulas, R_{obs} is in kpc, $\Delta\Theta$ is in arcseconds, and H_0 is in $\text{km sec}^{-1} \text{Mpc}^{-1}$.

2.4 Line strengths

It is useful to review the basic physics of absorption and combine this with empirical data concerning chemical abundances to predict (or rather, explain, at this point) the important absorption lines.

The basic equation of radiative transfer is

$$\frac{dI_\nu}{ds} = -\kappa_\nu I_\nu + \epsilon_\nu,$$

where I_ν is the radiation specific intensity, κ_ν is the opacity, and ϵ_ν is the emissivity. For line emission and absorption, this formula can be written in terms of the Einstein coefficients A_{21} , B_{12} , and B_{21} , which describe the rates for spontaneous emission, absorption, and stimulated emission. The opacity and emissivity are

$$\begin{aligned} \kappa_\nu &= \frac{h\nu_0}{c} N_1 B_{12} \left(1 - \frac{g_1 N_2}{g_2 N_1} \right) \phi(\nu) \\ \epsilon_\nu &= \frac{h\nu_0}{4\pi} N_2 A_{21} \phi(\nu), \end{aligned} \quad (2.5)$$

where h is Planck's constant, c is the speed of light, N_1 and N_2 are the number density in the two levels, g_1 and g_2 are the level degeneracies, ν_0 is the line frequency, and

$\phi(\nu)$ is the line profile. If N_1 and N_2 are related by the Boltzmann distribution¹, we get

$$\kappa_\nu = \frac{c^2}{8\pi} \frac{1}{\nu_0^2} \frac{g_1}{g_2} N_1 A_{21} \left[1 - \exp\left(-\frac{h\nu_0}{kT}\right) \right] \phi_\nu. \quad (2.6)$$

We have used $B_{12} = (g_2/g_1)A_{21}(c^3/8\pi h\nu^3)$, which comes from comparing the radiation of the two level system described by the Boltzmann distribution and the Einstein coefficients with the Planck distribution. Eqn. 2.6 shows that there are two very different regimes for the opacity to line radiation, depending on temperature and the line frequency. The term in brackets is the correction for stimulated emission. For $h\nu_0/kT \gg 1$, which is the case for optical lines with $T \lesssim 10^4$ K the correction is unity. However, for $h\nu_0/kT \ll 1$, as in typical radio lines such as HI 21 cm, stimulated emission nearly cancels the absorption and the opacity becomes

$$\kappa_\nu = \frac{c^2}{8\pi} \frac{1}{\nu_0} \frac{h}{kT} \frac{g_1}{g_2} N_1 A_{21} \phi_\nu.$$

2.4.1 HI 21 cm line

The 21 cm transition in neutral hydrogen is due to the difference in energy when the electron and nucleus spins are either aligned or anti-aligned. The Einstein coefficient for spontaneous emission is extremely small, $A_{21} = 2.868 \times 10^{-15} \text{ s}^{-1}$. The half life for emission is $\sim 10^7$ years, which is much longer than the collision times in typical astrophysical situations, even low density nebulae. Thus the population of the two levels is controlled entirely by collisions and can be described by the Boltzmann distribution at a temperature T_s . T_s is known as the “spin temperature”, and in most cases of interest it is identical to the gas kinetic temperature. If we plug the physical constants relevant to the 21 cm line into Eqn. 2.4, we get the important equation for 21 cm optical depth at velocity v as a function of HI column density (N_H) and spin

¹For the 21 cm transition, the spontaneous emission time scale is so long that the population is collisionally excited and hence LTE applies. For permitted optical lines in diffuse ISM conditions, the atoms are essentially entirely in the lower level and so we can neglect the N_2/N_1 term in Eqn. /refeqn:opacity.

temperature,

$$\tau(v) = \frac{N_H(v)}{1.82 \times 10^{20} \text{ cm}^{-2}} \frac{100 \text{ K}}{T_s}.$$

Since Galactic spin temperatures are typically observed to be around 100 K, this equation gives a good feeling for the column densities of neutral hydrogen which can be detected by HI 21 cm absorption. Such high column densities are normally found only in the disks of spiral galaxies.

As an aside, the HI column density which can be detected in optically thin emission is

$$N_H = 1.82 \times 10^{18} \left(\frac{T_b}{1 \text{ K}} \right) \text{ cm}^{-2},$$

where T_b is the brightness temperature observed at the telescope. Note that the expression is independent of the spin temperature and so the column density can be determined unambiguously.

2.4.2 Optical lines

For optical lines at temperatures less than 10^4 K the correction due to stimulated emission is small and so the opacity is proportional to the spontaneous emission coefficient and independent of temperature. Using Eqn. 2.6, and changing to the notation used in optical spectroscopy gives the line optical depth at velocity v as

$$\tau(v) = \frac{\pi e^2}{m_e c} f \lambda N_X(v) = 2.654 \times 10^{-15} f \lambda N_X(v),$$

where λ in Angstroms, f is the oscillator strength of the line, and N_X is the column density in atoms-cm^{-2} . Typical strong QSO absorption lines have $\log \lambda f \sim 2 - 3.5$. Morton, York, and Jenkins (1988) give a list of $\log \lambda f$ values for the strongest resonance lines of common galactic elements in the wavelength range 915 Å to 5900 Å.

We can compare the strength of optical absorption lines to the HI 21 cm line. Following the discussion of Savage et al. (1992), we use for the Mg II line, $f \lambda = 1.7 \times 10^3$ (Morton, York, and Jenkins 1988), $[\text{Mg}/\text{H}]_{\odot} = 3.9 \times 10^{-5}$ (Anders and

Grevesse 1989), and the Mg depletion $\delta(\text{Mg}) = 0.5$. These values give

$$\tau_{2796}(v) = \frac{N_H(v)}{1.1 \times 10^{16} \text{ cm}^2}. \quad (2.7)$$

Metal lines are thus a very sensitive probe for small column densities of gas. Determining which lines will be the strongest obviously requires knowledge of the relative abundances of each species. Using solar abundances reveals just what is expected, that in low-ionization environments (such as a galactic disk) the strong lines are Mg II and Fe II, and in high-ionization environments (such as a galactic halo) the strong lines are C IV and Si IV.

There is an important point to make about Eqn. 2.7. Although it implies one could detect Mg II at HI column densities down to $10^{14} - 10^{15} \text{ cm}^{-2}$, in fact the HI becomes optically thin to Lyman-limit radiation below 10^{17} cm^{-2} and the Mg II is further ionized. SS find evidence for this effect in their sample of Mg II absorbers. A corollary of this is that Mg II lines are almost always highly saturated, thus making abundance estimates difficult. The original claim that metal line absorbers are sensitive to very small columns of hydrogen *does* hold for C IV. This is evidenced by the very large galactocentric distances at which C IV absorption is detected.

A final note is that by far the most sensitive probe of HI is Ly- α , since column densities as low as 10^{13} cm^{-2} are detectable. The ratio of Ly- α to 21 cm optical depths is $\tau_{\text{Ly } \alpha} / \tau_{21 \text{ cm}} = 2.4 \times 10^8 (T_S / 100 \text{ K})$. However, the UV wavelength and more importantly confusion with the Ly- α clouds preclude use of this line for studying the same galaxy populations sampled by Mg II, C IV, and HI 21 cm.

2.5 Milky Way disk and halo interstellar medium

Before trying to establish that the metal-line absorbers are gas-rich galaxies which lie along the line of sight to the QSO, it is useful to present a general picture of the interstellar medium (ISM) of gas-rich galaxies. Since our own galaxy falls in this category and its ISM is by far the best characterized, we will primarily be drawing on Galactic ISM data for comparison to metal-line data.

Table 2.2: Local ISM properties

Component	f_v	f_m	n_H	T	Probes
Very cold molecular clouds	0.005	0.5	> 300	5-30	CO
Cold neutral H clouds	0.02-0.05	0.4	5-20	10-100	HI 21 cm
Warm neutral and ionized H	0.5	0.1?	0.3	6000-8000	H α
Hot ionized H	0.5	0.001	0.005	10^6	[O VI], X-rays

The local ISM is observed to be comprised of at least four distinct components, whose properties are summarized in Table 2.2. Here f_v is the volume filling fraction, f_m is the mass fraction, n_H is the hydrogen number density in atoms-cm $^{-2}$, and T is the temperature in Kelvins. The table and descriptions of the component properties are adapted from Knapp (1989) and Mihalas and Binney (1981).

Very cold molecular gas - This gas is found in giant molecular clouds and is associated with regions of star formation. Notice that at least half of the mass of the ISM is locked up in less than 1% of the volume. Rotational transitions of molecules, especially CO, are used to detect these regions.

Cold neutral hydrogen clouds - These clouds consist primarily of neutral atomic gas and contain nearly half the mass of the ISM in 2-5% of the volume.

Warm neutral and ionized hydrogen - These components fill roughly half of the volume of the ISM. The cold neutral clouds are surrounded by the warm neutral component, which may fill roughly 20% of the ISM volume. The extent of the warm component perpendicular to the Galactic disk is large and the column density through the disk (perpendicular to the plane) is 2×10^{20} cm $^{-2}$.

Hot ionized hydrogen - This component is seen in UV line absorption of highly ionized species such as O IV and others (Jenkins 1978a, Spitzer 1989), as well as soft X-ray emission (McCammon et al. 1983). This very hot gas is produced by supernova shocks (McKee and Ostriker 1977).

The basic theoretical framework for the energetics and dynamics of these components was first put forth by Field, Goldsmith, and Habing (1969), with a static

model. McKee and Ostriker (1977) then proposed a dynamical model in which pressure fluctuates locally depending on supernova rates. This model was successful for many years but is now yielding to improved observations. There are now many open questions, including the basic geometry and topology of the components. It is not clear if the “clouds” are really more like sheets or filaments, and if the hot component is pervasive, confined to regions near supernova remnant, or sponge-like. Fortunately, improvements in instrumental sensitivity and resolution are making it possible to observe in detail the ISM in nearby galaxies. This will be a tremendous help in understanding this complex problem. For instance, Dickey and Brinks (1993) used the VLA to observe HI 21 cm absorption in number of background continuum sources in M31 and M33. They were able to determine that these galaxies are similar to the Milky Way in the ratio of cool atomic gas to warm neutral gas. This is important because in the current understanding the warm neutral phase is not particularly robust against either ionization or cooling.

The detailed structure and content of the ISM in the Galactic halo is also not well known. The basic picture of a tenuous hot corona was first put forth by Spitzer (1956) to explain the stability (via pressure equilibrium) of neutral clouds which were observed well above the galactic plane. Ultraviolet observations of absorption at high latitude due to highly ionized species such as O IV, NV with the Copernicus satellite (Rogerson et al. 1973; York 1977; Jenkins 1978a,b) were central in confirming this picture. Detection of these ions is particularly important because the large ionization potential sets constraints on possible ionization mechanisms. In particular, photoionization by hot stars or the extragalactic EUV radiation can create C IV or Si IV, but NV and O IV are difficult.

There are two main classes of models to explain the wealth of Galactic halo data which is now available. These data reveal the halo to be a dynamically complex entity, with gas in several phases and stages of ionization and complexes of neutral gas with velocities (relative to the local standard of rest) as large as $\sim 300 \text{ km sec}^{-1}$ (Bajaja et al. 1985; Hulsbosch and Wakker 1988). The first class of models uses some non-thermal means such as cosmic-rays and galactic magnetic fields to support the hot medium, along with photoionization by the extragalactic EUV background

radiation (Chevalier and Fransson 1984; Hartquist and Morfill 1986; Bloemen 1987). These models correctly predict C IV and Si IV abundances, but as mentioned above is unable to fully account for the observed N V and O IV. The second class of models use supernovae to heat gas in the disk to 10^6 K and expell it into the halo (Shapiro and Field 1976; Bregman 1980). This gas then radiatively cools and falls back into the disk. This model can reproduce the observed amounts of C IV, N V, O IV, and Si IV (Shapiro and Benjamin 1991).

2.6 Metal-line absorber – galaxy connection

With a picture in mind of the general properties of the ISM in the Milky Way, we can proceed to present the evidence which establishes the connection between metal-line absorption systems and intervening gas-rich galaxies. We will start with indirect evidence and proceed to the direct and very compelling arguments.

Chemical species, ionization, and velocity profiles

The metal-line species which are seen QSO absorption systems include Mg II, C IV, Fe II, Al II, Si IV, Si II, Mg I, C II, Zn II, Cr II, Mn II, and Ca II. The first two are the strongest and most prevalent, and both have distinctive doublet wavelength and strength ratios that allow for positive identification. Savage and Jeske (1981) found in IUE spectra of hot stars in the LMC and SMC that many of these same species are also present in the Galaxy. Moreover they found that the line equivalent widths, relative abundances, and velocity profiles are also similar. The velocity profiles are particularly interesting. High resolution spectra of both Galactic absorbers and high redshift absorbers reveal that the absorption is actually due to many separate components, spread over velocities of 100 - 300 km sec⁻¹. In the case of strongly saturated lines like Mg II the variation in equivalent width is primarily due to the *number* of velocity components.

The recent work of Savage et al. (1992) using the Goddard High Resolution Spectrograph (GHRS) and the Faint Object Spectrograph (FOS) on the Hubble Space Telescope (HST) confirms the earlier work with better statistics. They compare

equivalent widths of 13 low- and high-ionization species in 6 Galactic sightlines to the widths in 33 damped Ly- α absorbers. Once several selection effects are accounted for, the distributions of equivalent width are consistent. It is important to remember that this primarily implies similarity of the kinematical properties and not necessarily the chemical properties.

High redshift absorption in the HI 21 cm line is also observed to be very similar to absorption in the Galaxy. Briggs and Wolfe (1983, hereafter BW) found that in the 21 cm absorbers the large column densities, low spin temperatures and presence of low-ionization metal species strongly suggest origin in the protected environment of a galactic disk similar to our own.

Clustering

The clustering properties of metal-line absorption systems are also consistent with origin in intervening galaxies. The standard diagnostic of clustering is the two-point correlation function for absorbers in each line of sight. For CIV selected systems, Young, Sargent, and Boksenberg (1982) and Sargent, Boksenberg, and Steidel (1988, hereafter SBS) found a significant excess over a poissonian distribution on scales less than 600 km sec^{-1} . Heisler, Hogan, and White (1989) analyzed the SBS data and found marginal evidence for clustering on scales between $1000 - 10000 \text{ km sec}^{-1}$. Much of the excess below 200 km sec^{-1} is probably due to multiple clouds in the same galaxy, while the larger velocities are likely due to galaxy-galaxy clustering and possibly even large scale structure. For Mg II absorbers, Petitjean and Bergeron (1989) found a significant excess on scales less than 300 km sec^{-1} . Using a much larger sample, but at lower resolution (350 km sec^{-1}) SS found large scale clustering on scales $600 - 5000 \text{ km sec}^{-1}$, significant at about $3 - 3.5\text{-}\sigma$.

Direct identification of absorbing galaxies

The evidence presented thus far presents a fairly convincing connection between metal-line absorbers and galaxies. However, the groundbreaking work of Bergeron and Boissé (1991) and subsequent work by Steidel (1992) has made this connection almost incontrovertible. They have directly identified the galaxies responsible for

Mg II absorption at $z \lesssim 1$ by imaging and spectroscopic confirmation. This allows detailed comparison of the individual absorption line properties with the galaxy properties such as luminosity, optical radius, and Hubble type. These investigations will be discussed further in Sec. 2.7.

2.7 Detailed empirical properties

2.7.1 Lyman- α forest

Statistical surveys of Ly- α absorber properties gave very inconsistent results prior to 1986 (Hunstead 1988). This was primarily a result of inhomogenous samples (especially with regard to equivalent width limits), insufficient spectral resolution, and insufficient understanding of the “inverse effect”, in which there is a lower density of absorbers near the QSO emission redshift.

Number density – The number of Ly- α absorbers per unit redshift can be fit by the form $n(z) = n_0(1+z)^\gamma$, with $n_0 = 3.5$ and $\gamma = 2.75 \pm 0.29$ (Lu, Wolfe, and Turnshek 1991). This result is valid over the redshift range $2 \lesssim z \lesssim 4$. Note that the large value of γ implies significant evolution of the absorbers in the sense that they were much more prevalent in the past. For low redshifts (accessible only with spacecraft observations), the parameters are $n_0 = 15 \pm 4$ and $\gamma = 0.7$ (Bahcall et al. 1993). If these absorbers are associated with normal galaxies then the absorption cross-section is very large, about 300 kpc.

Equivalent width – The rest equivalent width distribution was found by Sargent et al. (1980) to be well represented by $n(W) = (N^*/W^*)e^{-W/W^*}$ for $W \geq 0.16 \text{ \AA}$, with $W^* = 0.36 \pm 0.02 \text{ \AA}$. Murdoch et al. (1986) found roughly the same value for W^* but discovered a significant positive deviation for $W < 0.3 \text{ \AA}$. This trend was confirmed by higher resolution data (Atwood, Baldwin, and Carswell 1984).

Clustering – The clustering found in Ly- α absorbers at high redshift is either weak (Sargent 1988) or non-existent (Sargent, Young, and Schneider 1982).

Chemical composition – An important characteristic of Ly- α absorbers is the very low metallicities implied by the lack of associated heavy-element absorption.

Typical limits on metallicities (compared to solar) are 0.001 - 0.01. The only detections have come from statistical methods (summing up the spectral region corresponding to heavy-element lines at the redshifts of many Ly- α absorbers) (Norris et al. 1983) and from study of high column density systems (Chaffee et al. 1985; Boksenberg and Sargent 1983).

2.7.2 CIV

For the CIV doublet, major surveys have been carried out by Young, Sargent, and Boksenberg (1982), SBS, and Steidel (1990). These ground based studies are limited to the redshift range $1.06 \leq z \lesssim 4.2$. The main results of Steidel (1990) (which combined the spectra of SBS with spectra of QSOs with redshifts between 3.0 and 4.1) are the following:

Number density – The mean number of absorbers per unit redshift is $\langle N(z) \rangle = 2.57 \pm 0.34$ for $W_0 \geq 0.15 \text{ \AA}$, and $\langle N(z) \rangle = 1.56 \pm 0.24$ for $W_0 \geq 0.30 \text{ \AA}$, at $\langle z_{abs} \rangle \sim 1.9$. The number per unit redshift *decreases* with increasing redshift. The maximum likelihood fit of the data to the form $n(z) = n_0(1+z)^\gamma$ gives $\gamma = -1.26 \pm 0.56$, which is inconsistent with no evolution at $3.1\text{-}\sigma$ for $q_0 = 0.5$ and $4.0\text{-}\sigma$ for $q_0 = 0$. The evolution is even stronger for systems with large equivalent widths. It is argued that this evolution is due to an increasing abundance of carbon with time, and not because of changing ionization of the gas.

Equivalent width – The equivalent width distributions at $z \leq 2.2$ and $z > 2.2$ are statistically different with 94% confidence. This is taken to imply a change in the mean CIV column density with redshift. The change which is observed in the CIV is also supported by change in the average doublet ratio (ratio of equivalent widths of the two components) between high and low redshift.

Clustering – There is significant excess clustering over Poissonian on velocity scales $200 \leq \Delta v \leq 600 \text{ km sec}^{-1}$. This excess appears both at high redshifts ($z \geq 2.2$) and low redshifts.

2.7.3 Mg II

For the Mg II doublet, recent surveys include Lanzetta, Turnshek, and Wolfe (1989), Tytler et al. (1987), Sargent, Steidel, and Boksenberg (1988) (hereafter SSB1), Sargent, Steidel, and Boksenberg (1989), Caulet 1989, and SS. The sample of SS (which includes the data from SSB1) is by far the largest and is complete to a limiting rest equivalent width of 0.3 \AA over a redshift path length of 114.2 in 125 QSOs. The redshift range of ground-based observations of Mg II is $0.15 \leq z \lesssim 2$. The primary findings of SS are the following:

Number density – The mean number density of absorbers per unit redshift is $\langle N(z) \rangle = 0.97 \pm 0.10$ for $W_0 \geq 0.3 \text{ \AA}$, 0.52 ± 0.07 for $W_0 \geq 0.6 \text{ \AA}$, and 0.27 ± 0.05 for $W_0 \geq 1.0 \text{ \AA}$. In these samples the redshift of absorbers is $\langle z_{abs} \rangle \sim 1.2$. The redshift evolution can be fit by $n(z) = n_0(1+z)^\gamma$, with $\gamma = 0.78 \pm 0.42, 1.02 \pm 0.53$, and 2.24 ± 0.76 , for the three samples $W_0 \geq 0.3, 0.6$, and 1.0 \AA , respectively. The 0.3 \AA sample is consistent with no evolution, while the 1.0 \AA sample shows marginal evidence for evolution.

Equivalent width – The rest equivalent widths are consistent with both commonly used forms for the distribution, $n_W(W) = (N^*/W^*) \exp(-W/W^*)$, and $n_W(W) = CW^{-\delta}$. The maximum likelihood fits of the distribution parameters are $N^* = 1.55 \pm 0.20$, $W^* = 0.66 \pm 11$, $C = 0.38 \pm 0.03$, and $\delta = 1.65 \pm 0.09$. There is evidence that there is a turnover in the distribution below 0.3 \AA , which would imply that roughly 80% of all Mg II absorbers have $W_0 \geq 0.3 \text{ \AA}$. There is a correlation of increasing equivalent width with increasing redshift.

Clustering – There is excess clustering over poissonian on velocity scales $600 \leq \Delta v \leq 5000 \text{ km sec}^{-1}$, significant at $3.7\text{-}\sigma$. Most of this excess comes from strong absorbers, as is the case for C IV. Using a smaller sample of higher-resolution spectra, Petitjean and Bergeron (1989) found a significant excess on scales less than 300 km sec^{-1} . At much larger velocity scales the data in SS are consistent with the hypothesis that the absorbers are cosmologically and uniformly distributed.

2.7.4 Damped Ly- α

The major surveys on which damped Ly- α statistical results are based are done by Wolfe et al. (1986), Sargent, Steidel, and Boksenberg (1989) (hereafter SSB2), and Lanzetta et al. (1991). Lanzetta et al. (1991) have combined their new spectra with the spectra of the previous two surveys (covering 101 QSOs and $1.6 \lesssim z_{abs} \lesssim 4.1$) and they find the following:

Number density – The number density is $\langle n(z) \rangle = 0.16 \pm 0.03$ for $N(\text{HI}) \geq 4 \times 10^{20} \text{ cm}^{-2}$ if $N(\text{HI})$ is known or $W_0 \geq 14 \text{ \AA}$ otherwise, for $\langle z_{abs} \rangle \sim 2.4$. For no evolution in galaxy number density, this implies that the absorbing radius is larger than the present day spiral disk HI radius by a factor of 2.1 for $q_0 = 0$ and 3.9 for $q_0 = 0.5$. The absorber number density can be fit by $n(z) = n_0(1+z)^\gamma$ with $\gamma = 1.2 \pm 1.7$, consistent with both evolution and no evolution. The uncertainty will be greatly reduced with HST observations of low-redshift systems.

Clustering – No evidence for clustering on scales above 5000 km sec^{-1} is found, although the uncertainties are large. Clustering at the level seen in CIV is not ruled out. The distribution of absorbers is consistent with randomly distributed intervening objects.

HI column density – The neutral hydrogen column density is well fitted by the power-law $f(N) = BN^{-\beta}$, with $\log B = 12.33 \pm 0.07$ and $\beta = 1.67 \pm 0.19$. The observed column densities fall in the range $20.3 \leq \log N(\text{HI})/\text{cm}^{-2} \leq 21.8$. The mass density of the gas in damped Ly- α absorbers is consistent with present-day mass density of stars in spiral galaxies.

Metallicity and dust/gas ratio – Because damped Ly- α systems have by definition very large HI column densities, there is always a rich collection of low-ionization metal lines at the same redshift. The weaker transitions which are not saturated can be used to accurately determine chemical abundances. The Zn II and Cr II transitions are particularly useful for two reasons. First, these ions are dominant form of these elements in neutral HI clouds. Second, in the local ISM, Cr II is known to be heavily depleted relative to solar abundances because of accumulation into dust grains, whereas Zn II shows very little depletion. The ratio $N(\text{Zn II})/N(\text{HI})$ therefore gives a good estimate of metallicity and $N(\text{Cr II})/N(\text{Zn II})$ gives the dust/gas ratio. Both

these quantities are compared to values for the local ISM. For high-redshift damped Ly- α systems, it is found that the metallicity and dust/gas ratio are a factor of 5 - 10 lower than local values (Meyer and York 1992, and references therein). This is not surprising if these systems are young galactic disks where metal enrichment of the ISM is just beginning. However, Meyer and York (1992) find the same factor of 5 - 10 for 3C 286 which is only at redshift 0.692. Considering this is the epoch at which our sun was forming, one would expect to see conditions more similar to our present-day ISM. This metallicity and dust/gas ratio is also consistent with values observed in gas-rich dwarf galaxies. This object is taken as further evidence supporting the merging gas-rich dwarf scenario of QSO absorption lines. More observations will be needed to determine if it is anomalous.

2.7.5 HI 21 cm

In contrast to the optical absorption lines which have been discussed, the number of extragalactic HI 21 cm absorbers is very small. *All* of the known extragalactic systems for which the background radio source is outside the absorbing galaxy are listed in Table 2.3. The neutral hydrogen column density for each system is listed in units of 10^{21} cm^{-2} . The lack of absorbers is not for lack of trying (cf. Galt 1977; Perrenod and Chaisson 1979; Peterson and Foltz 1980) but rather attests to the extreme smallness of the 21 cm absorption cross section. This is also evident from the ratio of Ly- α to 21 cm optical depths, $\tau_{\text{Ly } \alpha} / \tau_{21\text{cm}} = 2.4 \times 10^8 (T_s / 100\text{K})$.

Reliable statistics concerning 21 cm absorption are not available because the surveys have had different strategies and sensitivities, and have often gone unpublished because of the lack of detections. It is reported in Briggs (1988) that R. Brown conducted a survey of 100 quasars in the range 750 - 1420 MHz and detected two absorbers (3C 196 and 3C 286). These two systems have been extensively investigated, but the survey itself is unpublished to our knowledge.

The lack of success in "blind" surveys has prompted researchers to concentrate on known absorption systems or known QSO/galaxy pairs. This is especially prudent because radio observations have small bandwidths (10-20 MHz) and so covering large redshift intervals is very time consuming. Since the 21 cm absorbers which are known

Table 2.3: Extragalactic HI 21 cm absorbers

Object	z_{em}	z_{abs}	$N(\text{HI})^a$	Refs. ^b
PKS 1229-021	1.038	0.395	0.9	1
3C 196	0.871	0.437	1.2	1
AO 0235+164	0.94	0.524	9	1
3C 286	0.849	0.692	0.9	1
MC 1331+170	2.081	1.776	0.8	1
PKS 1157+014	1.986	1.944	6	1
PKS 0458-020	2.286	2.038	6	1
3C 232	0.513	0.005	0.12	1,2,4
PKS 2020-370	1.050	0.028	0.15	1,3,4
PKS 1327-206	1.169	0.018	0.8	3,4
PKS 1413+135	0.26	0.247	3.9	5

^a Where no damped Ly- α observation is available, $T_s = 300$ K has been used to calculate $N(\text{HI})$.

^b References: (1) Briggs 1988 and references therein. (2) Stocke et al. 1991. (3) Boissé et al. 1988. (4) Carilli and Van Gorkam 1992. (5) Carilli, Perlman, and Stocke 1992.

all show a rich collection of low-ionization metal lines, one can build a sample selected for these lines without introducing bias. Briggs and Wolfe (1983) found two 21 cm absorbers in very sensitive observations of a sample of 18 Mg II selected absorption systems. This result makes sense because the observed cross section for Mg II absorption is about $\pi(3.5R_H)^2$, where R_H is the Holmberg optical radius, whereas the HI 21 cm cross section should be around πR_H^2 .

Despite the small number of known 21 cm absorbers, the extremely high velocity resolution and sometimes extended nature of the background sources means these systems can provide a wealth of information which is otherwise inaccessible.

2.7.6 Absorber kinematics

Most observations of QSO absorption lines have been made at relatively low resolution (2-6 Å), which is optimal for detection of the lines and doing statistics. However, as we have mentioned in Sec. 2.6, at high resolution the lines look strikingly different. A seemingly simple absorption doublet is revealed to have a complex structure

consisting of many separate components. For instance, in the $z_{abs} = 0.5240$ system in A0235+164, Lanzetta and Bowen (1992) find evidence for 16 components! The typical doppler velocity of resolved components is 2 - 20 km sec⁻¹.

An important implication of this result is that for strong absorbers such as Mg II or C IV, differences in equivalent width (measured at low resolution) are almost entirely due to differences in the velocity structure of the absorbing gas. This means that statistical results concerning equivalent widths are primarily addressing questions of kinematics rather than chemical abundances. High-resolution spectra in which the individual components are observed must be used to probe chemical composition. Such spectra also allow study of the detailed kinematics of absorption systems, which are presumably clouds in the disk and halo of high-redshift galaxies.

Lanzetta and Bowen (1992) have obtained high-resolution spectra (7 - 35 km sec⁻¹) of four systems and find a number of very interesting results concerning kinematics. Foremost among these is that the velocity fields for two of the systems appear to be dominated by systematic rather than random motions. The main evidence for this comes from what the authors term "ionization subclustering", wherein components of similar ionization have similar velocities. This implies that the velocity is correlated with the cloud position in the galaxy, and is strong evidence against the sub-galactic fragments model of absorbers (York et al. 86). It was also found that the velocity fields for each of the objects could be qualitatively reproduced with simple and reasonable models of the galaxy kinematics.

In the cases where the absorbing galaxy has been directly identified, it is possible to search for correlation between the equivalent width and the impact parameter (the radial distance from the galaxy center to the QSO line of sight). This has been done by Lanzetta and Bowen (1990) and Steidel (1992). Both these studies find a correlation between increasing impact parameter and decreasing equivalent width. This makes intuitive sense in the context of a spiral galaxy with a roughly spherical halo, so that sightlines near the galaxy center encounter more halo gas and also the disk.

2.7.7 Emission from absorption line systems

The initial successful identifications of galaxies responsible for high-redshift absorption were by Bergeron and Boissé (1991). They found a galaxy at the correct redshift for eight Mg II absorption systems with $z_{abs} \sim 0.5$. These galaxies are all relatively bright ($L \geq 0.3L^*$), with absorbing gas out to $R \sim 3.5R_H$, and high star formation rates. R_H is the Holmberg optical radius, defined as the semi-major axis of the 26.5 mag arcsec⁻² contour of surface brightness. A statistical analysis of their sample rules out a disk geometry for the absorbers.

Steidel (1992) has carried out an extensive program of Mg II absorber identification, the results of which greatly improve our understanding of absorption line systems at redshifts between 0.3 and 0.9. His results are quickly summarized as follows:

1. By a combination of multi-color broad-band imaging and follow-up spectroscopy, a confirmed or candidate absorbing galaxy is found *in every case*. Mg II selection of galaxies is equivalent to selection by H I column density $N(\text{H I}) \geq 3 \times 10^{17} \text{ cm}^{-2}$.
2. The optical and IR colors of the galaxies are consistent with mid- to late-type spirals.
3. The impact parameter is correlated with luminosity at high confidence and is consistent with relation for galaxy radius $R(L) = 46(L/L^*)^{0.2} \text{ kpc}$ for $H_0 = 75 \text{ km sec}^{-1} \text{ Mpc}^{-1}$.
4. There are very few intrinsically faint galaxies responsible for absorption. With modest luminosity evolution, the observed luminosity distribution at $z \sim 0.6$ is consistent with the distribution for relatively bright galaxies at the present epoch.
5. The population of “faint blue galaxies” are most likely not included in the absorption line selected sample.

2.8 Discussion

In contrast to the heavy-element systems, the Ly- α absorbers remain enigmatic. Their statistical properties are well understood, but their exact physical nature is still very much an open question. Sargent (1988) gives a review of the literature concerning possible theoretical interpretations. It is argued there that the clouds must be pressure-confined (as opposed to freely expanding or self-gravitationally confined). Recent observations at low redshift using the Hubble Space Telescope (HST) have found clustering among the Ly- α absorbers, but much less correlation between the absorbers and galaxies in the field (Morris et al. 1993). These clustering properties are consistent with the hypothesis that all galaxies brighter than $0.1 L^*$ have an effective cross-section for Ly- α absorption of between 0.5 to 1 Mpc. However, they also find at least one absorber in which there is no galaxy brighter than $M_B = -18$ within 4.8 Mpc.

One interesting diagnostic which can shed light on the two populations of absorbers is the neutral hydrogen column density distribution of QSO absorbers. Petitjean et al. (1993) have used data from the literature to calculate this distribution between $12.5 < \log N(\text{HI})/\text{cm}^{-2} < 22$. They find the data are not consistent with a single power-law (in contrast to Tytler (1987), whose methods have been criticized by Bechtold [1987]) and find instead that the data are well fit by two power-laws with a break (bending upward) at $N(\text{HI}) = 10^{15.5} \text{ cm}^{-2}$. This break could imply that there are two populations giving rise to the absorption. However, detailed calculations of absorption in a single population of very extended spiral disks can apparently produce a similar break (Charlton, Salpeter, and Hogan 1993), although the dynamical stability of such disks seems dubious.

Despite uncertainty with a possible connection to the Ly- α clouds, it is now widely accepted that metal-line absorption systems arise from clouds in the disk and extended galactic halo of intervening gas-rich galaxies. These conclusions are based on direct identification of absorbing galaxies below $z = 0.9$ as well as similarity of the derived absorber properties to those seen in clouds in the Galaxy and nearby galaxies. In particular, for HI 21 cm absorption, the large column densities, low spin temperatures,

low velocity widths, and presence of low-ionization metal species strongly suggest origin in the protected environment of a galactic disk similar to our own. The equivalent widths, velocity profiles, and multi-component nature of heavy-element systems such as Mg II and CIV also agree well with observations in the Milky Way.

The results from the first phase of the HST QSO absorption line key project are described in Bahcall et al. (1992). The main goal of this project is to connect the high-redshift ground based results to low-redshift systems which are in the ultraviolet. However, they observed only seven CIV absorbers not associated with the QSO, and just one Mg II. The only meaningful statistic which can be derived from this sample is that at $\langle z_{abs} \rangle \approx 0.3$ the number of CIV absorbers per unit redshift is $\langle N(z) \rangle = 0.9 \pm 0.4$. This is smaller than the value of $\langle N(z) \rangle \approx 2$ observed at $\langle z_{abs} \rangle \approx 1.3$. One very interesting result to come out of the HST data is the detection of several high-velocity clouds (HVC) which have velocities with magnitudes greater than 250 km sec^{-1} relative to the local standard of rest (Savage et al. 1992). These HVCs at high galactic latitude are all infalling toward us and are very suggestive of the heavy-element absorption clouds seen at high redshift.

Chapter 3

Lobe-dominated quasars with MgII absorption

The work in Secs. 3.1-3.4 is based on a paper which appeared in the *Astronomical Journal*, volume 105, page 2054. The contributing authors were Thomas Aldcroft, Martin Elvis, and Jill Bechtold. The radio and optical observations were carried out by M. E. and J. B., while T. A. did the majority of the analysis and was the primary author of the paper.

3.1 Introduction

It is now widely accepted that QSO metal line, damped Ly- α , and HI 21 cm absorption systems arise primarily from clouds associated with intervening galaxies. These systems exhibit a range of neutral hydrogen column densities from less than 10^{17} cm $^{-2}$ to more than 10^{21} cm $^{-2}$ (Petitjean et al. 1993 and references therein). Comparing these column densities to values observed in our Galaxy and nearby galaxies suggests that 21 cm absorption is most likely to occur in the disk whereas metal line absorption can occur in the disk or extended halo (Briggs and Wolfe, 1983, hereafter BW). Statistical correlations between MgII and 21 cm lines as well as cloud properties such as spin temperature, ionization levels, and component line profiles corroborate this picture (Savage and Jeske 1981; BW).

Despite the general success of this galactic absorption interpretation, there still exist problems and questions to be addressed. Foremost among these is the result that the mean free path for absorption is much shorter than expected based on statistical studies and models of the properties of the absorbing galaxies. Even after adopting the most extreme parameter values, the mean free path is still three times too short for CIV (Sargent, Boksenberg, and Steidel 1988) and two times too short for Mg II (Sargent, Steidel, and Boksenberg 1988) and damped Ly- α (Lanzetta et al. 1991). This is interpreted to imply either that galaxy halos are much larger than conventionally thought or that the number density of galaxies has evolved. Recent work on imaging the absorbing galaxies for redshifts less than about one (Bergeron and Boissé 1991; Bergeron, Cristiani, and Shaver 1992; Steidel and Dickinson 1992) indicates directly the existence of very large halos.

In addition to imaging techniques, one can learn about the linear size of absorbers at any redshift when there are two or more lines of sight intersecting the same system. This is generally not the case, but quasars with lobe-dominated extended radio emission provide distinct lines of sight in the optical and radio. If we observe HI 21 cm absorption at the same redshift as a known optical absorber we can then begin to define the absorber properties. This method is particularly useful because the typical angular scales of extended radio emission are well matched to galactic angular scales. For instance, at $z \approx 1.5$ ($H_0 = 100 h \text{ km s}^{-1} \text{ Mpc}^{-1}$ and $q_0 = 0$), 5 arcsec corresponds to $\sim 30 h^{-1} \text{ kpc}$. In addition to probing the overall size of halo absorbers, the presence of 21 cm absorption in a resolved background provides a means of measuring the sizes of individual absorbing clouds. This is done by analyzing the absorbed 21 cm flux in relation to the radio source surface brightness. In particular, a lower limit on the size can be derived by assuming the cloud is optically thick and covers the radio emission in the region of highest surface brightness. In the case of 3C 196, Brown et al. (1988) were able to conclude that the absorbing cloud is at least $2.25 h^{-1} \text{ kpc}$ across, which is surprisingly large.

To make efficient use of radio telescope time, the absorbing system redshifts should be determined optically. At high redshifts or if UV observations are available, the best line for this purpose is damped Ly- α , since this gives the HI column density directly.

At present, all systems for which this line gives a column density $N(\text{HI}) > 10^{21} \text{ cm}^{-2}$ have detectable 21 cm lines (Briggs 1988). However, if damped Ly- α is inaccessible, the low-ionization metal species which are associated with neutral hydrogen in our galaxy are used. The Mg II doublet is easily identified and is generally the strongest of these metal lines. In addition, it is observed in all HI absorbers for which spectra covering the redshifted Mg II lines have been obtained. The converse is not true, however, and BW found that only 2 of 18 systems selected for Mg II absorption showed HI 21 cm absorption. In the sample of lobe-dominated quasars which we define in this paper, the optical and extended radio emission from the quasar occupy different lines of sight. Nevertheless, the statistic from BW is the most appropriate information available and we shall use it to estimate the expected detection rates.

Since there are no radio synthesis telescopes which can do arcsecond resolution imaging in 21 cm at significant redshifts, we are limited to either VLBI at scales $\lesssim 0.1$ arcsecond or integral measurements of the 21 cm absorption. VLBI techniques have been successfully used to set lower limits of a few tens of parsecs on the absorber size in the compact sources 3C 286 and 0235+164 (Wolfe et al. 1976, 1978; Johnston et al. 1979). To set kpc-scale limits requires sources with arcsecond scale structure. This is the case for 3C 196, in which Foltz, Chaffee, and Wolfe (1988) found the absorber scale to exceed $6.5h^{-1}$ kpc, based on the radio measurements of Brown and Mitchell (1983) and Brown et al. (1988); and PKS 0458-020, where Briggs et al. (1989) set a lower limit on the absorber size of $8h^{-1}$ kpc. In PKS 0458-020 a significant portion of the radio flux comes from a compact core, and VLBI observations were required to rule out an absorber covering only the core. It is preferable to select quasars which have little core radio emission to assure that unambiguous limits can be set on the halo size, based on the angular separation of the optical and radio components.

Unfortunately, quasars with lobe-dominated radio emission which are suitable for absorption line work are intrinsically rare. They must be simultaneously bright, distant enough to assure a sufficient path length, and large enough in angular extent to be resolved at arcsecond resolution. Furthermore, lobe-dominated quasars are generally less luminous in the radio because the radiation is not enhanced by relativistic beaming effects. In this paper, we present and apply a procedure for the selection of

a sample of lobe-dominated quasars with Mg II absorption lines.

3.2 Radio Sample Selection

3.2.1 Finding Lobe-dominated Quasars

The first step in the search for extended 21 cm / Mg II systems is to start with a large quasar catalog and find lobe-dominated quasars which are observationally suited to HI 21 cm and Mg II absorption line work. Since there is no explicit morphological information in any large catalog we define a set of criteria which select quasars *likely* to have lobe-dominated extended radio structure. We then determine from the literature, or with new arcsecond scale observations, those which actually are lobe-dominated.

We searched the Veron-Cetty and Veron catalog (Veron-Cetty and Veron, 1989 hereafter VCV) for the quasars which meet the following criteria:

$$\begin{aligned}\alpha &\geq 0.4 \\ z_{em} &\geq 0.5 \\ \delta &\geq -30^\circ \\ m_V &\leq 19.5 \\ S(2.7 \text{ GHz}) &\geq 1 \text{ Jy.}\end{aligned}$$

Here S is the radio flux, α is the radio spectral index between 2.7 GHz and 5.0 GHz, defined in the sense $S \propto \nu^{-\alpha}$, z_{em} is the quasar emission redshift, δ is the declination, and m_V is the apparent visual magnitude. We also define lobe dominance as $LD = S_{lobes}/S_{total}$ evaluated at 1.5 GHz. This set of constraints will be referred to as the large catalog (LC) selection criteria.

The cut on the radio spectral index α is the least obvious of the criteria and the one most closely related to lobe dominance. Roughly speaking, typical values for the core and lobe spectral indices are $\alpha_{core} \sim 0$ and $\alpha_{lobe} \sim 1$. Since single dish measurements of the spectral index use the combined flux from the core and lobe components, there is a correlation between spectral index and lobe dominance. Current models of quasar physics and populations can make statistical predictions of the lobe dominance from

the spectral index (see Hughes 1991 and references therein), but there is still much uncertainty. Thus it is best for our purposes to regard the spectral index cut as an empirically derived parameter which we initially set conservatively to assure that nearly all lobe-dominated quasars are included.

The requirement that $z_{em} \geq 0.5$ is simply to assure a reasonable path length for each quasar. A redshift of $z \geq 0.15$ is required for ground based observations of the Mg II doublet. The cut on declination allows all of the objects to be observed from Northern hemisphere optical telescopes, the VLA, and one of the Green Bank or Arecibo radio dishes. The cut on visual magnitude assures that spectra can be obtained in a reasonable amount of time on a 4-meter class telescope. Finally, the radio flux limit allows for high resolution VLA imaging in snapshot mode as well as detailed 21 cm absorption line studies with large radio dishes.

This search selected 73 out of the 4234 quasars in the VCV catalog. In order to calculate the lobe dominance for each of these 73 candidate sources, we located radio maps at arcsecond scales at two frequencies, preferably 1.5 and 5 GHz. Most of these observations were done at the VLA, MERLIN, Cambridge 5 km, or Westerbork synthesis radio telescopes. With data at two frequencies we can estimate the lobe dominance at the redshifted 21 cm wavelength. We performed an extensive literature search, primarily using NED¹, and were able to find maps and lobe and core component fluxes for 54 of the sources. Of the remaining 19, we observed 15 at the VLA in A configuration at frequencies near 1.5 GHz and 5 GHz in October 1988. Since the sources are all bright, simple snapshot images were adequate for determination of component fluxes. The details of the observations and data reduction are given in Section 3.2.2. We currently have no information on the radio structure of the final four quasars.

In addition to compiling maps and component fluxes for each source, we also felt it useful to find reliable determinations of the single dish radio spectral indices. The values α_{VCV} (between 2.7 and 5 GHz) given in VCV are often taken from observations

¹The NASA/IPAC Extragalactic Database (NED) is operated by the Jet Propulsion Laboratory, California Institute of Technology, under contract with the National Aeronautics and Space Administration.

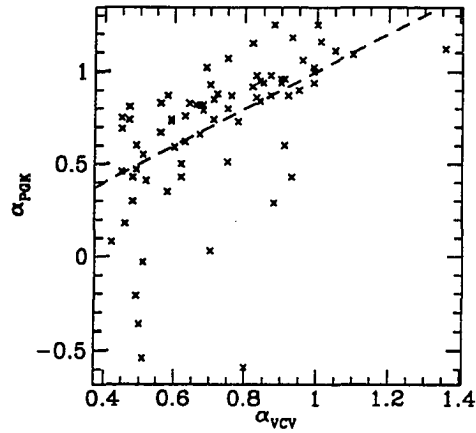


Figure 3.1: Accurate spectral index α_{PGK} vs. VCV catalog spectral index α_{VCV} . Dashed line shows $\alpha_{PGK} = \alpha_{VCV}$.

at different telescopes and/or different epochs and we found that they sometimes disagreed markedly with more reliable values. This is not surprising in light of the intrinsic source variability which is common as well as difficulties in absolute flux calibration. With this in mind, we found spectral indices α_{PGK} for all 73 quasars from four references, in the following order of preference:

1. Parkes survey, with 3 - 7 frequencies at nearly the same epoch (Wright and Otrupcek 1990). We fit a linear or quadratic function in $\log S - \log \nu$ space to determine the spectral index at 1.5 GHz.
2. Green Bank 1.4 GHz and 4.85 GHz surveys (White and Becker 1992; Gregory and Condon 1991)
3. Different surveys at 10 or more frequencies, with care taken to ensure consistency of observations (Kühr et al. 1981). They fit a linear or linear + exponential function in $\log S - \log \nu$ space and we used this fit to determine the spectral index at 1.5 GHz.

A scatter plot of α_{PGK} vs. α_{VCV} is shown in Fig. 3.1 and shows a general scatter

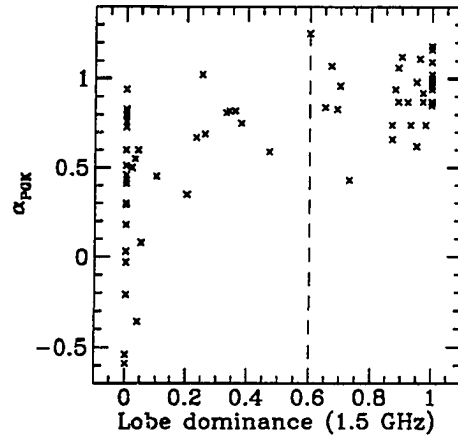


Figure 3.2: Spectral index vs. lobe dominance for quasars which meet LC selection criteria. Dashed line shows LD = 0.6, the cutoff above which quasars are classified as lobe-dominated.

of about ± 0.1 with occasional large deviations. We note that the large discrepancies occur more often at low spectral index, which is indicative of a core-dominated source that can have intrinsic variability on short time scales. The dashed line shows $\alpha_{PGK} = \alpha_{VCV}$ and indicates that $\alpha_{PGK} \approx \alpha_{VCV} + 0.1$. We do not understand the source of this bias.

In Fig. 3.2 we see a scatter plot of the spectral index α_{PGK} vs. lobe dominance for the 69 quasars selected from VCV for which we obtained detailed radio maps. The dashed line indicates LD= 0.6, the cutoff above which we classify quasars as lobe-dominated. Note that a number of the quasars have spectral index less than the VCV catalog cut of 0.4, because we have plotted the PGK value. In order to determine the optimum spectral index cut for future work (for instance, for a Southern hemisphere extension of our sample), we have plotted in Fig. 3.3 the fraction of quasars in our sample which are lobe-dominated f_{LD} versus spectral index cut α_{cut} , and the fraction of lobe-dominated quasars which are included f_{inc} versus α_{cut} . These ratios are defined

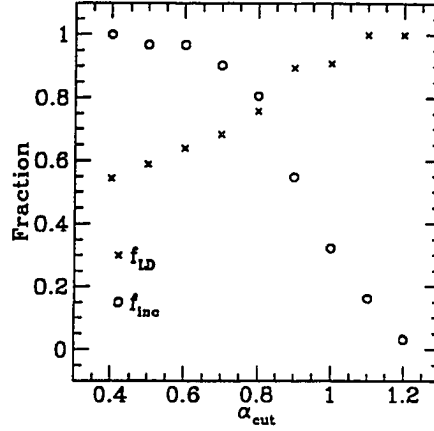


Figure 3.3:]
 Plots of f_{LD} and f_{inc} vs. α_{cut} . See text for explanation of symbols.

by

$$f_{LD}(\alpha_{cut}) \equiv N(LD \geq 0.6 \cap \alpha_{PGK} \geq \alpha_{cut})/N(\alpha_{PGK} \geq \alpha_{cut})$$

$$f_{inc}(\alpha_{cut}) \equiv N(LD \geq 0.6 \cap \alpha_{PGK} \geq \alpha_{cut})/N(LD \geq 0.6),$$

where N is the number of quasars meeting the specified conditions. Given the relatively small number of sources which are selected from VCV, the value $\alpha_{cut} = 0.6$ is a good spectral index cut. At this value about 65% of quasars selected from VCV are lobe-dominated and very few of the lobe-dominated quasars are excluded. Although this value is optimal for future work, in this sample we have already determined the lobe-dominance for the quasars using $\alpha_{cut} = 0.4$. We shall not discard any of this data. At the lower spectral index cut we find 45% (31 of 69) of quasars selected from VCV are lobe-dominated.

In Table 3.1 the key characteristics for the 31 lobe-dominated quasars are given. The lobe-dominance LD and the spectral index α_{PGK} are calculated as described previously, and the rest of the quantities are taken from VCV. The position is that of the optical source and the integrated flux $S(2.7 \text{ GHz})$ is in Jy.

Table 3.1: Lobe-dominated quasars

Source	Position (1950)		z_{em}	m_V	LD	α_{PGK}	$S(2.7)$	Refs. ^a
PKS 0000-17	00 00 48.5	-17 43 56	1.46	19.00	0.87	0.74	1.37	1
3C 2	00 03 48.8	-00 21 07	1.04	19.35	0.98	0.74	2.25	...
PKS 0155-10	01 55 14.1	-10 58 17	0.62	17.09	0.70	0.96	1.29	1
3C 68.1	02 29 27.0	34 10 56	1.24	19.00	1.00	0.98	1.38	1
3C 94	03 50 04.0	-07 19 56	0.96	16.49	1.00	1.18	1.40	1,2
3C 95	03 49 09.5	-14 38 07	0.61	16.22	1.00	1.09	1.44	2
PKS 0454-22	04 54 02.2	-22 03 56	0.53	16.10	0.87	0.66	1.36	3
3C 175	07 10 15.3	11 51 23	0.77	16.60	1.00	1.16	1.23	1,4
3C 181	07 25 20.1	14 43 47	1.38	18.92	1.00	0.94	1.24	1,3
3C 196	08 09 59.4	48 22 08	0.87	17.79	1.00	0.96	7.66	3
3C 205	08 35 10.0	58 04 52	1.53	17.62	0.97	0.92	1.11	3
3C 212	08 55 55.6	14 21 24	1.04	19.06	0.67	1.07	1.41	1
4C 41.21	10 07 26.1	41 47 24	0.61	16.20	0.73	0.43	1.04	1
PKS 1055+20	10 55 37.6	20 07 55	1.11	17.07	0.69	0.83	1.65	1
3C 254	11 11 53.2	40 53 41	0.73	17.98	1.00	1.00	1.45	1
PKS 1136-13	11 36 38.5	-13 34 06	0.55	16.17	0.89	0.87	2.71	4
3C 263	11 37 09.3	66 04 28	0.65	16.32	1.00	0.86	1.73	1
4C 31.38	11 53 44.1	31 44 47	1.56	18.96	0.65	0.84	1.68	1
3C 268.4	12 06 42.1	43 56 02	1.40	18.42	0.97	0.87	1.06	3
4C 53.24	12 13 01.5	53 52 36	1.06	18.00	1.00	0.85	1.40	1
3C 270.1	12 18 03.9	33 59 50	1.52	18.61	0.92	0.87	1.49	3
3C 275.1	12 41 27.6	16 39 18	0.56	19.00	0.95	0.98	1.36	...
PKS 1318+11	13 18 49.6	11 22 32	2.17	19.13	1.00	1.02	1.38	3
PKS 1327-21	13 27 23.4	-21 26 34	0.53	16.74	0.93	0.74	1.31	1
PKS 1335-06	13 35 31.2	-06 11 57	0.63	17.68	0.89	1.06	1.91	1
3C 298	14 16 38.8	06 42 21	1.44	16.79	0.60	1.25	2.71	3
PKS 1453-10	14 53 12.1	-10 56 38	0.94	17.37	1.00	0.87	2.43	1
3C 334	16 18 07.3	17 43 30	0.56	16.41	0.90	1.12	1.32	1
3C 336	16 22 32.4	23 52 01	0.93	17.47	0.96	1.11	1.39	5
PKS 1629+12	16 29 24.5	12 02 24	1.80	18.40	0.95	0.62	1.00	3
PKS 2115-30	21 15 11.2	-30 31 49	0.98	16.47	0.88	0.94	1.50	1

^aReferences: 1. Aldcroft, Bechtold, and Elvis *in prep.* 2. Tytler et al. 1987. 3.

Junkkarinen, Hewitt, and Burbidge 1991. 4. Boissé et al. 1992. 5. Steidel and Sargent 1992.

^bReferences: (1) Briggs 1988 and references therein. (2) Stocke et al. 1991. (3) Boissé et al. 1988. (4) Carilli and Van Gorkam 1992. (5) Carilli, Perlman, and Stocke 1992.

3.2.2 VLA Observations

We were unable to find adequate radio maps and component fluxes in the literature for 19 quasars and of these we observed 15 at the NRAO² Very Large Array in the A configuration (Thompson et al. 1980) on 10-11 Oct. 1988. These sources were bright enough to allow “snapshot mode” observations at 1.49 GHz and 4.63 GHz with a 50 MHz bandwidth. This gives full u - v plane coverage and allows mapping on angular scales of $\sim 1 - 30$ arcseconds at 1.5 GHz and $\sim 0.3 - 10$ arcseconds at 5 GHz. The primary calibration source 3C48 was observed once to establish instrumental gain, with the flux density taken to be 15.52 Jy at 1.49 GHz and 5.63 Jy at 4.63 GHz. For each quasar, a nearby secondary calibration source was observed to establish instrumental phase. No polarization measurements were performed.

The calibrated source maps were made at NRAO in Charlottesville using standard procedures in AIPS. The u - v data were re-gridded, Fourier transformed, and processed using the Clark accelerated CLEAN algorithm (Clark 1980). Maps which contained a suitable bright source were self-calibrated in order to increase the dynamic range. The resultant total intensity maps for objects which have significant resolved structure are shown in Figs. 3.4-3.6.

In two cases (3C 298 and PKS 1629+12) the 1.5 GHz image was badly degraded and we present maps and component fluxes at 5 GHz only. For the rest we show the maps at 1.5 and 5 GHz, plotted at the same position and scale for each object. The clean beam size and orientation for each map is indicated by the cross hatched ellipse in the upper or lower right hand corner, except in the cases where it is too small to be clearly drawn.

In Table 3.2 we summarize the source properties derived from our observations. Note that 3C 297 does not meet the LC selection criteria, but it was observed and we include it simply to present our determination of its radio structure. In columns 2 and 3 we give the position in 1950 coordinates of the center of each major component, as measured from the 5 GHz map. These are listed in order of increasing

²National Radio Astronomy Observatory is operated by Associated Universities, Inc., under cooperative agreement with the National Science Foundation.

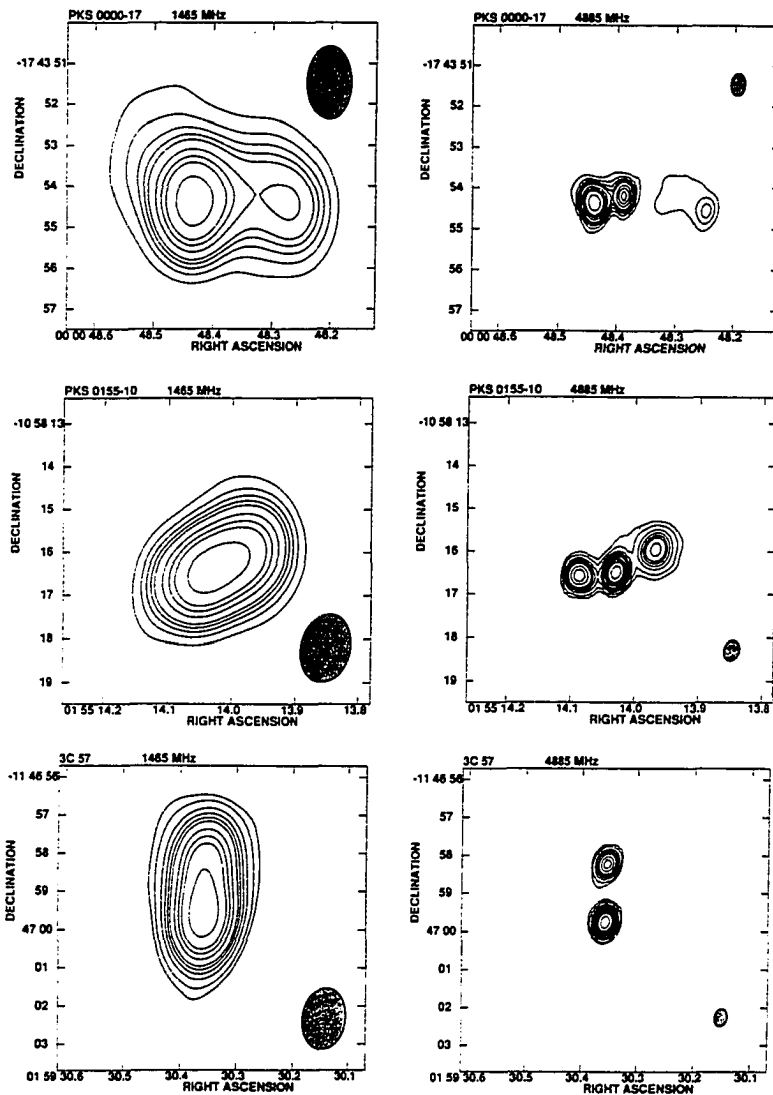


Figure 3.4: VLA maps at 1.5 GHz and 5 GHz. The coefficient of each contour level list is the peak flux. (a) PKS 0000-17 at 1465 MHz. Contour levels $1.016 \times (-0.04, 0.04, 0.08, 0.12, 0.16, 0.20, 0.30, 0.40, 0.50, 0.75)$ Jy beam⁻¹. (b) PKS 0000-17 at 4885 MHz. Contour levels $0.291 \times (-0.04, 0.04, 0.08, 0.12, 0.16, 0.20, 0.30, 0.40, 0.50, 0.75)$ Jy beam⁻¹. (c) PKS 0155-10 at 1465 MHz. Contour levels $0.940 \times (-0.04, 0.04, 0.08, 0.12, 0.16, 0.20, 0.30, 0.40, 0.50, 0.75)$ Jy beam⁻¹. (d) PKS 0155-10 at 4885 MHz. Contour levels $0.280 \times (-0.02, 0.02, 0.04, 0.08, 0.12, 0.16, 0.20, 0.30, 0.40, 0.50, 0.75)$ Jy beam⁻¹. (e) 3C 57 at 1465 MHz. Contour levels $1.557 \times (-0.02, 0.02, 0.04, 0.08, 0.12, 0.16, 0.20, 0.30, 0.40, 0.50, 0.75)$ Jy beam⁻¹. (f) 3C 57 at 4885 MHz. Contour levels $0.719 \times (-0.02, 0.02, 0.04, 0.08, 0.12, 0.16, 0.20, 0.30, 0.40, 0.50, 0.75)$ Jy beam⁻¹.

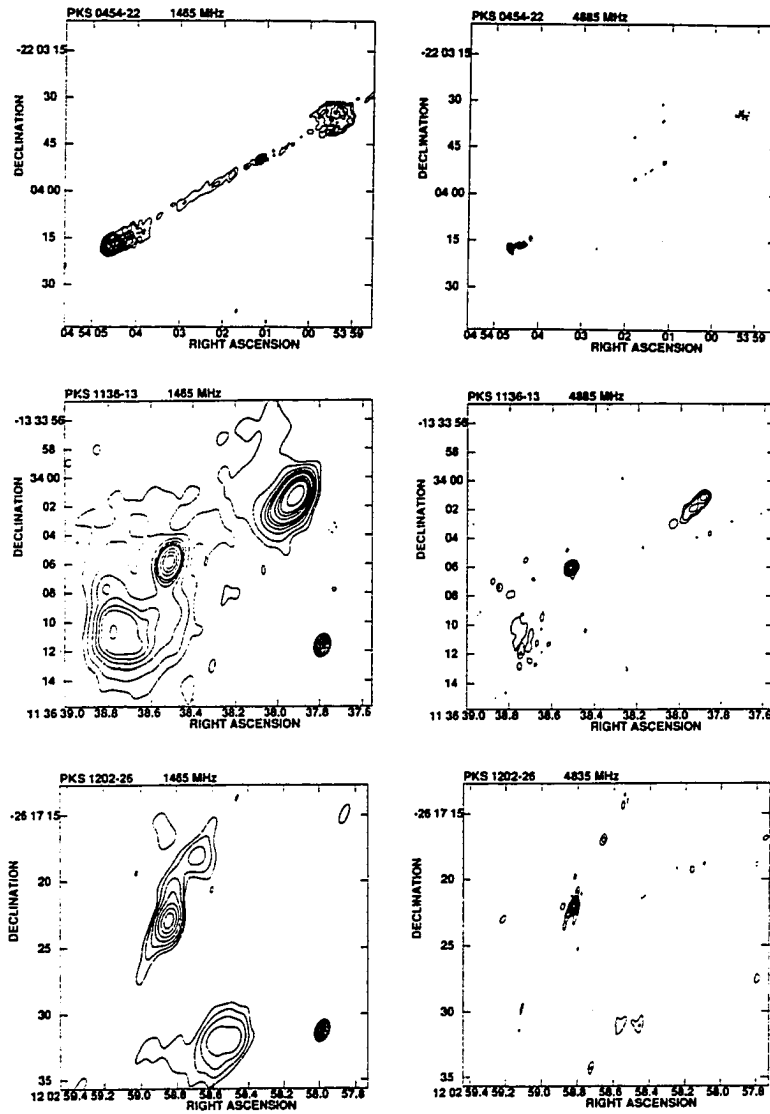


Figure 3.5: VLA maps at 1.5 GHz and 5 GHz. The coefficient of each contour level list is the peak flux. (a) PKS 0454-22 at 1465 MHz. Contour levels $0.233 \times (-0.01, 0.01, 0.02, 0.04, 0.08, 0.12, 0.16, 0.20, 0.30, 0.40, 0.50, 0.75)$ Jy beam⁻¹. (b) PKS 0454-22 at 4885 MHz. Contour levels $\times (-0.01, 0.01, 0.015, 0.02, 0.03, 0.04, 0.08, 0.12, 0.16, 0.20, 0.30, 0.40, 0.50, 0.75)$ Jy beam⁻¹. (c) PKS 1136-13 at 1465 MHz. Contour levels $0.656 \times (-0.02, 0.02, 0.04, 0.08, 0.12, 0.16, 0.20, 0.30, 0.40, 0.50, 0.75)$ Jy beam⁻¹. (d) PKS 1136-13 at 4885 MHz. Contour levels $0.395 \times (-0.02, 0.02, 0.04, 0.08, 0.12, 0.16, 0.20, 0.30, 0.40, 0.50, 0.75)$ Jy beam⁻¹. (e) PKS 1202-26 at 1465 MHz. Contour levels $0.569 \times (-0.02, 0.02, 0.04, 0.08, 0.16, 0.30, 0.50, 0.75)$ Jy beam⁻¹. (f) PKS 1202-26 at 4835 MHz. Contour levels $0.478 \times (-0.02, 0.02, 0.04, 0.08, 0.16, 0.30, 0.50, 0.75)$ Jy beam⁻¹.

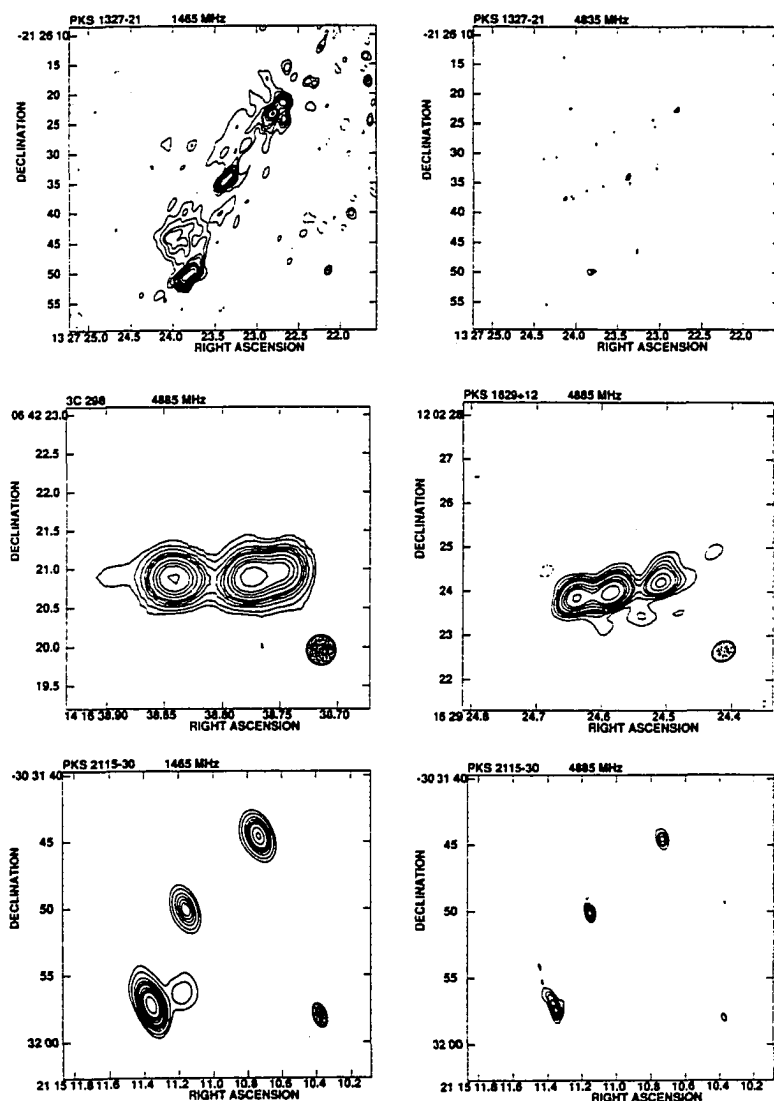


Figure 3.6: VLA maps at 1.5 GHz and 5 GHz. The coefficient of each contour level list is the peak flux. (a) PKS 1327-21 at 1465 MHz. Contour levels $0.122 \times (-0.08, 0.08, 0.12, 0.16, 0.20, 0.30, 0.40, 0.50, 0.75)$ Jy beam^{-1} . (b) PKS 1327-21 at 4835 MHz. Contour levels $0.113 \times (-0.08, 0.08, 0.16, 0.30, 0.50, 0.75)$ Jy beam^{-1} . (c) 3C 298 at 1465 MHz. Contour levels $0.525 \times (-0.02, 0.02, 0.04, 0.08, 0.12, 0.16, 0.20, 0.30, 0.40, 0.50, 0.75)$ Jy beam^{-1} . (d) 3C 298 at 4885 MHz. Contour levels $0.221 \times (-0.04, 0.04, 0.08, 0.12, 0.16, 0.20, 0.30, 0.40, 0.50, 0.75)$ Jy beam^{-1} . (e) PKS 2115-30 at 1465 MHz. Contour levels $1.124 \times (-0.02, 0.02, 0.04, 0.08, 0.12, 0.16, 0.20, 0.30, 0.40, 0.50, 0.75)$ Jy beam^{-1} . (f) PKS 2115-30 at 4885 MHz. Contour levels $0.213 \times (-0.02, 0.02, 0.08, 0.16, 0.30, 0.50, 0.75)$ Jy beam^{-1} .

right ascension. When the component is unresolved or only slightly resolved, we used the AIPS gaussian fitting procedure IMFIT to determine the center. Otherwise we give the approximate geometric center of the structure. In columns 4 - 7 we give the peak and integrated fluxes at 1.5 and 5 GHz for each component, in Jy beam^{-1} and Jy respectively. In the cases where the lobes are not clearly separated from the core, we fit an unresolved gaussian at the core position and resolved gaussians (with width parameters free) at the lobe positions. Otherwise we used the TVSTAT radiometry procedure to calculate component fluxes. The formal uncertainties in flux derived from the rms deviation over areas of blank sky are small, generally less than 0.004 Jy . However, the systematic errors caused by uncertainty in flux calibration and other phases of the data reduction are most likely larger than this formal error and so we only quote fluxes to the nearest 0.01 Jy or Jy beam^{-1} . In column 8 we list the largest angular size LAS in arcseconds between the core and emission associated with each component. Column 9 lists the position angle PA in degrees between the core and component, measured counterclockwise from vertical. Column 10 gives the spectral index α for each component.

3.3 Finding MgII Absorption Systems

The next step in defining the HI 21 cm sample is to find Mg II absorption systems in optical spectra of the sources. Approximately half of the lobe-dominated quasars in our sample have adequate spectra available in the literature and we observed most of the remainder during the period June 1988 to May 1989 on the Palomar 5.08 m telescope³ using the Double Spectrograph or at the Multiple Mirror Telescope⁴ using the Blue or Red Spectrographs. These new spectral observations include a number of quasars which are not lobe-dominated, and so the details and statistical analyses of this sample will be presented in a subsequent paper. From our observations and from

³Palomar Observatory is owned and operated by the California Institute of Technology.

⁴The Multiple Mirror Telescope Observatory is a joint facility of the University of Arizona and the Smithsonian Institution.

Table 3.2: VLA observations

Source	Position (1950)			S_{peak} (1.49 GHz)	S_{int}	S_{peak} (4.63 GHz)	S_{int}	LAS (")	PA (°)	α
PKS 0000-17	00 00 48.29	-17 43 54.3		0.34	0.69	0.05	0.17	2.0	-101	1.16
	48.39	54.2		0.13	0.13	0.16	0.19	-0.32
	48.44	54.4		0.94	1.23	0.29	0.43	0.7	106	0.87
PKS 0155-10	01 55 13.97	-10 58 16.0		0.53	0.59	0.09	0.22	1.0	-60	0.82
	14.03	16.5		0.81	0.81	0.27	0.29	0.85
	14.09	16.6		0.30	0.30	0.14	0.18	0.9	96	0.42
3C 57	01 59 30.35	-11 46 58.2		0.97	1.10	0.35	0.39	1.5	-6	0.86
	30.36	59.7		1.44	1.44	0.75	0.79	0.50
PKS 0237-23	02 37 52.79	-23 22 06.3		5.33	6.66	2.80	3.16	0.62
PKS 0454-22	04 53 59.4	-22 03 35		0.03	0.72	0.01	0.39	34	-59	0.51
	54 01.14	03 49.7		0.23	0.25	0.12	0.14	0.48
	54 04.5	04 18		0.04	1.23	0.01	0.60	58	121	0.60
PKS 0736-06	07 36 30.26	-6 20 03.6		1.28	1.48	0.83	1.02	0.31
PKS 1136-13	11 36 37.9	-13 34 01		0.66	2.04	0.10	0.38	10	-61	1.40
	38.51	06.0		0.39	0.49	0.40	0.47	0.03
	38.8	11		0.20	1.97	0.02	0.46	6.5	140	1.21
PKS 1202-26	12 02 58.5	-26 17 32		0.16	0.79	0.02	0.37	11	-157	0.63
	58.69	18.1		0.06	0.28	0.02	0.11	4.3	-24	0.78
	58.82	22.0		0.57	0.72	0.49	0.59	0.17
B2 1211+33	12 11 32.80	33 26 26.0		0.86	1.08	0.50	0.60	0.49
PKS 1327-21	13 27 22.79	-21 26 22.6		0.10	1.30	0.03	0.13	14	-36	1.91
	23.38	33.9		0.09	0.19	0.11	0.17	0.09
	23.82	50.0		0.12	1.41	0.03	0.21	17	159	1.58
3C 297	14 14 47.60	-3 46 55.9		0.85	1.16	0.28	0.44	0.80
3C 298	14 16 38.75	6 42 21.0		0.35	0.35	0.5	-77	...
	38.78	20.9		0.54	0.54
	38.84	20.9		0.48	0.48	0.9	90	...
PKS 1629+12	16 29 24.51	12 02 24.2		0.09	0.13	1.0	-79	...
	24.58	24.0		0.22	0.27
	24.61	23.9		0.18	0.21	0.5	103	...
4C -02.79	20 03 32.20	-2 32 14.3		1.97	2.08	0.94	0.97	0.63
PKS 2115-30	21 15 11.73	-30 31 44.5		0.47	0.52	0.09	0.11	9.4	-53	1.29
	11.15	50.1		0.27	0.28	0.16	0.17	0.41
	11.35	57.3		1.12	1.51	0.21	0.45	7.6	160	1.01
PKS 2251+24	22 51 44.39	24 29 24.0		1.81	1.91	0.66	0.73	0.80

the literature we now have spectra for 29 of the 31 quasars which have lobe-dominated radio emission. The unobserved sources 3C 2 and 3C 275.1 appeared fainter than their published magnitudes, and so we were unable to get useful optical spectra for them.

In Table 3.3 we summarize the properties of the redshift systems which were found. We give rest equivalent widths W_0 or $5\text{-}\sigma$ limits in \AA for Mg II and Mg I lines. In column 8 the frequency ν_{21} in MHz of the redshifted 21 cm line is given. Columns 9 - 11 list the estimated component fluxes $S_C(\nu_{21})$, $S_{L1}(\nu_{21})$, and $S_{L2}(\nu_{21})$ in Jy based on extrapolating a power-law for the flux. These fluxes are from the core and two lobes, respectively. This shows that all of the sources are very lobe-dominated at the frequency of interest. Columns 12 - 15 give the minimum and maximum scale in kiloparsecs, at the intervening galaxy, of the bright extended radio emission. Put another way, the angular scales (measured from the optical center) over which strong radio emission is detected in the lobes define minimum and maximum linear scales at the distance of the absorbing galaxy. The values given are calculated for Hubble constant $H_0 = 100h \text{ km s}^{-1} \text{ Mpc}^{-1}$ and are to be multiplied by h^{-1} .

3.3.1 Notes on Individual Objects

Here we report on the detection of other metal lines at the redshifts given in Table 3.3.

PKS 0454-22. Robertson et al. (1988) also found Ca II and Fe II in the $z = 0.4745$ absorber and showed the Ca II is very underabundant with respect to Mg II and Fe II. They also saw Fe II in the $z = 0.4833$ absorber.

3C 181. In the spectrum published by Anderson et al. (1987) there appears to be a CIV absorption feature at $z \approx 1.17$ corresponding to the $z = 1.1694$ Mg II lines we found.

3C 196. This well studied object has absorption at $z = 0.43685$ in HI 21 cm against an extended radio source (Brown and Mitchell 1983; Brown et al. 1988) as well as Fe II, Mn II, Mg II, Mg I, and Ca II (Foltz, Chaffee, and Wolfe 1988).

3C 205. Barthel, Tytler, and Thomson (1990) also observed three Fe II lines at $z = 0.4353$.

3C 268.4. Anderson et al. (1987) also see two Fe II lines at $z = 0.4124$.

Table 3.3: MgII Absorption Line Systems

Source	z_{em}	z_{abs}	$W_0(\text{MgII})$ $\lambda 2796$	$W_0(\text{MgII})$ $\lambda 2803$	$W_0(\text{MgI})$ $\lambda 2852$	Ref. ^a	ν_{21}	S_C	S_{L1}	S_{L2}	R_{min} ($q_0=0$)	R_{max}	R_{min} ($q_0=0.5$)	R_{max}
3C 68.1	1.240	0.7755	1.55	1.45	< 1.0	1	800	< 0.1	> 6	> 1	40	149	33	123
PKS 0454-22	0.534	0.4745	1.37	1.34	0.21	2	963	0.3	1.6	0.9	94	228	84	202
		0.4833	0.47	0.23	...	2	958	0.3	1.6	0.9	95	230	84	203
3C 175	0.768	0.4629	0.66	0.25	0.33	1	971	< 0.1	1.4	2.1	77	116	69	103
3C 181	1.382	1.1694	0.39	0.22	< 0.2	1	655	< 0.1	1.8	0.7	17	23	13	17
3C 196	0.871	0.4368	2.00	1.88	0.88	3	989	< 0.1	6.8	8.1	7	11	7	10
3C 205	1.534	1.4353	0.62	0.61	< 0.04	4	583	0.2	1.9	3.4	48	60	34	43
		1.4383	0.26	0.28	< 0.08	4	583	0.2	1.9	3.5	48	60	34	43
3C 268.4 ^b	1.400	0.4124	> 0.6	> 0.6	...	5	1006	0.1	1.9	0.5	18	22	16	20
PKS 1318+11	2.171	0.8388	0.74	0.42	< 0.05	4	772	< 0.1	0.9	0.6	10	20	8	17
		1.0540	0.68	0.63	< 0.05	4	692	< 0.1	1.0	0.6	11	22	9	17
3C 336	0.927	0.4720	0.80	0.67	< 0.30	6	965	0.2	1.4	2.4	31	63	28	56
		0.6560	1.29	1.70 ^c	< 0.35	6	858	0.2	1.5	2.7	37	74	31	63
		0.6602	1.70 ^c	0.52	< 0.35	6	856	0.2	1.5	2.7	37	74	31	63
		0.8914	1.55	1.27	< 0.30	6	751	0.2	1.8	3.1	42	84	34	67
PKS 1629+12	1.795	0.5316	0.68	0.86	0.84	4	927	0.2	0.7	1.0	3	4	3	4
		0.9004	1.06	0.67	0.44	4	747	0.2	0.9	1.1	4	5	3	4

^aReferences: 1. Aldcroft, Bechtold, and Elvis *in prep.* 2. Robertson *et al.* 1988. 3. Foltz, Chaffee, and Wolfe 1988. 4. Barthel, Tytler, and Thomson 1990. 5. Anderson *et al.* 1987. 6. Steidel and Sargent 1992.

^bAuthors identify line but give no equivalent widths. The line appears saturated at their 60 km s^{-1} resolution, thus we can derive the conservative lower limit given.

^cLines blended.

3C 336. Steidel and Dickinson (1992) have obtained further imaging and spectroscopic observations of this system. They tentatively associate the $z = 0.472$ absorber with an intrinsically faint galaxy which resembles the “faint blue galaxies” of deep imaging surveys. They also find a galaxy cluster at $z = 0.66$, the same redshift of one of the Mg II absorbers.

PKS 1629+12. Barthel, Tytler, and Thomson (1990) also observed four Fe II lines near $z = 0.9004$.

3.4 Conclusions

We have outlined a method for finding lobe-dominated quasars which contain Mg II absorption systems. In these objects the radio emission occupies a line of sight different from the optical. If HI 21 cm absorption is observed at the optical Mg II system redshift, unambiguous limits can be placed on the linear size of the absorber. We obtained the necessary data, from the literature and from new optical and VLA observations, to assemble a sample based on our selection criteria.

From the 4234 QSOs in the VCV catalog, we find 73 that meet our selection criteria, which are based on spectral index, optical and radio brightness, redshift, and declination. The spectral index cut preferentially selects lobe-dominated quasars and the other constraints assure suitability for Northern hemisphere optical and 21 cm absorption line study. We then obtained or located arcsecond resolution radio maps at frequencies near 1.5 and 5 GHz for 69 of these sources and find that 31 are lobe-dominated ($S_{lobes}/S_{total} > 0.6$). From the literature and new observations, we obtained optical spectra for 29 of these 31 quasars and we find 17 Mg II absorption systems, with redshifts between 0.3 and 1.4 and Mg II $\lambda 2796$ rest equivalent widths between 0.3 and 2.0 Å. One of these systems, 3C 196, is already a well studied 21 cm absorber.

The sample of lobe-dominated quasars we have presented here is nearly complete in the following sense: (1) We selected nearly all quasars in VCV for which absorption line work in the Northern hemisphere is feasible. (2) We obtained detailed radio maps and component fluxes for 95% of the selected quasars. (3) From Fig. 3.2 we see that

there is a significant drop in the number of lobe-dominated quasars at spectral index less than 0.6. Unless there is a population of quasars with different properties, we can then infer that we have found most of the quasars suitable for extended 21 cm / Mg II study.

For this project, we are primarily interested only in the existence of Mg II absorbers in our sample and not their statistical properties. Thus we used optical spectra from the literature in addition to our observations, and the Mg II sample is inhomogeneous and we make no statistical inferences from this data. We can, however, use the statistics of Steidel and Sargent (1992) to estimate the number of Mg II systems which exist in our sample at given rest equivalent width limits W_0 . The accessible redshift path length for Mg II is defined as the sum over all quasars of $(z_{em} - 0.15)$, where z_{em} is the QSO emission redshift and the value 0.15 represents the redshift at which the Mg II line is shifted to 3200 Å. In the 31 quasars in our list the redshift path length is approximately 22. For $W_0 \geq 0.3$ Å, we would expect 21 ± 2 systems, and for $W_0 \geq 0.6$ Å we would predict 11 ± 2 systems. These values then give a fair estimate of the total number of Mg II absorbers against lobe-dominated quasars which meet the LC selection criteria.

The next obvious step in this program is to carry out the search for redshifted 21 cm at large radio telescopes such as the NAIC 305 meter reflector near Arecibo or the NRAO 140 ft telescope at Green Bank. Preparations are currently underway for these observations. Any new 21 cm absorbers which we find will be subject to extensive followup investigation in the optical and radio. One very interesting possibility is that of mapping the extended Faraday rotation in order to probe the magnetic field of the intervening galaxy. Kronberg, Perry, and Zukowski (1992) have recently done such a mapping of PKS 1229-021 at seven frequencies at the VLA. They found a clear oscillation over the length of the radio jet, suggesting a magnetic field structure similar to M81. Wolfe, Lanzetta, and Oren (1992) concluded from a statistical study that magnetic fields were significantly larger in early galactic disks than in early halos. Thus Faraday mapping is particularly well suited for study of extended 21 cm absorbers and affords a unique opportunity to study the magnetic fields of high-redshift galaxies.

We thank the staff members at the VLA, the Multiple Mirror Telescope, and Palomar observatory for their assistance. We also thank M. Birkinshaw for assistance in understanding the VLA calibrations and for comments on the manuscript. The work of T. L. A. was supported by NASA grant NGT-50938 awarded by the NASA Graduate Student Researchers Program. J. B. was supported by RII-8800660 and AST-9058510 from the National Science Foundation. M. E. was supported by NASA contracts NAS8-30751 (HEAO-2) and NAS8-39073 (ASC), and by NASA grant NASW-2201 (LTSA).

3.5 Planned HI 21 cm observations

In Secs. 3.1-3.4 we defined a sample of Mg II absorption systems which occur in lobe-dominated quasars. This sample provides us with the redshifts at which to search for HI 21 cm absorption in the extended radio emission of these quasars. In this section we will consider in detail the issues connected with carrying out these observations.

3.5.1 Sensitivity and integration time calculations

An obvious first step in considering HI 21 cm observations is to assess the practicality of making observations of the line using existing radio telescopes, receivers, and spectral processing back ends. As we have mentioned, the cross section for absorption is quite small and so these observations are feasible at only the largest radio dishes. It is a useful exercise to calculate the integration time required to achieve a limiting 21 cm optical depth limit for a certain radio telescope and receiver configuration. In particular, the way in which the integration time scales with various parameters provides insight into the appropriate source classes.

The effective “Antenna” noise temperature T_A for an integration of time t_{int} and frequency bin width Δf is given by $T_A = \eta T_{sys}(\Delta f t_{int})^{-1/2}$. Here η is a factor of order unity which depends on the exact receiver configuration (see e.g. Rohlfs 1990, p. 142). T_A gives the size of the rms fluctuations in the observed radio spectrum. To compare with the expected source strength, we multiply by the antenna gain K_s . For

the Green Bank 140' telescope it is observed that $\eta = 3$, $K_s = 3.8 \text{ Jy K}^{-1}$, and near frequencies of 800 MHz, $T_{\text{sys}} \approx 50 \text{ K}$. Thus we have the general relation that S/N , the signal to noise per bin, for a source flux S_{T} , is given by

$$S/N = \frac{S_{\text{T}}}{1 \text{ Jy}} \frac{1}{\eta K_s} \left(\frac{T_{\text{sys}}}{1 \text{ K}} \right)^{-1} \left(\frac{\Delta f}{1 \text{ kHz}} \right)^{1/2} \left(\frac{t_{\text{int}}}{1000 \text{ s}} \right)^{1/2}.$$

Now consider more specifically the case of 21 cm absorption, where there is an absorbing cloud at redshift z , which has 21 cm optical depth τ (recall this is related to the neutral hydrogen density and the spin temperature), characteristic velocity width Δv , and covering fraction f_c . Since the radio emission of quasars can be quite extended, the covering fraction (the projected absorbing cloud area over radio emission area) can be small and this is an important factor. Assuming the spectrum has been smoothed to the resolution matching the characteristic velocity width, then we have

$$\begin{aligned} S/N &= 0.686 \left(\frac{\eta}{3} \right)^{-1} \left(\frac{K_s}{3.8 \text{ Jy K}^{-1}} \right)^{-1} \left(\frac{T_{\text{sys}}}{50 \text{ K}} \right)^{-1} \\ &\times \left(\frac{S_{\text{T}}}{3 \text{ Jy}} \right) \left(\frac{f_c \tau}{0.01} \right) \left(\frac{\Delta v}{10 \text{ km s}^{-1}} \right)^{1/2} \left(\frac{t_{\text{int}}}{1 \text{ hr}} \right)^{1/2} (1+z)^{-1/2}. \end{aligned}$$

We can now easily use this equation to solve for the needed integration time for a particular source at any radio telescope. As an example, we will use the parameters for the NRAO Green Bank 140' dish, with $S/N = 3$, $z = 0.5$, and using Total Power Mode (i.e. position switching, in which half the time is spent on-source and half the time off-source). Then we have

$$t_{\text{int}} = 7.6 f_u \left(\frac{T_{\text{sys}}}{50 \text{ K}} \right)^2 \left(\frac{S_{\text{T}}}{3 \text{ Jy}} \right)^{-2} \left(\frac{f_c \tau}{0.01} \right)^{-2} \left(\frac{\Delta v}{10 \text{ km s}^{-1}} \right)^{-1} \text{ hrs}, \quad (3.1)$$

where we now also include f_u , the fraction of data which is uncorrupted by interference, as discussed in the next section.

3.5.2 Sources of Radio Frequency Interference

The calculation in the previous section was made assuming some fixed thermal noise temperature depending on the antenna and receiver characteristics, but in reality we must also contend with contamination from external sources. The three main sources of interference are man-made radio frequency interference (RFI) outside of the radio astronomy restricted bands, solar interference, and standing waves at the radio dish. These can all be important and they influence strongly the nature and execution of radio observations. This is especially true in the search for redshifted HI 21 cm (1421 MHz) absorption, since at $z > 0.42$ the line is redshifted out of the restricted band.

Man-made RFI

The strength and frequency of man-made RFI is strongly dependent on the local regulation of the airwaves. The project described in this chapter has been carried out thus far with two sites in mind for the radio observations – the NAIC 300m dish near Arecibo, Puerto Rico; and the NRAO 140' dish in Green Bank, VA. Unfortunately, the Arecibo receiver carriage house is undergoing a major upgrade at this time and operating on only a limited basis. This leaves the Green Bank telescope, which is much smaller but compensates by having more sensitive receivers and better spectral processing units. The information about man-made RFI which follows applies only to the Green Bank site, and has been provided by the extraordinarily helpful staff and researchers at NRAO, in particular Robert Brown and Wesley Sizemore. As will be described in Sec. 3.5.3, we have been granted 5 nights there in November, 1993 to search for 21 cm absorption.

The potential sources of RFI in the range 500 to 1400 MHz are summarized in Table 3.4. This table illustrates the challenge of trying to do 21 cm absorption line work at redshifts above 0.5, since much of the band is potentially subject to RFI. Fortunately, the situation is not as hopeless as it might appear at first glance. The Green Bank telescope is located in a “radio quiet” zone, which means that the cellular and special mobile radio communications are prohibited and these bands should be

Table 3.4: Potential sources of RFI between 500 - 1400 MHz

Band (MHz)	Description
512.0 - 608.0	UHF TV broadcasting channels 21 - 36.
614.0 - 806.0	UHF TV broadcasting channels 38 - 69.
806.0 - 825.0	Special mobile radio - Mobile band
825.0 - 845.0	Cellular radio - Mobile bands "A" and "B"
851.0 - 870.0	Special mobile radio - Base station band
870.0 - 890.0	Cellular radio - Base station bands "A" and "B"
894.0 - 896.0	Aeronautical mobile - Airphone
896.0 - 901.0	Special mobile radio - mobile band
902.0 - 928.0	Amateur radio band
935.0 - 940.0	Special mobile radio - Base station band
960.0 - 1215.0	Aeronautical radio navigation

clear. The only frequencies used in the amateur band are 919 - 921 MHz and these are generally very weak. On the other hand, the aeronautical mobile band which is used by public telephones on commercial aircraft is very active and strong, and so is completely unusable. It is so strong in fact that a notch filter will be installed in the receiver electronics to permanently exclude these transmissions. The aeronautical radio navigation band is used by non-commercial aircraft for airborne radar, and the RFI is unpredictable from day to day. Recent monitoring of this band at Green Bank indicates that it is clear most of the time, and that the interference events are generally short and last only a few seconds. This is subject to change, especially if there is unusual military activity, but in the past the military have been cooperative in keeping transmissions to a minimum while observers are using this band.

The UHF TV channels are, unfortunately, quite visible most of the time even in the radio quiet zone. With the rather large antenna (surely the envy of every TV addict), channels originating from as far away as Pittsburg can be seen. Even in this band, there is still hope. The channels are separated by 6 MHz, and each one has three carriers - video, audio, and color (which is down in strength from the other two by ~ 15 dB). The 3 dB bandwidth of these signals are 0.20, 0.10, and 0.12 MHz

respectively. Thus if the observed line is sufficiently far from these carriers, the receiver electronics are not saturated, and the spectral analysis hardware can reject the narrow interference lines, then useful spectroscopy can still be done. In fact, this is the case at Green Bank, where they have available a powerful spectral analysis back-end called the Spectral Processor. This machine and our planned utilization of it are discussed in Sec. 3.5.3.

Solar interference can be a problem during daytime observations since the sun has a brightness temperature of nearly 10^6 K. Even in a 40-50 dB sidelobe this can cause a significant (spurious) contribution to the signal. This is a problem because in total power mode the telescope response function at the position of the sun can vary drastically with small changes in pointing. However, observation of narrow spectral absorption lines is still possible since only the shape of the continuum is affected.

The final source of interference is standing waves between the telescope primary and various support structures, housings, wires, etc. This arises when the continuum source (the quasar in our case) is strong enough that the energy in the reflected waves which arrive in phase with the direct waves is a significant fraction of the system noise power. The phase of the reflected waves is obviously wavelength dependent and so the interference is manifested as an anomalous sine wave component in the continuum. For the 140' telescope the period is about 7 MHz, and so again this is not a problem in observing narrow spectral features.

3.5.3 Green Bank 140' Program

We have been granted 5 nights at the NRAO Green Bank 140' telescope in November 1993 to search for 21 cm absorption in lobe-dominated quasars with Mg II absorption line systems. In Table 3.5 we give our list of systems, with columns for source name, position, quasar emission redshift, absorber redshift, Mg II rest equivalent widths in Angstroms, redshifted 21 cm frequency in MHz, estimated source flux at ν_{21} in Jy, and planned observation time in hours. We estimate the integration time using Eqn. 3.1, assuming the following: a system noise temperature of 50 K; an absorption line velocity width of 10 km s^{-1} ; observation in position-switching mode; $f_u = 0.7$ (fraction of uncorrupted data); and $f\tau = 0.03$ at $3\text{-}\sigma$ confidence. Note that the

Table 3.5: Source list for Green Bank HI 21 cm absorption observations

Source	Position (1950)		z_{em}	z_{abs}	$W_0(\text{MgII})$		ν_{21}	$S(\nu_{21})$	t_{int}
3C 68.1	02 29 27.0	34 10 56	1.240	0.7755	1.55	1.45	800.0	> 7	2.0
PKS 0454-22	04 54 02.2	-22 03 56	0.534	0.4745	1.37	1.34	963.3	2.8	12.5
					0.4833	0.47	0.23	957.6	2.8
3C 175	07 10 15.3	11 51 23	0.768	0.4629	0.66	0.25	970.9	3.5	8.0
3C 181	07 25 20.1	14 43 47	1.382	1.1694	0.39	0.22	654.7	2.5	(16.0) ^a
3C 205	08 35 10.0	58 04 52	1.534	1.4353	0.62	0.61	583.3	5.5	3.5
					1.4383	0.26	0.28	582.5	5.6

^aActual observing time will be only 2 hours. See text.

multiple systems in PKS 0454-22 and 3C 205 can be observed simultaneously.

We will observe these sources at the frequencies listed using the 300 - 1000 MHz front end receiver. Of the 7 absorption line systems, 3 require the 500 - 750 MHz feed and 4 require the 750 - 1000 MHz feed. For all the measurements we will use the Spectral Processor back end, which has the excellent noise rejection capability necessary below 1000 MHz. We will use a bandwidth of 5 MHz, giving us velocity resolution adequate for 21 cm absorption line study and covering an ample frequency range near the absorber redshift.

The Spectral Processor generates a 512 channel fourier transform of the signal every 12.8 μsec and was developed primarily for use in pulsar timing measurements. It can also be used effectively for conventional spectroscopy by time averaging. Since it is a full fourier transform machine, the essentially monochromatic sources of RFI (both inside and outside the passband) have much reduced effect on neighboring frequencies, compared to a conventional autocorrelator.

As discussed previously, the band 500 - 1000 MHz is subject to significant radio interference and so it was surveyed in March 1993 by Wes Sizemor for potential sources of RFI. The lines in our list at 800 MHz and above were found to free from interference at the sensitivity of the 40' monitoring dish. The lines in 3C 205 lie in the UHF TV band, but are sufficiently far from the carrier frequencies that the source spectrum can be obtained. The line in 3C 181 is only 90 kHz from the color carrier for UHF 44 and so at this time we will devote only 2 hours to access the characteristics

of this signal in the direction of 3C 181.

Since RFI between 500 and 1000 MHz can be substantially reduced during night-time hours, our observations are scheduled between 2200h and 0700h local time. Another technique we will utilize to minimize RFI corruption of data is very short integration times, from 2 minutes to as short as 2 seconds. As was mentioned, much of the observed RFI comes in short nearly-monochromatic bursts of large amplitude, and this technique can greatly increase the percentage of usable data. It should be mentioned that our observing program is somewhat unusual and difficult and will require non-standard observing techniques and data analysis techniques to be successful. The observing proposal was reviewed enthusiastically at Green Bank and we have confidence that with their able assistance we will reach our sensitivity goals.

3.5.4 Future possibilities

The prospects for future HI 21 cm observations look both uncertain and hopeful. On the one hand, the radio airwaves are becoming more crowded and more noisy. Personal telecommunications are gaining immense popularity and the trend is not likely to reverse. With this popularity will come the inevitable political pressure to open up new bands for private and commercial use. From this perspective the prospects for doing HI 21 cm observations at redshifts above 0.5 near highly populated areas may be grim. On the other hand, improvements in radio telescope technology, most notably in the dish design and back-end signal processing, show promise of keeping us one step ahead of the airwave crowding. The 100 m Green Bank Telescope which is currently under construction will utilize a unique design for the receiver arm which is asymmetric and presents a much lower cross-section for scattering of radio waves. This will significantly reduce interference as well as deliver improved sensitivity (Hall and King 1992). Another example is the Westerbork Synthesis Radio Telescope, which is currently in the process of upgrading their receivers to do 300 - 400 MHz by 1994 and 700 - 1100 MHz by 1996. They will limit interference by having high quality back-ends with very many spectral channels.

As was mentioned earlier, the line feeds for the NAIC 300 m dish at Arecibo are currently being replaced by a Gregorian dual-reflector feed which will be fully tunable.

When completed, this facility will be ideal for 21 cm absorption line work, since the radio environment there is still relatively quiet.

The final project which is extremely exciting for people in the field and for our project in particular is the Giant Metrewave Radio Telescope array (GMRT) which is being developed in India (see e.g. Swarup 1990). This array will consist of 30 fully steerable dishes, each 45 m in diameter, with an overall size comparable to the VLA. The receivers will cover the range 30 - 1420 MHz. The location in India makes this facility much less susceptible to radio interference. The pending ability (both at GMRT and Westerbork) to actually *image* high redshift 21 cm absorbers means that discovering these absorbers should have high priority. We reiterate here that most 21 cm absorbers currently known occur in quasars with compact radio emission, so that arcsecond-scale synthesis imaging will not be revealing. This is in contrast to the sample we have defined.

Chapter 4

Absorption in a sample of 56 quasars

In Chapter 3 we found Mg II absorption in lobe-dominated quasars so that we can look for 21 cm absorption at those redshifts. In order to find those optical absorbers in the sample of 69 quasars a substantial program of observations was carried out at the Multiple Mirror Telescope and the Palomar 5.08 m telescope between June 1988 and May 1989. During a total of 13 nights, 56 quasars were observed. In addition to simply identifying strong absorption systems for the 21 cm program, this survey is useful for characterizing the statistical properties of absorption line systems. Since the majority of quasars in the sample are at moderate redshift ($z_{em} = 0.7$ to 1.5), our spectra are most useful for finding Mg II systems, which can be detected over the range $z_{abs} \approx 0.2$ to 2.0 using ground-based telescopes.

The starting point for our sample of quasars is the list of 69 objects for which we obtained detailed morphological information on the radio emission, as described in Chapter 3. Thirteen of these objects were not observed for the following reasons: Instrumental problems such as bad bias or wrong object observed; object fainter than published magnitude when observed; redshift below 0.62 (which gave it a low priority); and good spectrum already available in literature. For one object there was no reason other than limited telescope time. With the exception of the last two, none of these could cause a statistical bias in the observations. The important point to

be drawn from this is that we can use all of the spectra which we obtained, despite the fact that several of them had well known absorption systems at the time of the observations. Our sample is based on criteria completely independent of any known optical absorption properties, and the excluded objects will introduce negligible bias.

4.1 Observations and data reduction

The observations at the Palomar 5-meter Telescope used Double Spectrograph (Oke and Gunn 1982) The spectra were flatfielded using a long quartz comparison lamp exposure obtained during the day. In February 1988 the TI-CCD #432 was used in the blue side of the spectrograph with the 1200 l mm^{-1} grating in first order, and a $2''$ slit. The resulting resolution is 75 km sec^{-1} (FWHM). The TI-CCD #167 was used in the red side with the 1200 l mm^{-1} grating in first order, with resulting spectral resolution of 100 km sec^{-1} . Both sides were flattened with dome flats, and bias frames were obtained and subtracted in the usual way. Iron-argon and helium-neon-argon lamp exposures were taken every hour during the night to calibrate the pixel-to-wavelength transformation. Standard stars Ross 34 and G 138-31 were observed in order to identify telluric absorption features. Finally, in July 1988 the same TI-CCDs were used, with 1200 l mm^{-1} gratings being used in both red and blue sides in 1st order. Calibration was carried out in the same way as in February 1988 with the stars BD 33-2642 and Feige 110 being used for telluric comparisons. In the data taken on July 1988, there was a severe problem with the flat-fielding below 4100 \AA . For unknown reasons the position of defects on the chip appears to have been unstable by one to two pixels in the wavelength direction. This means that in many of these spectra there are spurious features which appear to be absorption lines. For this reason we do not apply our line finding algorithm to this spectral region, nor include it in any statistical analyses.

In Table 4.1 we show a journal of our observations. In this table is the object name, quasar emission redshift, wavelength range in Angstroms, FWHM spectral resolution in Angstroms, date, instrument, integration time in minutes, and spectrum identification. In the instrument column, P200 DS is the Palomar Double Spectrograph,

MMT blue is the MMT blue channel, and MMT red is the MMT low-resolution echellette spectrograph. For observations with the P200 DS and MMT blue channel, the spectral resolution is the average resolution of several calibration lamp lines over the width of the spectrum. For the MMT echellette observations the resolution is given in terms of X_λ which is defined by $X_\lambda = \lambda/3000 \text{ \AA}$.

4.2 QSO spectra

In Fig. 4.1 we show all of the spectra which we obtained in this survey. Each spectrum is labeled by the quasar name, quasar emission redshift, and the spectrum number. This number corresponds to the number in the journal of observations given in Table 4.1. At the bottom of each spectrum the error array of $1-\sigma$ deviations is plotted. The error array is plotted as a thick line in regions which are considered “bad” and are not searched for absorption lines or used in any calculations. Some of the spectra are flux calibrated and the y-axis is labeled “Relative Flux (f_ν)”, while the rest are not flux calibrated. In each spectrum we also mark the statistically significant absorption lines which are listed in Table 4.2.

Table 4.1: Journal of observations

Object	z_{em}	Wavelength	FWHM ^a	Date	Instrument	t_{int}	Sp. #
Q0056-0009	0.717	3104 - 4829	4.7	10-Jul-88	P200 DS	50	1
		4817 - 7251	6.5	10-Jul-88	P200 DS	50	2
Q0159-1147	0.670	3111 - 5064	1.5	05-Mar-89	MMT blue	30	1
Q0229+1309	2.065	4240 - 8175	$3.5X_{\lambda}$	05-Dec-88	MMT red	60	1
Q0229+3410	1.240	4668 - 8167	$3.7X_{\lambda}$	05-Dec-88	MMT red	120	1
Q0237-2322	2.224	4314 - 8170	$3.7X_{\lambda}$	05-Dec-88	MMT red	30	1
Q0350-0719	0.962	4277 - 8124	$3.7X_{\lambda}$	04-Dec-88	MMT red	40	1
Q0420-0127	0.915	4239 - 8181	$3.7X_{\lambda}$	05-Dec-88	MMT red	30	1
Q0538+4949	0.545	3196 - 5064	1.6	05-Mar-89	MMT blue	120	1
Q0610+2605	0.580	3166 - 5071	1.6	08-Nov-88	MMT blue	100	1
Q0642+4454	3.400	4249 - 8178	$3.7X_{\lambda}$	05-Dec-88	MMT red	60	1
Q0710+1151	0.768	3111 - 5071	1.6	08-Nov-88	MMT blue	40	1
Q0725+1443	1.382	4239 - 8178	$3.7X_{\lambda}$	05-Dec-88	MMT red	60	1
Q0736-0620	1.898	4240 - 8178	$3.7X_{\lambda}$	05-Dec-88	MMT red	30	1
Q0809+4822	0.871	3123 - 5119	1.6	08-Jan-89	MMT blue	120	1
Q0835+5804	1.534	4229 - 8173	$3.7X_{\lambda}$	05-Dec-88	MMT red	30	1
Q0855+1421	1.043	4494 - 10175	$3.5X_{\lambda}$	06-May-89	MMT red	90	1
Q0859-1403	1.327	3111 - 5069	1.6	08-Nov-88	MMT blue	30	1
		4434 - 10196	$3.3X_{\lambda}$	11-Apr-88	MMT red	30	2
Q0906+4305	0.670	3111 - 5065	1.6	08-Nov-88	MMT blue	60	1
Q1007+4147	0.613	3150 - 5067	1.6	08-Nov-88	MMT blue	15	1
Q1040+1219	1.029	3126 - 5123	1.6	08-Jan-89	MMT blue	60	1
Q1055+2007	1.110	3140 - 5122	1.6	08-Jan-89	MMT blue	30	1
		4303 - 8115	3.5	12-Apr-88	MMT red	30	2
Q1111+4053	0.734	3123 - 5064	1.6	05-Mar-89	MMT blue	60	1
Q1136-1334	0.554	3117 - 5061	1.6	05-Mar-89	MMT blue	53	1
Q1137+6604	0.652	3111 - 5063	1.6	05-Mar-89	MMT blue	20	1
Q1148-0007	1.982	4480 - 10145	$3.5X_{\lambda}$	07-May-89	MMT red	30	1
Q1153+3144	0.418	4444 - 10108	$3.5X_{\lambda}$	12-Apr-89	MMT red	100	1
Q1156+2931	0.729	3153 - 5066	1.6	08-Jan-89	MMT blue	55	1
Q1206+4356	1.400	4480 - 10169	$3.5X_{\lambda}$	06-May-89	MMT blue	45	1
Q1213+5352	1.065	4483 - 10131	$3.2X_{\lambda}$	07-May-89	MMT red	45	1
Q1218+3359	1.519	3137 - 4712	4.9	09-Jul-88	P200 DS	30	1
		4821 - 7249	6.6	09-Jul-88	P200 DS	30	2
Q1229-0207	1.038	4486 - 10125	$3.5X_{\lambda}$	06-May-89	P200 DS	20	1
Q1318+1122	2.171	3206 - 4712	4.9	10-Jul-88	P200 DS	40	1
		4817 - 7251	6.7	10-Jul-88	P200 DS	40	2
Q1327-2126	0.528	3175 - 5065	1.6	05-Mar-89	MMT blue	60	1
Q1328+2524	1.055	4438 - 10216	$3.3X_{\lambda}$	12-Apr-89	MMT blue	50	1
Q1328+3045	0.846	3104 - 4749	4.9	10-Jul-88	P200 DS	30	1
		4817 - 7251	6.7	10-Jul-88	P200 DS	30	2
Q1335-0611	0.625	3111 - 5066	1.6	05-Mar-89	MMT blue	95	1
Q1354-1512	1.890	4483 - 10175	$3.2X_{\lambda}$	07-May-89	MMT red	75	1

^a $X_{\lambda} = \lambda/3000 \text{ \AA}$

Table 4.1: - *cont'd* - Journal of observations

Object	z_{em}	Wavelength	FWHM ^a	Date	Instrument	t_{int}	Sp. #
Q1437+6224	1.090	4462 - 10175	$3.3X_{\lambda}$	06-May-89	MMT red	90	1
Q1442+1011	3.530	4435 - 10186	$3.3X_{\lambda}$	12-Apr-89	MMT red	74	1
Q1453-1056	0.938	3282 - 4855	5.1	09-Jul-88	P200 DS	20	1
		4821 - 7249	6.5	09-Jul-88	P200 DS	20	2
Q1458+7152	0.905	3740 - 4613	2.5	18-Jun-88	P200 DS	30	1
		4683 - 5981	3.8	18-Jun-88	P200 DS	30	2
Q1508-3231	1.191	3104 - 4740	4.9	10-Jul-88	P200 DS	30	1
		4817 - 7251	6.7	10-Jul-88	P200 DS	30	2
Q1618+1743	0.555	3104 - 4738	4.9	10-Jul-88	P200 DS	20	1
		4817 - 7251	6.7	10-Jul-88	P200 DS	20	2
Q1622+2352	0.927	3742 - 4613	2.4	16-Jun-88	P200 DS	90	1
		4684 - 5982	3.5	16-Jun-88	P200 DS	90	2
Q1629+1202	1.795	3137 - 4717	5.1	09-Jul-88	P200 DS	40	1
		4821 - 7249	6.7	09-Jul-88	P200 DS	40	2
		3740 - 4613	2.5	18-Jun-88	P200 DS	60	3
		4683 - 5981	3.8	18-Jun-88	P200 DS	60	4
Q1634+6251	0.988	4580 - 10061	$3.3X_{\lambda}$	07-May-89	MMT red	135	1
Q1828+4842	0.695	3104 - 4764	5.0	10-Jul-88	P200 DS	25	1
		4817 - 7251	6.5	10-Jul-88	P200 DS	25	2
		3740 - 4613	2.5	17-Jun-88	P200 DS	60	3
		4694 - 5981	3.6	17-Jun-88	P200 DS	60	4
		4539 - 10104	$3.5X_{\lambda}$	06-May-89	P200 DS	30	5
Q1901+3155	0.635	3742 - 4613	2.4	16-Jun-88	P200 DS	60	1
		4684 - 5982	3.6	16-Jun-88	P200 DS	60	2
Q2003-0232	1.457	3250 - 4714	5.0	09-Jul-88	P200 DS	50	1
		4821 - 7249	6.5	09-Jul-88	P200 DS	50	2
		3742 - 4613	2.5	16-Jun-88	P200 DS	60	3
		4684 - 5982	3.6	16-Jun-88	P200 DS	60	4
Q2044-0247	0.942	3740 - 4613	2.5	18-Jun-88	P200 DS	67	1
		4758 - 5981	3.8	18-Jun-88	P200 DS	67	2
Q2115-3031	0.980	3189 - 4855	5.1	09-Jul-88	P200 DS	20	1
		4821 - 7249	6.6	09-Jul-88	P200 DS	20	2
Q2143-1541	0.700	3122 - 4736	4.9	10-Jul-88	P200 DS	45	1
		4817 - 7251	6.7	10-Jul-88	P200 DS	45	2
Q2223+2102	1.959	3137 - 4766	5.1	09-Jul-88	P200 DS	45	1
		4821 - 7249	6.7	09-Jul-88	P200 DS	45	2
Q2230+1128	1.037	3137 - 4855	5.1	09-Jul-88	P200 DS	44	1
		4821 - 7249	6.7	09-Jul-88	P200 DS	44	2
Q2249+1832	1.757	3104 - 4712	4.9	10-Jul-88	P200 DS	50	1
		4817 - 7251	6.7	10-Jul-88	P200 DS	50	2
Q2251+2429	2.328	3137 - 4855	5.0	09-Jul-88	P200 DS	45	1
		4821 - 7249	6.7	09-Jul-88	P200 DS	45	2
		4277 - 8123	6.5	04-Dec-88	MMT red	90	3

^a $X_{\lambda} = \lambda/3000 \text{ \AA}$

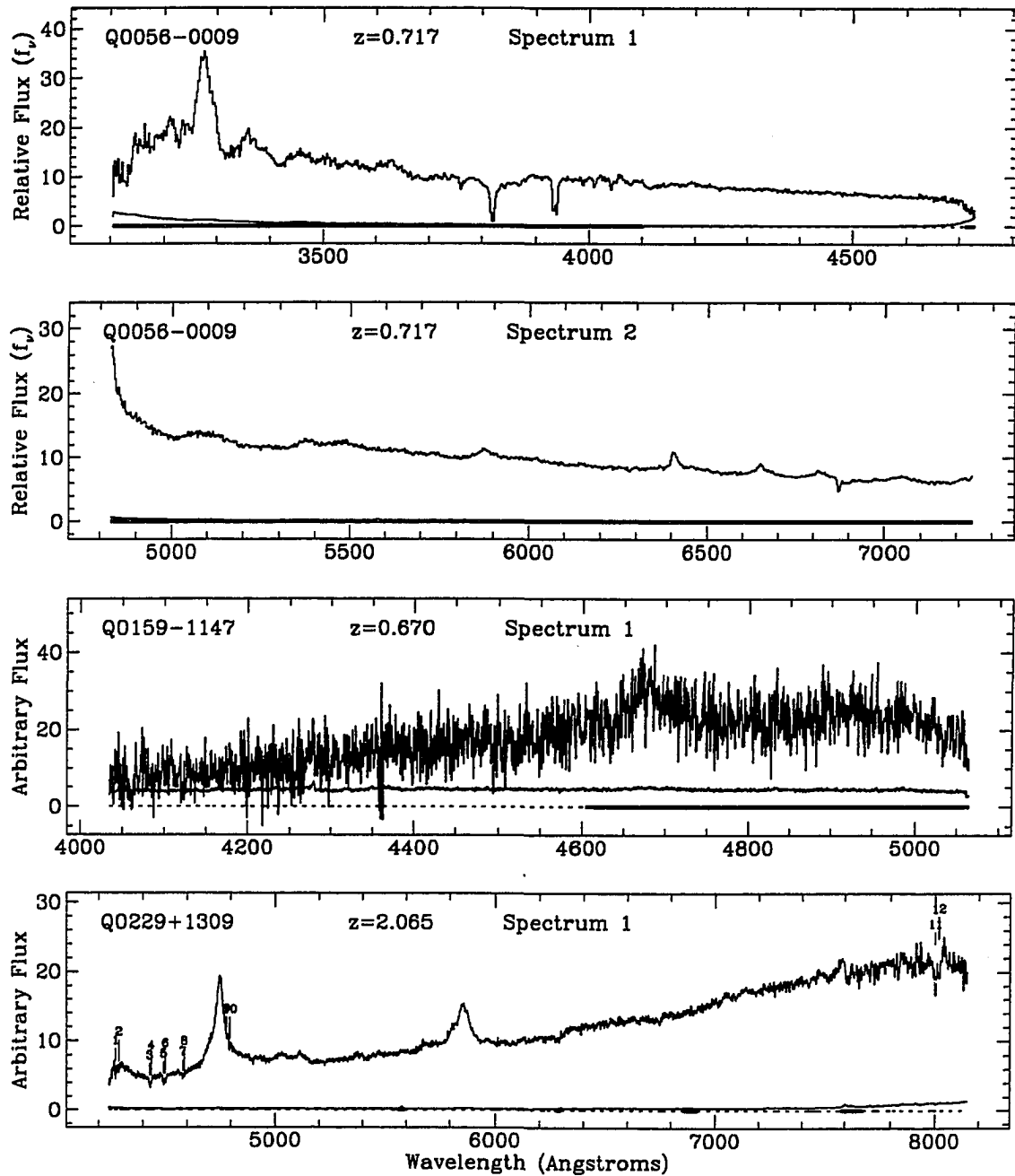


Figure 4.1: Quasar spectra

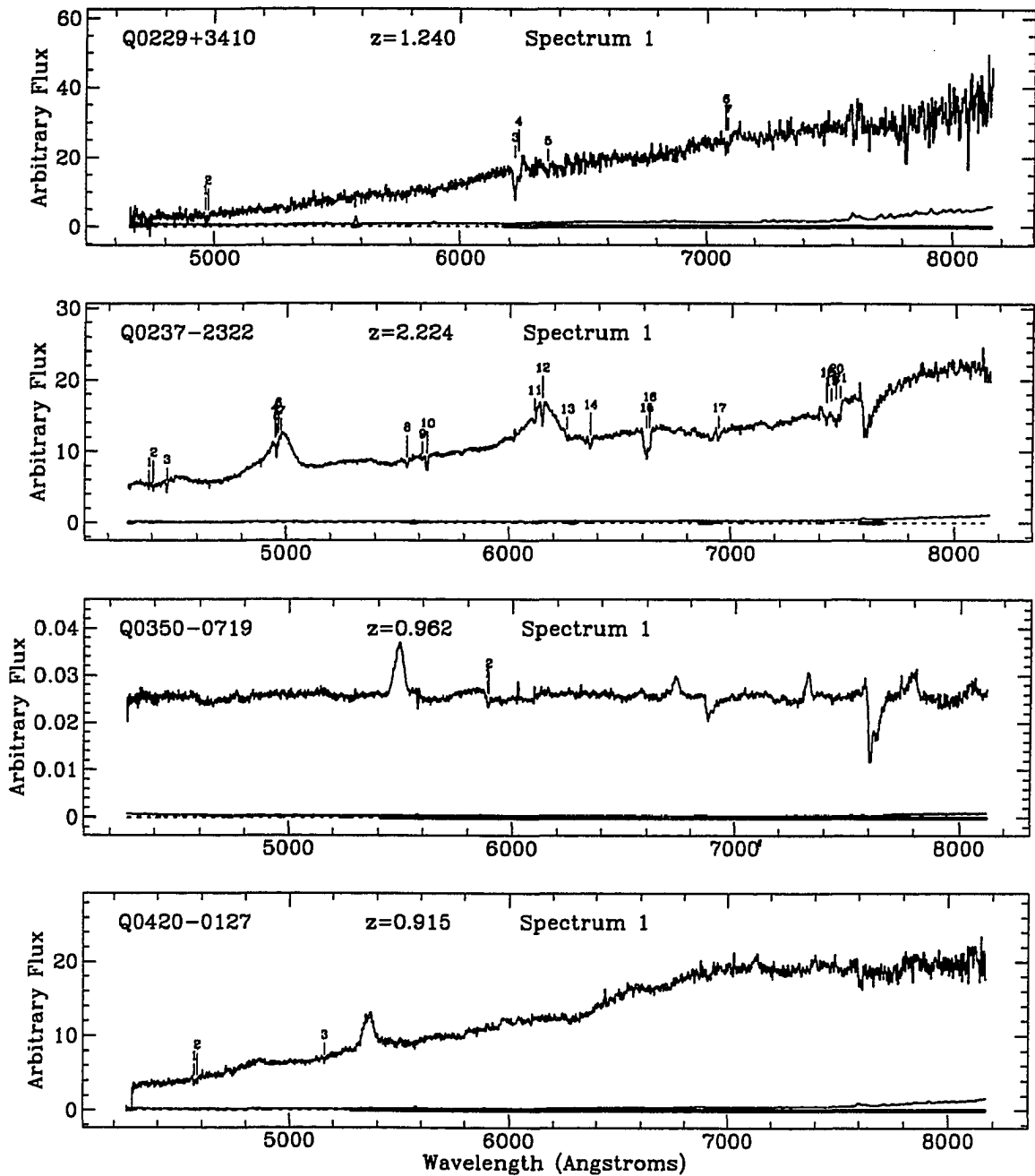


Figure 4.1: Quasar spectra

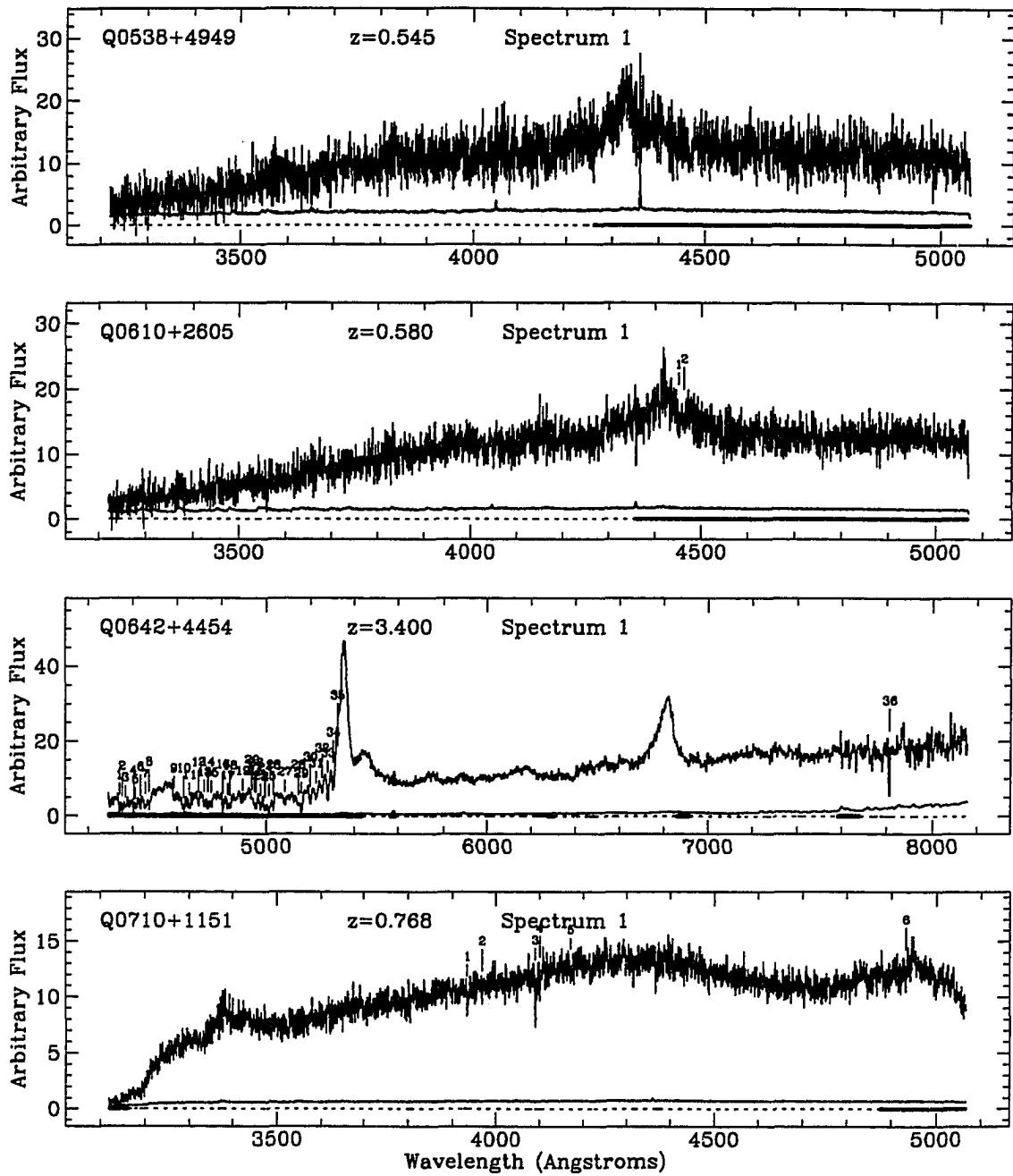


Figure 4.1: Quasar spectra

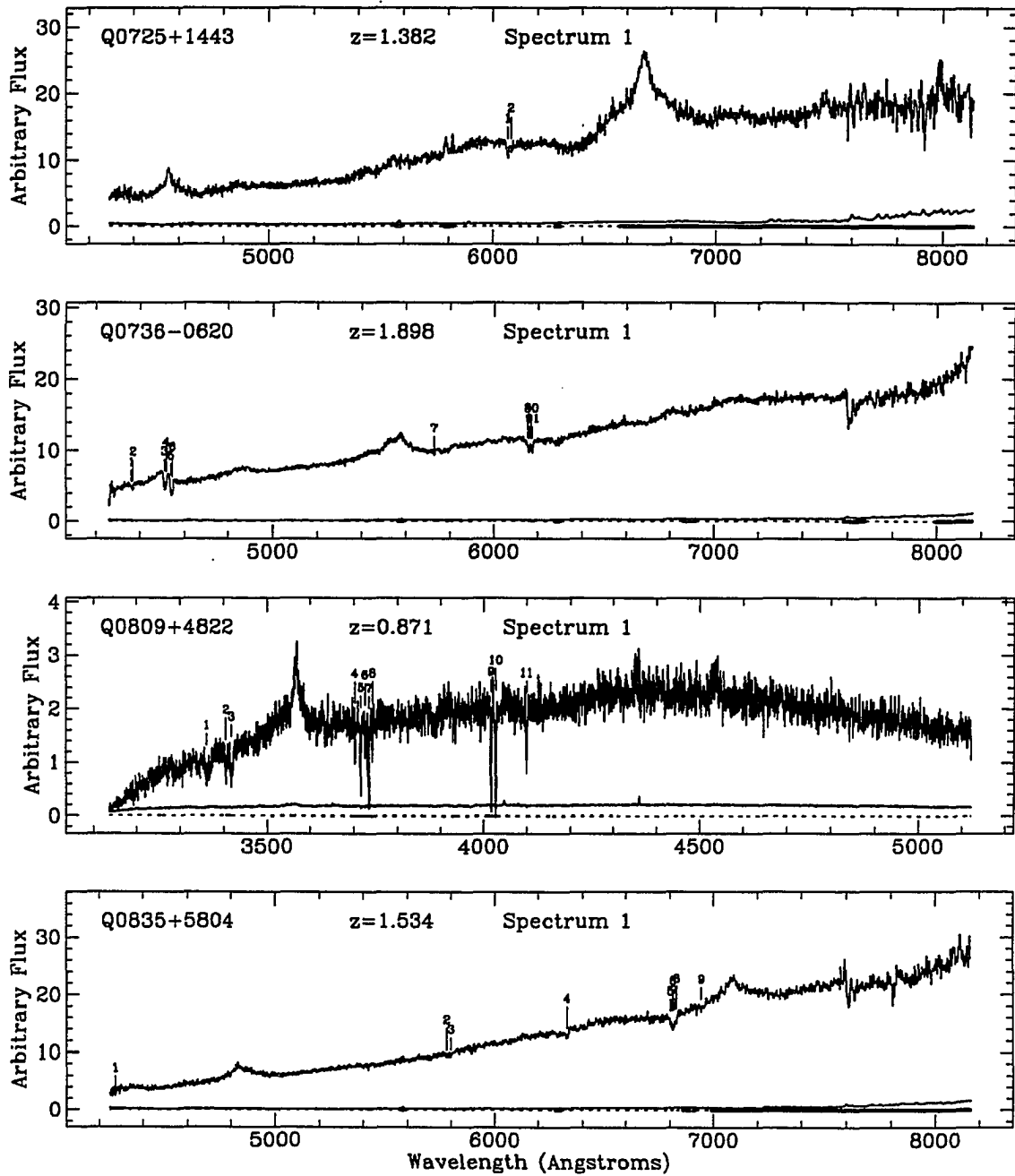


Figure 4.1: Quasar spectra

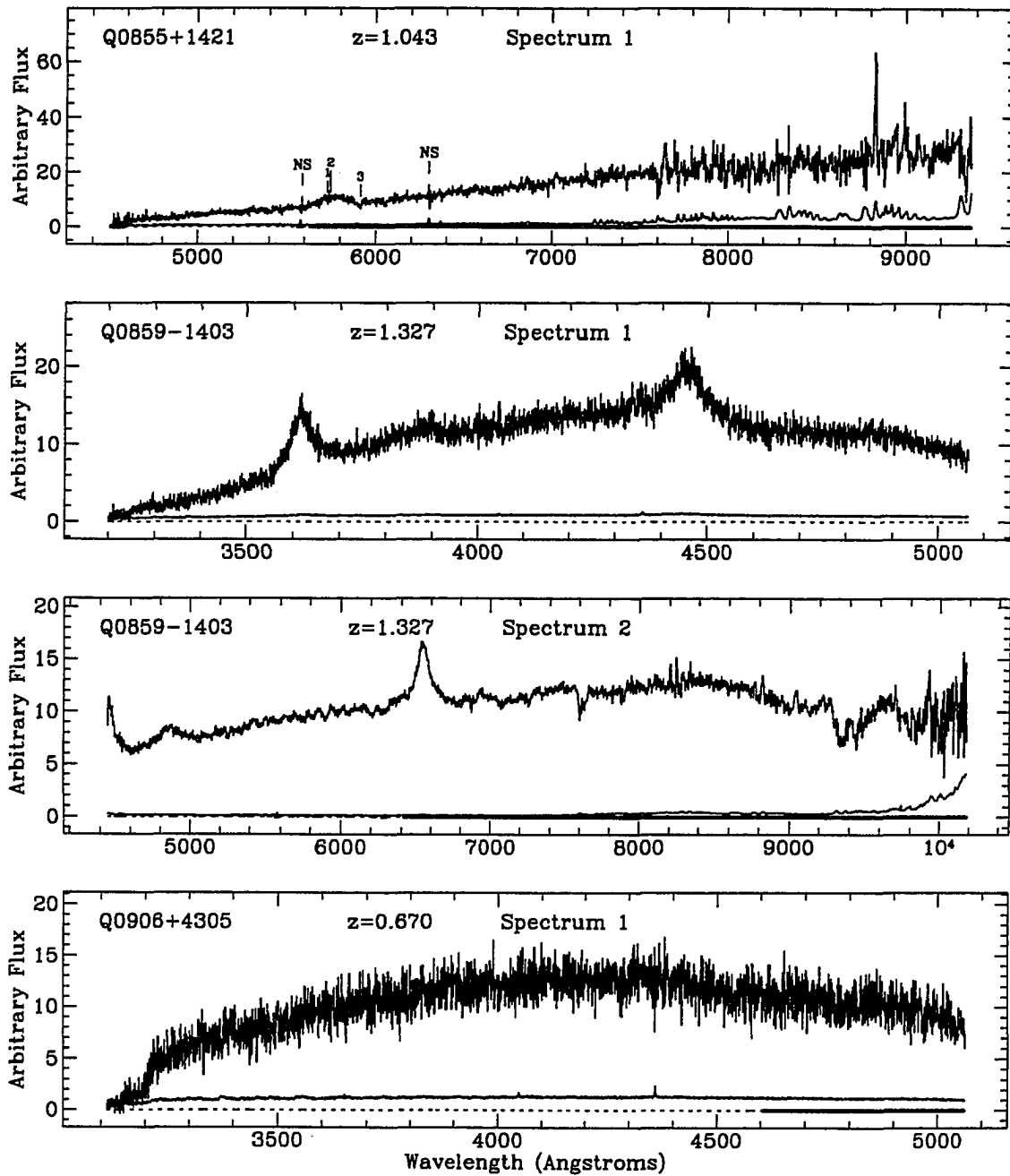


Figure 4.1: Quasar spectra

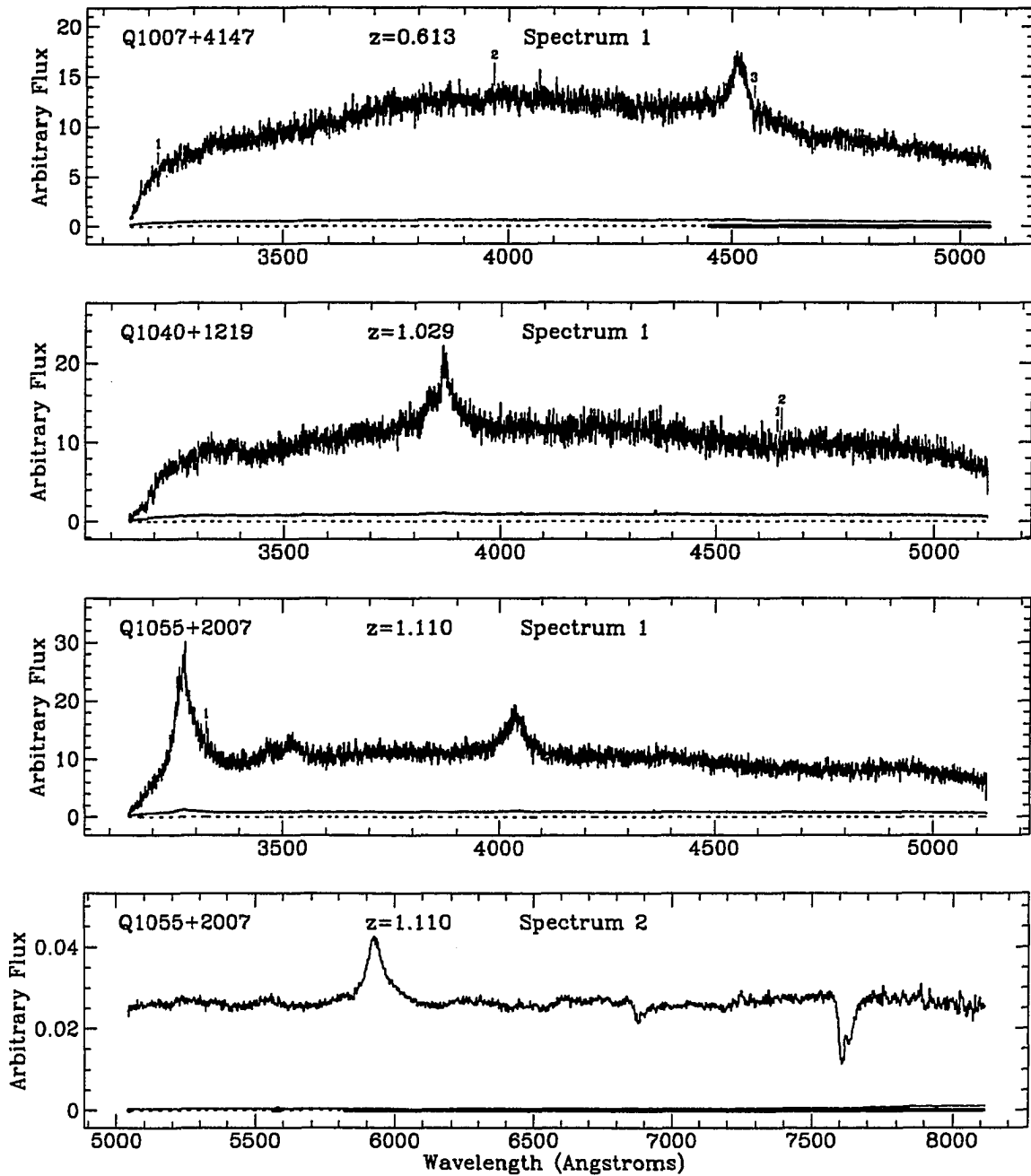


Figure 4.1: Quasar spectra

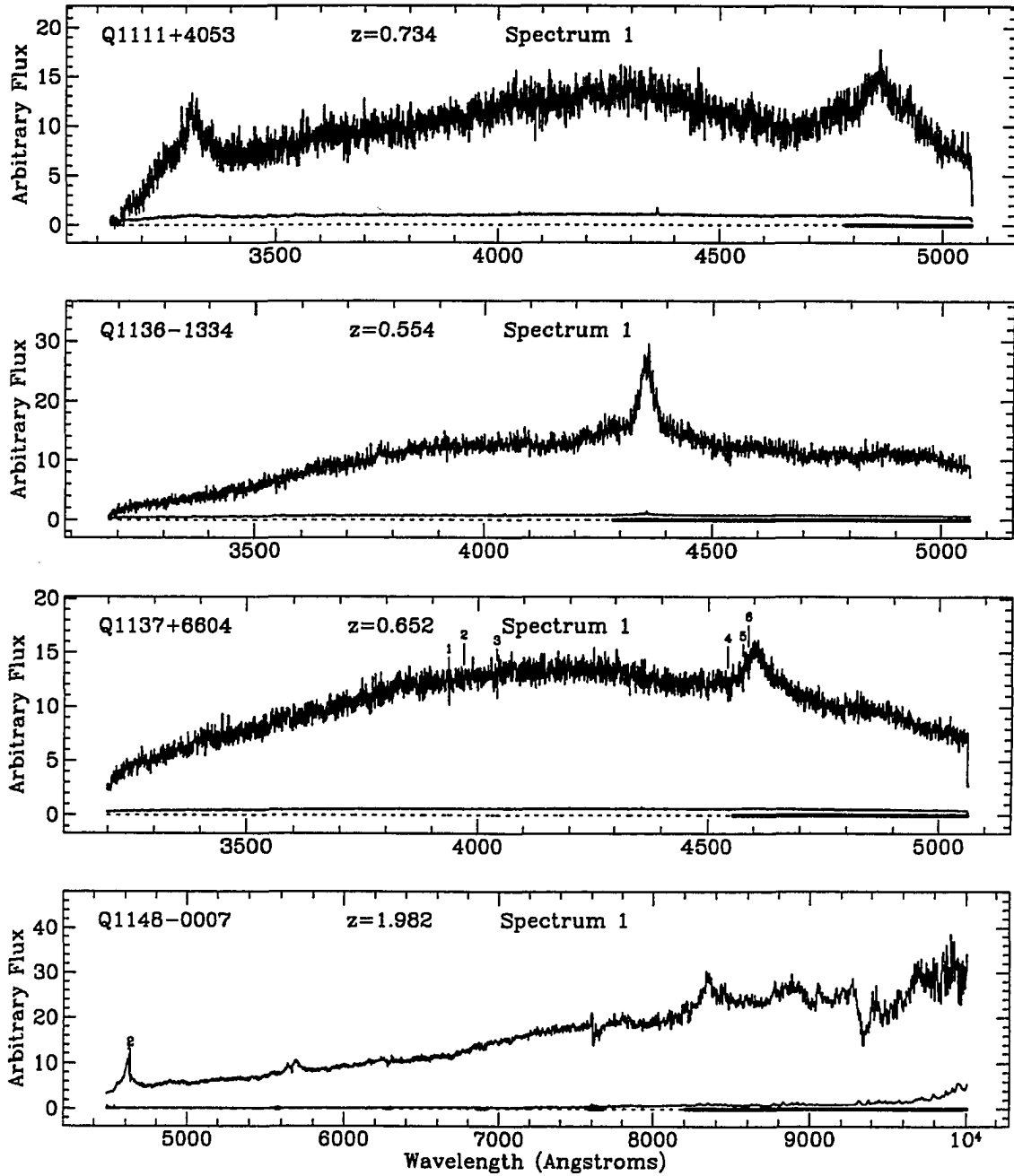


Figure 4.1: Quasar spectra

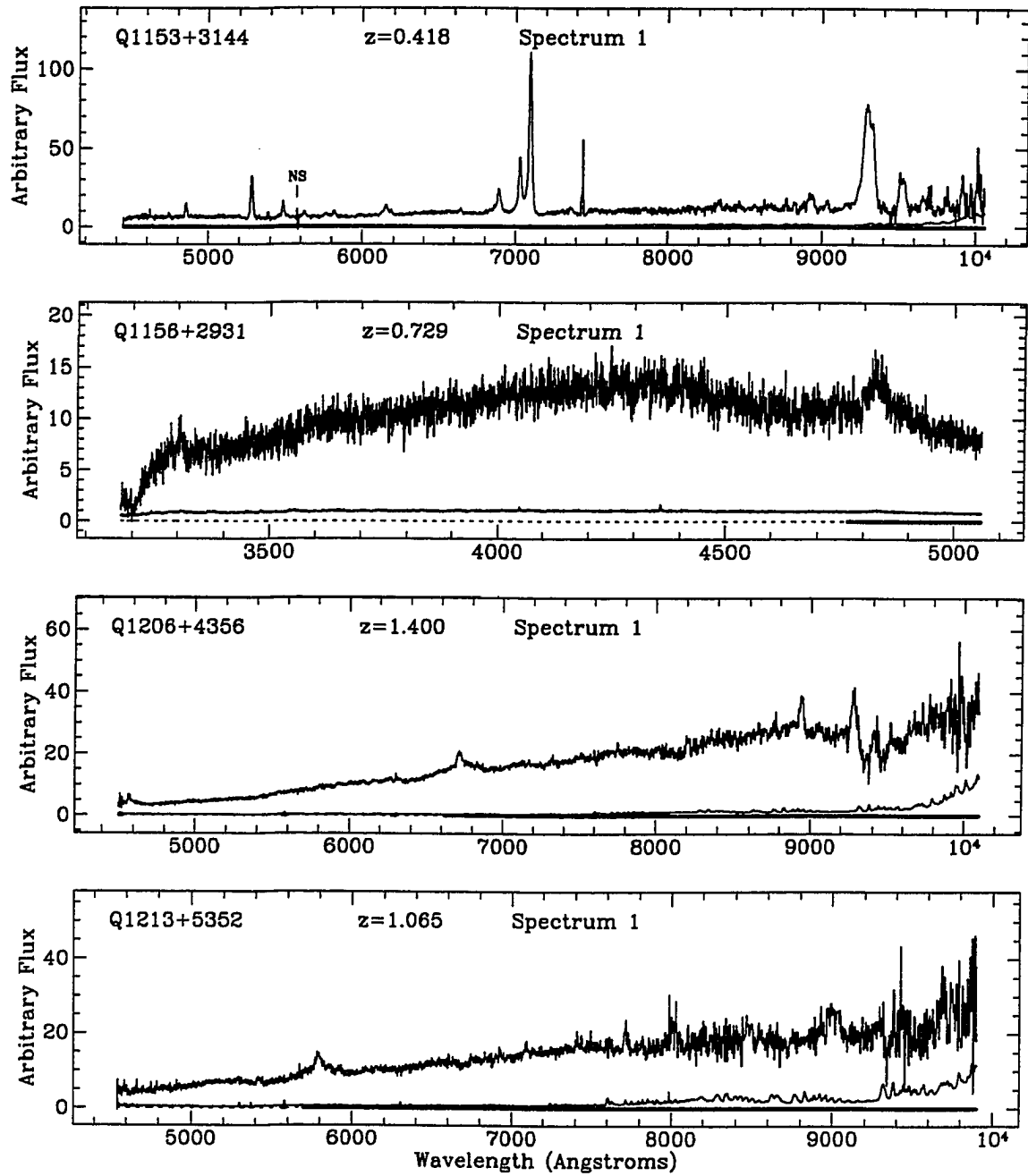


Figure 4.1: Quasar spectra

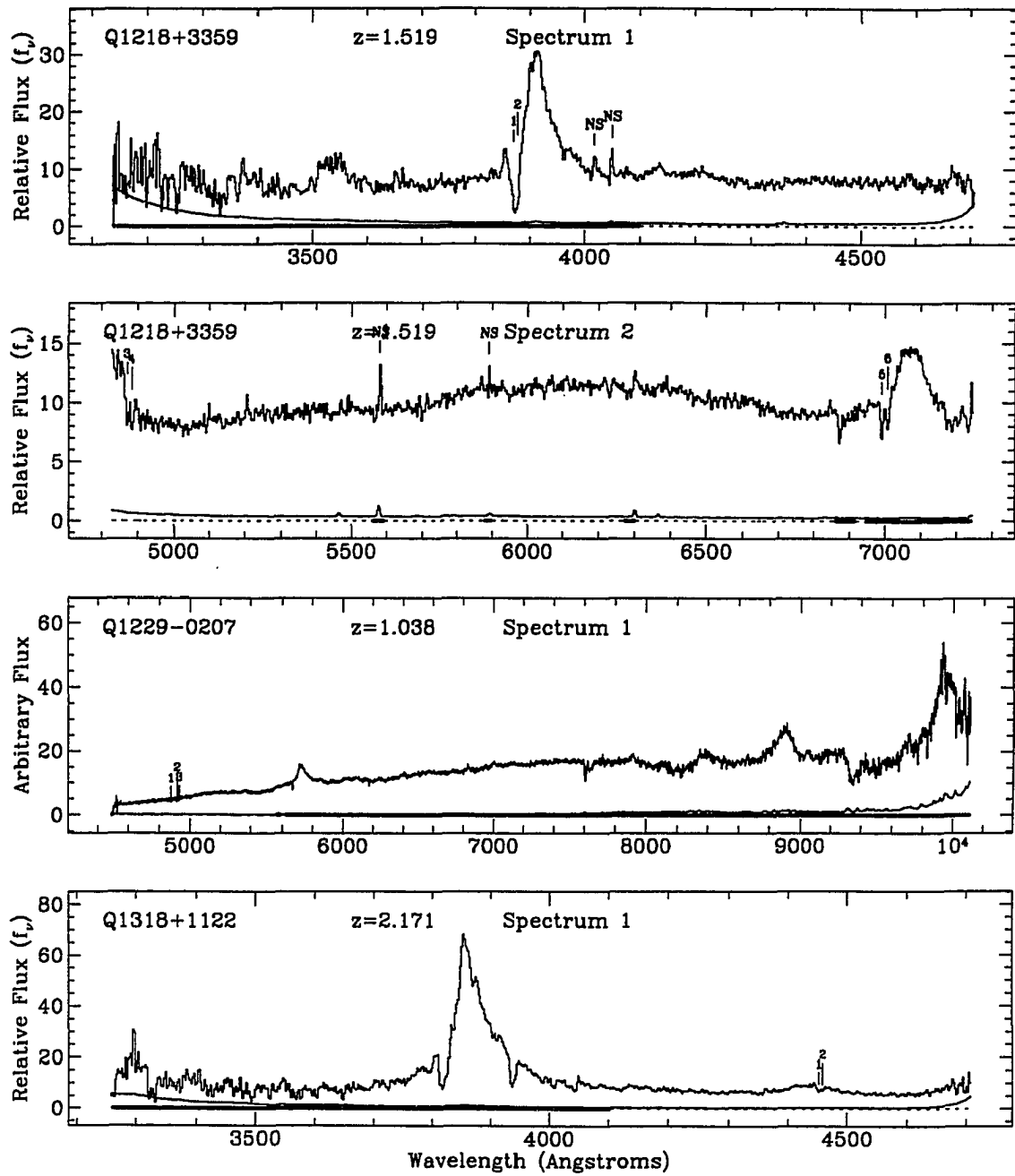


Figure 4.1: Quasar spectra

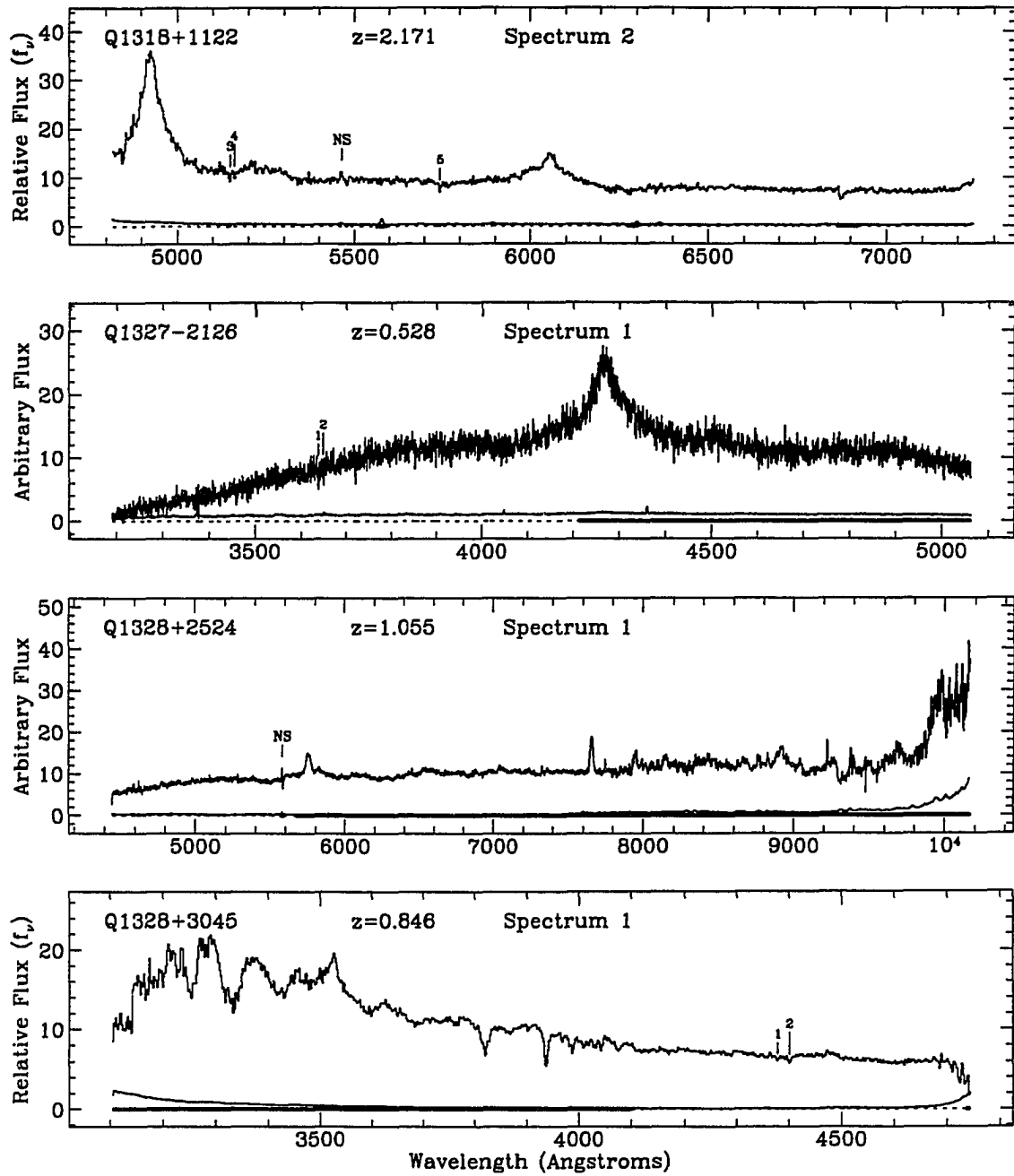


Figure 4.1: Quasar spectra

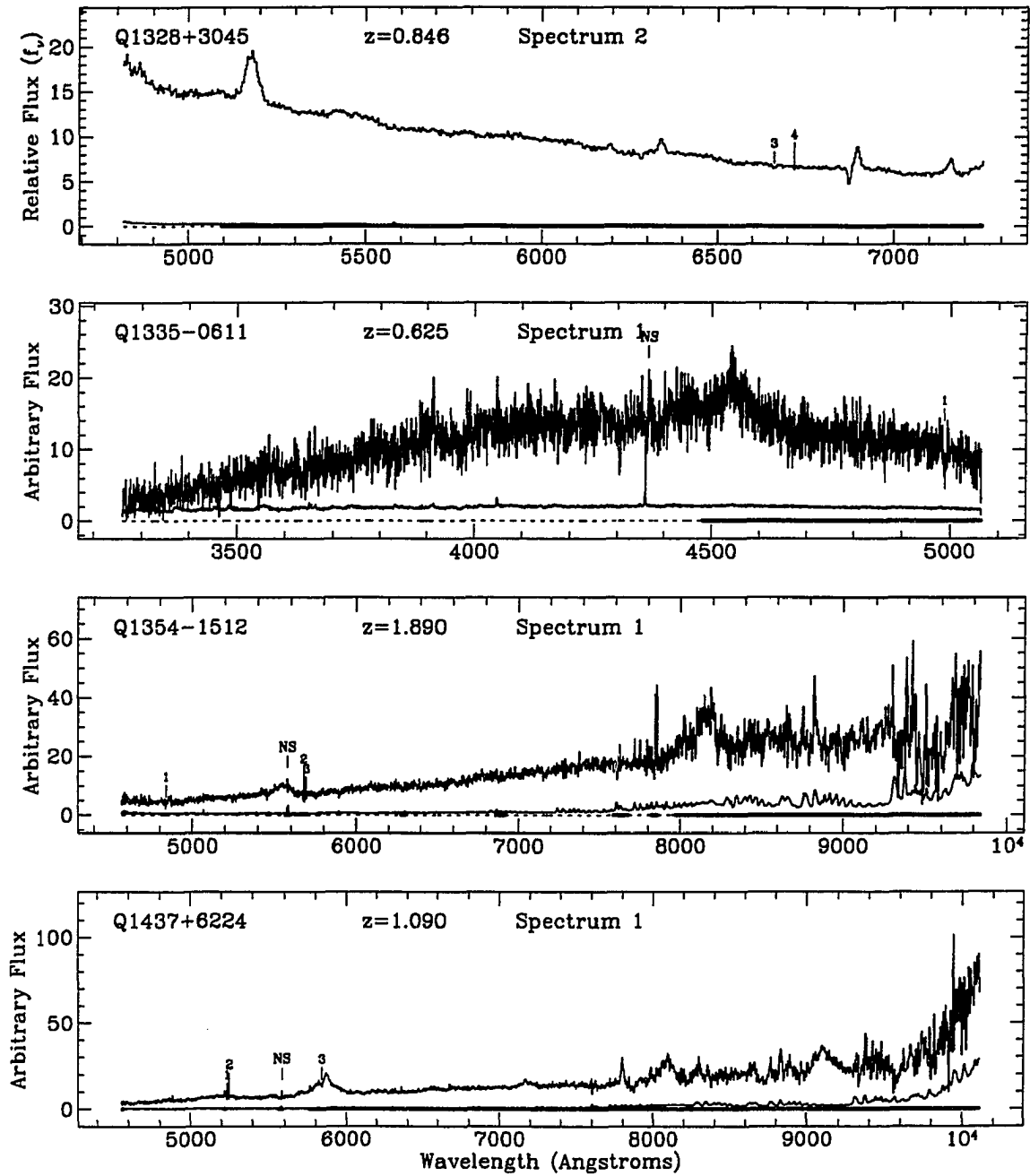


Figure 4.1: Quasar spectra

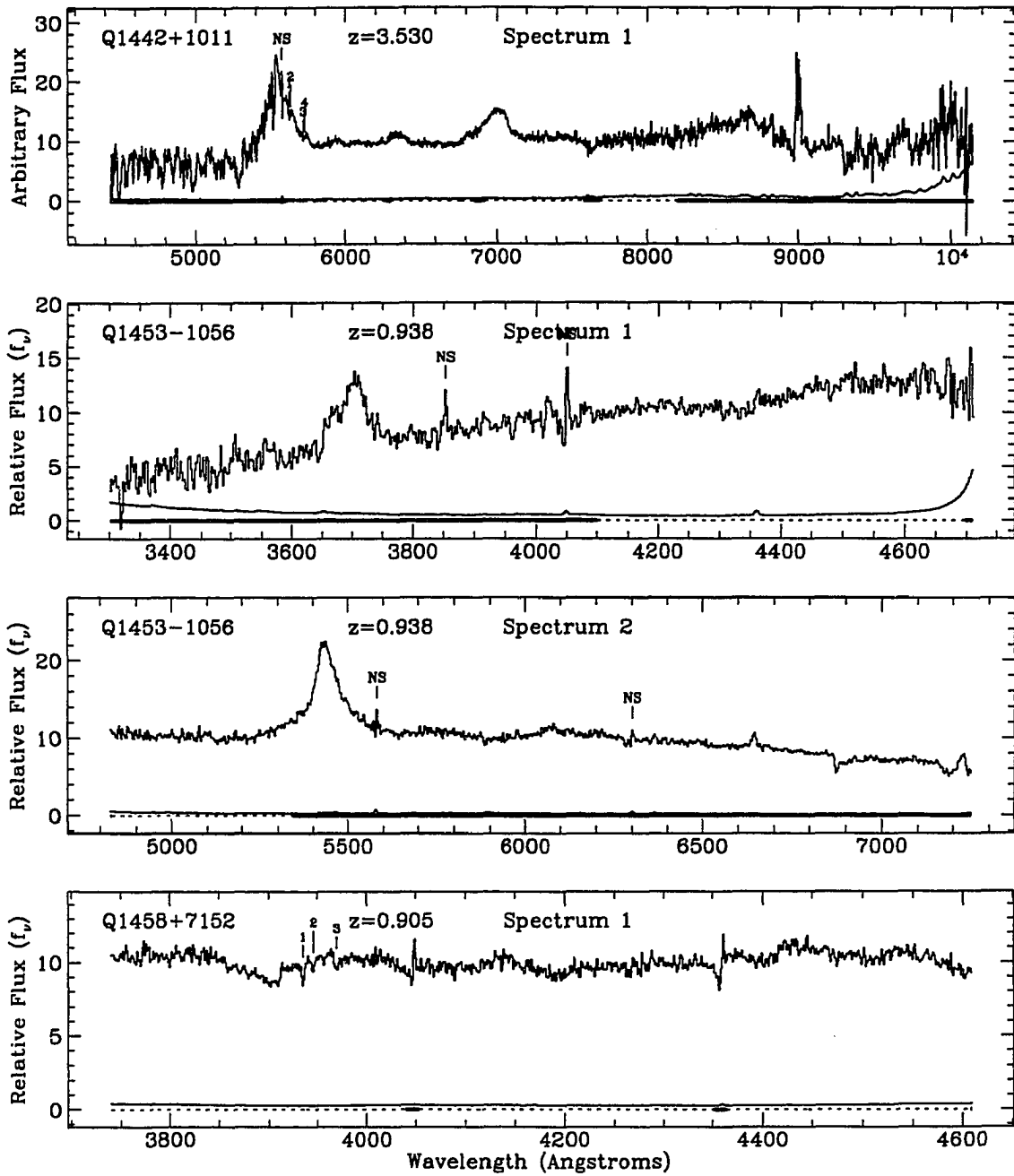


Figure 4.1: Quasar spectra

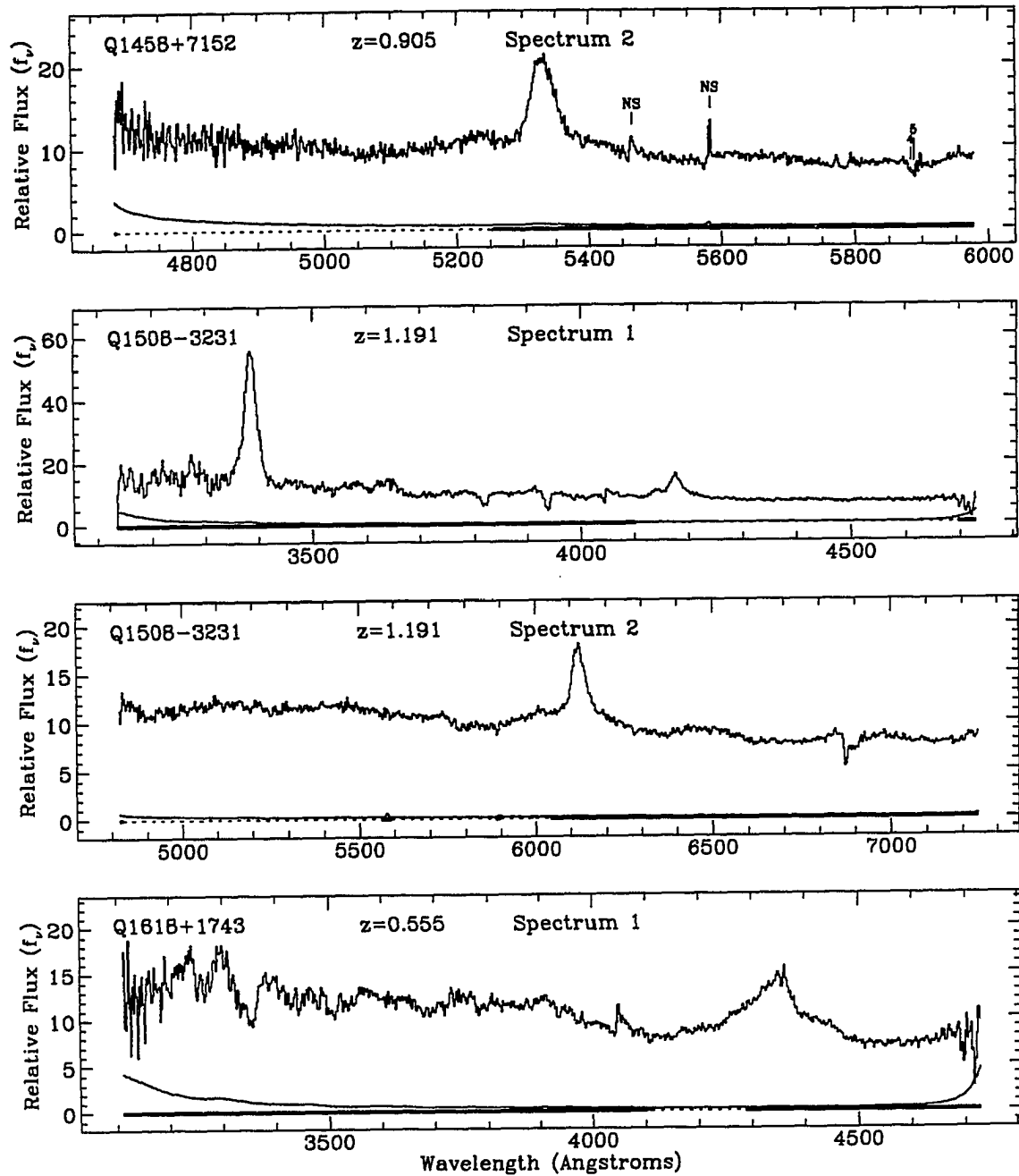


Figure 4.1: Quasar spectra

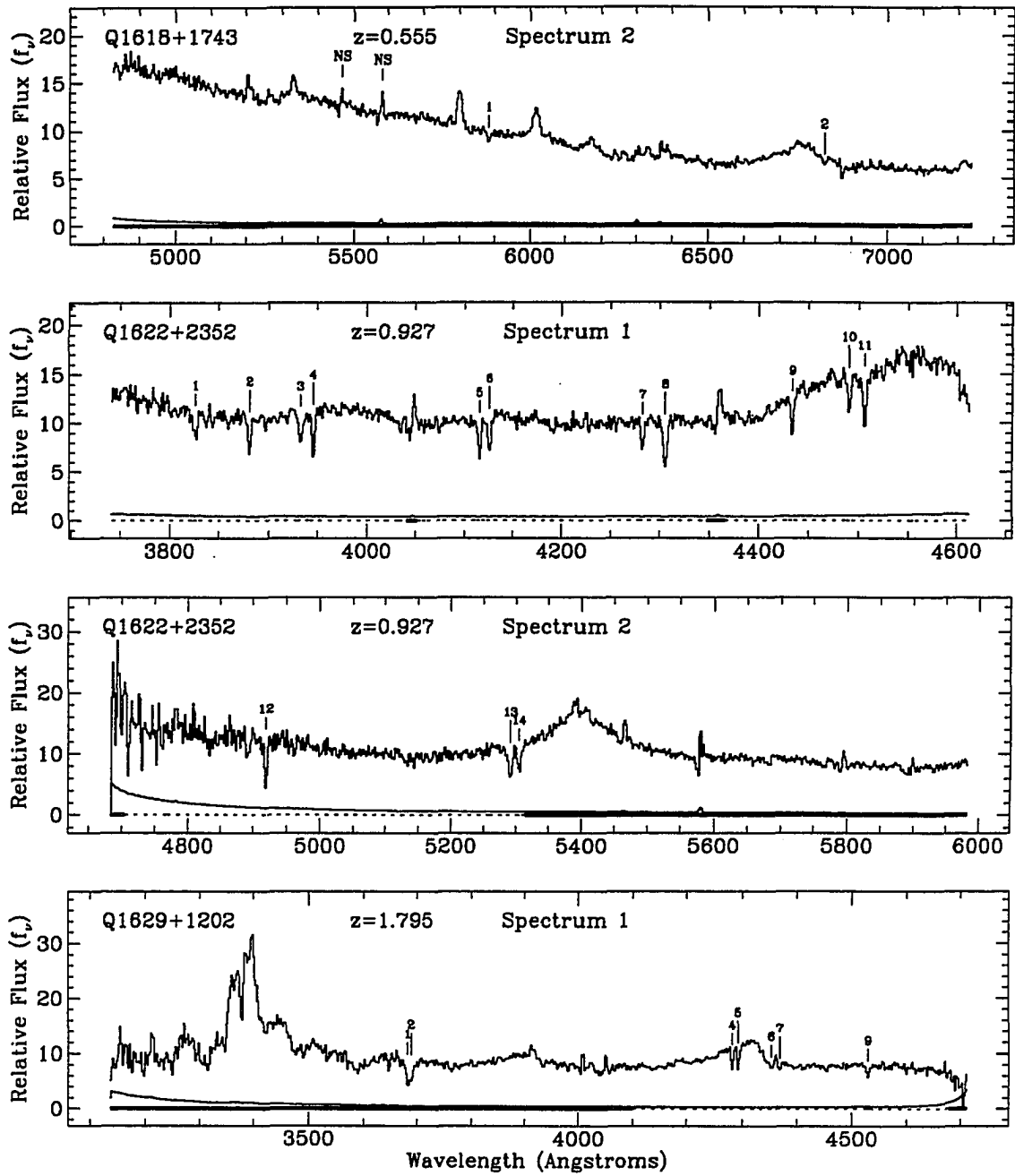


Figure 4.1: Quasar spectra

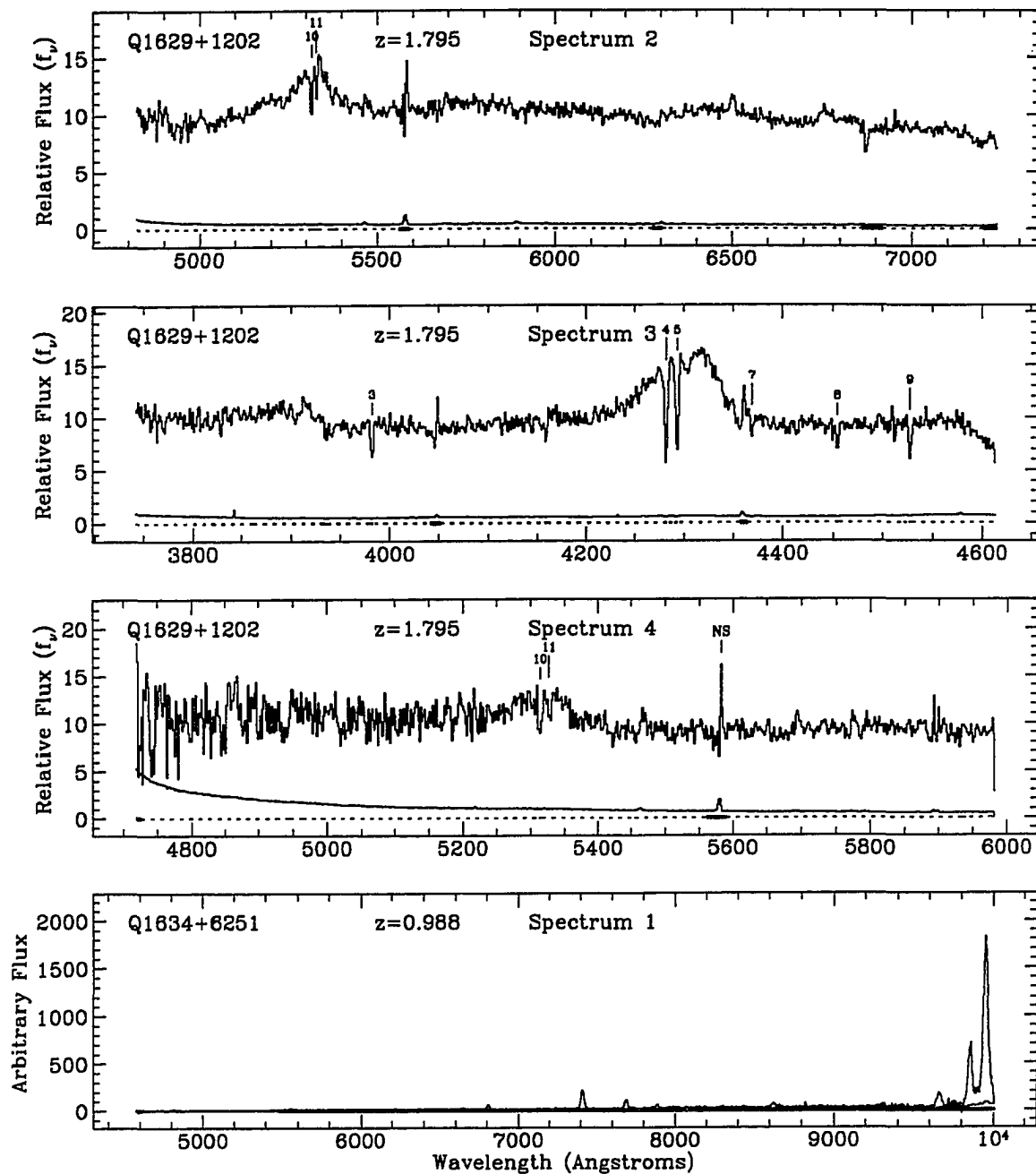


Figure 4.1: Quasar spectra

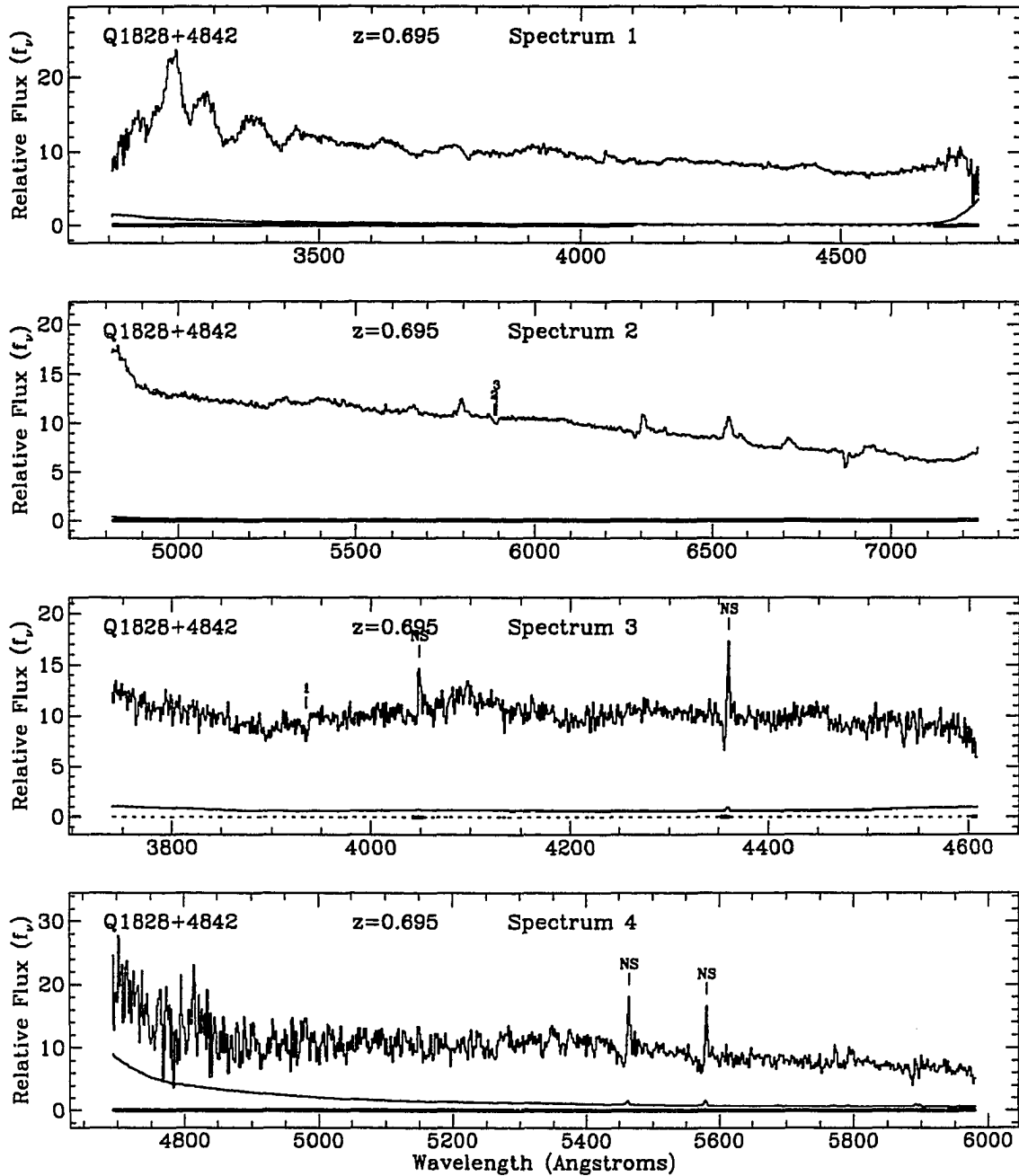


Figure 4.1: Quasar spectra

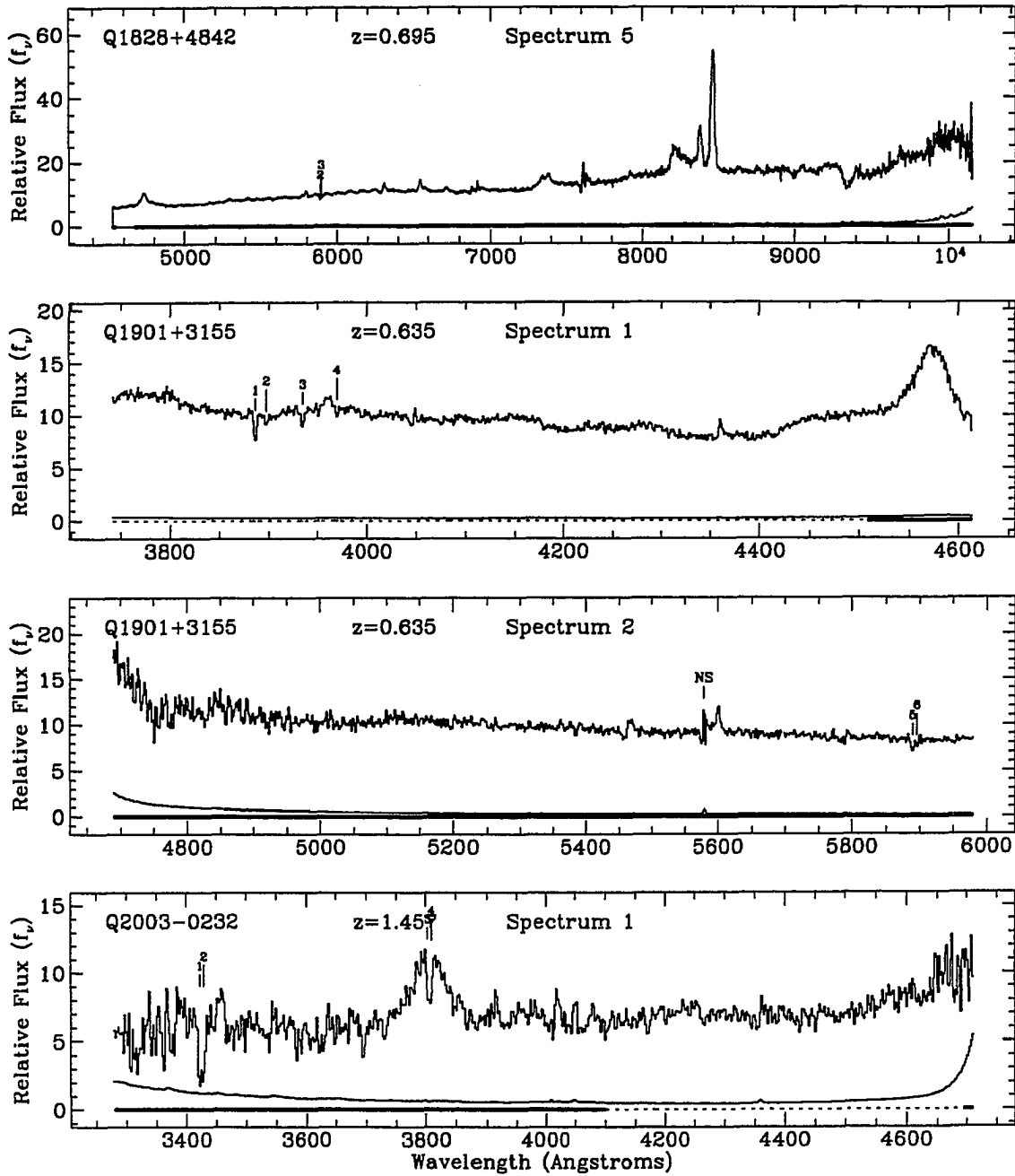


Figure 4.1: Quasar spectra

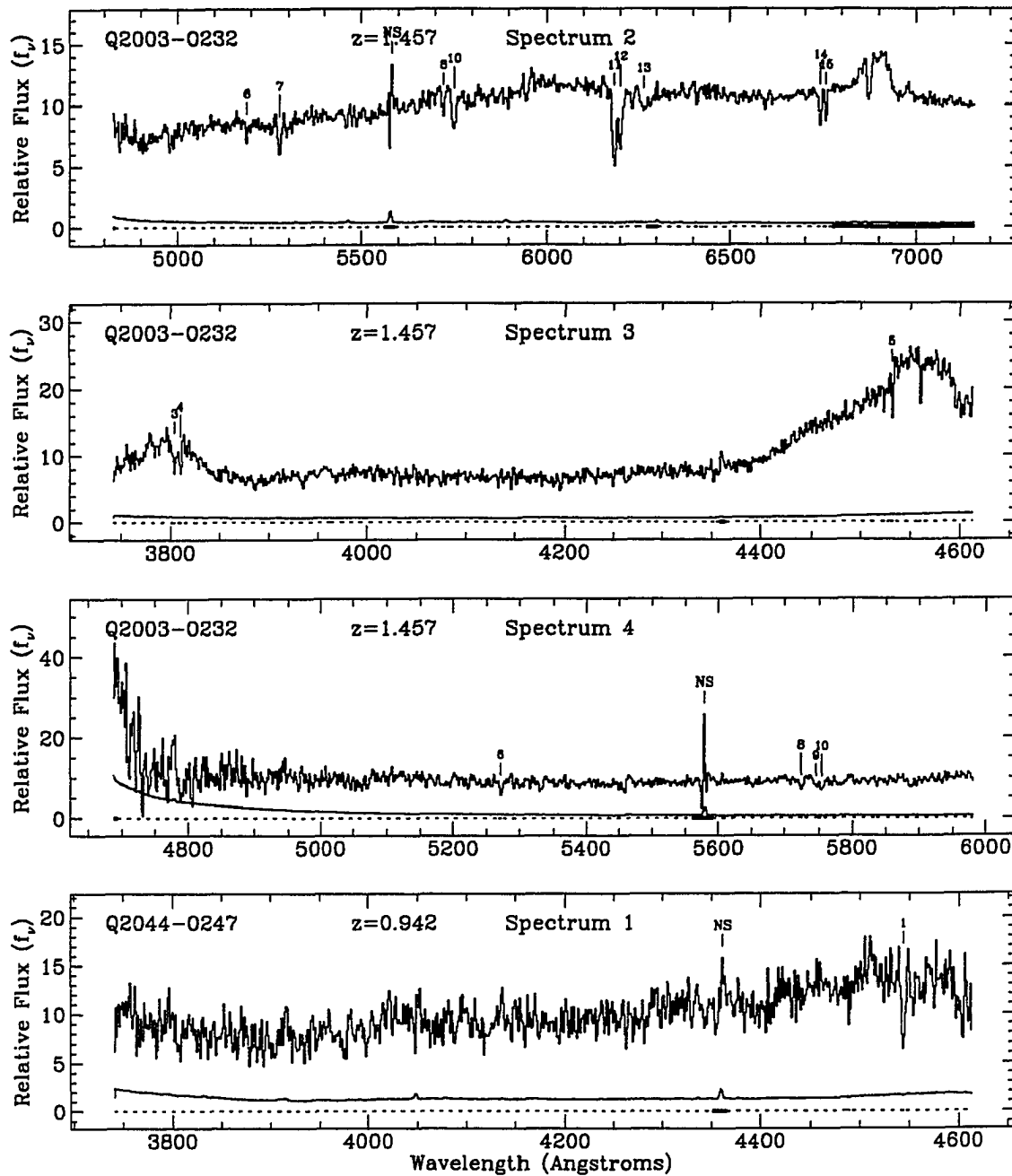


Figure 4.1: Quasar spectra

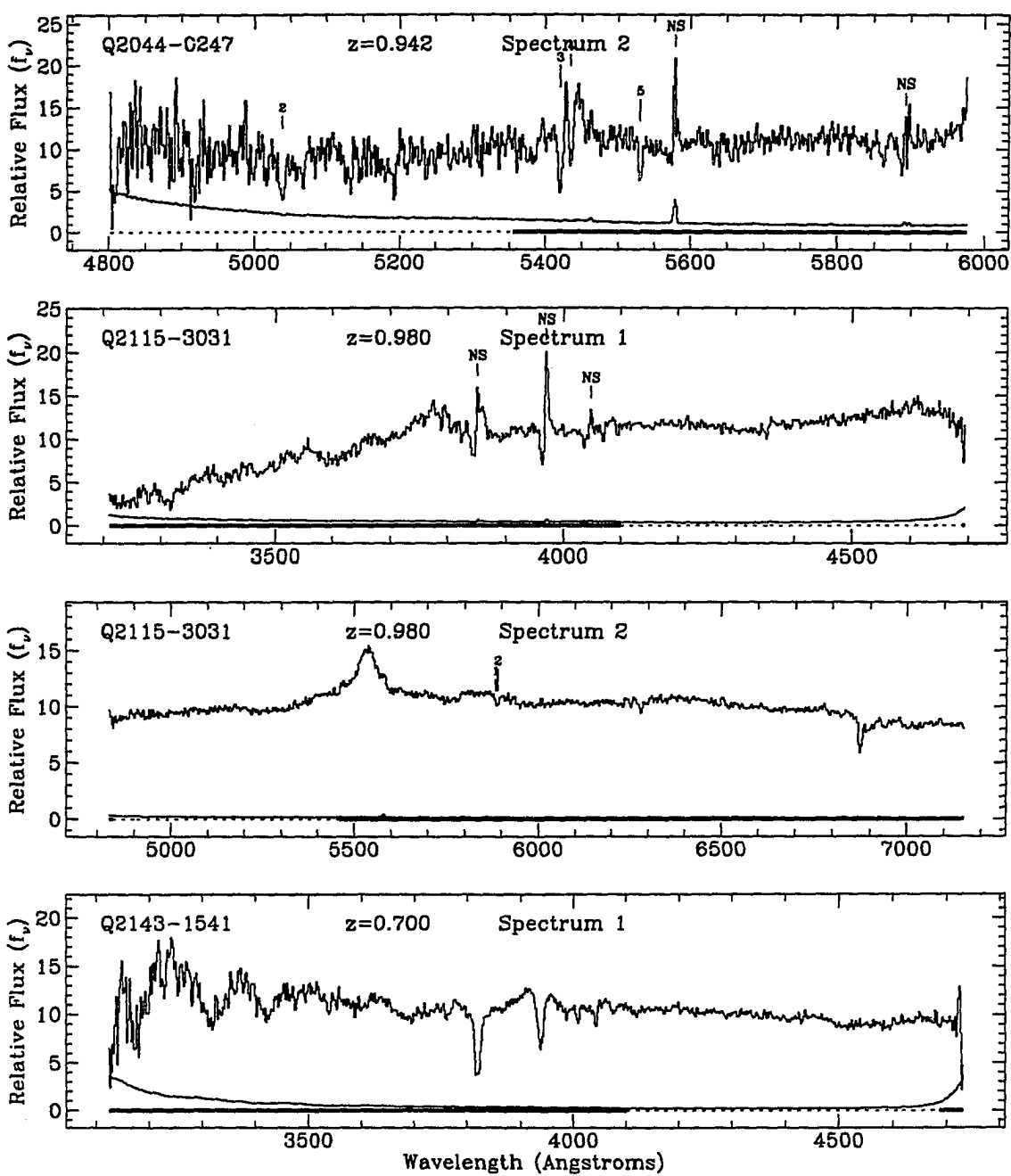


Figure 4.1: Quasar spectra

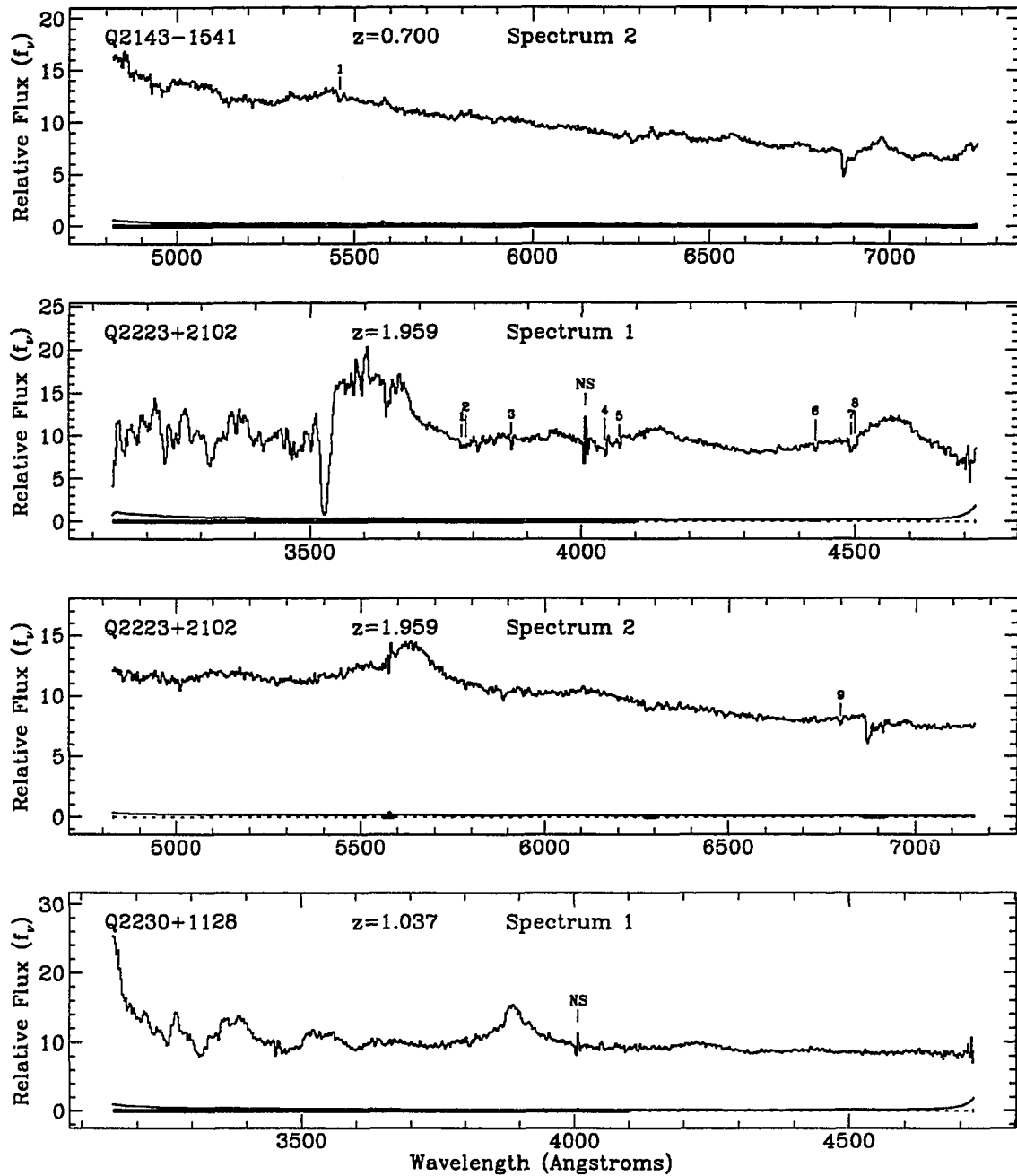


Figure 4.1: Quasar spectra

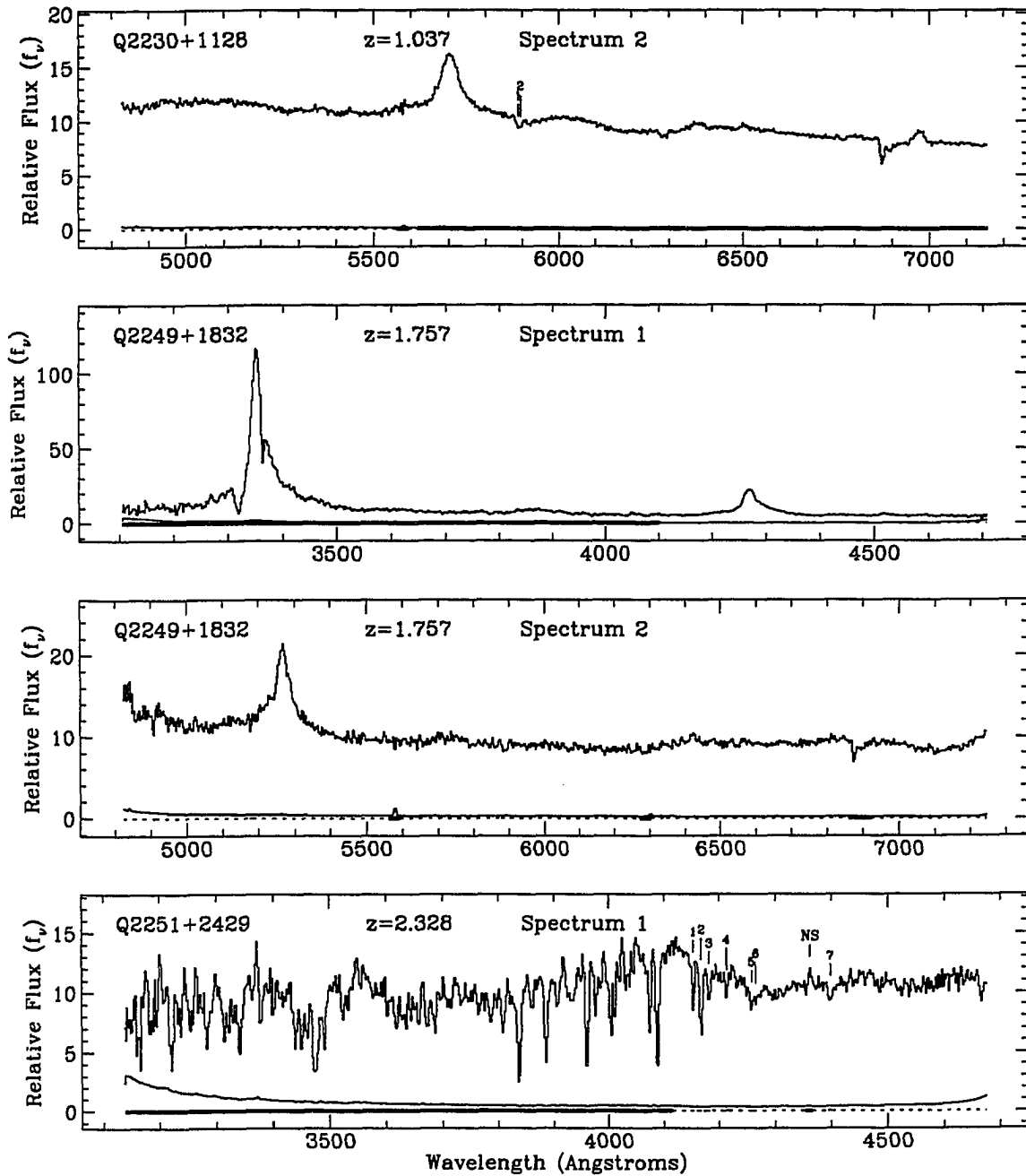


Figure 4.1: Quasar spectra

4.3 Line extraction

The process of finding absorption lines in QSO spectra is conceptually a simple three-step process. First, determine a smooth continuum which represents the emission intrinsic to the quasar. Second, find points in the spectrum which deviate from that continuum at a level which could not reasonably be due to instrumental noise. Third, identify the absorbing lines and their redshifts using a table of commonly occurring interstellar absorption lines. The actual implementation of this process, however, turns out to be much less trivial and requires reasonably complex computer codes and, to varying degrees, subjective human decision making. As such, in this section we will describe in some detail the process we used for line extraction and identification. At the end of the section we give the line list which forms the basis of our statistical analysis of absorber properties.

A goal of researchers in the field has been to produce a fully automated absorption line extraction code which takes as input a QSO spectrum and produces as output a line list. This would not only be convenient but would also allow a good statistical characterization of the code via Monte Carlo methods with simulated spectra. Schneider et al. (1992) have produced a large and complex code which can be run at various levels of interaction, including a fully automatic mode. However, even this program has been observed to miss lines or give poor continuum fits, and so there is still some need for human interaction. The more typical approach is semi-automatic identification and this has been our approach to the problem.

The first step in doing line extraction is to mark regions in the spectrum which are unusable for any number of reasons. Typical examples are bad night sky subtraction, presence of O_2 bands, or residual cosmic rays. Although the spectrum error array will show a peak near strong night sky lines (indicating lower sensitivity), it is sometimes the case that the actual spectral deviations are disproportionately large near the line. This means the error array is inaccurate in that neighborhood and the data there must be ignored. O_2 bands are generally seen in spectra at high airmass, especially if a standard star observation was not made at a similar airmass. Since absorption line work does not require flux calibration, this is common. In the spectra we present

here, we generally observed only two standard stars per night and as a consequence we are obliged to ignore the spectral regions with possible O₂ contamination. Note that one of bands near 6280 Å is weak and not well known, and is probably responsible for an unidentified line in Q1148-0007 in SS.

Fitting the QSO continuum¹ is one of the more difficult steps and often requires some human intervention. In the presence of both absorption and emission, defining the continuum can be ambiguous. Most absorption lines not associated with the QSO have velocity widths less than 300 km s⁻¹ and so with broad emission lines the continuum is usually well defined. For narrow emission lines this is not so, but fortunately they are rare in the high redshift QSOs common in these studies. The standard approach for calculating the continuum is as follows. First divide the spectrum into bins which are N_{SM} pixels wide and take the average over each bin. N_{SM} is chosen to be larger than absorption line width and smaller than the typical scale for continuum variations. A cubic spline is fit to these averaged points and this defines the continuum. Pixels which deviate negatively from the continuum by more than a fixed number of standard deviations (usually 3.0) are flagged to be rejected in subsequent iterations. This process is repeated until it has converged, usually taking no more than three iterations. The simplicity of this algorithm is appealing; unfortunately it almost always fails to fit the region near emission lines because the overall best value of N_{SM} is too large to fit these regions. This is primarily because the wavelength scale for variations in the QSO spectrum is much less in the region of QSO emission lines than elsewhere. We have experimented briefly with algorithms in which the bin size is adjusted dynamically in response to the second derivative of the continuum, but these proved unsatisfactory. We instead settled for setting the continuum by hand in the vicinity of sharp emission lines.

Once the continuum is fit, we are in a position to evaluate several aspects of the deviations via two diagnostic tools in our software. The first diagnostic is a plot of χ^2_{ν} (deviation squared per degree of freedom) calculated in each of the N_{SM} wide bins.

¹In the context of absorption line work, everything intrinsic to the QSO is the “continuum”, even broad or narrow emission lines.

The second diagnostic is a histogram plot of the number count of pixels versus deviation squared for the entire spectrum. A plot of the expected gaussian distribution is shown for reference. These two tools allow easy identification of systematic trends in the spectrum such as bad cosmic ray subtraction, bad continuum fitting, fringing, inaccurate estimate of detector noise, a problem with the CCD such as bad bias subtraction, or even something catastrophic such as noticing that the wrong object was placed in the spectrograph slit! An example of these plots is given in Fig. 4.2. In the upper plot of χ^2_ν deviation we clearly see that the deviations in the lower wavelength region are inconsistent with the error array. The lower plot of the gaussian statistics shows the character of the problem, wherein there is a very non-gaussian component on top of the underlying instrumental noise. The central region of the plot shows that the instrumental noise is well characterized by the error array. It turns out that in this spectrum there was a severe problem with the CCD bias subtraction and we were forced to reject it completely. A more common occurrence in these diagnostic plots is that the rms deviation is off from the expected value by a small constant factor over the entire spectrum. This results if the actual CCD noise characteristics differ somewhat from the “published” values. One can then refine the error array by scaling it by a constant factor so that $\chi^2_\nu = 1$ for the spectrum. We performed this normalization for the spectra in our sample.

Once satisfied that the continuum fit is good and that the error array accurately reflects the rms deviations in the spectrum, we can proceed to finding statistically significant absorption lines. Since these lines are generally not resolved, the appropriate measure of their strength is not their depth but rather their equivalent width. This is defined as $EW = \int [1 - y(\lambda)/c(\lambda)] d\lambda$, where $y(\lambda)$ is the spectrum, $c(\lambda)$ is the continuum, and the integral is taken over a region covering the entire line. To assess the statistical significance of a line we also need the uncertainty σ_{EW} . In addition, we also need to calculate the line central wavelength ($\bar{\lambda}$) and the line width (FWHM). There are several different ways one can go about calculating these line parameters, and we use three: the straightforward definition; optimal extraction; and gaussian fitting. Each of these methods has advantages in different regimes and so by calculating all three we can determine the most accurate values.

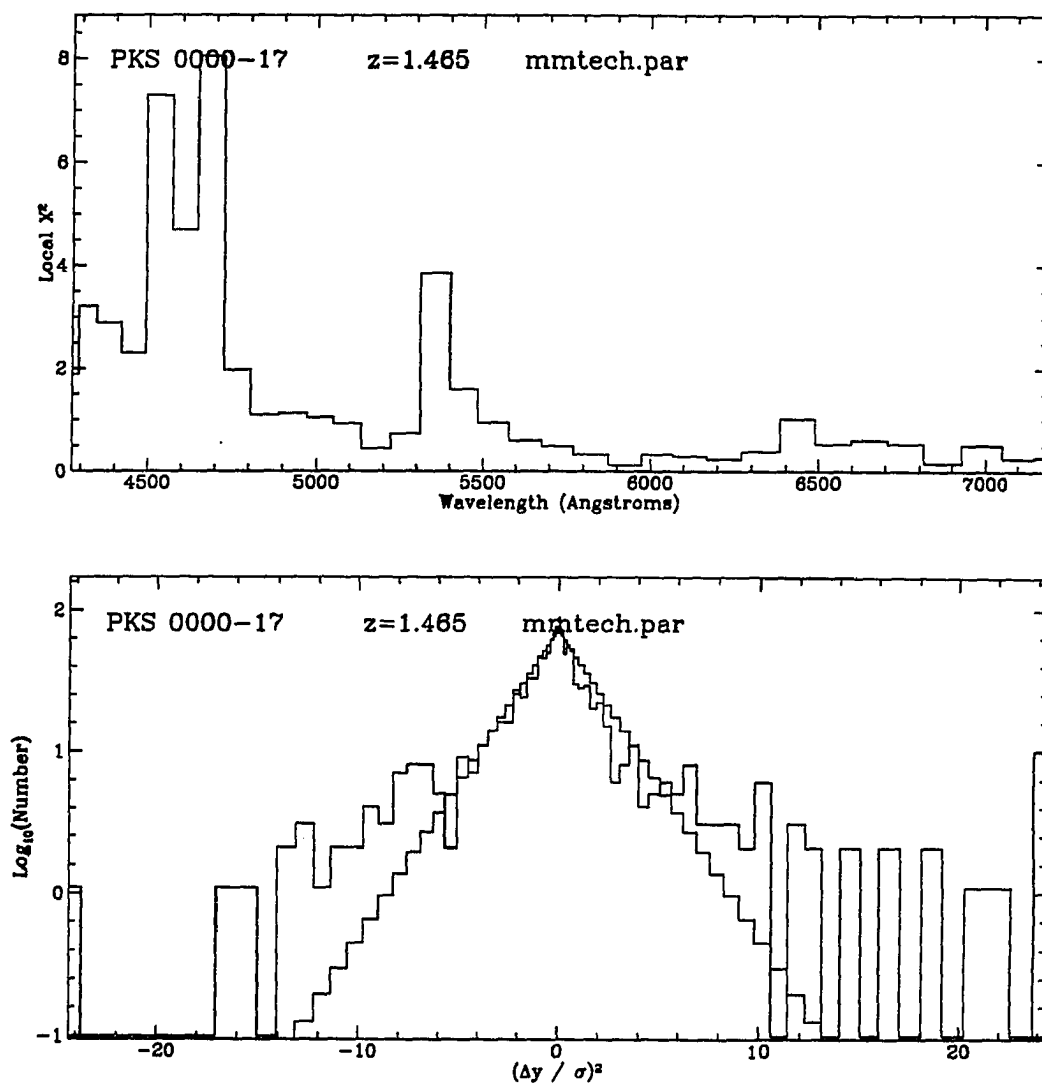


Figure 4.2: Example of the local χ^2 deviation on top and the histogram of gaussian deviations on bottom. In the lower plot the actual deviations are compared to the theoretical gaussian distribution. The spectrum used in these plots suffers from a sever bias subtraction problem.

For a discrete spectrum the straightforward definition of equivalent width and weighted line center gives us

$$\begin{aligned}
 EW &= \sum_i (1 - y_i/c_i) d\lambda_i \\
 \sigma_{EW}^2 &= \sum_i (d\lambda_i s_i/c_i)^2 \\
 \bar{\lambda} &= \sum_i x_i (1 - y_i/c_i) \\
 \sigma_{\bar{\lambda}}^2 &= \sum_i \left(\frac{s_i(\lambda_i - \bar{\lambda})}{c_i \sum_j (1 - y_j/c_j)} \right)^2.
 \end{aligned} \tag{4.1}$$

Here y_i , c_i , s_i , λ_i , and $d\lambda$ are the discrete spectrum, continuum, uncertainty, wavelength, and wavelength interval at pixel i . The estimate for the line center is $\bar{\lambda}$. In these equations all the sums are over pixels near the line, since extending the sum further away merely increases the uncertainty. Note also that any pixels which are marked as “bad” are skipped in these sums. The exact extent of the region over which we sum is discussed later.

Since the profile of absorption lines is approximately known *a priori*, we can improve the signal to noise (S/N) in Eqn. 4.1 by doing an optimal extraction at each point in the spectrum based on the known profile. This method is described in Schneider et al. (1992) and Horne (1986), and we present it here (in our notation) to provide context for understanding subsequent discussion. An important point here is that we use this as our basis for *detecting* lines which are statistically significant. However, the assumed profile may be somewhat different than the actual profile, so we use Eqn. 4.1 and gaussian fitting to determine the final line parameters.

For moderate resolution spectra (200 - 400 km s⁻¹), most absorption lines are at best marginally resolved and so a gaussian with width equal to the spectrograph instrumental resolution (PSF) is an excellent profile for optimal extraction. The equivalent width and uncertainty of a unresolved line with centered at pixel i is then

$$EW_i = d\lambda_i \frac{\sum_{j=-J}^J P_j y_{i+j} \eta_{i+j}}{\sum_{j=-J}^J P_j^2 \eta_{i+j}} \tag{4.2}$$

$$\sigma_{EW_i} = d\lambda_i \frac{\sqrt{\sum_{j=-J}^J P_j y_{i+j} \eta_{i+j}}}{\sum_{j=-J}^J P_j^2 \eta_{i+j}},$$

where $\eta_i = 0$ if the pixel i has been rejected for some reason and $\eta_i = 1$ otherwise, and P_j is the instrumental PSF centered at $j = 0$ and having negligible area beyond pixels $\pm J$. The significance level (SL_i) of a possible line detection at pixel i is simply $SL_i = EW_i/\sigma_{EW_i}$. The central wavelength and significance level (SL) for the line using optimal extraction is determined by the peak of a quadratic fit to SL_{i-1} , SL_i , and SL_{i+1} . If $SL_i \geq C_{SL}$ for a possible line, then we flag this as a detection and add the line to the significant line list. It is important to note that Schneider et al. (1992) make a distinction between SL and S/N. In their terminology the different labels refer to the significance for optimal extraction as opposed to any other method. We make no such distinction, and instead make clear in each case the particular method which is used.

The final method for determining line parameters is multicomponent gaussian fitting using non-linear least-squares optimization. We use routines in Press et al. (1992) in addition to our own routines for calculating the fitting functions and their derivatives. Gaussian fitting has the advantage that barely resolved components can be deconvolved, and the FWHM is naturally calculated. Our software has the facility to fit gaussian components independently or to fit for doublets with assumed wavelength ratios and equal widths.

The procedure used in our automatic line finding routine is as follows. The optimally extracted equivalent width EW_i is calculated over the entire spectrum, and the peaks of the regions which have $SL_i \geq C_{SL}$ are flagged as significant lines and added to a line list. The line parameters thus calculated are called the ‘‘PSF’’ values. Then a gaussian is fit to each of these lines, except that multiple (non-doublet) gaussians are fit if neighboring lines are blended. These line parameters are the ‘‘gaussian’’ values. Finally, Eqn. 4.1 is used to calculate the ‘‘definition’’ parameters. The sum in this case is carried out over pixels containing 95% of the line equivalent width, according to the gaussian FWHM.

As mentioned previously, each of these methods is best in a different regime. The

“PSF” has the highest SL except in extreme cases, but is not terribly reliable for determining the actual line parameters. The “gaussian” method is best for determining the parameters if there are blended components, but it fails if the line is non-gaussian and the spectrum S/N is not sufficient to reliably deconvolve the components. The “definition” method is terrible if components are blended, but otherwise gives the best results since it does not assume a gaussian line profile.

Once a line list consisting of wavelengths and the other line parameters (calculated by all three methods) has been produced, then we interactively try to determine their identities. This is facilitated in our software by a feature which shows the positions of common strong interstellar absorption lines at any redshift. The most common identifiable feature will be a doublet such as Mg II, C IV, Ca II, or Na I, and these are easily recognized by their wavelength ratios and doublet (or line EW) ratios. When the correct redshift has been found, two or more of the significant lines (including the doublet lines) will match precisely with the interstellar lines. In addition one may find weaker lines which would not be considered significant without independent corroborating evidence.

4.3.1 Results of line extraction in our sample

In Table 4.2 we list the absorption lines found in our sample of quasars. The columns are absorption line wavelength and uncertainty in Å, observed equivalent width and uncertainty in Å, detection significance level, identification (if any) and corresponding redshift (with uncertainty on the last digit in parentheses), and spectrum number. The uncertainty in wavelength and redshift takes account of noise in the spectrum and rms deviations in the wavelength calibration.

Table 4.2: Absorption lines in sample

No.	λ_{abs}	$\sigma(\lambda)$	EW	$\sigma(EW)$	SL	ID	z_{abs}	Sp.#
Q0056-0009			PHL 923				$z_{em} = 0.717$	
— No lines detected —								
Q0159-1147			3C 57				$z_{em} = 0.670$	
— No lines detected —								
Q0229+1309			PKS 0229+13				$z_{em} = 2.065$	
1	4278.6	0.8	1.49	0.13	10.8			1
2	4292.4	0.8	0.65	0.12	6.6			1
3	4431.0	0.8	1.82	0.12	13.3	CIV(1548)	1.8620(5)	1
4	4438.4	0.8	1.16	0.12	10.4	CIV(1550)	1.8620(5)	1
5	4494.5	0.8	1.78	0.10	17.3	CIV(1548)	1.9030(5)	1
6	4501.3	0.8	1.20	0.10	11.4	CIV(1550)	1.9026(5)	1
7	4580.1	1.0	0.40	0.09	10.3	CIV(1548)	1.9583(7)	1
8	4587.1	1.1	0.42	0.09	9.9	CIV(1550)	1.9579(7)	1
9	4781.1	0.8	0.39	0.06	6.8	MgII(2796)	0.7098(3)	1
10	4795.8	0.8	0.46	0.07	6.9	MgII(2803)	0.7106(3)	1
11	4902.0	0.8	0.47	0.09	7.6			1
12	8001.3	1.2	2.20	0.30	7.9	MgII(2796)	1.8613(4)	1
13	8017.4	0.8	2.02	0.32	5.5	MgII(2803)	1.8598(3)	1
Q0229+3410			3C 68.1				$z_{em} = 1.240$	
1	4731.0	1.0	5.51	0.91	6.1	MgII(2796)	0.6918(4)	1
2	4742.1	0.9	11.29	0.91	8.0	MgII(2803)	0.6915(3)	1
3	4965.5	0.9	3.89	0.73	4.8	MgII(2796)	0.7757(3)	1
4	4976.4	0.8	4.15	0.67	5.6	MgII(2803)	0.7750(3)	1
5	6221.8	0.9	7.90	0.25	19.1	MgII(2796)	1.2250(3)	1
6	6236.6	0.8	4.63	0.25	14.3	MgII(2803)	1.2245(3)	1
7	6353.4	1.2	1.19	0.32	4.3	MgI(2853)	1.2269(4)	1
8	7081.7	1.5	1.13	0.27	5.5	NaI(5891)	0.2020(3)	1
9	7089.2	1.7	1.15	0.27	5.0	NaI(5897)	0.2021(3)	1
Q0237-2322			PKS 0237-23				$z_{em} = 2.224$	
— No lines detected —								

Table 4.2: Absorption lines in sample

No.	λ_{abs}	$\sigma(\lambda)$	EW	$\sigma(EW)$	SL	ID	z_{abs}	Sp.#
Q0350-0719			3C 94		$z_{em} = 0.962$			
1	5891.7	1.7	0.37	0.09	5.9	NaI(5891)	0.0000(3)	1
2	5897.6	0.8	0.44	0.09	6.4	NaI(5897)	0.0000(1)	1
Q0420-0127			PKS 0420-01		$z_{em} = 0.915$			
1	4565.8	0.9	1.50	0.14	10.1	MgII(2796)	0.6328(3)	1
2	4579.3	0.8	1.31	0.13	8.2	MgII(2803)	0.6334(3)	1
3	4741.7	1.1	0.61	0.12	6.2			1
4	5160.9	1.0	0.66	0.09	6.1			1
Q0538+4949			3C 147		$z_{em} = 0.545$			
— No lines detected —								
Q0610+2605			3C 154		$z_{em} = 0.580$			
— No lines detected —								

Table 4.2: Absorption lines in sample

No.	λ_{abs}	$\sigma(\lambda)$	EW	$\sigma(EW)$	SL	ID	z_{abs}	Sp.#
	Q0642+4454		OH 471			$z_{em} = 3.400$		
1	4299.2	0.9	2.55	0.48	5.0			1
2	4339.9	0.8	6.83	0.35	16.7			1
3	4352.0	1.0	6.47	0.39	12.4			1
4	4366.3	1.2	4.18	0.44	6.3			1
5	4404.4	0.8	2.40	0.44	7.6			1
6	4412.7	1.1	4.25	0.42	7.6			1
7	4436.4	0.9	3.60	0.37	8.7			1
8	4457.3	0.9	7.76	0.28	15.7			1
9	4475.3	0.9	8.11	0.22	20.2			1
10	4502.4	1.0	1.17	0.21	5.2			1
11	4532.9	5.7	1.11	0.18	7.9			1
12	4584.3	1.0	3.22	0.22	10.7			1
13	4628.9	0.9	6.80	0.40	10.8			1
14	4655.4	0.9	3.68	0.39	9.4			1
15	4694.8	0.8	3.48	0.26	12.4			1
16	4722.3	0.9	5.27	0.24	16.8			1
17	4738.5	1.0	6.81	0.28	15.5			1
18	4753.6	1.1	5.47	0.34	10.8			1
19	4806.5	0.8	5.27	0.34	15.3			1
20	4828.5	0.8	6.07	0.35	11.7			1
21	4896.6	0.8	1.96	0.30	7.5			1
22	4906.7	1.2	2.16	0.29	6.4			1
23	4954.1	0.9	8.93	0.29	17.1			1
24	4975.4	0.9	5.20	0.34	12.6			1
25	4995.5	0.9	6.18	0.36	13.7			1
26	5011.7	0.9	10.44	0.43	15.7			1
27	5032.8	0.8	5.39	0.30	17.1			1
28	5084.1	0.9	7.03	0.25	15.7			1
29	5159.4	0.8	10.17	0.23	31.7			1
30	5199.8	0.8	5.09	0.21	19.2			1
31	5225.7	0.9	5.41	0.18	19.3			1
32	5252.2	0.8	2.92	0.17	14.8			1
33	5279.2	0.8	6.35	0.14	36.4			1
34	5305.5	0.8	6.72	0.10	51.7			1
35	5323.3	0.8	0.68	0.09	9.4			1
36	5339.1	0.8	0.00	0.08	6.2			1
37	5499.7	1.1	1.03	0.19	5.3			1
38	5940.5	1.7	1.62	0.25	5.0			1
39	6390.7	2.1	3.80	0.29	5.8			1
40	7811.4	0.9	4.18	0.74	6.7			1

Table 4.2: Absorption lines in sample

No.	λ_{abs}	$\sigma(\lambda)$	EW	$\sigma(EW)$	SL	ID	z_{abs}	Sp.#
Q0710+1151			3C 175		$z_{em} = 0.768$			
1	3139.1	0.4	1.58	0.26	5.1			1
2	3934.8	0.4	0.49	0.06	6.2	CaII(3934)	0.0000(1)	1
3	3969.6	0.3	0.26	0.06	4.0	CaII(3969)	0.0000(1)	1
4	4090.9	0.3	0.90	0.06	12.0	MgII(2796)	0.4629(1)	1
5	4101.3	0.2	0.39	0.06	5.8	MgII(2803)	0.4629(1)	1
6	4932.3	0.3	0.33	0.06	5.1			1
Q0725+1443			3C 181		$z_{em} = 1.382$			
1	6066.7	1.0	1.25	0.16	7.9	MgII(2796)	1.1695(4)	1
2	6080.4	0.8	0.83	0.16	4.5	MgII(2803)	1.1688(3)	1
Q0736-0620			PKS 0736-06		$z_{em} = 1.898$			
1	4362.1	0.9	0.92	0.10	8.2	CIV(1548)	1.8175(6)	1
2	4369.3	0.9	0.50	0.09	8.8	CIV(1550)	1.8175(6)	1
3	4510.0	0.8	2.27	0.06	41.5	CIV(1548)	1.9131(5)	1
4	4517.6	0.8	1.63	0.06	31.4	CIV(1550)	1.9131(5)	1
5	4538.6	0.8	3.06	0.06	55.3	CIV(1548)	1.9316(5)	1
6	4544.8	0.8	2.41	0.06	42.4	CIV(1550)	1.9306(5)	1
7	5729.7	1.5	0.31	0.08	4.2	FeII(2600)	1.2036(6)	1
8	6154.8	1.4	0.39	0.08	9.4	MgII(2796)	1.2010(5)	1
9	6161.5	0.9	0.76	0.08	16.3	MgII(2796)	1.2034(3)	1
10	6171.2	0.8	0.41	0.08	10.0	MgII(2803)	1.2012(3)	1
11	6176.3	0.8	0.73	0.08	12.6	MgII(2803)	1.2030(3)	1
Q0809+4822			3C 196		$z_{em} = 0.871$			
1	3359.7	0.7	1.63	0.15	5.3	FeII(2344)	0.4332(3)	1
2	3406.0	0.4	1.04	0.13	6.0	FeII(2374)	0.4344(2)	1
3	3418.9	0.4	1.44	0.14	6.7	FeII(2382)	0.4348(2)	1
4	3702.6	0.3	0.84	0.11	7.6	MnII(2577)	0.4369(1)	1
5	3716.1	0.3	1.97	0.09	16.9	FeII(2586)	0.4367(1)	1
6	3727.1	0.3	0.58	0.11	5.5	MnII(2594)	0.4365(1)	1
7	3735.4	0.3	2.60	0.09	20.8	FeII(2600)	0.4366(1)	1
8	3744.1	0.3	0.82	0.12	6.1	MnII(2606)	0.4365(1)	1
9	4017.7	0.2	2.91	0.08	25.9	MgII(2796)	0.4368(1)	1
10	4028.0	0.2	2.79	0.08	24.3	MgII(2803)	0.4367(1)	1
11	4099.4	0.3	1.38	0.09	11.9	MgI(2853)	0.4369(1)	1

Table 4.2: Absorption lines in sample

No.	λ_{abs}	$\sigma(\lambda)$	EW	$\sigma(EW)$	SL	ID	z_{abs}	Sp.#
Q0835+5804			3C 205		$z_{em} = 1.534$			
1	4274.2	0.8	1.11	0.23	5.4			1
2	5780.1	1.1	0.54	0.11	5.1	FeII(2374)	1.4343(5)	1
3	5798.6	1.2	0.48	0.11	4.6	FeII(2382)	1.4336(5)	1
4	6330.1	1.2	0.71	0.13	5.4	FeII(2600)	1.4345(5)	1
5	6807.2	5.2	0.86	0.14	7.8	MgII(2796)	1.4343(*)	1
6	6814.5	1.9	1.15	0.14	10.7	MgII(2796)	1.4369(7)	1
7	6825.4	0.8	0.76	0.16	6.5	MgII(2803)	1.4346(3)	1
8	6832.2	0.8	0.58	0.16	5.2	MgII(2803)	1.4370(3)	1
9	6944.8	1.6	0.49	0.14	3.6	MgI(2853)	1.4342(6)	1
Q0855+1421			3C212		$z_{em} = 1.043$			
1	5909.5	1.7	5.27	0.37	7.5			1
Q0859-1403			PKS 0859-14		$z_{em} = 1.327$			
— No lines detected —								
Q0906+4305			3C 216		$z_{em} = 0.670$			
— No lines detected —								
Q1007+4147			4C 41.21		$z_{em} = 0.613$			
1	3222.1	0.3	0.66	0.08	6.5			1
2	3968.0	0.4	0.37	0.05	5.0	CaII(3969)	-0.0004(1)	1
3	4547.8	0.4	0.53	0.05	6.4			1
Q1040+1219			3C 245		$z_{em} = 1.029$			
1	4640.3	0.4	0.90	0.09	6.6	MgII(2796)	0.6594(1)	1
2	4650.5	0.4	0.72	0.09	5.0	MgII(2803)	0.6588(2)	1
Q1055+2007			PKS 1055+20		$z_{em} = 1.110$			
1	3323.6	0.4	0.57	0.07	5.8			1
Q1111+4053			3C 254		$z_{em} = 0.734$			
— No lines detected —								

Table 4.2: Absorption lines in sample

No.	λ_{abs}	$\sigma(\lambda)$	EW	$\sigma(EW)$	SL	ID	z_{abs}	Sp.#
Q1136-1334		PKS 1136-13			$z_{em} = 0.554$			
— No lines detected —								
Q1137+6604		3C 263			$z_{em} = 0.652$			
1	3935.2	0.3	0.24	0.05	5.4	CaII(3934)	0.0001(1)	1
2	4041.8	0.3	0.27	0.05	5.1			1
3	4544.4	0.3	0.27	0.05	5.2			1
4	4587.4	0.2	0.20	0.05	4.5	MgII(2803)	0.6363(1)	1
Q1148-0007		PKS 1148-00			$z_{em} = 1.982$			
1	4624.0	0.8	0.57	0.07	9.5	CIV(1548)	1.9867(5)	1
2	4633.3	0.8	0.86	0.08	11.9	CIV(1550)	1.9878(5)	1
Q1153+3144		4C 31.38			$z_{em} = 1.557$			
— No lines detected —								
Q1156+2931		4C 29.45			$z_{em} = 0.729$			
— No lines detected —								
Q1206+4356		3C 268.4			$z_{em} = 1.400$			
1	9240.9	0.9	1.91	0.35	6.7			1
Q1213+5352		4C 53.24			$z_{em} = 1.065$			
— No lines detected —								
Q1218+3359		3C 270.1			$z_{em} = 1.519$			
1	3870.7	1.4	6.91	0.15	36.3	CIV(1548)	1.5001(9)	1
2	3877.2	0.3	6.48	0.14	38.3	CIV(1550)	1.5002(2)	1
3	4871.8	0.9	2.17	0.34	5.8	MgII(2796)	0.7422(3)	2
4	4884.7	1.0	1.80	0.36	4.8	MgII(2803)	0.7423(3)	2
5	6991.4	0.4	3.13	0.14	18.5	MgII(2796)	1.5002(1)	2
6	7008.1	0.5	2.84	0.14	15.3	MgII(2803)	1.4997(2)	2

Table 4.2: Absorption lines in sample

No.	λ_{obs}	$\sigma(\lambda)$	EW	$\sigma(EW)$	SL	ID	z_{abs}	Sp.#
Q1229-0207		PKS 1229-02		$z_{em} = 1.038$				
1	4875.6	0.8	0.79	0.13	7.2			1
2	4913.5	0.8	0.72	0.13	7.1	MgII(2796)	0.7571(3)	1
3	4926.0	0.8	0.69	0.12	6.7	MgII(2803)	0.7571(3)	1
Q1318+1122		PKS 1318+11		$z_{em} = 2.171$				
1	4452.2	0.6	1.38	0.20	6.7	CIV(1548)	1.8757(4)	1
2	4458.7	1.1	0.31	0.22	3.7	CIV(1550)	1.8751(7)	1
3	5148.9	0.9	1.02	0.25	4.7	MgII(2796)	0.8413(3)	2
4	5745.6	0.9	0.99	0.23	4.7	MgII(2796)	1.0547(3)	2
Q1327-2126		PKS 1327-21		$z_{em} = 0.528$				
1	3638.6	0.3	0.72	0.14	4.9	MgII(2796)	0.3012(1)	1
Q1328+3045		3C 286		$z_{em} = 0.846$				
1	4378.6	0.6	0.30	0.07	4.4	FeII(2586)	0.6928(2)	1
2	4401.0	0.5	0.69	0.07	9.2	FeII(2600)	0.6926(2)	1
3	6661.3	1.1	0.44	0.08	4.7	CaII(3934)	0.6929(3)	2
Q1328+2524		3C 287		$z_{em} = 1.055$				
— No lines detected —								
Q1335-0611		PKS 1335-06		$z_{em} = 0.625$				
1	4988.4	0.7	2.05	0.19	5.1			1
Q1354-1512		PKS 1354-15		$z_{em} = 1.890$				
1	4838.8	0.9	3.59	0.43	5.4			1
2	5679.1	0.9	2.49	0.35	7.4	MgII(2796)	1.0309(3)	1
3	5694.5	0.8	1.63	0.43	3.5	MgII(2803)	1.0312(3)	1
Q1437+6224		OQ663		$z_{em} = 1.090$				
1	5236.0	0.8	1.10	0.16	7.8	MgII(2796)	0.8724(3)	1
2	5248.5	0.8	1.22	0.16	7.2	MgII(2803)	0.8721(3)	1
3	5843.7	1.0	1.78	0.13	10.0			1

Table 4.2: Absorption lines in sample

No.	λ_{abs}	$\sigma(\lambda)$	EW	$\sigma(EW)$	SL	ID	z_{abs}	Sp.#
Q1442+1011		OQ 172		$z_{em} = 3.530$				
1	5624.6	0.3	0.84	0.08	11.8	CIV(1548)	2.6330(2)	1
2	5634.0	0.0	0.41	0.08	6.2	CIV(1550)	2.6330(0)	1
Q1453-1056		PKS 1453-10		$z_{em} = 0.938$				
1	4011.3	0.6	1.17	0.23	5.1			1
Q1458+7152		3C 309.1		$z_{em} = 0.905$				
1	3934.8	0.2	0.39	0.06	7.1	CaII(3934)	0.0000(1)	1
2	3945.6	0.4	0.20	0.06	3.5	AlI(3945)	0.0001(1)	1
3	3968.8	0.5	0.33	0.05	5.1	CaII(3969)	-0.0002(1)	1
4	5883.2	0.5	0.64	0.11	5.3	NaI(5891)	-0.0014(1)	2
5	5888.0	0.3	0.76	0.11	7.6	NaI(5897)	-0.0016(1)	2
Q1508-3231		PKS 1508-05		$z_{em} = 1.191$				
— No lines detected —								
Q1618+1743		3C 334		$z_{em} = 0.555$				
1	5884.1	1.0	0.85	0.14	5.3			2
2	6353.0	1.5	2.04	0.14	6.5			2
3	6825.3	1.0	0.98	0.14	5.6			2
Q1629+1202		PKS 1629+12		$z_{em} = 1.795$				
1	3981.8	0.2	1.06	0.11	9.1	FeII(2600)	0.5313(1)	3
2	4281.8	0.1	2.00	0.07	24.0	MgII(2796)	0.5312(0)	3
3	4282.0	0.3	1.53	0.12	14.9	MgII(2796)	0.5313(1)	1
4	4292.7	0.3	1.62	0.11	16.7	MgII(2803)	0.5312(1)	1
5	4293.1	0.1	2.05	0.07	23.5	MgII(2803)	0.5313(0)	3
6	4353.6	0.8	1.08	0.15	6.0			1
7	4368.6	0.6	0.82	0.15	5.6	MgI(2853)	0.5312(2)	1
8	4369.3	0.3	0.44	0.11	4.4	MgI(2853)	0.5315(1)	3
9	4454.4	0.3	0.69	0.12	5.5	FeII(2344)	0.9002(1)	3
10	4527.5	0.3	1.02	0.14	6.9	FeII(2382)	0.9001(1)	3
11	4528.5	0.6	1.41	0.20	6.9	FeII(2382)	0.9005(2)	1
12	5314.0	0.6	1.69	0.24	5.8	MgII(2796)	0.9003(2)	4
13	5315.3	0.4	2.05	0.17	11.5	MgII(2796)	0.9008(1)	2
14	5328.5	0.6	0.95	0.18	6.2	MgII(2803)	0.9006(2)	2

Table 4.2: Absorption lines in sample

No.	λ_{abs}	$\sigma(\lambda)$	EW	$\sigma(EW)$	SL	ID	z_{abs}	Sp.#
Q1634+6251		3C 343				$z_{em} = 0.988$		
— No lines detected —								
Q1828+4842		3C 380				$z_{em} = 0.695$		
1	3935.0	0.5	0.69	0.12	4.2	CaII(3934)	0.0001(1)	3
2	4074.6	0.1	0.70	0.11	5.1	MgII(2803)	0.4534(0)	3
3	5885.5	0.9	0.40	0.06	6.7	NaI(5891)	-0.0010(1)	2
4	5894.7	0.3	0.47	0.06	8.3	NaI(5897)	-0.0005(0)	2
Q1901+3155		3C 395				$z_{em} = 0.635$		
1	3887.2	0.1	0.62	0.05	11.7	MgII(2796)	0.3901(0)	1
2	3897.4	0.1	0.23	0.05	3.9	MgII(2803)	0.3902(0)	1
3	3934.5	0.3	0.58	0.05	9.5	CaII(3934)	-0.0001(1)	1
4	3969.8	0.3	0.26	0.05	5.1	CaII(3969)	0.0001(1)	1
5	5889.0	0.5	0.65	0.08	7.8	NaI(5891)	-0.0004(1)	2
6	5895.1	0.3	0.32	0.08	4.1	NaI(5897)	-0.0004(1)	2
Q2003-0232		4C -02.79				$z_{em} = 1.457$		
1	3422.8	0.8	3.20	0.73	6.5	CIV(1548)	1.2108(5)	1
2	3429.3	0.3	3.48	0.73	5.3	CIV(1550)	1.2114(2)	1
3	3803.6	0.5	1.46	0.23	7.5	CIV(1548)	1.4568(3)	1
	3804.4	0.2	1.21	0.15	6.2	"	1.4573(1)	3
4	3810.1	0.3	1.42	0.23	7.0	CIV(1550)	1.4569(2)	1
	3810.4	0.1	0.94	0.15	6.1	"	1.4571(1)	3
5	4531.4	0.3	0.53	0.10	6.1			3
6	5188.3	0.9	0.84	0.26	3.9	FeII(2344)	1.2132(4)	2
7	5271.8	0.6	1.67	0.32	4.8	FeII(2382)	1.2125(3)	4
8	5274.7	0.6	2.05	0.25	7.8	FeII(2382)	1.2137(3)	2
9	5722.0	0.9	1.10	0.20	4.9	FeII(2586)	1.2121(4)	2
10	5723.8	0.6	1.15	0.19	5.1	FeII(2586)	1.2128(2)	4
11	5745.1	0.9	1.02	0.19	3.5	FeII(2382)	1.4111(4)	4
12	5749.8	0.6	2.77	0.20	10.4	FeII(2600)	1.2113(2)	2
13	5753.5	0.7	1.31	0.19	5.6	FeII(2600)	1.2127(3)	4
14	6184.7	0.4	5.87	0.16	28.3	MgII(2796)	1.2117(1)	2
15	6200.0	0.5	4.37	0.17	20.1	MgII(2803)	1.2115(2)	2
16	6264.6	0.9	1.36	0.19	4.3	FeII(2600)	1.4093(4)	2
17	6741.4	0.4	1.63	0.13	13.3	MgII(2796)	1.4108(1)	2
18	6757.5	0.4	1.45	0.13	11.6	MgII(2803)	1.4104(1)	2

Table 4.2: Absorption lines in sample

No.	λ_{obs}	$\sigma(\lambda)$	EW	$\sigma(EW)$	SL	ID	z_{abs}	Sp.#
Q2044-0247			3C 422		$z_{em} = 0.942$			
1	4544.0	0.3	2.32	0.24	7.4	FeII(2344)	0.9384(1)	1
2	5038.6	1.1	4.16	0.78	3.6	FeII(2600)	0.9378(4)	2
3	5420.0	0.4	5.60	0.27	13.2	MgII(2796)	0.9382(1)	2
4	5434.7	0.3	4.01	0.23	11.8	MgII(2803)	0.9385(1)	2
5	5531.0	0.6	2.59	0.30	7.3	MgI(2853)	0.9387(2)	2
Q2115-3031			PKS 2115-30		$z_{em} = 0.980$			
1	5885.5	1.5	0.47	0.10	4.9	NaI(5891)	-0.0010(3)	2
2	5891.6	1.5	0.43	0.11	5.9	NaI(5897)	-0.0010(2)	2
Q2143-1541			PKS 2143-15		$z_{em} = 0.700$			
1	5457.4	1.0	0.75	0.09	6.6			2
Q2223+2102			PKS 2223+21		$z_{em} = 1.959$			
1	3779.8	0.6	0.64	0.09	7.1	CIV(1548)	1.4414(4)	1
2	3786.3	0.7	0.44	0.09	5.7	CIV(1550)	1.4416(4)	1
						+SiII(1304)	1.9028(5)	1
3	3871.1	0.4	0.57	0.08	7.8	CII(1334)	1.9007(3)	1
4	4043.6	0.4	0.92	0.09	11.8	SiIV(1393)	1.9012(3)	1
5	4069.9	0.5	0.52	0.08	6.9	SiIV(1402)	1.9014(3)	1
6	4429.0	0.6	0.38	0.08	5.2	SiII(1526)	1.9010(4)	1
7	4493.4	0.4	1.09	0.08	12.8	CIV(1548)	1.9023(3)	1
8	4500.3	0.3	0.76	0.08	10.1	CIV(1550)	1.9019(2)	1
9	6800.5	0.7	0.50	0.08	6.4	FeII(2344)	1.9010(3)	2
Q2230+1128			CTA 102		$z_{em} = 1.037$			
1	5888.5	6.6	0.47	0.08	8.4	NaI(5891)	-0.0005(*)	2
2	5894.7	0.3	0.65	0.08	7.6	NaI(5897)	-0.0005(0)	2
Q2249+1832			3C 454		$z_{em} = 1.757$			
1	3782.1	0.9	2.07	0.21	6.5			1
2	3808.9	0.7	1.18	0.20	5.8			1
3	3975.3	0.6	1.38	0.20	6.8	MgII(2796)	0.4216(2)	1
4	3984.9	0.9	0.82	0.20	4.0	MgII(2803)	0.4214(3)	1

Table 4.2: Absorption lines in sample

No.	λ_{abs}	$\sigma(\lambda)$	EW	$\sigma(EW)$	SL	ID	z_{abs}	Sp.#
	Q2251+2429		PKS 2251+24			$z_{em} = 2.328$		
1	4151.9	0.4	1.49	0.12	14.3	NV(1238)	2.3515(3)	1
2	4166.7	0.4	2.75	0.12	22.1	NV(1242)	2.3526(3)	1
3	4180.4	0.5	1.03	0.13	8.4	NV(1242)	2.3637(4)	1
4	4212.6	2.5	0.31	0.13	4.2	CII(1334)	2.1566(*)	1
5	4256.5	0.7	1.01	0.14	6.6	CIV(1548)	1.7493(4)	1
6	4264.4	0.3	0.42	0.14	3.7	CIV(1550)	1.7499(2)	1
7	4397.5	0.9	1.02	0.14	5.4	SiIV(1393)	2.1551(7)	1
8	4891.7	0.5	1.97	0.24	8.6	CIV(1548)	2.1596(3)	2
9	4900.9	0.3	2.10	0.24	9.6	CIV(1550)	2.1603(2)	2
10	5193.3	0.3	2.36	0.14	16.7	CIV(1548)	2.3544(2)	2
11	5200.5	0.3	1.28	0.14	13.7	CIV(1550)	2.3535(2)	2
12	5209.7	0.3	4.85	0.12	43.5	CIV(1548)	2.3650(2)	2
13	5218.9	0.3	4.43	0.13	38.9	CIV(1550)	2.3653(2)	2
14	5857.7	0.3	0.53	0.13	4.5	MgII(2803)	1.0894(1)	2

4.4 Notes on individual objects

Q0056-0009 (PHL 923, $z_{em} = 0.717$)

No previous lines were reported for this object, and no lines were detected in our spectrum. Spectrum #1 for this object suffers from the flattening problem in the July 1988 spectra.

Q0159-1147 (3C 57, $z_{em} = 0.670$)

This object was observed previously by Tytler et al. (1987) who found no absorption lines in the range 4021 - 4929 Å. We also find no lines.

Q0229+1309 (PKS 0229+13, $z_{em} = 2.065$)

This object has previously been studied by Sargent, Boksenberg, and Steidel (1988) (SBS) in range 3950 - 4975 Å. They identified Mg II systems at $z_{abs} = 0.3723$ and 0.4177, and C IV at $z_{abs} = 1.8622$, 1.9024, and 1.9584. Mg II at the latter two C IV redshifts is not in our spectral coverage. Of the unidentified lines in our spectra, one was also seen and unidentified by SBS, and another is possibly present in their published spectrum. Bergeron and Boissé (1991) have imaged this field and they find a nearby emission line galaxy at $z = 0.417$, but were unable to find a candidate for the $z_{abs} = 0.3723$ system. In our spectra we confirm the C IV lines and find an Mg II system:

$z_{abs} = 1.8609$: This strong system is most likely associated with the $z_{abs} = 1.8622$ C IV system of SBS. Although the line wavelength ratio is rather poor, the system is fit adequately ($\chi^2_{\nu} = 0.7$) by an Mg II doublet. The redshift discrepancy is probably due to wavelength calibration error at this high wavelength.

Q0229+3410 (3C 68.1, $z_{em} = 1.240$)

This object has no previously reported absorption lines. We find the following absorption systems:

$z_{abs} = 0.2022$: We observe a Na I doublet at this redshift.

$z_{abs} = 0.7754$: This strong system is fit well by a single Mg II doublet at spectral resolution. The two lines have equal equivalent widths to within the measurement uncertainties.

$z_{abs} = 1.2248$: This very strong Mg II doublet has an apparent ejection velocity of 2000 km s^{-1} with respect to the quasar.

Q0237-2322 (PKS 0237-23, $z_{em} = 2.224$)

This object has an unusually large number of strong absorption systems, and has been studied by SS, SBS, Lanzetta et al. (1987), and Boissé and Bergeron (1985). See SS for a comprehensive discussion of the known absorption systems. In our spectrum we find no new absorption systems.

Q0350-0719 (3C 94, $z_{em} = 0.962$)

This quasar was previously studied by Tytler et al. (1987) who found no absorption lines in the range $4021 - 4931 \text{ \AA}$. We find only Galactic NaI absorption in our spectrum.

Q0420-0127 (PKS 0420-01, $z_{em} = 0.915$)

Wills et al. (1980) observed this object in the approximate range $3650 - 6700 \text{ \AA}$ and found an Mg II system at $z_{abs} = 0.633$, but they give no quantitative treatment of the spectrum. Yanny (1992) presents narrow band [O II] $\lambda 3727$ photometry of this field and finds at least 7 nearby candidate emission line objects. Yanny and York (1992) take this and similar objects as evidence favoring the disappearing starburst or merging dwarf scenario at $z \gtrsim 0.5$. We find no new absorbers in our spectrum.

Q0538+4949 (3C 147, $z_{em} = 0.545$)

No absorption lines are previously reported and we find none as well.

Q0610+2605 (3C 154, $z_{em} = 0.580$)

No absorption lines are previously reported. We find a tentative associated Mg II absorber.

$z_{abs} = 0.5920$: This tentative Mg II system has an apparent infall velocity of 2300 km s^{-1} relative to the quasar.

Q0642+4454 (OH 471, $z_{em} = 3.400$)

SSB2 obtained a spectrum of this object in the range $3150 - 7000 \text{ \AA}$ and found Mg II absorption at $z_{abs} = 1.2464$ and CIV absorption at 2.9724, 3.1338, and 3.2483. Khare, York, and Green (1989) reported several tentative absorber systems, but none are confirmed by SSB2 even though they could have been observed. In our spectrum, which has lower S/N than SSB2, we find no identified lines redward of the Ly- α forest.

Q0710+1151 (3C 175, $z_{em} = 0.768$)

Boissé et al. (1992) obtained a spectrum in the range $3190 - 3946 \text{ \AA}$ and found only Galactic Ca II($\lambda 3934$) absorption. We confirm both members of the Ca II doublet and find an Mg II absorber:

$z_{abs} = 0.4630$: This moderate strength Mg II system has tentative Mg I absorption, with a detection significance $3.4\text{-}\sigma$.

Q0725+1443 (3C 181, $z_{em} = 1.382$)

Anderson et al. (1987) obtained a high-resolution spectrum of this object covering the range $3150 - 4025 \text{ \AA}$ and found an associated CIV absorber at $z_{abs} = 1.3878$. We see no evidence for the corresponding Mg II in our spectrum, but we find one new Mg II system:

$z_{abs} = 1.1694$: This is a definite Mg II absorber. The corresponding CIV is apparent in the spectrum of Anderson et al. (1987) although they do not identify it.

Q0736-0620 (PKS 0736-06, $z_{em} = 1.898$)

This quasar was previously observed by Young, Sargent, and Boksenberg (1982) (YSB), in the range 3500 - 5150 Å. They found associated CIV absorption at $z_{abs} = 1.9132$ and 1.9310. We confirm these systems and find another CIV system (not associated) and an Mg II complex:

$z_{abs} = 1.2009, 1.2035$: This definite Mg II complex is clearly asymmetric but is fit well with two Mg II doublets at the spectral resolution. There is evidence for Mg I at both these redshifts, but they cannot be confirmed because they fall in an O₂ band which was visible in a number of our spectra at high air mass. Notice the prominent O₂ band near 7600 Å. We also see evidence for Fe II with 3- σ and 4- σ detections of $\lambda 2382$ and $\lambda 2600$, respectively. The corresponding CIV is out of the range of YSB.

$z_{abs} = 1.8175$: This weak but definite system would appear in the spectrum of YSB at about a 3.7 σ significance.

Q0809+4822 (3C 196, $z_{em} = 0.871$)

This object has a famous and well studied absorption system at $z_{abs} = 0.43685$ which gives rise to a host of metal line species (see Foltz, Chaffee, and Wolfe 1988, who present excellent high-resolution spectra covering 3300 - 4200 Å and 5150 - 5950 Å) and HI 21 cm absorption (Brown et al. 1988; Brown and Mitchell 1983). The 21 cm absorption is especially significant because it occurs in a resolved background source, which allows useful limits to be placed on the absorber size (Foltz, Chaffee, and Wolfe 1988; Brown et al. 1988). We find no additional absorption systems in our spectrum.

Q0835+5804 (3C 205, $z_{em} = 1.534$)

BTT obtained a high S/N spectrum of this object covering the range 3980 - 7750 Å and found Mg II systems at $z_{abs} = 1.4353, 1.4382$ and 1.5427. Anderson et al. (1987) found an associated CIV complex centered at $z_{abs} = 1.5373$. We confirm the complex at $z_{abs} = 1.436$ (although our absolute redshifts disagree by about 0.0010) and add a detection of Fe II($\lambda 2374$) for the lower redshift member. We find no additional absorption systems.

Q0855+1421 (3C212, $z_{em} = 1.043$)

This object has no previously reported absorption systems. The night sky subtraction in our spectrum is worse than normal. We see an unidentified but significant broad absorption complex just redward the Mg II emission. This complex is consistent with Na I absorption at -600, 150, and 750 km sec⁻¹. We find the following associated Mg II system:

$z_{abs} = 1.0490$: This is a moderate strength associated system. In our spectrum the peak of the Mg II emission is at $z_{em} = 1.055$, giving an apparent ejection velocity of 900 km s⁻¹.

Q0859-1403 (PKS 0859-14, $z_{em} = 1.327$)

SS previously studied this object in the range 3900 - 6995 Å and found no absorption lines. Boissé et al. (1992) obtained a spectrum covering 3185 - 3946 Å and found a very tentative Mg II absorber at $z_{abs} = 0.2095$. Our spectrum is not sensitive enough to have detected this system.

Q0906+4305 (3C 216, $z_{em} = 0.670$)

No absorption lines have been previously reported and we find none in our spectrum. This object has a peculiar continuum/emission line shape, in that the Mg II emission is almost non-existent. Smith and Spinrad (1980) first reported the redshift based primarily on an emission line presumed to be [O II](3727).

Q1007+4147 (4C 41.21, $z_{em} = 0.613$)

No absorption lines have been previously reported for this object. We find three significant lines, all unidentified. One of them is near the wavelength of Galactic Ca II but since the other doublet member is not observed we make no identification.

Q1040+1219 (3C 245, $z_{em} = 1.029$)

There are no previously reported absorption lines for this object. We find a single Mg II system:

$z_{abs} = 0.6591$: We have some reservation about this system because the calculated redshifts of the doublet members disagree by 0.0006. A fit with an Mg II doublet (with wavelength ratio constrained) clearly shows the wavelength ratio problem, but the fit has $\chi^2_{\nu} \approx 1$ and so we make the identification.

Q1055+2007 (PKS 1055+20, $z_{em} = 1.110$)

No absorption lines are previously reported for this object. We find only a single unidentified line on the red wing of the C IV emission.

Q1111+4053 (3C 254, $z_{em} = 0.734$)

There are no previously reported absorption lines for this object, and we found none.

Q1136-1334 (PKS 1136-13, $z_{em} = 0.554$)

Boissé et al. obtained a spectrum for this object and found Galactic Ca II(3934) absorption. We find no significant absorption lines in our spectrum.

Q1137+6604 (3C 263, $z_{em} = 0.652$)

No absorption lines have been previously reported for this object. We find a Galactic Ca II absorber and a tentative associated Mg II system:

$z_{abs} = 0.6360$: Optimal extraction of the Mg II doublet members gives significance levels of 3.9σ and 4.5σ respectively, with adequate agreement of the redshifts to within the uncertainties.

Q1148-0007 (PKS 1148-00, $z_{em} = 1.982$)

This object has been studied by SBS and YSB, who found C IV absorption at $z_{abs} = 1.4669$ and 1.9861 . SS studied this object in the range $5148 - 8947 \text{ \AA}$ and found no identified absorption lines. The unidentified line they report at 6280.0 \AA is most likely a weak atmospheric O₂ band. At the position of their line at 8854.8 \AA , we observe the equivalent width $W_{obs} = 0.24 \pm 0.23$, in contrast to their value $W_{obs} = 1.37 \pm 0.17$. We find no new absorption systems in our spectrum.

Q1153+3144 (4C 31.38, $z_{em} = 0.418$)

The redshift for this object was erroneously reported to be $z_{em} = 1.557$ by Burbidge and Kinman (1966), although they did note that their spectrum might also be consistent with a redshift of 0.413. Our spectrum clearly shows that this object is a Seyfert galaxy at redshift $z_{em} = 0.418$. Because of the low redshift it makes no contribution to our statistical sample. We find no absorption lines in this spectrum.

Q1156+2931 (4C 29.45, $z_{em} = 0.729$)

There are no previously reported absorption lines for this object, and we find none.

Q1206+4356 (3C 268.4, $z_{em} = 1.400$)

Anderson et al. (1987) studied this object in the range 3150 - 4025 Å and they found Mg II absorption at $z_{abs} = 0.4124$ and associated C IV absorption at $z_{abs} = 1.3767$ and 1.3963. We find no absorption lines in our spectrum. At the position of Mg II at $z_{abs} = 1.38$ the $1-\sigma$ rest equivalent width limit in our spectrum is 0.05 Å.

Q1213+5352 (4C 53.24, $z_{em} = 1.065$)

There are no previously reported absorption lines for this object, and we find none.

Q1218+3359 (3C 270.1, $z_{em} = 1.519$)

Anderson et al. (1987) studied this object in the range 3320 - 4200 Å and they found associated C IV absorption at $z_{abs} = 1.5004$. We confirm this doublet in our spectra, find the corresponding Mg II, and find a new Mg II absorption system. Note that spectrum #1 for this object suffers from the flattening problem in the July 1988 spectra:

$z_{abs} = 0.7423$: This sMg II system is lies at the edge of the steep red wing of the C III](1909) emission and so the continuum placement is uncertain.

$z_{abs} = 1.5000$: This strong associated Mg II system is certain.

Q1229-0207 (PKS 1229-02, $z_{em} = 1.038$)

This object was studied by Briggs et al. (1985) over the ranges 3410 - 4050 Å and 5000 - 5910 Å. They observed the Mg II system at $z_{abs} = 0.395$, along with the corresponding Mg I and Fe II. This system is also a 21 cm absorber (BW). In our spectrum we find one unidentified line and a new Mg II absorber:

$z_{abs} = 0.7571$: This moderate strength system falls between the two spectra of Briggs et al. (1985).

Q1318+1122 (PKS 1318+11, $z_{em} = 2.171$)

BTT observed this object over the range 3880 - 7750 Å and they found Mg II absorption at $z_{abs} = 0.8388$ and 1.0541, and C IV at $z_{abs} = 1.8755$. Our spectrum #1 for this object suffers from the flattening problem in the July 1988 spectra. In our spectra we confirm the Mg II at $z_{abs} = 0.8388$ and the C IV system. The Mg II line is detected at a significance level below our 5- σ threshold and hence is not included in the statistical analysis. For the $z_{abs} = 1.0541$ system, we see the Mg II(2796) line at 4.7- σ but find no evidence for the Mg II(2803) line at a 4.5- σ level.

Q1327-2126 (PKS 1327-21, $z_{em} = 0.528$)

No previous absorption lines are reported for this object. We find a single tentative Mg II absorber:

$z_{abs} = 0.3015$: This system is regarded as tentative because it falls below our 5- σ significance cutoff.

Q1328+2524 (3C 287, $z_{em} = 1.055$)

No previous absorption lines are reported for this object and we find none.

Q1328+3045 (3C 286, $z_{em} = 0.846$)

This object contains the well-studied absorption system at $z_{abs} = 0.6927$. At this redshift absorption has been observed in metal lines (Meyer and York 1992, and references therein), HI 21 cm (Briggs 1988), and damped Ly- α (Cohen et al. 1992).

Spectrum #1 for this object suffers from the flattening problem in the July 1988 spectra. In our spectrum we find Fe II at $z_{abs} = 0.6927$ and no other lines. The Mg II doublet falls in the dichroic gap of the double spectrograph.

Q1335-0611 (PKS 1335-06, $z_{em} = 0.625$)

There are no previously reported absorption lines for this object and we find only one unidentified line.

Q1354-1512 (PKS 1354-15, $z_{em} = 1.890$)

There are no previously reported absorption lines for this object. We find one new Mg II absorber:

$z_{abs} = 1.0309$: This is definite Mg II system. The unidentified line at 4838 Å is at the correct wavelength for Fe II(2382), but we see no Fe II(2600) and so we reject this identification.

Q1437+6224 (OQ663, $z_{em} = 1.090$)

No absorption lines are previously reported for this object. We find a broad unidentified line which occurs in the quasar Mg II emission and a new Mg II absorber:

$z_{abs} = 0.8723$: This is a moderate strength Mg II system.

Q1442+1011 (OQ 172, $z_{em} = 3.530$)

This object was observed by SBS in the range 5500 - 7150 Å. They found definite CIV absorption at $z_{abs} = 2.6336$ and possible absorption at $z_{abs} = 2.6705$, 2.6939, 3.0473, and 3.1101. BTT observed this object in the range 3875 - 7750 Å and did not identify any of these systems. In our spectrum we confirm the $z_{abs} = 2.6336$ and 2.6939 systems (the latter at low confidence), but not any of the others in SBS. Our $1-\sigma$ limit on W_{obs} is about 0.7 - 1.0 Å in this region, compared to 0.5 - 0.8 Å in SBS. We find no other significant lines redward of Ly- α . We have not determined wavelengths for the Ly- α forest lines in our spectrum because the spectrum of BTT is at higher resolution.

Q1453-1056 (PKS 1453-10, $z_{em} = 0.938$)

This object has no previously reported absorption lines, and we find none. Spectrum #1 for this object suffers from the flattening problem in the July 1988 spectra.

Q1458+7152 (3C 309.1, $z_{em} = 0.905$)

This object was previously studied by SS in the wavelength range 3100 - 6995 Å, and they found only two unidentified lines near 5900 Å. We see only the lower wavelength line, which in our spectrum is consistent with Na I at a velocity of -450 km sec⁻¹. We find in addition Galactic Ca II and possible Al I. These are apparent in the spectrum of SS but are not identified.

Q1508-3231 (PKS 1508-05, $z_{em} = 1.191$)

No absorption lines are previously reported for this object, and we find none. Spectrum #1 for this object suffers from the flattening problem in the July 1988 spectra.

Q1618+1743 (3C 334, $z_{em} = 0.555$)

No absorption lines are previously reported for this object, and we find only two unidentified lines. Spectrum #1 for this object suffers from the flattening problem in the July 1988 spectra.

Q1622+2352 (3C 336, $z_{em} = 0.927$)

SS studied this object in the range 3100 - 6995 Å and found Mg II absorption at $z_{abs} = 0.4721, 0.6562, 0.6601, \text{ and } 0.8915$. We confirm these systems in our spectra and find no other absorption lines.

Q1629+1202 (PKS 1629+12, $z_{em} = 1.795$)

BTT obtained a spectrum of this object covering the range 3870 - 7750 Å and found a strong Mg II system with Mg I at $z_{abs} = 0.5316$, and found Mg II, Mg I, and Fe II at $z_{abs} = 0.9004$. Our spectrum #1 for this object suffers from the flattening problem

in the July 1988 spectra. In our spectra we confirm the lines in BTT and find in addition Fe II(2600) at $z_{abs} = 0.5313$ and a new C IV absorber:

$z_{abs} = 1.3790$: This likely C IV absorption system is out of the range of BTT. We find no evidence for the corresponding Mg II. This system would be certain except that it falls in the badly flattened portion of the spectrum. However, there are no prominent defects near this position on the CCD and so this system is unlikely to be an artifact. There may also be Si IV absorption at this redshift, but these lines fall in the Ly- α forest and so we cannot make a positive identification.

Q1634+6251 (3C 343, $z_{em} = 0.988$)

No absorption lines are previously reported for this object, and we find none. This object is a Seyfert 2 galaxy with very little continuum emission.

Q1828+4842 (3C 380, $z_{em} = 0.695$)

Boissé et al. (1992) studied this object in the range 3139 - 3946 Å and found no lines. Spectrum #1 for this object suffers from the flattening problem in the July 1988 spectra. In our spectra we find only Galactic Na I and tentative Ca II.

Q1901+3155 (3C 395, $z_{em} = 0.635$)

There are no previously reported absorption lines for this object. We find in our spectra a new Mg II absorber and Galactic Ca II and Na I:

$z_{abs} = 0.3901$: The doublet ratio for this system is on the border of acceptability at 2.7 ± 0.7 .

Q2003-0232 (4C -02.79, $z_{em} = 1.457$)

There are no previously reported absorption lines for this object. Spectrum #1 for this object suffers from the flattening problem in the July 1988 spectra, but the lines we find are far away from known defects on the CCD or are corroborated otherwise. We find in our spectra a rich collection of lines from three absorption systems:

$z_{abs} = 1.212$: This very strong system is seen in CIV, Mg II, and four Fe II lines. It is apparent from the poor redshift match among different lines in these spectra that the uncertainty in the wavelength calibration is around 2-3 Å, rather more than the formal value.

$z_{abs} = 1.411$: This certain Mg II system shows absorption in the two strongest Fe II lines, but not CIV.

$z_{abs} = 1.457$: This is a definite associated CIV absorber.

Q2044-0247 (3C 422, $z_{em} = 0.942$)

There are no previously reported absorption lines for this object. In our spectra we find one strong associated Mg II absorption system:

$z_{abs} = 0.9384$: This definite associated system shows absorption in Mg II, Mg I, and two Fe II lines. Note that our spectra did not cover Fe II(2382) at this redshift.

Q2115-3031 (PKS 2115-30, $z_{em} = 0.980$)

There are no previously reported absorption lines for this object. We find only a likely Galactic Na I absorber in our spectra. The components are not resolved but the line was well fit with a Na I doublet. Spectrum #1 for this object suffers from the flattening problem in the July 1988 spectra.

Q2143-1541 (PKS 2143-15, $z_{em} = 0.700$)

There are no previously reported absorption lines for this object. Our spectra yield only one unidentified line. Spectrum #1 for this object suffers from the flattening problem in the July 1988 spectra.

Q2223+2102 (PKS 2223+21, $z_{em} = 1.959$)

BTT obtained a spectrum spectrum of this object covering 3870 - 7750 Å and they find a rich system at $z_{abs} = 1.9019$ showing CIV, Si II(1526), and Fe II(2344) absorption. Our spectrum #1 for this object potentially suffers from the flattening problem in the July 1988 spectra. However, it is apparent that this spectrum is not badly affected,

since we are able to make reasonable identifications for the lines which appear. We confirm the lines in BTT and find additional lines at this redshift. We also find a new tentative CIV system:

$z_{abs} = 1.4407$: This is a tentative CIV absorber in which the CIV(1550) line is blended with SiII(1304) from the $z_{abs} = 1.9019$ system. If this line is entirely SiII(1304), then it is much too strong and the redshift match is poor.

$z_{abs} = 1.9019$: In this definite system we find FeII(2344), CIV, SiII(1526), SiIV(1402), SiIV(1393), CII(1334), and possibly SiII(1304). FeII(2374) and FeII(2382) may be present in our spectrum but unfortunately happen to lie in an O₂ band.

Q2230+1128 (CTA 102, $z_{em} = 1.037$)

Anderson et al. (1987) studied this object in the wavelength range 4040 - 5240 Å and found no absorption lines. We find only Galactic NaI in our spectra, which was unresolved but fit well with a NaI doublet. Spectrum #1 for this object suffers from the flattening problem in the July 1988 spectra.

Q2249+1832 (3C 454, $z_{em} = 1.757$)

BTT studied this object in the range 3870 - 7800 Å. They tentatively identify an Mg II system at $z_{abs} = 0.782$, and either Mg II at $z_{abs} = 1.1045$ or Galactic NaI. However, the poor redshift matches in both these systems and confusion with Galactic NaI make the Mg II identifications unlikely. In our spectra, we rule out the $z_{abs} = 0.782$ system at 2.5- σ level. We confirm the latter system of BTT, but it is significant in our spectrum only at 4- σ . We would attribute this line to an unresolved Galactic NaI doublet. We find no other confirmed absorption lines in our spectra. Spectrum #1 for this object suffers from the flattening problem in the July 1988 spectra.

Q2251+2429 (PKS 2251+24, $z_{em} = 2.328$)

This object was previously studied by BTT in the range 3870 - 7730 Å. They found Mg II absorption at $z_{abs} = 1.0901$ and CIV absorption at $z_{abs} = 1.7495, 2.1554, 2.352,$ and 2.3626. In our spectra we confirm the lines they see and find in addition SiII(1393)

at $z_{abs} = 2.1555$. No additional systems are present. The detection significance level of the Mg II system is below our threshold and it is not included in our statistical analysis. Spectrum #1 for this object suffers from the flattening problem in the July 1988 spectra.

4.5 Statistical analysis

In the first part of this chapter we have assembled a list of absorption lines which were extracted from the spectra in our sample according to a well-defined procedure. For each spectrum we also have a corresponding array which gives the $5\text{-}\sigma$ detection limit (as a function of wavelength) for the rest equivalent width of an unresolved line. As we pointed out at the beginning of the chapter, the sample of quasars was selected based on properties which are unrelated to absorber characteristics, so we have an unbiased sample. It is thus possible to do a statistical analysis of the properties of the absorption lines. Since the redshifts of quasars in our sample are mostly in the range 0.6 to 1.5, we only do Mg II absorber statistics.

4.5.1 Sample properties

The first step is to calculate for each spectrum the $5\text{-}\sigma$ detection limit in equivalent width above which an unresolved line could have been detected. Since both the quasar continuum and the night sky emission vary with wavelength, the detection limit array is obviously a function of wavelength as well. In addition, the *observed* equivalent width scales as $1 + z_{abs}$ compared to the *rest frame* (or intrinsic) equivalent width. This means that it is easier to detect weaker systems at higher redshifts. In order to compare the intrinsic properties of the absorbers it is customary to quote both detection limits and equivalent widths in the absorber rest frame. This of course requires that we define the particular absorbing element, such as Mg II. Henceforth, unless otherwise stated, all equivalent widths are Mg II rest frame equivalent widths and all absorber redshifts are based on the Mg II doublet at 2796.35 and 2803.53 Å.

In Fig. 4.3 we show the $5\text{-}\sigma$ detection limits in each of the spectra as a function of

redshift. The plots have been clipped above 2.5 \AA , and regions in which Mg II is not observable at all are shown with the limit set to zero. Because there is uncertainty about the physical nature and environment of absorbers very near the quasar itself (*refs*), we exclude any regions with a velocity relative to the quasar of less than 5000 km sec^{-1} . We also apply the same criteria near the Ly- α emission peak to avoid possible misidentification of Ly- α absorption lines. These excluded regions, along with the O₂ bands and the dichroic gap of the Double Spectrograph are apparent in the plots of Fig. 4.3.

The overall sensitivity and size of our sample can be summarized in the plots of Fig. 4.4. The left plot shows the integrated redshift path length as a function of 5- σ rest equivalent width detection limit. This is defined by

$$\mathcal{Z}(W_0) = \sum_k \int \delta(\mathcal{W}_k(z) \leq W_0) dz, \quad (4.3)$$

where $\mathcal{W}_k(z)$ is the detection limit in the k^{th} quasar at redshift z , and $\delta(\text{condition})$ is one if the *condition* is true and zero otherwise. For comparison, the path length in the combined samples of SS and SSB1 is 114.2 at $W_0 = 0.3 \text{ \AA}$ and 131.1 at $W_0 = 1.0 \text{ \AA}$. In the right plot of Fig. 4.4 we show the number of quasar sightlines versus redshift at various equivalent width limits. This function is given by

$$S(z, W_0) = \sum_k \delta(\mathcal{W}_k(z) \leq W_0).$$

The thickest line is $S(z, 0.3 \text{ \AA})$, the medium line is $S(z, 0.6 \text{ \AA})$, and the thinnest line is $S(z, 1.0 \text{ \AA})$.

In Table 4.3 we list the Mg II absorption systems which form the basis of our statistical analysis. In these lines the stronger member ($\lambda 2796$) is detected at better than 5- σ confidence and the weaker member is detected at better 3.5- σ confidence. Our sample is complete at these limits. The lines which are identified in Table 4.2 with a “?” are not included in our analysis.

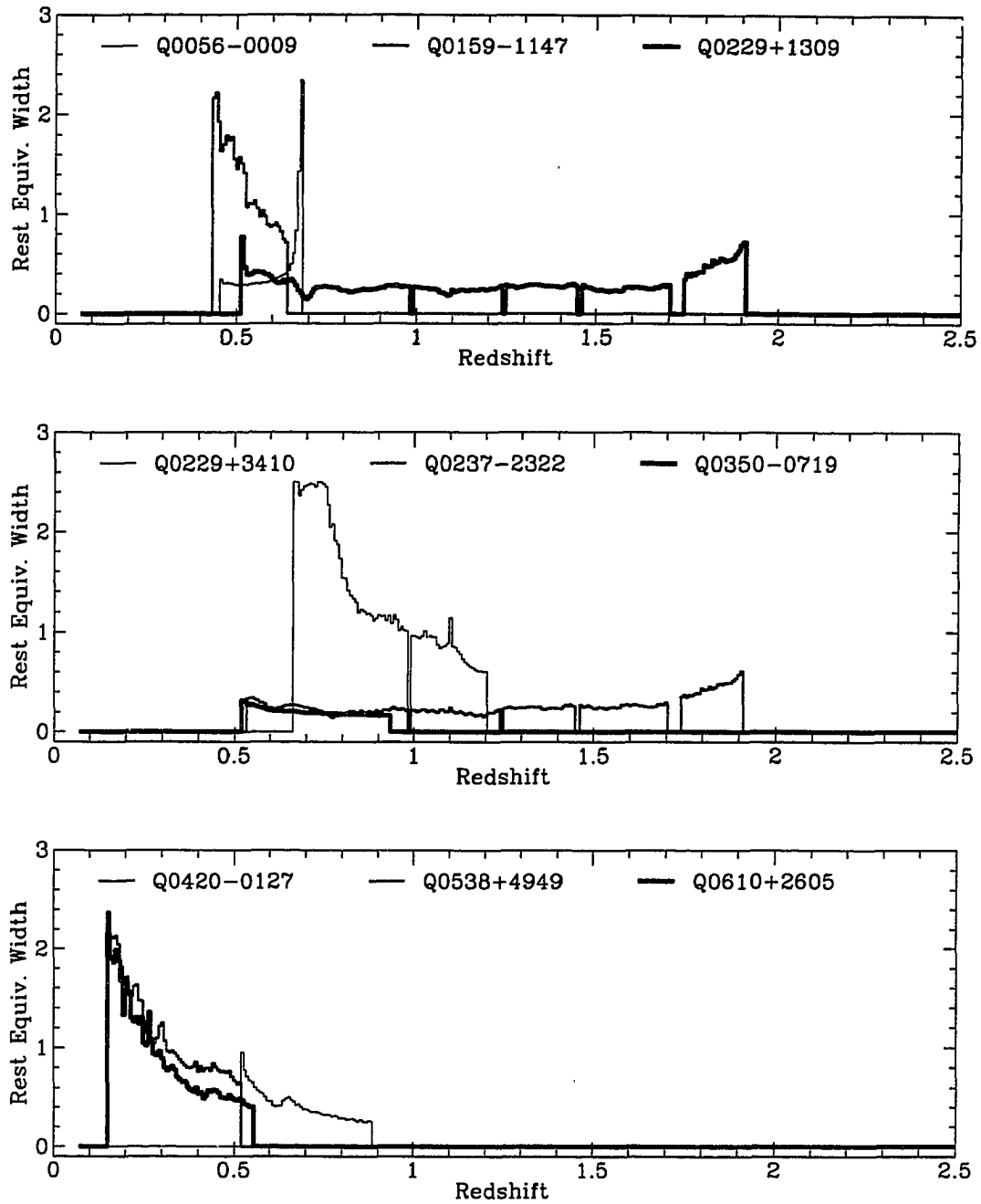


Figure 4.3: Rest equivalent width limits

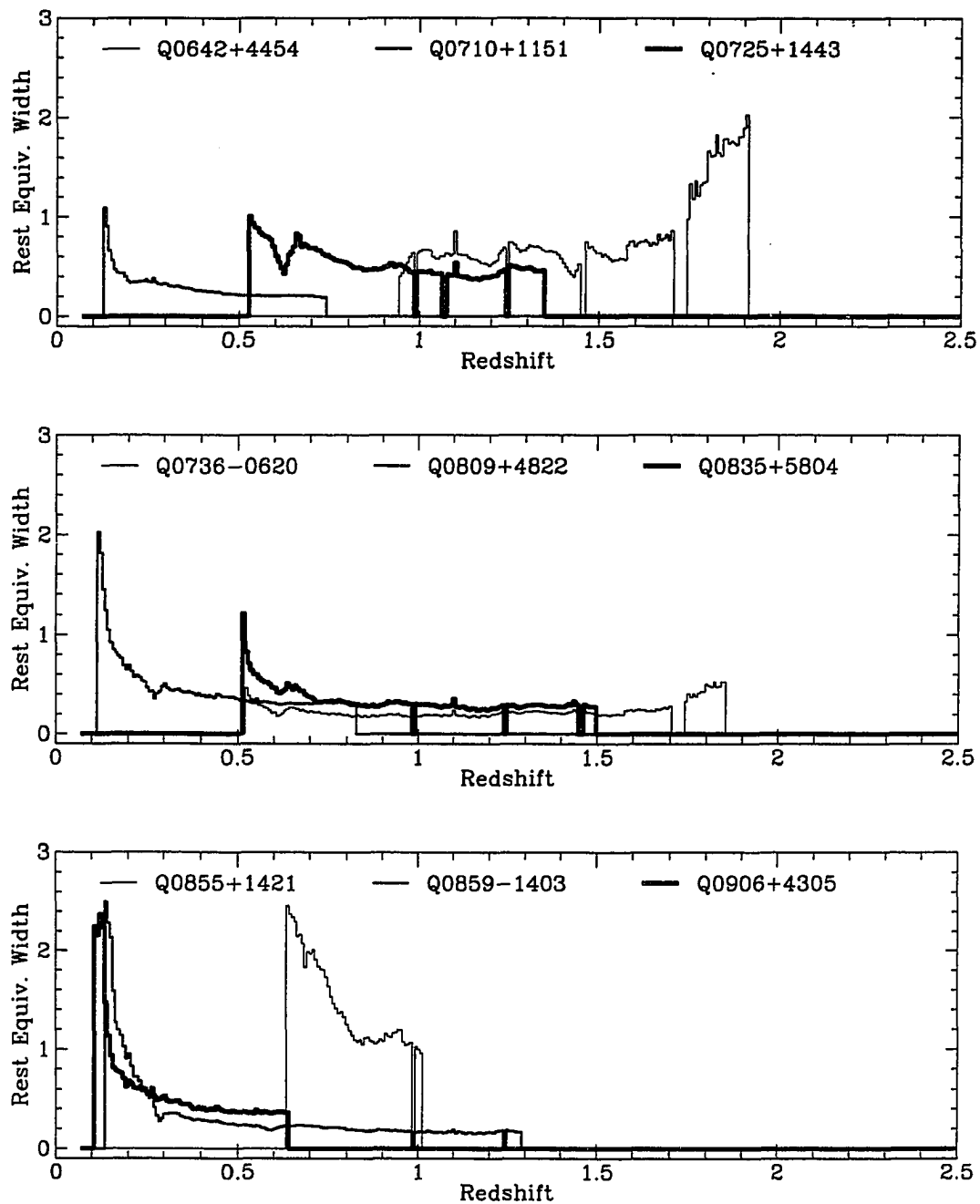


Figure 4.3: Rest equivalent width limits

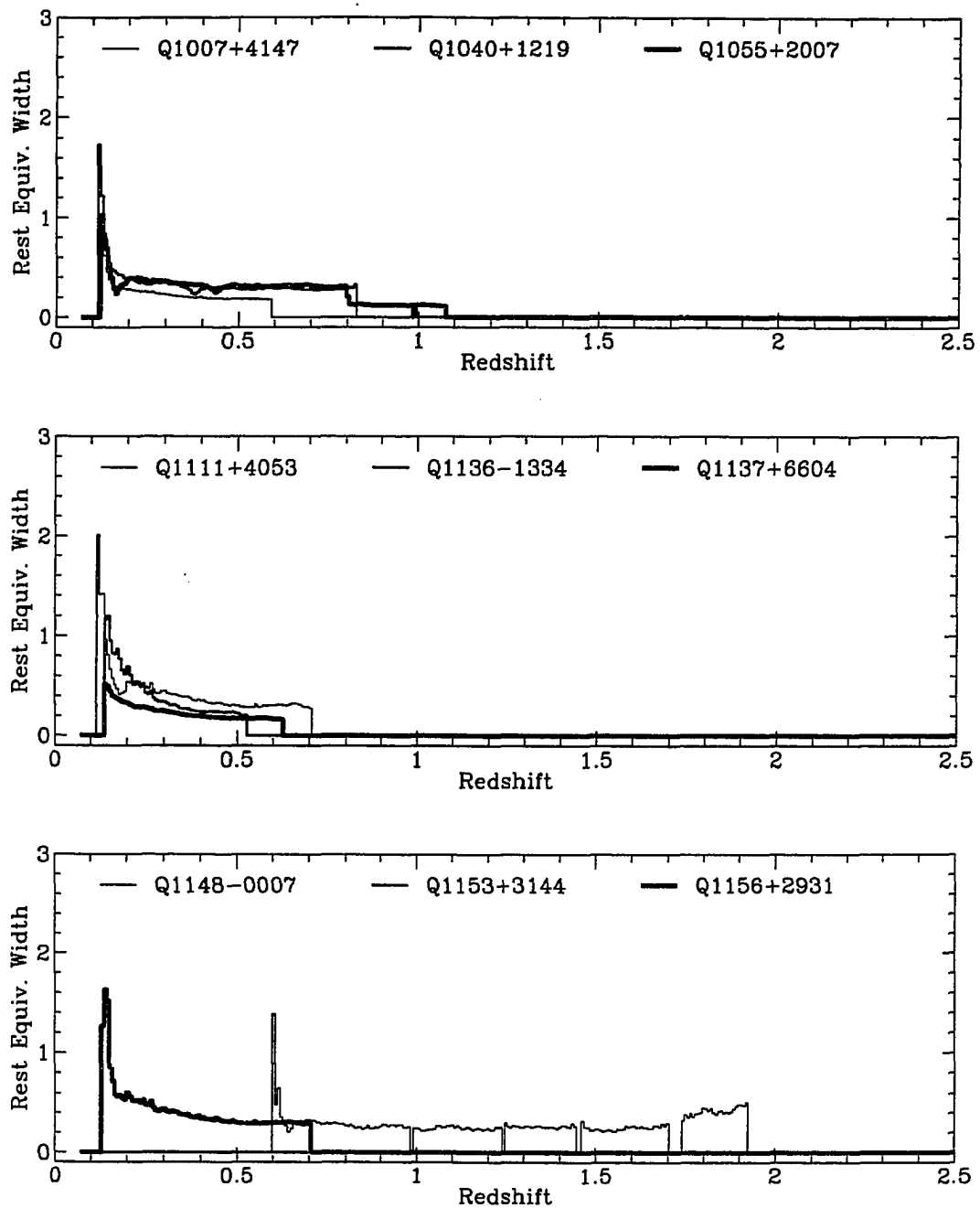


Figure 4.3: Rest equivalent width limits

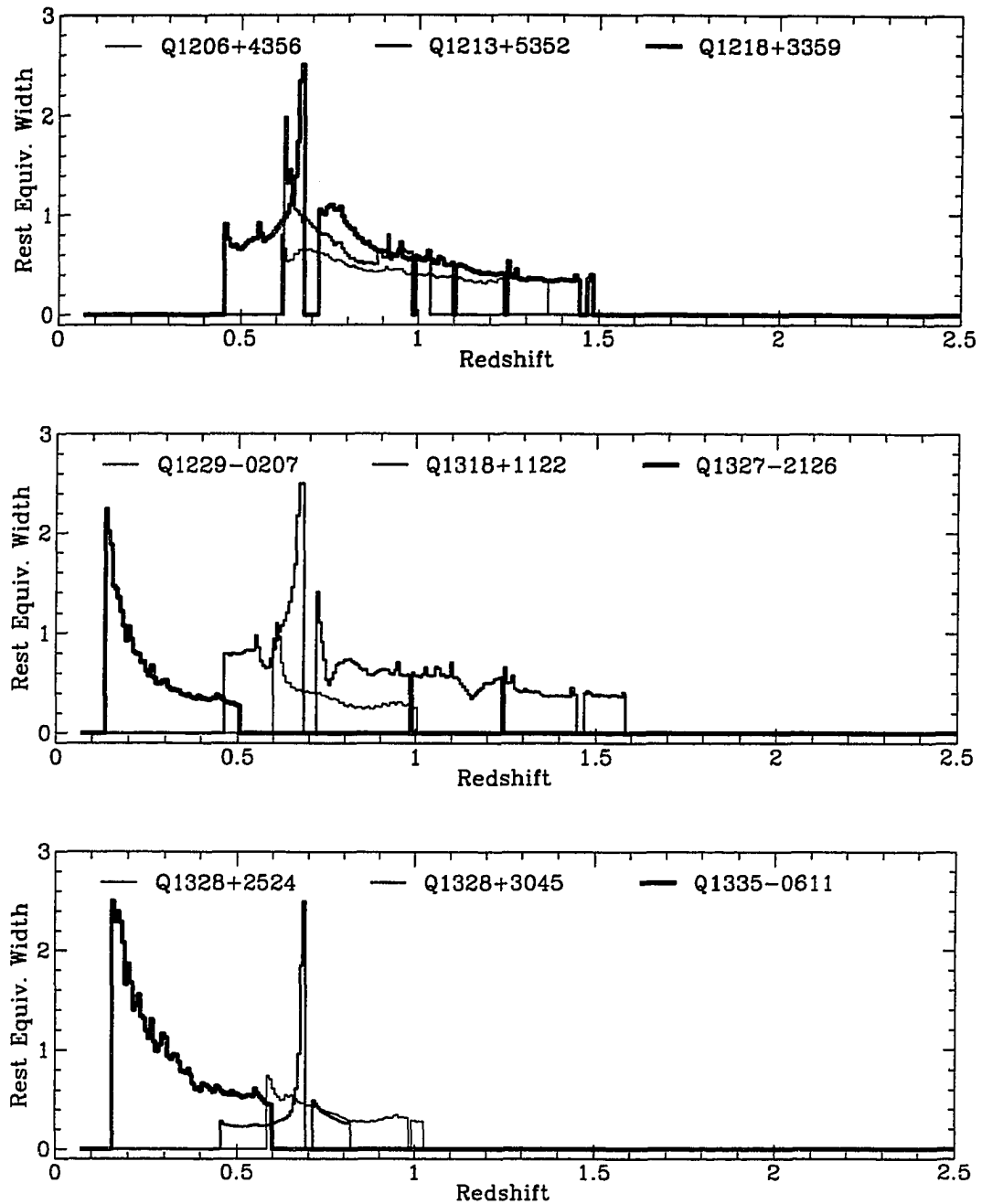


Figure 4.3: Rest equivalent width limits

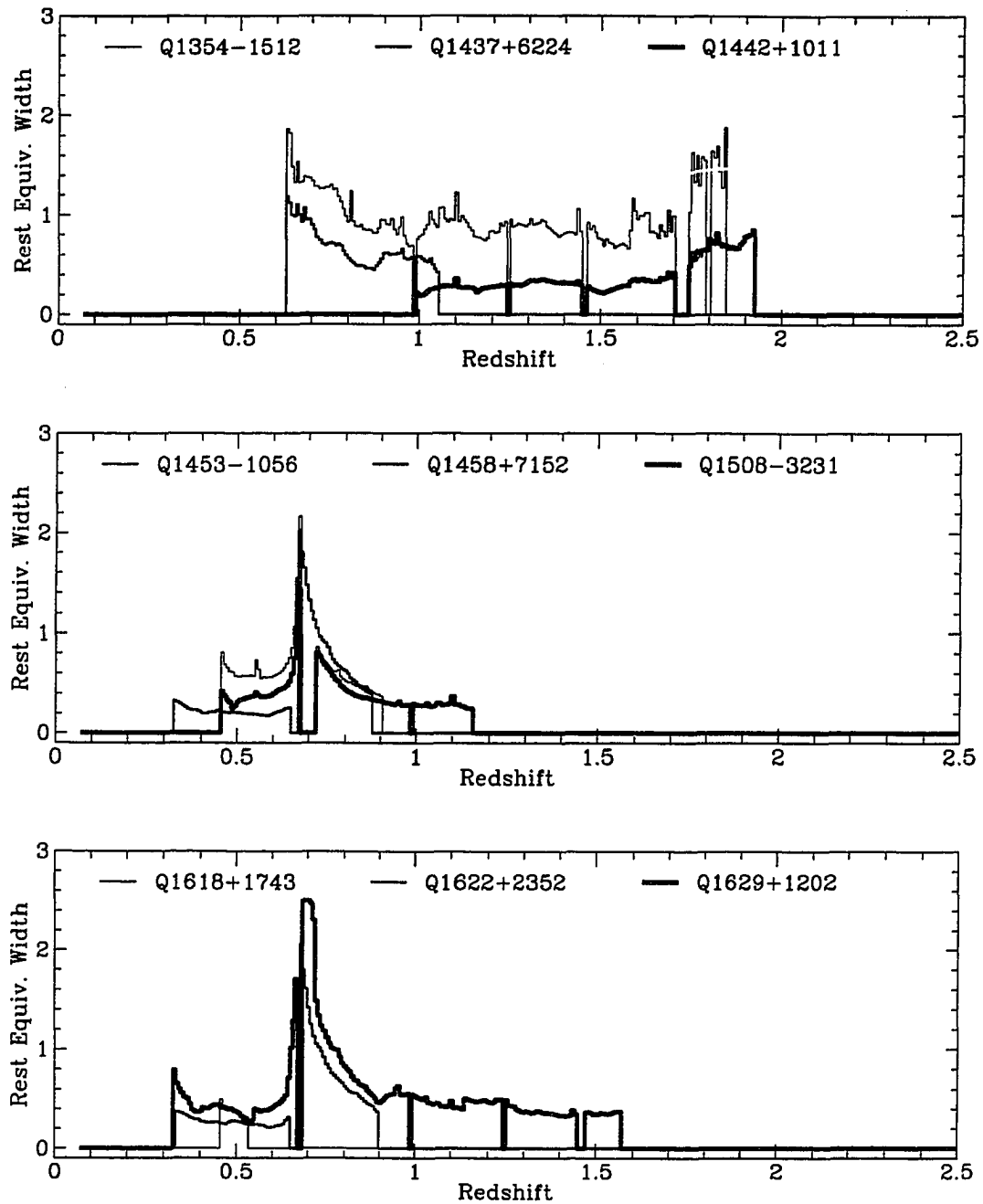


Figure 4.3: Rest equivalent width limits

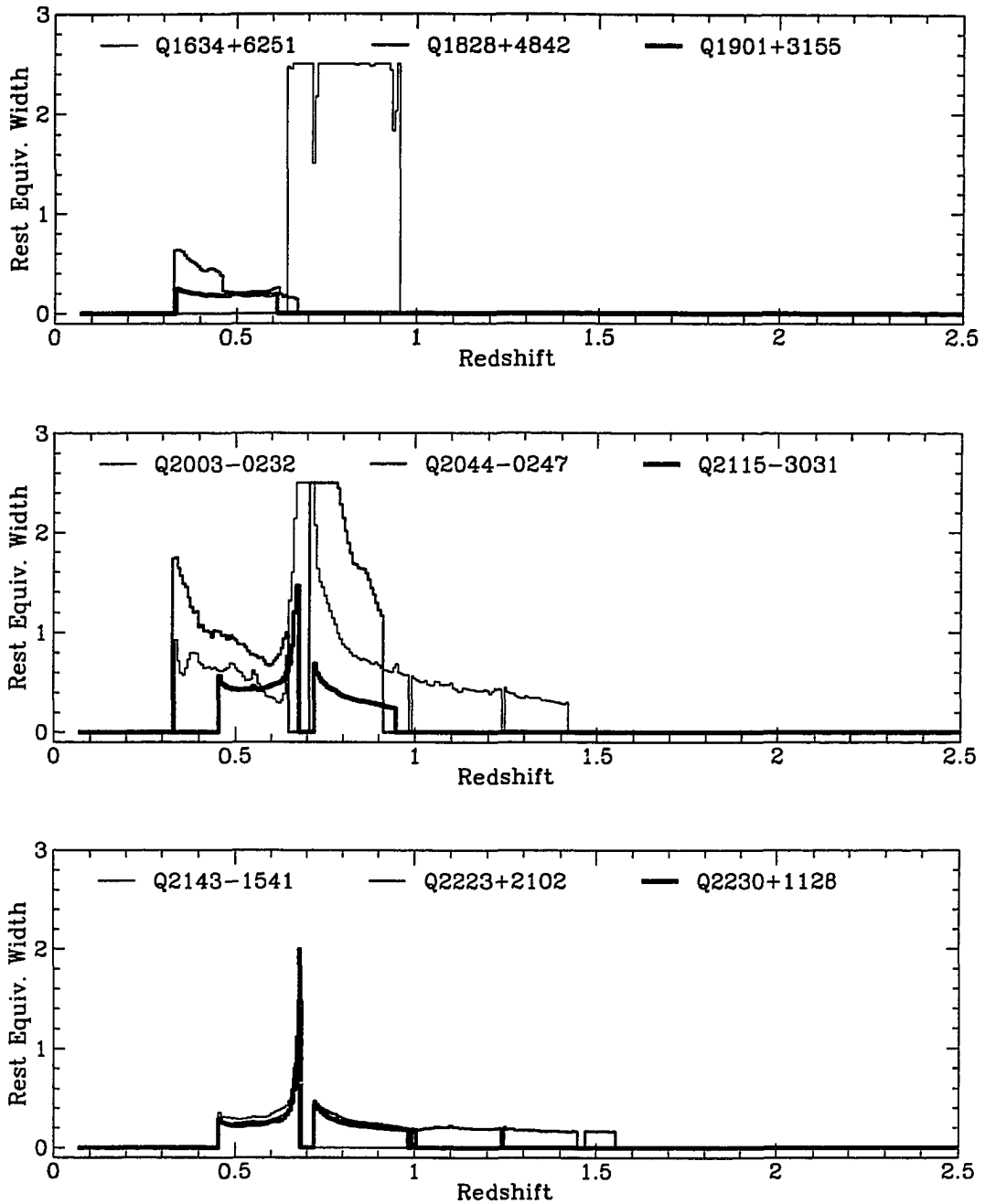


Figure 4.3: Rest equivalent width limits

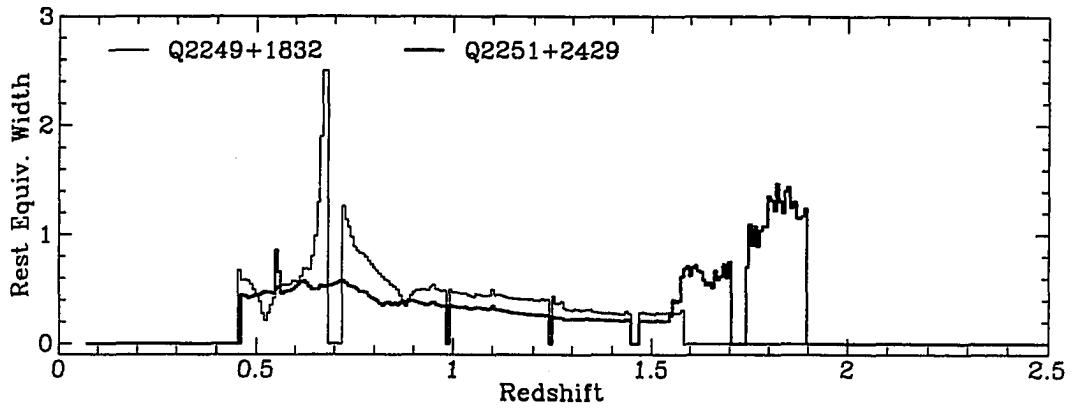


Figure 4.3: Rest equivalent width limits

Table 4.3: MgII $\lambda 2796, \lambda 2803$ absorption lines

Object	z_{em}	z_{abs}	$W_0(\lambda 2796)$	$W_0(\lambda 2803)$	$W_0(\text{MgI } \lambda 2852)$
Q0229+1309	2.065	1.8609(4)	1.02(14)	0.70(14)	<0.57
Q0229+3410	1.240	0.7754(3)	1.92(41)	2.02(36)	<1.13
		1.2248(3)	3.47(16)	2.14(16)	0.56(16)
Q0237-2322	2.224	1.3647(3)	1.91(8)	1.43(8)	<0.16
		1.6582(3)	0.55(5)	0.42(5)	...
		1.6719(3)	0.80(5)	0.61(5)	...
Q0420-0127	0.915	0.6330(3)	1.02(10)	0.86(10)	<0.36
Q0710+1151	0.768	0.4630(1)	0.62(6)	0.29(5)	0.24(8)
Q0725+1443	1.382	1.1694(4)	0.62(9)	0.36(8)	<0.28
Q0736-0620	1.898	1.2009(5)	0.19(5)	0.16(4)	...
		1.2035(3)	0.49(4)	0.41(5)	...
Q0809+4822	0.871	0.4367(1)	2.12(11)	2.03(10)	1.03(10)
Q0835+5804	1.534	1.4330(6)	0.25(7)	0.31(7)	0.21(6)
		1.4365(4)	0.51(7)	0.34(7)	<0.20
Q0855+1421	1.043	1.0491(3)	0.76(16)	0.50(14)	...
Q1040+1219	1.029	0.6591(1)	0.58(10)	0.42(10)	<0.19
Q1218+3359	1.519	0.7423(3)	1.34(29)	1.08(29)	<0.74
		1.5000(1)	1.25(9)	1.16(9)	...
Q1229-0207	1.038	0.7571(3)	0.52(7)	0.48(7)	<0.22
Q1354-1512	1.890	1.0309(3)	1.28(21)	0.73(22)	<0.88
Q1437+6224	1.090	0.8723(3)	0.71(9)	0.64(9)	<0.42
Q1622+2352	0.927	0.4718(1)	0.95(7)	1.02(8)	<0.20
		0.8920(2)	1.64(13)	1.21(12)	...
Q1629+1202	1.795	0.5313(0)	1.40(7)	1.35(7)	0.31(8)
		0.9008(1)	1.20(9)	0.69(9)	<0.39
Q1901+3155	0.635	0.3901(0)	0.45(4)	0.15(4)	<0.13
Q2003-0232	1.457	1.2116(1)	2.65(14)	2.17(15)	<0.31
		1.4106(1)	0.74(7)	0.62(7)	...
Q2044-0247	0.942	0.9384(1)	2.84(21)	2.17(18)	1.41(23)

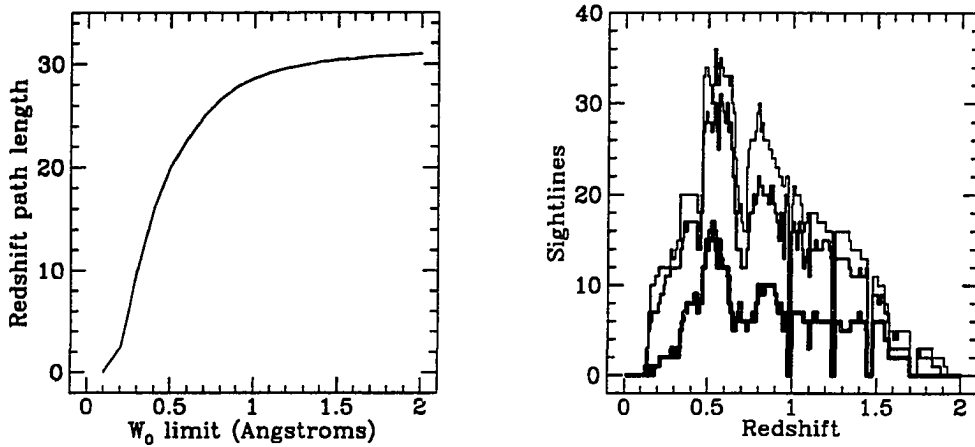


Figure 4.4: On the left is redshift path length vs. rest equivalent width limit. On the right is sightlines vs. redshift for various equivalent width limits. The thickest line is for $W_0 = 0.3 \text{ \AA}$, the medium line is for $W_0 = 0.6 \text{ \AA}$, and the thinnest line is for $W_0 = 1.0 \text{ \AA}$.

4.5.2 Calculation of distribution functions

In this section we describe the method we use for computing the parametric functions used for characterizing the redshift evolution and equivalent width distributions of the MgII absorbers. In all cases we use the maximum likelihood method for determining the best fit of the function to the unbinned data. We are basically following the algorithm outlined by Murdoch et al. (1985), but change notation so that different equivalent width limits are allowed for a single QSO. This notation change also simplifies several equations and conceptually clarifies the algorithm.

First recall the most common form for the distribution function (SYBT; Murdoch et al. 1985) which was discussed in Sec. 2.6. This gives the number density of absorbers per unit redshift per unit EW:

$$n(z, W) = \frac{\partial^2 N(z, W)}{\partial z \partial W} = \frac{A_0}{W^*} (1+z)^\gamma \exp(-W/W^*). \quad (4.4)$$

The goal then is to find the values of γ and W^* for which the probability of observing

the actual data set is maximized.

To compute this function or related functions for the set of observed spectra, the first step is to break the all of the spectra up into contiguous regions \mathcal{R}_k (where $k = 1, K$) in which the detection EW limit is less than \mathcal{W}_k . Each region \mathcal{R}_k is then characterized by the EW limit, the start and end redshifts z_{k0} and z_{km} , and the QSO identification \mathcal{Q}_k . The value \mathcal{Q}_k is simply a unique identifier which specifies the QSO in which region \mathcal{R}_k is defined. For a single equivalent width limit \mathcal{W}_a we define the sample $\mathcal{S}(\mathcal{W}_a)$ to be the collection of regions \mathcal{R}_k with $\mathcal{W}_k = \mathcal{W}_a$. With these definitions the expected number of absorption line systems becomes

$$N = \frac{A_0}{W^*} \sum_{k=1}^K \int_{z_{k0}}^{z_{km}} (1+z)^\gamma dz \int_{\mathcal{W}_k}^{\infty} \exp(-W/W^*) dW \quad (4.5)$$

$$\equiv A_0 \sum_{k=1}^K \omega_k, \quad (4.6)$$

where $\omega_k \equiv I_k e^{-\mathcal{W}_k/W^*}$ and $I_k \equiv (\gamma+1)^{-1} [(z_{km}+1)^{\gamma+1} - (z_{k0}+1)^{\gamma+1}]$. The normalization A_0 in the distribution function is eliminated by setting $A_0 = N_{obs}/\sum_k \omega_k$, where N_{obs} is the actual number of lines observed in the spectra.

In theory, one could choose the regions to be one pixel wide and set \mathcal{W}_k equal to the local EW limit, thus making maximum use of all the data. This has been implemented in the data analysis software for the HST quasar absorption line key project. However, this method is computationally expensive for large data sets. A good compromise is to define a discrete set of rest equivalent width limits E_i (e.g. 0.0, 0.3, 0.6, 1.0, and 2.0 Å). Then we go through the spectra and set $\mathcal{W}_k = E_i$ for the contiguous regions in which the local EW limit is everywhere between E_{i-1} and E_i . We can have as many E_i as is convenient computationally.

Now assume that the N_{obs} absorption line systems in the spectra have redshifts z_i and rest equivalent widths W_i . Each of these systems must have $W_i \geq \mathcal{W}_k$ for the region in which it occurs. The expected number of systems $dN(z_i, W_i)$ in QSO \mathcal{Q}_i with redshift in the range z_i to $z_i + dz$ and equivalent width in the range W_i to

$W_i + dW$ is simply

$$dN(z_i, W_i) = \sum_k \delta(Q_i = Q_k) \delta(z_{k0} \leq z_i < z_{km}) \delta(W_i \geq W_k) n(z_i, W_i) dz dW.$$

The probability of the i^{th} line actually occurring in this interval at (z_i, W_i) is $p(z_i, W_i) dz dW = dn(z_i, W_i)$, which gives us

$$p(z_i, W_i) dz dW = \frac{N_{obs}}{W^* \sum_k \omega_k} \sum_k \delta(Q_i = Q_k) \delta(z_{k0} \leq z_i < z_{km}) \delta(W_i \geq W_k) (1 + z_i)^\gamma e^{-W_i/W^*} dz dW.$$

The likelihood of the observed set of lines occurring is $\prod_i p(z_i, W_i) dz dW$. Taking the logarithm of this and ignoring all terms which are independent of γ and W^* gives

$$L = \gamma \sum_i \ln(1 + z_i) - \sum_i W_i/W^* - N_{obs} \ln(\sum_k \omega_k) - N_{obs} \ln W^*. \quad (4.7)$$

Note that for notational convenience we have redefined the list of lines to include only those lines which have $\delta(z_{k0} \leq z_i < z_{km}) \delta(W_i \geq W_k) = 1$ for some k .

The optimal values γ_0 and W_0^* for the parameters occur at the maximum of likelihood function, which we find by solving for $\partial L/\partial \gamma = 0$ and $\partial L/\partial W^* = 0$. These equations are easily written out and take the functional form $\gamma = F(\gamma, W^*)$ and $W^* = G(\gamma, W^*)$. The solutions can be found by any number of numerical techniques, including simple iteration.

The uncertainties on the optimal values (ignoring any covariance) are given by

$$\sigma_\gamma = \left(\frac{\partial L}{\partial \gamma} \right)_{\gamma=\gamma_0}^{-1/2} \quad \sigma_{W^*} = \left(\frac{\partial L}{\partial W^*} \right)_{W^*=W_0^*}^{-1/2}.$$

We can also find the uncertainties by determining the change in each parameter (separately) which reduces the log likelihood function by 1/2. These methods are valid if the likelihood is approximately gaussian near the maximum, a condition which is empirically observed to hold true.

For comparison with results in the literature we also define and calculate the

individual distribution functions $n(W)$, the number of absorbers per unit equivalent width, and $n(z)$, the number of absorbers per unit redshift interval. These obviously depend on the equivalent width limits and the redshift range covered in the survey. Thus $n(z)$ is always given with the survey equivalent width limit, and $n(W)$ is usually quoted along with the average redshift. The dependence of $n(W)$ on redshift is weak, and SS find that increasing redshift is correlated with increased rest equivalent width at confidence levels between approximately 80% to 97% for various statistical tests.

The distribution $n(W)$ is normalized so that

$$\int_{W=W_0}^{\infty} n(W) dW = \langle N(z) \rangle,$$

where $\langle N(z) \rangle$ is number of absorbers per unit redshift in that sample. One functional form taken for this distribution, introduced by Sargent et al. (1980), is

$$n(W) = \frac{N^*}{W^*} \exp(-W/W^*). \quad (4.8)$$

For a sample with a single EW limit W_0 , the parameter N^* is easily found to be $N^* = \langle N(z) \rangle \exp(W_0/W^*)$. However, if the survey has very different equivalent width limits the calculation is not so simple. Of course, one can always just pick an EW limit and do the preceding calculation, but this means throwing out known absorbers and covered redshift path length, thereby increase statistical uncertainty. We can make a simple approximation to get around this difficulty. The normalization of $n(W)$ in effect makes it just the number of absorbers per equivalent width *per unit redshift*, averaged over the redshift in the sample. With this in mind, we can approximate $n(W)$ by integrating $n(z, W)$ over a unit redshift interval at the average z of the sample. This gives

$$n(W) \approx \int_{(z)-1/2}^{(z)+1/2} \frac{A_0}{W^*} (1+z)^\gamma \exp(-W/W^*) dz.$$

Using the value for γ determined by the method described previously, the value of

N^* is easily found to be

$$N^* \approx \frac{1}{\gamma_0 + 1} \left[(1.5 + \langle z \rangle)^{\gamma_0 + 1} - (0.5 + \langle z \rangle)^{\gamma_0 + 1} \right] \frac{N_{obs}}{\sum_k \omega_k}.$$

Another functional form for the equivalent width distribution which fits low redshift samples somewhat better (Tytler et al. 1987) is

$$n(W) = CW^{-\delta}.$$

For a uniform sample (with a single equivalent width limit) both parameters are easily calculated with the maximum likelihood method. For a non-uniform sample we must first calculate δ by a maximum likelihood fit of $n(z, W) = A_0 W^{-\delta} (1+z)^\gamma$ to the observed data, and then use the method just described to estimate C . Note that in doing these calculations it is generally necessary to introduce an upper cutoff W_{cut} in the equivalent width instead of integrating to infinity. A typical value for the cutoff is the highest W_i observed in the sample. This is because the integral of the power law form converges rather slowly and so the lack of very strong absorbers in the data has a large effect on the overall fit. This is illustrated in Fig. 4.5, where we have plotted the binned values of $n(W)$ for sample MG1 of SS, along with the maximum likelihood fits for $W_{cut} = 3.3 \text{ \AA}$ (solid line) and $W_{cut} = \infty$ (dashed line). The latter is clearly a poor fit. It is stated in SS that the best fit value for δ does not depend on the exact choice of the upper cutoff. However, using their sample MG1 we have derived the best fit values of C and δ as a function of the upper cutoff W_{cut} and find a *strong* dependence, especially near 3 \AA . This is shown in Fig. 4.6. The variation in δ with small changes in W_{cut} is much greater than the formal uncertainties in the fit. Thus this power law form of the distribution requires the cutoff as an additional parameter. Alternatively, upon inspection of the binned data in Fig. 4.5 it is apparent that the data would be fit very well by a power law with a break above 1.3 \AA . However, we feel that unless some physical model can predict one of these forms, the data do not currently justify the additional parameters.

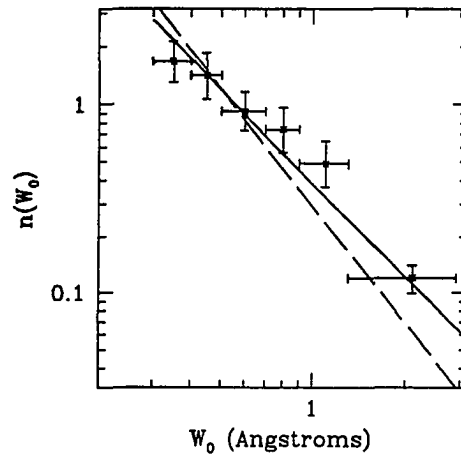


Figure 4.5: The distribution of equivalent widths for sample MG1 of SS is shown, binned for display purposes. The curves are the maximum likelihood fits of the distribution $n(W) = CW^{-\delta}$ to the unbinned data. The solid line is fit with an upper cutoff of 3.3 \AA and the dashed line is fit with no upper cutoff.

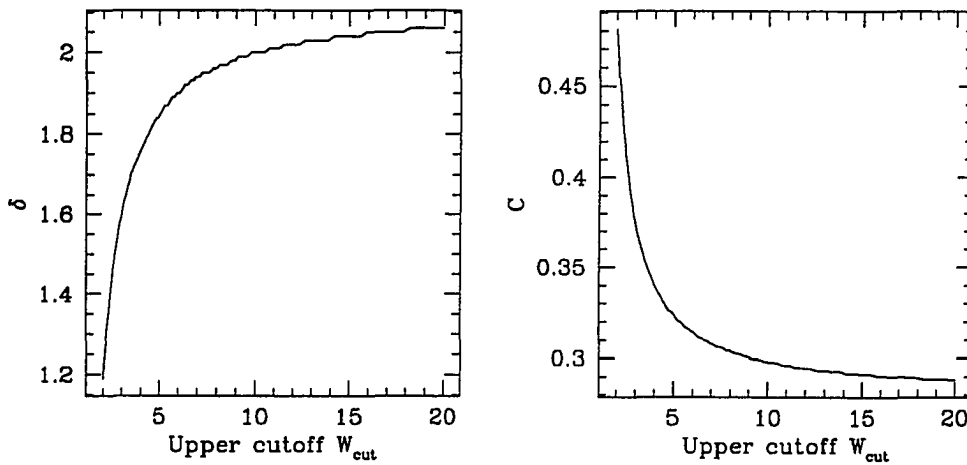


Figure 4.6: Power law distribution function parameters C and δ as a function of the upper cutoff W_{cut} used in the maximum likelihood fitting.

The form of $n(z)$ is simply

$$n(z) = N_0(1+z)^\gamma, \quad (4.9)$$

where N_0 is often called $\left(\frac{dN}{dz}\right)_0$. N_0 represents the linear density of absorbers at zero redshift. This distribution function is only well-defined for a uniform sample and is a strong function of the equivalent width limit W_0 . Once the functional parameters for $n(z, W)$ are determined, we have

$$n(z) = \int_{W_0}^{\infty} n(z, W) dW$$

Unfortunately, because the uncertainty on the redshift evolution parameter γ is generally large, the uncertainty on N_0 is correspondingly large.

The results of our statistical analysis of our sample of 56 quasars are given in Table 4.4. Here N_{obs} is the number of observed lines. \mathcal{Z} is the redshift path length for the sample, $\langle z \rangle$ is the average redshift of absorbers in the sample, $\langle N(z) \rangle$ is the average number of absorbers per unit redshift, and $\gamma_0, W_0^*, \text{ and } N_0^*$ are the best fit values for the model parameters given in Eqns. 4.4, 4.8, and 4.9.

We have calculated the distribution parameters for a number of different subsamples of our data as well as the large data set of SS and SSB1. The samples are defined as follows:

- | | |
|---------|---|
| A | Our entire sample, analyzed using an array of W_0 limits. Parameters which depend on a uniform equivalent width limit are not calculated. |
| A2,3 | Lines in our sample which are in S(0.6 Å) and S(1.0 Å), respectively. |
| MG1,2,3 | Lines from SS and SSB1 which are in S(0.3 Å), S(0.6 Å), and S(1.0 Å), respectively. |
| MG | MG2 + MG3 |
| A-MG | Sample A, with regions in MG excluded. This sample is thus independent of the SS and SSB1 data. |
| A+MG | Sample A combined with sample MG. In the case of overlapping regions in the same QSO, the MG data are used. |
- Samples MG2 and MG3 were assembled from the published tables and plots of

Table 4.4: Results of statistical analysis

Sample	N_{obs}	\mathcal{Z}	$\langle z \rangle$	$\langle N(z) \rangle$	γ_0	W_0^*	N_0^*
A	20	...	1.00	...	1.41 ± 1.00	0.62 ± 0.13	1.42 ± 0.22^a
A+MG	89	...	1.13	...	1.21 ± 0.42	0.65 ± 0.07	1.47 ± 0.14^a
A-MG	15	...	0.93	...	0.98 ± 1.16	0.56 ± 0.13	1.40 ± 0.27^a
A2	16	26.6	1.03	0.60 ± 0.15	1.87 ± 1.20	0.58 ± 0.14	1.71 ± 0.62
MG1	111	114.2 ^b	1.12	0.97 ± 0.10^b	0.78 ± 0.42^b	0.60 ± 0.06	1.55 ± 0.20^b
A2+MG2	82	153.3	1.13	0.53 ± 0.06	1.11 ± 0.46	0.64 ± 0.07	1.36 ± 0.21
A2-MG	12	21.2	0.93	0.57 ± 0.16	2.07 ± 1.42	0.53 ± 0.13	1.77 ± 0.77
MG2	70	132.0	1.14	0.53 ± 0.06	1.04 ± 0.49	0.66 ± 0.08	1.31 ± 0.21
A3	8	31.9	0.98	0.25 ± 0.09	1.26 ± 1.64	0.62 ± 0.22	1.26 ± 0.84
A3+MG3	45	161.0	1.26	0.28 ± 0.04	2.37 ± 0.67	0.68 ± 0.10	1.22 ± 0.32
MG3	39	134.6	1.31	0.29 ± 0.05	2.58 ± 0.73	0.70 ± 0.11	1.22 ± 0.34

^aCalculated using approximate formula described in text.

^bTaken directly from SS and not calculated with our software.

equivalent width detection limits in SS and SSB1. These samples were then analyzed in exactly the same way as our own data. For sample MG1, determining the regions which comprise $\mathcal{S}(0.3 \text{ \AA})$ from the published plots is much more difficult. Since our sample has a small redshift path length at this limit, there is little point in combining our data with MG1 for redshift evolution calculations. However, the equivalent width distribution calculations can be done using only the line lists.

In Fig. 4.7 we plot the observed values of $n(W)$, binned for display purposes. This plot is an important diagnostic to verify that the “black box” maximum likelihood fitting is indeed giving reasonable results. The solid line in the figure is the plot of $n(W)$ using the form in Eqn. 4.8 and the values for N^* and W^* given in the last row of Table 4.4. The dashed line is the same function using the values derived by SS of $N^* = 1.55 \pm 0.20$ and $W^* = 0.66 \pm 0.11$. Although our values are somewhat lower than found by SS, they are clearly consistent within the uncertainties.

As in the previous discussions, the calculation of the binned values of $n(W)$ is not straightforward in the case that the spectra have very different equivalent width limits. The method we used is an approximation, but in the cases where we can check

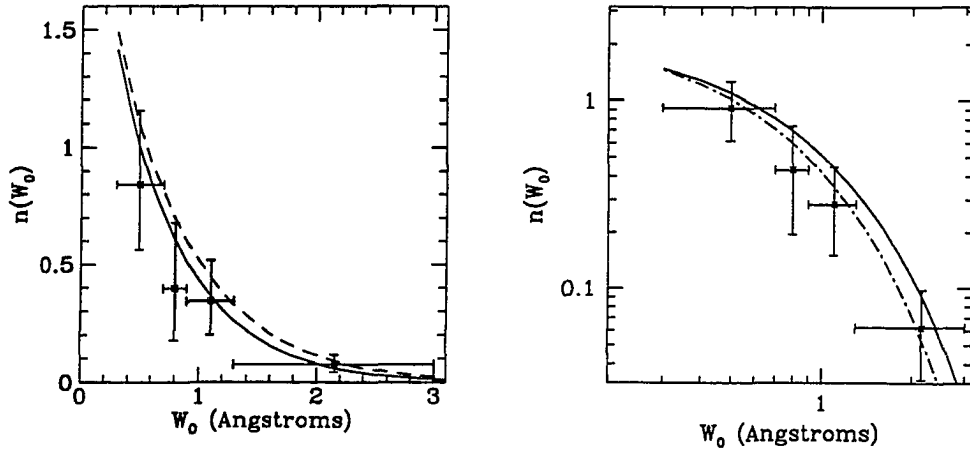


Figure 4.7: Number of absorbers per unit equivalent width. The solid line is the maximum likelihood fit to our data for $n(W)$ and the dashed line is the best fit curve given by SS. The same data are plotted in linear and logarithmic axes.

the results it gives good agreement.

Define $\mathcal{N}(\mathcal{W}_a, \mathcal{W}_b)$ to be the number of absorbers in $\mathcal{S}(\mathcal{W}_a)$ with $\mathcal{W}_a \leq W_i < \mathcal{W}_b$. Then the binned distribution $n(\mathcal{W}_a, \mathcal{W}_b)$ is just

$$n(\mathcal{W}_a, \mathcal{W}_b) = \frac{\mathcal{N}(\mathcal{W}_a, \mathcal{W}_b)}{\mathcal{Z}(\mathcal{W}_a)(\mathcal{W}_b - \mathcal{W}_a)}.$$

Recall that $\mathcal{Z}(\mathcal{W}_a)$ is defined by Eqn. 4.3. However, some absorbers near the detection limit with $\mathcal{W}_a \leq W_i < \mathcal{W}_b$ may not be in $\mathcal{S}(\mathcal{W}_a)$. We can make maximum use of available data by dividing $(\mathcal{W}_a, \mathcal{W}_b)$ into N_W subregions defined by $w_i = i(\mathcal{W}_b - \mathcal{W}_a)/N_W + \mathcal{W}_a$ and approximating

$$n(\mathcal{W}_a, \mathcal{W}_b) = \frac{1}{N_W} \sum_{i=1}^{N_W} n(w_{i-1}, w_i).$$

If we make N_W large enough then $\mathcal{N}(w_{i-1}, w_i)$ will be either 0 or 1 and we can replace

the above equation by a sum over all the N lines detected in the spectra, giving

$$n(\mathcal{W}_a, \mathcal{W}_b) = \sum_{i=1}^N \frac{\delta(\mathcal{W}_a \leq W_i < \mathcal{W}_b)}{\mathcal{Z}(W_i)(\mathcal{W}_b - \mathcal{W}_a)}.$$

The fractional uncertainty in this quantity is given by the standard counting statistics (Poisson deviations) on the number of lines with $\mathcal{W}_a \leq W_i < \mathcal{W}_b$.

4.6 Discussion

The primary conclusion we draw from our new sample is that it is statistically consistent in all cases with the larger sample of SS and SSB1. In all cases our independent samples (such as A-MG) give redshift and equivalent width distribution parameter values which are consistent with SS and SSB1, but with larger uncertainties. By combining our new data with the published data, we have reduced the uncertainties in the distribution parameters, in most cases by 10 - 20%.

The value of γ_0 is clearly seen to be a function of the sample equivalent width limit. For the 0.3 Å (MG1) and 0.6 Å samples (MG2 and A2), the distribution of absorber redshifts is consistent with no evolution in galaxy number density and cross-section, for $q_0 = 0$ to 0.5. However, the strong absorbers in the 1.0 Å samples (MG3 and A3) are inconsistent with no evolution at 2- to 3- σ , in the sense that the overall cross-section was larger in the past. There are many factors which can determine the absorption cross-section, including physical size, filling factor, galaxy number density, galaxy kinematics, and overall ionizing radiation field. Thus interpretation of evolution is difficult, especially because the extended gaseous halos are so poorly understood. However, SS give one possible scenario in which the halo gas is infalling from the intergalactic medium. The strongest absorbers (the ones which evolve) are those near the disk for which the dynamical time scale for infall is shortest.

The value of the equivalent width distribution parameter W_0^* is independent of equivalent width limit for all of the samples. As we have mentioned, the equivalent width of MgII absorbers is most directly determined by the velocity profile and number of individual absorbing components. Thus measuring the distribution is

mostly a study of galaxy kinematics. The physical motivation for the form $n(W) = N^*/W^* \exp(-W/W^*)$ is not well established.

Chapter 5

Conclusion

In Part I of the thesis we discussed the theoretical considerations, design, fabrication, and experimental testing of vibration isolation systems for use in gravitational radiation detectors. From a theoretical standpoint the most important results dealt with evaluating the efficiency of particular spring designs (in particular the dimensionless constants which characterize the distribution of stress and compliance within the spring) and fundamental limitations on passive isolation. The latter result points out the difficulty in achieving isolation over very wide bandpasses, as is necessary for laser interferometers. There are several possible strategies for wide-band isolation, including active systems, cascading isolators optimized for different frequencies, and de-tuning the spring internal resonances. Active isolation in six-DOF is a very interesting problem in control theory; however it is not clear if this technique can be usefully applied to gravity wave isolators. De-tuning the spring resonances can be successful in simple one-dimensional models, but application to complex six-DOF isolators is questionable. Cascading isolators is thus the best solution.

Experimentally, we were able to model very accurately the dynamical properties of the suspension isolation system. There had been concern that we would have difficulty fully understanding these complex isolators, but at this point those fears are laid to rest. An important implication of our success is that we can design and fabricate isolators with very little prototyping and iteration. This has been done for an isolator designed for testing the thin-film niobium transducer under development

at Stanford. We are also able to quantify with much more accuracy and confidence the actual performance of the isolation system.

As an epilogue to Part I, at the present time all four suspension isolators have been fabricated, as well as all the associated suspension parts. The cryostat which will house the entire structure is essentially done and has been successfully cold shocked and leak tested. The assembly of the antenna and its suspension system and integration into the cryostat is then the next order of business.

In Part II of the thesis, I switched gears and took up the study of QSO heavy-element absorption systems in order to learn about high-redshift galaxies. This work was done in collaboration with professors from Steward Observatory (University of Arizona) and the Center for Astrophysics (Harvard).

Chapter 2 was devoted to a general overview of the empirical properties of absorption line systems and included some of the necessary background to put these properties in context. We showed the evidence which establishes that the QSO heavy-element absorption lines are due to intervening gas-rich galaxies.

In Chapter 3 we assembled a sample of lobe-dominated quasars (wherein the extended radio emission in the lobes dominates the core emission) with Mg II absorbers. This sample will allow the use of different lines of sight between optical and radio components to investigate physical properties of moderate redshift galaxy halos and interstellar disk clouds. The method for defining this sample was given, and we also gave a detailed description of our upcoming 21 cm observations to take place at the Green Bank 140' telescope in November 1993.

In Chapter 4 we described observations, line extraction techniques, and statistical analysis of 56 quasars which were taken from the work in Chapter 3. Our conclusion is that the redshift and equivalent width distributions of the new spectra are consistent with previously obtained results in the literature. The redshift distribution is consistent with no evolution of absorber properties, except for the strongest absorption systems, which have a larger cross-section in the past.

Appendix A

Findsl – A program for QSO absorption line analysis

Findsl is a part of a package of programs for QSO absorption line analysis which total over 8000 lines of FORTRAN and C code. It features a graphical user interface, including standard tools such as continuum fitting, finding significant lines, multi-component gaussian fitting, and line identification facilities. In addition it has routines to plot statistics of deviations from the continuum, to assure that the error array and continuum fit are reasonable. The program allows for simple ASCII data files for input of the spectrum, but then uses for storage a FITS binary table file, which is both much faster to read/write and more flexible. Parameters controlling the **findsl** analysis for each spectrum are stored in free format parameter files. These provide a record of the analysis and are useful when a large number of spectra are being processed.

In sum, most features which the author felt would be useful and expedient in doing absorption line extraction were implemented. A fair amount of effort was put into making the code modular and readable, so future improvements should be possible.

As was mentioned, **findsl** is part of a package intended to take a set of reduced spectra (possibly quite inhomegenous) and produce plots and statistically complete line lists, all in photo-ready form for publishing.

A.1 Building and installing

`Findsl` consists of a number of FORTRAN and C programs, which are linked with SM¹ (formerly SuperMongo) and FITSIO² with the supplied makefile. To build the program, edit the file `Makefile` and change the first two lines to correctly specify where the needed libraries reside. Then type `make`. See the SM manual if there are problems in linking with SM or the X11 libraries. Finally, you should make an alias for the executable and insert this in your `.cshrc` file or else include the executable's directory in your search path.

A.2 General Usage

`Findsl` is started from the Unix prompt by typing `findsl prefix`, where the parameter file is named `prefix.par`. It is possible to omit the parameter file name, and you will be prompted for it by the program. The parameter file name can also be specified including the `".par"` extension. Other extension names for the parameter file are not recommended. The format and usage of the parameter file is discussed in detail in Section A.6.

The intended usage of `findsl` is that each object have a separate directory, called by the name of the object. In this directory are the data and parameter files. The parameter file contains detailed information about the spectra and how they have been processed and analyzed. If there are several spectra with identical wavelength solutions, they can be combined and then processed as a single spectrum. For instance, typical data from the Palomar 200" double spectrograph might contain 3 sets of spectra from the blue and red channel. These would then be handled using two `prefix`'s, blue and red.

In addition to the parameter files specific to each object, it is also recommended that you have parameter file called `.findsl.par` in your home directory. This supplies

¹Copyright 1990 Robert Lupton and Patricia Monger.

²Author Dr. William Pence, NASA/GSFC.

defaults for any parameters not found in the local files, and is especially useful for specifying the plot device, the comparison line and bad region files, and the standard continuum fitting and line identification parameters.

After `findsl` has successfully read the parameter file, it attempts to open the FITS file specified by the `datafile` parameter. This file contains in binary table format all the detailed information used in analysis with `findsl`. This includes the processed spectrum, original (raw) spectrum, continuum, and several status bits for each pixel. If it is unable to find the FITS file, the program will look for the ASCII data file specified by the `fs1.infil` parameter. This format provides a simple means of supplying spectra to `findsl` without dealing with FITS files. However, `findsl` writes data exclusively in FITS format.

Once the spectrum has been read the program gives some basic information about the spectrum and it is displayed in the graphics window. Note that often (for unknown reasons) the initial plot when `findsl` starts is not completely drawn. Simply hit "r" to redraw it. The program is controlled primarily by single keystroke commands, issued with the mouse in the graphics window. `Findsl` is ready for such a command when it displays a crosshair in the window and has issued a prompt in the text window. If you attempt to type at other times, the results are unpredictable. In particular, if you type a command and you see the letter echoed to the screen, *but the command is not executed*, then move the mouse into the text window and hit the delete key several times. Otherwise the program will likely crash the next time you do any numeric input. This is the fault of FORTRAN.

The many commands available in `findsl` are divided into several functional categories – Continuum fitting; Plot manipulation; Line identification and fitting; Spectrum manipulation; and Miscellaneous. The miscellaneous commands require only one keystroke, while the rest require a single prefix keystroke followed by the command. A number of commands then need subsequent input as indicated by prompts in the text window. With few (or no) exceptions, if the subsequent input can be uniquely specified with a single keystroke, then the cursor should remain as a crosshair in the graphics window and you just type the one key. Otherwise (for instance, when a number or filename must be entered) the crosshair turns into an arrow and you must

move it into the text window before you can type. The program beeps annoyingly if you do not.

A number of commands in `findsl` require that you specify with the mouse cursor a range of points or a repeated series of points. Examples include `Zoom` and `pan` current plot window and `List EW` between cursor positions. In all cases, the positions must always be specified from left to right. In addition, any commands dealing with line doublets assume that you are specifying the lower wavelength member.

A.3 Command summary

Here we give a summary of the commands available in `findsl`. This is identical to the information given by the help command (“h”).

Miscellaneous commands (no prefix)

- c: Identify CIV line and do not record in SL list
- h: Print one line summary of commands
- i: Identify a line and do not record in SL list
- m: Identify MgII line and do not record in SL list
- n: No trial redshift for comparison lines
- o: Print current cursor coordinates
- q: Quit program
- r: Refresh current plot
- t: Enter trial redshift for comparison lines
- u: Toggle flag for plotting continuum
- w: Write data (spectrum and sig. lines) to files
- x: Expand x range of current plot window (pan out)
- z: Zoom and pan current plot window

f: Continuum fitting commands

- f: Fit continuum
- p: Set continuum fit parameters

l: Line commands

- c: Identify CIV line and record in SL list
- e: List EW between cursor positions
- f: Find all significant lines (destroy current ones)
- g: Fit gaussians to spectrum and give line stats
- i: Identify a line and record in SL list
- l: List significant lines
- m: Identify MgII line and record in SL list
- n: Add a night sky line at cursor position
- r: Recalc. gauss. fits and equiv. widths for SL list
- s: Add/delete a significant line at cursor position
- u: Unidentify a line and record in SL list

p: Plot commands

- b: Plot spectrum smoothed with boxcar or PSF
- c: Change plot characteristics
- d: Plot local χ^2 versus wavelength
- e: Plot equivalent width
- f: Save current plot in postscript file
- g: Plot statistics of deviations
- n: Plot spectrum normalized to continuum
- p: Send current plot to printer
- s: Plot current spectrum
- x: Change x-axis limits
- y: Change y-axis limits

s: Spectrum manipulation commands

- b: Set bad regions of spectrum
- c: Set continuum manually
- l: Set pixels which are part of a significant line

- o: Restore original spectrum
- s: Set spectrum to cursor values or delete
- u: Scale uncertainty so $\chi^2 = 1$

A.4 Command descriptions

A.4.1 Miscellaneous commands – no prefix

These commands require no prefix. The “miscellaneous” commands might also be called “most common” commands, since many of them are in this section because they are used frequently and it is desirable to execute them with only one keystroke.

Graphical

r: Refresh current plot

Redraws the current plot. This is especially useful since SM's X-window driver is lazy and does not redraw the screen when part of it is uncovered.

u: Toggle flag for plotting continuum

Toggles the flag controlling whether or not the continuum fit is plotted. This is equivalent to setting the appropriate plot characteristic in the plot commands section.

x: Expand x range of current plot window (pan out)

Expands by a factor of two the current wavelength range displayed. This in effect pans out. The y-axis is autoscaled within the new window.

z: Zoom and pan current plot window

Allows for zooming in on a region of the plot, or else panning out to the full plot. If panning is desired, the second keystroke must be “p”. For zooming, the first “z” keystroke defines the lower-left corner and the second “z” defines the upper-right

corner.

Lines and identifications

c: Identify CIV line and do not record in SL list

i: Identify a line and do not record in SL list

m: Identify MgII line and do not record in SL list

This sets the current `trial_z` so that the identified line is at the current cursor position. In the case of doublets, the lower wavelength member of the doublet is used. With `trial_z` set, the comparison lines will be displayed at that redshift. Although the `trial_z` will snap to a nearby significant line, the identifications are NOT recorded in the significant line list. These commands are for testing possible identifications.

n: No trial redshift for comparison lines

Turn off the comparison lines. This is equivalent to (but faster than) setting `trial_z` = 0.0 with the "t" command.

t: Enter trial redshift for comparison lines

Manually set the trial redshift (`trial_z`) and display comparison lines at that redshift. If the entered value is 0.0, no lines are shown. If galactic or zero redshift lines are desired, then enter a very small non-zero number.

Misc. and I/O

h: Print one line summary of commands

Print help, which is a one line summary of commands. It is also possible to get help on just one section of commands by typing the command prefix and then "h".

o: Print current cursor coordinates

Print the x-y coordinates at the current cursor position.

q: Quit program

Quit `findsl`, with options to save the spectrum and significant line files.

w: Write data (spectrum and sig. lines) to files

Save current spectrum and significant line files to disk.

A.4.2 Spectrum manipulation commands – Prefix “s”

This section contains commands that modify the current spectrum values and characteristics on a pixel by pixel basis. The “spectrum” is actually internally represented by 10 arrays, each containing the number of pixels of the originally input spectrum.

The arrays are:

- x** The wavelength of each pixel. This is never modified.
- yo, so** The original input spectrum and error arrays. These are never modified.
- y, c, s** The current spectrum, continuum, and error arrays. These can be changed by the spectrum manipulation commands. Examples include setting the continuum manually, editing bad pixels, rescaling the error array, and so on. One can always restore the original spectrum with the “o” command in this section.
- ys, cs, ss** The plot spectrum, continuum, and error arrays. These are the arrays that are used in any displayed spectrum plot, and are generally set by routines in the “plot” commands. For instance, if you plot the normalized spectrum, the normalized values are calculated and stored in these arrays. Unlike the previous arrays, these are not saved to disk.
- flg** An integer array containing logical status bits for each pixel. These are modified by the commands in this section and affect the plotted color of pixels, whether they are searched for significant lines, and whether they are used in calculations such as continuum fitting and χ^2 deviation.

The logical status bits are:

BadPixel	Bad pixel. Displayed in Magenta; not used in any calculations; not searched for significant lines.
SLPixel	Possibly part of significant line. Displayed in blue; not used in calculations; searched for significant lines.
Deleted	Deleted pixel. Not displayed; not used in calculations; not searched for significant lines.
ContFrozen	The continuum has been set by user and is frozen so that subsequent continuum fits can not change this pixel.
NightSkyLine	This is identified as a night sky line. This puts a NS symbol on the plot at pixel position, but doesn't affect calculations or significant line searching. The region around NS line should be marked as bad.

b: Set bad regions of spectrum

Set or unset regions of the spectrum which are unsuitable for continuum fitting or significant line searches, but should still be displayed (**BadPixel** bit). Useful for bad night sky subtraction and O₂ bands. The affected region is marked by the cursor positions when the "b" and the "s" (to set) or "u" (to unset) keys are pressed. This command is not repetitive.

c: Set continuum manually

This allows the continuum to be set manually with the cursor in regions where the automatic fitting routine has failed. This normally happens near QSO emission features. The initial "c" marks the first point or the beginning of the affected region. The available options are then "s" to set continuum (by linear interpolation from last point to current cursor position), "u" to unfreeze the continuum in affected region, or "q" to quit continuum setting mode. This command is repetitive, so a smooth curve can be drawn with many "s" keystrokes.

l: Set pixels which are part of a significant line

Set or unset pixels in marked region to be potentially part of a significant line (**SLPixel** bit). The region is marked by the cursor position at the "l" and the "s" (to

set) or “u” (to unset) keystrokes. This command is not repetitive.

o: Restore original spectrum

Copy the original spectrum (in the `yo` and `so` arrays) to the current spectrum and clear all logical status bits.

s: Set spectrum to cursor values or delete

Manually set spectrum values by linear interpolation between cursor positions or delete/undelete pixels in marked region. The initial “s” keypress marks the first point (for setting) or the left side of the region (for deleting). After this you have the option of “s” to repeatedly set spectrum by linear interpolation, “d” to mark as deleted the region (set Deleted bit) or “u” to restore points in the deleted region.

u: Scale uncertainty so $\chi^2 = 1$

Calculate the χ^2_{ν} (deviation squared per degree of freedom) and rescale the error array so that it is unity. Only good pixels (`BadPixel`, `SLPixel`, and `Deleted` all false) are used. In the case where most of the spectrum is continuum with only sparse absorption lines (i.e. typical metal line systems, as opposed to the Ly- α forest) this can give a better estimate of the true error array, depending on your confidence in the detector noise characteristics. Experience with Palomar 200” and MMT data shows that χ^2_{ν} often ranges from 0.6 - 2.0, while formally for 1000 points it must be very near 1.0 if the error array is correct. See also the `plot gaussian deviations` command.

A.4.3 Plot commands – prefix “p”

b: Plot spectrum smoothed with boxcar or PSF

Plot spectrum smoothed by a boxcar filter or by the instrumental PSF. The latter option is selected by inputting a negative radius for the boxcar filter. The error array is adjusted accordingly.

c: Change plot characteristics

Toggle one of the following local characteristics which control the plot layout and which curves are drawn. Pressing the single digit identifier does the toggle.

- 0 - Label object name
- 1 - Label file name
- 2 - Label quasar z
- 3 - Label smooth radius
- 4 - Plot significant lines
- 5 - Plot night sky lines
- 6 - Plot one-sigma curves
- 7 - Plot siglim curves
- 8 - Plot continuum fit
- 9 - Plot baseline

d: Plot local χ^2 versus wavelength

Plots the local χ^2_{ν} versus wavelength. The spectrum is divided into regions which are `splall.nsmooth` pixels wide and the χ^2_{ν} is calculated in each regions. This plot is useful for discovering where the continuum fitting or spectrum is bad. Only good pixels are used.

e: Plot equivalent width

Plots the calculated equivalent width in Angstroms versus wavelength. This is useful with the siglim curves plotted, to show which lines are considered significant.

f: Save current plot in postscript file

Saves the current plot in a postscript file. User can select the default filename provided by entering "d" at the prompt, or else type a different filename. Any existing file with the same name will be overwritten. This option requires that you have somewhere a modified version of the default SM graphcap file which includes the following entry:

```
postl_file| write normal postscript in landscape mode to file $1: \
      :SY=mv $F $1:tc=postland:
```

You can copy the SM default `graphcap` (whose location is specified by your `.smongo` setup file) into your own directory and make this change, or else have your system manager add this entry.

g: Plot statistics of deviations

Plots a histogram of number count of pixels versus deviation squared ($[(y(i) - c(i))/s(i)]^2$, where $y(i)$, $c(i)$, and $s(i)$ are the spectrum, continuum, and uncertainty). Negative deviations are to the left and positive deviations are on the right. The y-axis is logarithmic, so that if the noise is actually gaussian one should see a linear drop on each side which follows the true gaussian distribution plotted in red. This is useful for spotting systematic trends in the data such as bad cosmic ray subtraction, bad continuum fitting, fringing, inaccurate estimate of detector noise, or even the Ly- α forest! On the negative deviations side one typically sees the cutoff at 3σ where pixels are rejected during continuum fitting.

n: Plot spectrum normalized to continuum

Plot spectrum normalized to continuum.

p: Send current plot to printer

Print current plot in landscape mode. This gives a fairly faithful reproduction of the screen, assuming the graphics window aspect ratio is around 2.7:1.

s: Plot current spectrum

Plot current spectrum, removing any smoothing and zooming to include the entire spectrum. This also turns off the display of a gaussian line fit if one was generated.

x: Change x-axis limits

y: Change y-axis limits

These options allow manual entry of x and y axis limits. If the lower limit given is greater than the upper limit, then autoscaling is enabled for that axis.

A.4.4 Continuum fitting commands – Prefix “f”

f: Fit continuum

Fit continuum using a simple cubic spline fitting routine. As usual, only good points are used in fit. First the spectrum is divided into `nsmooth` wide bins and averaged in each bin. `Nsmooth` is initially set to the value of the parameter `splall.nsmooth`. Then a cubic spline is fit to these averaged points. Points which deviate negatively by more than `splall.siglim` standard deviations are flagged as possible significant lines and rejected for subsequent iterations of the fit. This process is repeated `splall.niter` times. Generally the fit doesn't change after 2 to 3 iterations. The smoothing value can be changed interactively using the “p” command. There is also a facility in the program to change the bin width locally depending on the magnitude of the second derivative of the continuum fit. In theory this should allow better fitting of emission features, but in practice it seems easier to hand fit these regions.

p: Set continuum fit parameters

Interactively change fitting parameters. `Nsmooth` is the number of bins which are averaged before doing a spline fit to derive the continuum. `Dscale` is the feedback parameter controlling the increase in density of averaging bins. The exact relationship is given by

$$\text{binsize} = \text{nsmooth} \left(1 + \text{dscale} \cdot \left| \frac{d^2 c(i)}{di^2} \right| \right)^{-1},$$

where $c(i)$ is the continuum at pixel i . This simple formalism helps somewhat in fitting QSO emission features, but it is recommended that `dscale` be set to zero.

A.4.5 Finding and identifying significant lines – Prefix “l”

This section contains commands for finding and identifying the significant absorption lines. The details of the automatic line finding routine, various algorithms for calculating equivalent width, and the data contained in the significant line lists are described under the “f” command.

-
- c:** Identify CIV line and record in SL list
 - i:** Identify a line and record in SL list
 - m:** Identify MgII line and record in SL list

These commands are identical to those in the Miscellaneous section except that the identifications are recorded in the significant line list if a line is found near the cursor. Note that the program does not currently support multiply identified lines (i.e. blends of distinct absorption systems). You can fake it by editing the SL file and putting in the multiple identifications. The line listing program (`linelist`) will correctly deal with them.

-
- e:** List EW between cursor positions and record in SL list

Calculates the EW and weighted wavelength mean using the “definition” algorithm (see “f” command). If the wavelength is near a significant line, the values are recorded in the significant line list.

-
- f:** Find all significant lines (destroy current ones)

The automatic line identification routine proceeds as follows. The optimally extracted “PSF” observed equivalent width EW_p and uncertainty $\sigma(EW_p)$ are calculated by convolution of the spectrograph PSF with the spectrum. This is following the method outlined by Schneider et al. (199?) from the HST Quasar Absorption Line Key Project. Using the PSF gives an optimal extraction so long as the lines are not highly resolved. The line detection criterion is that the significance level satisfies $EW/\sigma(EW) > \text{fsl.siglim}$.

Once the spectrum has been processed and all significant lines found, two more estimates of the EW of each line are made. First, the gaussian EW and error are found by a gaussian fit with three free parameters (area, width, and center wavelength). If adjacent significant lines are within a specified distance, then the gaussian components for all the lines are fit simultaneously. Second, the definition EW by calculating $EW = \sum_i (y(i)/c(i) - 1)d\lambda(i)$, using the gaussian FWHM to determine the limits and integrate over 95% of the line absorption. The corresponding central

wavelength is a weighted mean over the line profile. This second method gives a better estimate of the line parameters for asymmetric lines, but is inadequate if lines are blended.

Thus for each significant line, the following set of numbers is calculated three different ways:

$$\lambda \quad \sigma(\lambda) \quad EW \quad \sigma(EW) \quad SL \quad FWHM \quad \sigma(FWHM)$$

SL is the significance level, defined as $EW/\sigma(EW)$. These values are all recorded in the significant line list. Also included are the estimated line velocity width in km sec^{-1} and χ^2_ν of the gaussian fit. In addition, when a line is identified, the corresponding redshifts are calculated. All this information can be listed by executing the "l" command.

g: Fit gaussians to spectrum and give line stats

Simultaneously fit up to 9 gaussian components to spectrum. After selecting this command, you interactively specify the initial guess at the gaussians with the graphical cursor. The program then performs a non-linear least-squares fit. You can only do fitting when the regular spectrum is currently plotted (e.g. not the equivalent width or normalized spectrum).

There are two separate modes for this command which should probably be initiated with different keystrokes, but for now you are responsible for using the two modes properly.

In the first mode the gaussian parameters are all varied independently. Following the prompts, you mark your initial guess at the peak and center, and then the half-width at half-maximum (HWHM). For each of these you can choose to fit for the parameter by hitting the spacebar or fix the parameter at the initial guess by hitting "f". In addition, for the HWHM you can hit "s" to fix the width to the spectral resolution. After the guesses have been given, you are asked to mark the left and right sides of the fit region. Note that the continuum is taken as the zero level so it is not always necessary to include a large region outside the gaussian.

The second mode is for fitting doublets of a particular species. In this mode the line wavelength ratios are fixed and the gaussian widths are constrained to be equal. You can fit multiple components but you are limited to doublets of the same species.

Thus an MgII doublet blended with another single line cannot currently be fit in this mode. The initial guess for the left hand member of the doublet is specified as described above for independent lines. You can still fix values or use the spectral resolution. Then when marking the wavelength center and peak of the right hand member, hit "m" for MgII, "c" for CIV, or "n" for NaI. The HWHM is irrelevant, but be sure to move the cursor before hitting a key. When fitting multiple components, the order of specifying the lines is important (left, then right of one doublet, then to the next doublet). In doublet mode, the uncertainties of the dependent parameters are set to zero. This makes it clear how the fit was done.

After fitting, the calculated fit is plotted in green on top of the spectrum. It will continue to be plotted until you plot a different kind of spectrum or issue the plot spectrum command ("ps").

If a significant line is found near the fitted center wavelength, the gaussian components will be updated to the new values. An important exception to this is that if the line has been identified already, the redshift of the absorber is currently NOT updated. This only happens if you identify again the line. This will be changed in a future version. The program which produces the final line lists recomputes the redshift anyway, so this is not a terrible problem.

l: List significant lines

For each line the PSF, definition, and gaussian values are listed, in that order. At the end of the long format list, a summary of the significant lines is given. The values listed here are generated by selecting and averaging various combinations of the detailed numbers, and are by no means meant to be accurate final numbers.

n: Add a night sky line at cursor position

Mark the pixel at the cursor position to be a badly subtracted night sky line. Make sure to zoom in enough so that you are resolving the pixels on the screen and can mark the peak. Note also that this is for display purposes only and the region should be marked as bad as well.

r: Recalc. gauss. fits and equiv. widths for SL list

Given the current line list, this routine recalculates the gaussian and definition line parameters, exactly as in the original line finding algorithm. Watch out if you have carefully hand-fit any gaussians, as this information will be overwritten.

s: Add/delete a significant line at cursor position

Manually add a significant line which was not found by the automatic line finding algorithm, at the cursor position. The PSF line values are taken from the spectrum at the exact position specified (no peak finding as in automatic algorithm). The gaussian and definition line values are supposed to be calculated automatically, but are currently left blank and must be hand-fit with "g" and "e". This will be fixed. If this command is executed at the position of an existing line, then the line is deleted.

u: Unidentify a line and record in SL list

Remove the line identification for the line near the cursor, but leave it in the significant line list.

A.5 Spectrum file data format

The spectrum can be input to `findsl` in one of two formats, either as a simple ASCII data file in column format, or as a FITS binary table. The latter is much faster and more flexible, but more difficult in simple applications. Should you wish to write a program to deal with the output spectra produced by `findsl`, the simplest course is to copy and modify the `read_spec()` and `write_data()` routines in `findsl_IO.F`. The FITSIO package which is used and its documentation are available by anonymous ftp from `tetra.gsfc.nasa.gov` in directory `/pub/fitsio3`.

The ASCII data format for the spectrum is very simple and consists of a single line for each pixel containing the follow fields separated by spaces: `x y s c flg`. These are, respectively, wavelength, spectrum value, $1-\sigma$ uncertainty, continuum, and status flag. The last two fields are there primarily for backwards compatibility with

old program versions and can be set to zero. The input is FORTRAN free format, so spacing is not important, but all fields must have an entry.

A.6 Parameter file keywords

The parameter file keywords and their values provide general information needed for every spectrum (such as file names for various input and output functions) as well as information specific to each spectrum (such as instrumental FWHM and object name). They are read as FORTRAN free format into strings. This has the important consequence that any values starting with a numeric digit (such as 3C196) must be enclosed in quotes or the program crashes. This is a ridiculous feature of FORTRAN, but not too hard to live with. In the parameter file, any line beginning with “!” is ignored, so you can group logically connected keywords or give comments. In addition, any text after the keyword and value is ignored. In Table A.1 we list all the valid keywords, as well as their normal usage, default value, and description. The normal usage is divided into three categories: “Req’d” for required; “Supp’d” for normally supplied, meaning that in most cases this is different from spectrum to spectrum; and “Omit’d” for normally omitted. The last value means that the default value in your *.findsl.def* will usually suffice, or else that *findsl* will generate the normal default. In the default column, *prefix* refers to the prefix of the specified parameter file *prefix.par*. The *convert* group of keywords are used by other programs which combine spectra and write the output in the ASCII data format. Those programs are unsophisticated in choosing defaults and so all parameters are required.

Table A.1: Parameter file keywords

Keyword	Usage	Default	Description
<code>plotdev</code>	Omit'd		Interactive graphics plotting device which is used by SuperMongo. This has been thoroughly tested for the 'X11' device, and 'xterm' is known to have problems with keyboard input.
<code>dispcor</code>	Omit'd	'air'	Medium for which the wavelength solution was generated. Legal values are 'air' or 'vacuum'.
<code>fwhm</code>	Req'd		Full width at half maximum of the instrumental PSF in the wavelength direction.
<code>fwhm_units</code>	Supp'd	'angstroms'	Units in which the FWHM is specified. Legal values are 'angstroms' or 'pixels'.
<code>qso_z</code>	Req'd		Emission redshift of the QSO.
<code>objname</code>	Supp'd	<i>current dir.</i>	QSO name. Defaults to the name of the subdirectory containing the spectrum.
<code>badfil</code>	Omit'd		Input file containing known bad regions in spectra, <i>e.g.</i> O ₂ bands.
<code>datafile</code>	Omit'd	<i>prefix.fits</i>	Fits file containing complete information on spectrum. This is normally written and updated only by <code>findsl</code> .
<code>compfile</code>	Omit'd		Input file containing comparison QSO absorption lines for identification of absorber redshifts.
<code>plotfile</code>	Omit'd	<i>prefix.ps</i>	Output postscript file for plots.
<code>SLfile</code>	Omit'd	<i>prefix.SL</i>	Output file containing detailed characteristics of identified lines.
<code>SLfile_summ</code>	Omit'd	<i>prefix.SLs</i>	Output file containing summary of line characteristics.
<code>splall.nsmooth</code>	Supp'd		Boxcar smooth radius for cubic spline fitting of continuum.
<code>splall.niter</code>	Supp'd		Number of iterations in sigma-rejection fitting of continuum.
<code>splall.sigma</code>	Supp'd		Rejection factor in continuum fitting. This only applies to negative deviations.
<code>splall.growdiam</code>	Supp'd		Region around a rejected pixel which is also rejected. Specified in terms of the FWHM.
<code>fsl.infil</code>	Omit'd	<i>prefix.dat</i>	Input text datafile in simple format.
<code>fsl.sigma</code>	Supp'd		Minimum significance level for identification of lines.
<code>convert.infil</code>	Req'd		Input data file (FITS or other formats, depending on specific conversion program).
<code>convert.infil2</code>	Omit'd		Optional additional files to be converted and combined.
<code>convert.badfil</code>	Req'd		Input file containing bad wavelength regions.
<code>convert.wstart</code>	Req'd		Start wavelength of conversion.
<code>convert.wend</code>	Req'd		End wavelength of conversion.
<code>convert.normlz</code>	Req'd		Flag specifying whether spectrum should be normalized.
<code>convert.nrmstart</code>	Req'd		Start wavelength for calculating normalization.
<code>convert.nrmend</code>	Req'd		End wavelength for calculating normalization.

Bibliography

- Anders, E. and Grevesse, N. 1989, *Geochim. Cosmochim. Acta*, 53, 197.
- Anderson, S. F., Weymann, R. J., Foltz, C. B., and Chaffee, F. H. 1987, *A.J.*, 94, 279.
- Atwood, B., Baldwin, J. A., and Carswell, R. F. 1985, *Ap.J.*, 292, 58.
- Bahcall, J. N., et al. 1992, *preprint*.
- Bahcall, J. N., Jannuzi, B. T., Schneider, D. P., and Hartig, G. F. 1993, *Ap.J.*, 405, 491.
- Bajaja, E., Cappa de Nicolau, C. E., Cersosimo, J. C., Loiseau, N., Martín, M. C., Morras, R., Olano, C. A., and Pöppel, W. G. L. 1985, *Ap.J.Suppl.*, 58, 143.
- Barthel, P. D., Tytler, D. R., and Thomson, B. 1990, *Astr.Ap.Suppl.*, 82, 339.
- Bechtold, J. 1987, in *High Redshift and Primeval Galaxies*, eds. J. Bergeron, D. Kunth, B. Rocca-Volmerange, and J. Tran Thanh Van, (Singapore: Editions Frontière).
- Bechtold, J. and Ellingson, E. 1993, *Ap.J.*, 396, 20.
- Bergeron, J. and Boissé, P. 1991, *Astr.Ap.*, 243, 344.
- Bergeron, J., Cristiani, S., and Shaver, P. A. 1992, *Astr.Ap.*, 257, 417.
- Bloeman, J. B. G. M. 1987, *Ap.J.*, 322, 694.

- Boissé, P. and Bergeron, J. 1985, *Astr.Ap.*, 145, 59.
- Boissé, P., Boulade, O., Kunth, D., Tytler, D., and Vigroux, L. 1992, *Astr.Ap.*, 262, 401.
- Boksenberg, A. and Sargent, W. L. W., 1983, in *Proc. 24th Liège Symposium, Quasars and Gravitational Lenses* (Liège: Institut d'Astrophysique).
- Bregman, J. N. 1980, *Ap.J.*, 236, 577.
- Briggs, F. W. 1988, in *QSO Absorption Lines*, eds. J. C. Blades, D. A. Turnshek, and C. A. Norman (Cambridge: Cambridge Univ. Press), 275.
- Briggs, F. W., Turnshek, D. A., Schaeffer, J., Wolfe, A. M., 1985, *Ap.J.*, 293, 387.
- Briggs, F. W. and Wolfe, A. M. 1983, *Ap.J.*, 268, 76. (BW)
- Briggs, F. H., Turnshek, D. A., Schaeffer, J., and Wolfe, A. M. 1985, *Ap.J.*, 293, 387.
- Briggs, F. H., Wolfe, A. M., Liszt, H. S., Davis, M. M., and Turner, K. L. 1989, *Ap.J.*, 341, 650.
- Brown, R. L., Broderick, J. J., Johnston, K. J., Benson, J. M., Mitchell, K. J., and Waltman, W. B. 1988, *Ap.J.*, 329, 138.
- Brown, R. L. and Mitchell, K. J. 1983, *Ap.J.*, 264, 87.
- Burbidge, E. M. and Kinman, T. D. 1966. *Ap.J.*, 145, 654.
- Burbidge, G., O'Dell, S. C., Roberts, D. H., and Smith, H. E. 1977, *Ap.J.*, 218, 33.
- Carilli, C. L., Perlman, E. S., and Stocke, J. T. 1992, *Ap.J. (Letters)*, 400, L13.
- Carilli, C. L. and Van Gorkom, J. H. 1992, *Ap.J.*, 399, 373.
- Caulet, A. 1989, *Ap.J.*, 340, 90.
- Chaffee, Jr., F. H., Foltz, C. B., Roser, H. J., Weymann, R. J., and Latham, D. W. 1985, *Ap.J.*, 292, 362.

- Charlton, J. C., Salpeter, E. E., and Hogan, C. J. 1993, *Ap.J.*, 402, 493.
- Chevalier, R. A. and Fransson, C. 1984, *Ap.J.*, 279, L43.
- Clark, B. G., 1980, *Astr.Ap.*, 89, 377.
- Cohen, R. D., Beaver, E. A., Junkkarinen, V. T., Barlow, T. A., Lyons, R. W., and Simth, H. E. 1992, *Ap.J.*, submitted.
- Dickey, J. M. and Brinks, E. 1993, *Ap.J.*, 405, 153.
- Field, G. B., Goldsmith, D. W., and Habing, J. J. 1969, *Ap.J.*, 155, L149.
- Foltz, C. B., Chaffee, Jr., F. H., and Wolfe, A. M. 1988, *Ap.J.*, 335, 35.
- Galt, J. A. 1977, *Ap.J. (Letters)*, 214, L9.
- Gregory, P. C. and Condon, J. J. 1991, *Ap.J.Suppl.*, 4, 1011.
- Hall, R. and Lee Jong King 1992, *IEEE Antennas and Propagation Society International Symposium* (New York: IEEE).
- Hartquist, T. W. and Morfill, G. E. 1986, *Ap.J.*, 311, 518.
- Horne, K. D. 1986, *Pub.A.S.P.*, 98, 609.
- Hughes, P. A. ed. 1991, *Beams and Jets in Astrophysics* (Cambridge: Cambridge Univ. Press).
- Hulsbosch, A. N. M. and Wakker, B. P. 1988, *Astr.Ap.Suppl.*, 75, 191.
- Hunstead, R. W. in *QSO Absorption Lines*, eds. J. C. Blades, D. A. Turnshek, and C. A. Norman (Cambridge: Cambridge Univ. Press).
- Jenkins, E. B. 1978a, *Ap.J.*, 219, 845.
- Jenkins, E. B. 1978b, *Ap.J.*, 220, 107.
- Johnston, K. J., Broderick, J. J., Condon, J. J., Wolfe, A. M., Weiler, K., Genzel, R., Witzel, A., and Booth, R. 1979, *Ap.J.*, 234, 466.

- Junkkarinen, V., Hewitt, A., and Burbidge, G. 1991, *Ap.J.Suppl.*, 77, 203.
- Khare, P., York, D. G., and Green, R. 1989, *Ap.J.*, 347, 627.
- Knapp, G. R. 1990, in *The Interstellar Medium in Galaxies*, eds. H. A. Thronson, Jr. and J. M. Shull (The Netherlands: Kluwer).
- Kronberg, P. P., Perry, J. J., and Zukowski, E. L. H. 1992, *Ap.J.*, 387, 528.
- Kühr, H., Witzel, A., Pauliny-Toth, I. I. K., and Nauber, U. 1981, *Astr.Ap.Suppl.*, 45, 367.
- Lanzetta, K. M. and Bowen, D. 1990, *Ap.J.*, 357, 321.
- Lanzetta, K. M. and Bowen, D. 1992, *Ap.J.*, 391, 48.
- Lanzetta, K. M., Turnshek, D. A., and Wolfe, A. M. 1987, *Ap.J.*, 322, 739.
- Lanzetta, K. M., Wolfe, A. M., Turnshek, D. A., Limin Lu, McMahon, R. G., and Hazard, C. 1991, *Ap.J.Supp.*, 77, 1.
- Lu, L., Wolfe, A. M., and Turnshek, D. A. 1991, *Ap.J.*, 367, 19.
- McCammon, D., Burrows, D. N., Sanders, W. T., and Kraushaar, W. L. 1983, *Ap.J.*, 269, 107.
- McKee, C. F. and Ostriker, J. P. 1977, *Ap.J.*, 218, 148.
- Meyer, D. M. and York, D. G. 1992, *Ap.J.*, 399, L121.
- Mihalas, D. and Binney, J. 1981, *Galactic Structure* (New York: Freeman).
- Morris, S. L., Weymann, R. J., Dressler, A., McCarthy, P. J., Smith, B. A., Terrile, R. J., Giovanelli, R., and Irwin, M. 1993. *preprint*.
- Morton, D. C., York, D. G., and Jenkins, E. B. 1988, *Ap.J.Suppl.*, 68, 449.
- Oke, J. B. and Gunn, J. E. 1982, *Pub.A.S.P.*, 94, 586.

- Perrenod, S. C. and Chaisson, E. J. 1979, *Ap.J.*, 232, 49.
- Peterson, B. M. and Foltz, C. B. 1980, *Ap.J.*, 242, 879.
- Petitjean, P. and Bergeron, J. 1989, *Astr.Ap.*, 231, 309.
- Petitjean, P., Webb, J. K., Rauch, M., Carswell, R. F., Lanzetta, K. 1993, *M.N.R.A.S.*, in press.
- Press, W. H., Teukolsky, S. A., Vetterline, W. T., Flannery, B. P. 1992, *Numerical Recipes in Fortran* (New York: Cambridge University Press).
- Robertson, J. G., Morton, D. C., Blades, J. C., York, D. G., and Meyer, D. M. 1988, *Ap.J.*, 325, 635.
- Rogerson, J. B., York, D. G., Drake, J. F., Jenkins, E. B., Morton, D. C., and Spitzer, L. 1973, *Ap.J. (Letters)*, 181, L110.
- Rohlf, K. 1990, *Tools of Radio Astronomy* (New York: Springer-Verlag).
- Sargent, W. L. W. 1988, in *QSO Absorption Lines*, eds. J. C. Blades, D. A. Turnshek, and C. A. Norman (Cambridge: Cambridge Univ. Press).
- Sargent, W. L. W., Boksenberg, A., and Steidel, C. C. 1988, *Ap.J.Suppl.*, 68, 639. (SBS)
- Sargent, W. L. W., Steidel, C. C., and Boksenberg, A. 1988, *Ap.J.*, 334, 22. (SSB1)
- Sargent, W. L. W., Steidel, C. C., and Boksenberg, A. 1989, *Ap.J.Suppl.*, 69, 703. (SSB2)
- Sargent, W. L. W., Young, P., Boksenberg, A., Tytler, D. 1980, *Ap.J.Suppl.*, 42, 41.
- Sargent, W. L. W., Young, P., Schneider, D. P. 1982, *Ap.J.*, 256, 374.
- Savage, B. D. and Jeske, N. A. 1981, *Ap.J.*, 244, 768.
- Savage, B. D. et al. 1992, Preprint.

- Schneider, D. P. et al. 1992, *Preprint*.
- Shapiro, P. R. and Benjamin, R. A. 1991, *Pub.A.S.P.*, 103, 923.
- Shapiro, P. R. and Field, G. B. 1976, *Ap.J.*, 205, 762.
- Smith H. E. and Spinrad, H., 1980, *Ap.J.*, 236, 419.
- Spitzer, L. 1992, in *Astrophysics: recent progress and future possibilities*, eds. B. Gustafsson and P. E. Nissen (Copenhagen: Munksgaard).
- Steidel, C. C. 1990, *Ap.J.Suppl.*, 72, 1.
- Steidel, C. C. 1992, To appear in *The Evolution of Galaxies and Their Environment*, eds. J. M. Shull and H. Thronson (Kluwer), in press.
- Steidel, C. C. and Dickinson, M. 1992, *Ap.J.*, 394, 81.
- Steidel, C. C. and Sargent, W. L. W. 1992, *Ap.J.Suppl.*, 80, 1. (SS)
- Stoche, J. T., Case, J., Donahue, M., Shull, J. M., and Snow, T. P 1991, *Ap.J.*, 374, 72.
- Swarup, G. 1990, *Indian J. Radio and Space Physics*. 19, 493.
- Thompson, A. R., Clark, B. G., Wade, C. M., and Napier. P. J. 1980, *Astr.Ap.Suppl.*, 44, 151.
- Tytler, D. 1987, *Ap.J.*, 321, 49.
- Tytler, D., Boksenberg, A., Sargent, W. L. W., Young, P., and Kunth, D. 1987, *Ap.J.Suppl.*, 64, 667.
- Veron-Cetty, M.-P. and Veron, P. 1989, *ESO Scientific Report*, No. 7. (VCV)
- Weedman, D. W. 1986, *Quasar Astronomy*, (New York: Cambridge University Press).
- Weinberg, S. 1972, *Gravitation and Cosmology*, (New York: John Wiley & Sons).

- White, R. L. and Becker, R. H. 1992, *Ap.J.Suppl.*, 79, 331.
- Wills, B. J., Netzaer, H., Uomoto, A. K., and Wills, D. 1980, *Ap.J.*, 237, 319.
- Wolfe, A. M., Broderick, J. J., Condon, J. J., and Johnston, K. J. 1976, *Ap.J.*, 208, 47.
- Wolfe, A. M., Turnshek, D. A., Smith, H. E., and Cohen, R. D. 1986, *Ap.J.Suppl.*, 61, 249.
- Yanny, B., York, D. G., and Williams, T. B. 1990, *Ap.J.*, 351, 377.
- York, D. G. 1974, *Ap.J.*, 213, 43.
- York, D. G., Dopita, M., Green, R., and Bechtold, J. 1986, *Ap.J.*, 311, 610.
- Young, P., Sargent, W. L. W., and Boksenberg, A. 1982, *Ap.J.Suppl.*, 48, 455. (YSB)
- . 1978, *Ap.J.*, 222, 757.
- Wolfe, A. M., Lanzetta, K. M., and Oren, A. L. 1992, *Ap.J.*, 388, 17.
- Wright, A. E. and Otrupcek, R. E. 1990, PKSCAT90, The Southern Radio Source Database V1.01.